HAL
open science

Nouvelles applications des ultrasons en cardiologie : quantifier la rigidité des structures cardiaques et la modifier

Olivier Villemain

To cite this version:

Olivier Villemain. Nouvelles applications des ultrasons en cardiologie : quantifier la rigidité des structures cardiaques et la modifier. Imagerie. Université Sorbonne Paris Cité, 2017. Français. NNT : 2017USPCB056 . tel-02180611

HAL Id: tel-02180611

https://theses.hal.science/tel-02180611v1

Submitted on 11 Jul 2019

HAL is a multi-disciplinary open access archive for the deposit and dissemination of scientific research documents, whether they are published or not. The documents may come from teaching and research institutions in France or abroad, or from public or private research centers.

L'archive ouverte pluridisciplinaire **HAL**, est destinée au dépôt et à la diffusion de documents scientifiques de niveau recherche, publiés ou non, émanant des établissements d'enseignement et de recherche français ou étrangers, des laboratoires publics ou privés.

UNIVERSITE PARIS DESCARTES (Paris V)
Ecole Doctorale : Frontière du Vivant / C.R.I.
Laboratoire : Institut Langevin
Spécialité : Physique Acoustique

Thèse de doctorat en Physique

Année 2017

Présentée et soutenue publiquement par

Olivier Villemain

Le mercredi 8 novembre 2017

Nouvelles Applications des Ultrasons en Cardiologie : Quantifier la rigidité des structures cardiaques et la modifier.

Jury de Thèse :

- Dr Julien Magne..... Rapporteur
- Pr Bijan Ghaleh..... Rapporteur
- Pr Damien Bonnet..... Examinateur
- Dr Xavier Iriart..... Examinateur
- Dr Mickael Tanter..... Examinateur
- Pr Emmanuel Messas..... Co-Directeur de Thèse
- Dr Mathieu Pernot..... Directeur de Thèse

Résumé de Thèse

Cette thèse avait pour but d'élargir le champ d'application des ultrasons en cardiologie, dans le domaine de l'imagerie et dans le domaine de la thérapie.

Concernant l'imagerie, ce sont les capacités, les atouts et les limites des ultrasons à hautes cadences d'image (ultrafast echo) qui ont été explorés. Dans un premier temps, nous avons montré la possibilité et l'intérêt d'estimer la rigidité du myocarde par ultrason en pratique clinique, chez l'enfant et chez l'adulte. La technique de l'élastographie par onde de cisaillement, utilisant une nouvelle approche de l'imagerie par sommation cohérente harmonique ultrarapide (imagerie non-linéaire), a été appliquée pour la première fois chez l'humain en cardiologie. De plus, nous avons montré que la rigidité du foie, également estimée grâce à l'élastographie par onde de cisaillement, était directement corrélée aux pressions de remplissage du cœur droit, qui sont difficiles à évaluer de manière quantitative en pratique clinique. Dans un second temps, nous nous sommes intéressés à caractériser l'orientation des fibres myocardiques durant le cycle cardiaque en développant l'imagerie du tenseur de rétrodiffusion ultrasonore en trois dimensions. Le but était de réaliser la preuve de concept sur un cœur battant afin d'ouvrir sur les possibilités d'applications. Dans un troisième temps, le doppler de puissance en ultrafast echo nous a permis d'estimer les capacités des ultrasons à visualiser et analyser les flux (et donc les débits) intra coronariens. C'est à l'heure actuelle la seule technique d'imagerie clinique ayant une résolution spatiale (et temporelle) suffisante pour voir les flux dans des vaisseaux ayant un diamètre inférieur à 500 micromètres. Enfin, l'ultrafast echo nous a permis de visualiser les micro déplacements du myocarde, qui sont eux-mêmes initiés par l'activité électrique intra-myocardique, dans un intervalle de temps très réduit. Ceci est le couplage électromécanique, et y avoir accès par ultrason ouvrirait de multiples perspectives. Nous avons commencé à l'appliquer chez le fœtus humain et chez l'adulte en transthoracique.

Concernant la thérapie, nous avons exclusivement utilisé les effets mécaniques des ultrasons focalisés à hautes intensités (phénomène de cavitation). Plusieurs équipes avaient déjà montré que cela était applicable en médecine cardiovasculaire, notamment pour perforer le septum inter-atrial (zone musculaire séparant les deux oreillettes cardiaques) ou pour détruire un thrombus intravasculaire. Nous avons décidé de montrer que le phénomène de cavitation peut avoir deux autres applications distinctes : 1) la section de cordage valvulaire mitral, qui est une technique utilisée actuellement en chirurgie (donc à cœur ouvert et en circulation extra-corporelle) visant à diminuer une fuite valvulaire à cause de cordage restrictif ; 2) l'assouplissement des feuillets valvulaires calcifiés, qui est une maladie représentant un enjeu de santé publique touchant des millions de personnes, et n'ayant à ce jour aucune stratégie non invasive disponible et applicable en pratique clinique. Pour ces deux applications, nous avons réalisé des preuves de concept in vitro puis in vivo à cœur battant, sur modèle animal (ovin). L'application humaine sera la prochaine étape.

C'est donc la translation de nouvelles technologies ultrasonores vers des applications cliniques en cardiologie qui a motivé et guidé ce travail de thèse.

Remerciements

A mes mentors durant cette thèse

A **Mathieu Pernot (dit « Dr Pernot », dit également « l'Homme qui connait mieux la cardio que les cardiologues »)**, mon directeur de thèse. En écrivant ces quelques lignes sur toi, je pense surtout à nos heures de discussions sur tous les projets dans lesquels tu as eu le courage et l'envie de m'intégrer, à nos débats toujours enrichissants et constructifs, et aussi à nos fous rires sur tout et n'importe quoi (mais surtout sur n'importe quoi). Je pense aussi à nos heures en voiture, à nos heures de manip', à nos heures de préparation de manip', à nos heures de modification de manip' et parfois, à nos manip' qui ont roulé comme sur des roulettes (j'en ai compté 4 sur 1259). Mais finalement, durant ces trois années à tes côtés, je pense que c'est surtout ta capacité à nous encadrer et à nous soutenir (nous tes thésards) qui m'a le plus marqué. Tu as été un manager exceptionnel, par ton soutien et ta présence quotidienne, par ton envie de transmettre et de continuer à t'enrichir de la curiosité des plus jeunes comme moi, et par ton désir du travail propre (du moins intellectuellement car c'est clair que ton bureau est toujours dans un état franchement bordelique). Merci pour ta confiance, ton soutien et ta merveilleuse bienveillance à mon égard. Merci aussi de m'avoir toujours mis dans les conditions optimales pour que je donne le meilleur de moi-même.
J'avais conscience en commençant dans ton équipe à Langevin que tu prenais un risque un embauchant un « médecin » dans ce monde de physiciens. Grâce à toi, j'ai pu tout donner pour faire de mon mieux.
Tu resteras pour toujours mon directeur de thèse, mais dans mon cœur tu es devenu un ami et un modèle.

A **Emmanuel Messas** (**dit « Le Boss », dit également « l'Homme qui fera un jour son 20h à TF1 »**), mon co-directeur de thèse. Merci Emmanuel de m'avoir accueilli si chaleureusement et si positivement dans nos projets. Tu m'as dès le début donné les moyens et les libertés de m'investir totalement afin que je puisse y apporter un maximum. Tes nombreux conseils ont toujours été bienveillants et constructifs. Me dirigeant vers la cardiologie congénitale, nous savions dès le début que mon investissement se limiterait à nos projets de recherche mais nous avons su optimiser cela. Durant ma première année, tu m'as remonté le moral plus d'une fois (« mais t'inquiète, c'est normal que tous les moutons meurent au début ! Moi à Boston j'ai en tué 60 avant d'en avoir un qui ait tenu… ! »). Tu étais à la fois extrêmement positif et motivant, tout en restant très attentif à mes difficultés et mes problèmes sur les projets. Tu as pris le relai quand il fallait (avec cette très chère URC-CIC notamment…). Et puis qu'est-ce que tu m'as fait rire… Tout en restant toujours exigeant !
Toi aussi, comme Mathieu, tu faisais un pari en aidant un jeune médecin qui n'était pas destiné à travailler dans ton unité. Notre productivité scientifique, je l'espère, aura été à la hauteur de tes attentes.

A **Mickael Tanter (dit « Micka », dit également « l'Homme le plus cool du monde »)**, directeur de mon labo de recherche. Tu m'as accueilli dès le début comme un des vôtres, en

m'aidant à m'intégrer et à partager avec tes équipes. Toujours le sourire, toujours positif, toujours exigeant mais respectueux du travail accompli. J'ai dit à ma femme que j'aimerai bien te ressembler un jour… En plus tu es hyper beau gosse ! Ahahah ! Un immense merci.

Aux autres membres du jury :

A **Damien Bonnet (dit « Monsieur Bonnet », dit également « l'Homme qui est plutôt fort en cardiologie pédiatrique »)**, mon Chef de service. Vous m'avez toujours consacré le temps qu'il fallait, même si je sais qu'avec vous il ne faut pas perdre de temps. Merci pour votre bienveillance et votre soutien à mon égard, depuis le début. Vous m'avez fait aimer votre spécialité médicale, vous m'avez poussé à aller m'exercer un peu aux Antilles (« Ce sera bien pour toi, c'est complémentaire. Et puis faut aller voir ailleurs quand on est jeune »), vous m'avez fait faire une belle thèse de médecine. Et surtout, vous m'avez fait confiance durant cette thèse de science loin de vous et de votre service, tout en m'aidant et me conseillant quand il le fallait.

A **Xavier Iriart (dit « Xavi », dit également « l'Homme au pouce en or »)**. Tu es devenu un ami il y a quelque temps, grâce à une sombre personne qui nous a reliés. Mais si tu es là, dans mon jury, c'est pour tes qualités de médecin, d'échographiste reconnu, et de personne toujours curieuse et avide d'échanger sur la médecine et ses évolutions. Après l'histoire ne dira jamais si tu n'es pas plutôt venu principalement pour le pot et la grosse soirée qui sont prévus après la soutenance…

A **Julien Magne (dit « il est sympa et très fort celui-là il parait, ce serait super qu'on lui propose d'être dans le jury de thèse »)**. Merci pour votre envie de partager sur des thématiques qui nous rapprochent. Vous êtes un chercheur qui travaille au milieu de médecins, et à nouveau vous faites l'effort aujourd'hui de venir dans un environnement nouveau pour discuter, recevoir et transmettre. Un bel exemple à suivre.

A **Bijan Ghaleh (dit « l'Homme qui est toujours souriant et motivé alors qu'il a eu des triplés ! »)**. Merci pour ta disponibilité et ton enthousiasme pour venir échanger durant cette soutenance. Ce fut un réel plaisir de venir travailler dans ton équipe à Créteil durant les différents projets sur lesquels nous avons collaboré. Un plaisir humain, car tout le monde était particulièrement sympa, et un plaisir intellectuel à travers nos échanges et nos discussions toujours enrichissantes et exigeantes.

A ma famille :

A ma femme **Marine (dit « Amour », dit également « Heureusement que j'ai ma femme dans ma vie… »)**. Nous avons la chance de tout partager, de tout se dire et surtout, de savoir se dire les choses qui vont bien. Donc tu sais déjà tout. Mais je vais quand même profiter de ces quelques lignes pour te rappeler ceci :

- Tu es la plus belle chose qui soit arrivée dans ma vie et, les années passant, j'en suis de plus en plus certain. Tu es une femme exceptionnelle, et tu es ma femme. Plus j'y pense, plus je me dis que j'ai vraiment eu de la chance que tu aies toujours cru en moi, tu m'aies toujours respecté dans mes choix, et que tu m'aies toujours soutenu.
- Je suis extrêmement fier de toi et des choses que tu entreprends. On est encore jeunes, la vie nous prépare des surprises (bonnes ou mauvaises), on a déjà vécu quelques surprises (bonnes ou mauvaises), mais on croit plus que tout à notre bonheur. Et je sais que quand on sera un peu plus vieux, on sera fiers de nous. On se regardera, dans les yeux, et puis on sourira…
- Tu es devenue la mère de mes enfants durant cette thèse de science. Si je résume : on a commencé à faire des manips ensemble, parfois ça a marché, parfois non (comme d'hab quoi), mais nos résultats finaux sont tellement intéressants que ça donne vraiment envie de continuer sur ce projet et d'obtenir d'autres résultats ! Je te laisse écrire le projet de recherche et on voit ensemble si on a le financement pour se lancer…
- Je t'aime

A ma petite fille **Joséphine (dit « Bibou »).** Après Délibération du jury, tu as été élue la plus belle trouvaille de l'ensemble de mon travail de thèse. Je suis déjà si fier de toi… Nous relirons ensemble dans quelques années ces lignes écrites en aout 2017 et cela nous permettra de nous rappeler tous les bons moments passés ensemble depuis ta naissance, tous les bisous que je t'ai faits (et que tu m'as faits en retour), et de se faire un câlin car c'est probablement quand je t'ai dans mes bras que je me sens le mieux.

A mon petit bébé **Romy (dit « Bébé Romy », mais encore en attente d'un surnom officiel)**. Voilà, ton papa a fini ses études. A ton tour maintenant… Mais avant de te lancer dans ces choses sérieuses, n'oublie pas d'apprendre à sourire, à rire, à pleurer, à observer et souvent j'espère à t'émerveiller. Bon, faudra aussi apprendre à marcher, parler et manger mais ne t'inquiète pas, ton Papa sera toujours là pour t'aider (si tu en as besoin bien entendu).

A **mes parents**, qui m'ont appris à aimer la vie, à aimer être curieux, à aimer découvrir et comprendre les choses. Vous m'avez surtout toujours apporté l'affection dont on a besoin pour croire en soi. Et croyez-moi, un jeune chercheur a besoin d'avoir un bon moral…

A **mes frères et sœur**, qui ont toujours été mes amis et mes moteurs. Quand je regarde 20 ans en arrière, j'aurais tout donné pour nous voir tous les 4 dans l'état dans lequel on se trouve aujourd'hui. Ça a marché, on a assuré. RDV dans 20 ans, autour d'un bon whisky, en se marrant parce que on aura tout foutu en l'air. Eheheh.

A **ma grand-mère (dit « Mamine »)**.

A ma belle-famille, notamment à **Anne** et à **Bernard**, mes beaux-parents. Vous m'avez toujours accueilli avec l'affection et la gentillesse qui donne envie de vite revenir passer du temps avec vous. Vous voudriez me voir plus, je le sais, mais sachez que c'est réciproque. Encore merci pour tout votre temps consacré à mes enfants, ça me rend extrêmement heureux.

Et à **Achilles (dit « H »)**, mon petit filleul qui nous a quitté beaucoup trop vite. En rédigeant cette thèse, j'ai beaucoup pensé à toi. En fait, je pense à toi tous les jours, sans exception je pense. Tu me manques, j'espère que tu es bien là où tu es.

A mes collègues et amis durant cette thèse :

A **Mafalda (dit « Maf' », dit également « ma petite biche »).** J'ai bien réfléchi, et il m'est paru évident de te citer en premier. Du début à la fin, on a fait les trucs ensemble. Tous les projets, on les a partagés et on s'est mutuellement apporté. Merci pour ta patience à mon égard, merci pour tes sourires, merci pour tes pétages de plombs où tu te mets à gueuler puis à devenir toute rouge. Merci pour ta rigueur, ton exigence, et ta soif inépuisable de comprendre les choses.

A **Justine (dit « Just-In », dit également « ma petite biche », même si ça t'a fait péter un câble)**. On est vite devenu potes et on a toujours bien bossé ensemble. J'ai aimé ta patience, ton plaisir du travail bien fait, et ton franc parler. Tu pèses 50 kg toute mouillée mais j'ai jamais eu envie de trop t'emmerder… J'ai pas aimé ton obsession pour le rangement, notamment pour mes tasses de café. Ça c'est le truc qui me rend heureux d'avoir fini ma thèse ; je vais enfin pouvoir foutre le bordel tranquille sans toi dans les parages…

A **Hicham (dit « l'Homme le plus beau de l'Institut Langevin »)**. Mec, on s'est connu car on devait fabriquer une pompe hydraulique qui devait faire office de cœur artificiel. Tu m'as fait découvrir les cartes arduino, les joints étanches et les impressions sur machine 3D. Je t'ai fait découvrir l'OM, Mario Kart et les pizzerias du coin. Chacun ses forces mon pote, mais bordel qu'est ce que j'ai aimé bossé avec toi mon vieux. Je te souhaite le meilleur.

A Bastien **(dit « Le Cérébral »)**. Beaucoup de manip, d'apprentissage et de conseils à tes côtés. Tu as été hyper précieux pour ma thèse. Tu es un gars en or. J'espère que ça se passe à Grenoble, et que tu es heureux.

A **Wojciech (dit « l'Homme le plus calme du monde »).** Tu m'as accompagné durant mes premiers pas de néo-chercheur, tu m'as manqué durant mes derniers pas de vieux thésard. Toi, quand tu fais quelque chose, tu le fais toujours bien. Une des qualités les plus précieuses à mes yeux.

A **David (dit « Mate », dit « l'Homme qui murmurait aux ostia des coronaires »**). On s'est quand même bien marré sur nos manips à Créteil, entre les libanais et autres conneries… Notre trip à Séville restera mon meilleur souvenir avec toi. Deux potes qui présentent leur boulot ensemble. Et tu nous manques à Paris maintenant ! J'espère que Los Angeles vaut vraiment le coup…

A **Victor (dit « l'Homme qui était complètement taré »)**. Tout a commencé avec un petit séjour à Bordeaux pour des manips (ou plutôt pour des bonnes bouffes et du bon pinard…). Il nous reste des projets à conclure, alors ça me rassure. On va continuer à se voir et ça c'est bien cool !

A **Clément (dit « Papadacci », dit également « Allez l'OM »)**. Durant ma thèse, ce type a gagné tous les prix de thèse qui existent (soit un pactole de 952.000 euros il parait), il a vécu à New-York, il s'est marié au Brésil puis il est revenu au labo. Une machine.

A **Martin (dit « l'Homme le plus mauvais à Mario Kart, quelque soit la console »**). Tu m'as fait beaucoup rire, tu étais un peu barjo mais un barjo qu'on aime, qui nous fait marrer et qu'on a envie de faire rire. Toujours un plaisir de rentrer dans votre bureau les gars pour vous marcher dessus.

A **Stéphane (dit « l'Homme qui avait le corps d'un conseiller fiscaliste mais le cerveau de sociopathe multirécidiviste »)**. Un jour ou l'autre mon pote on va se recroiser, à l'hôpital ou dans ta start-up, et là ça va faire très mal…

A **Jérome (dit « l'Homme qui code plus vite que son ombre »)**. Merci pour tous tes petits coups de main, du code doppler aux multiples GUI pour médecin (donc 2 boutons maxi mon gars !). Et merci pour ce projet passionnant sur les bruits de Korotkoff. On va le finir celui-là !

A **Charlotte (dit « la Femme la plus relax du XXIème siècle »)**. A nos soirées à Tel Aviv, à nos checks dans le bureau. Toujours le sourire, toujours le mot sympa, toujours attentive et dispo. Bref, la meuf au top !

A **Ilya**, mon stagiaire qui a bien bossé comme un stagiaire qui bosse dur. Tu n'as jamais rien lâché, alors que je t'en demandais toujours un peu plus. Une belle rencontre, j'espère que tu es heureux mon vieux (et que ta copine arrête de te faire des nœuds dans la tête ! Merde alors !).

A **Guillaume (dit « Tiens voilà enfin un collègue médecin dans le labo »)**. Bon courage mon vieux pour la suite de tes projets, j'espère que ça va bien avancer comme tu le souhaites.

Et les autres, tous aussi précieux :

- A **Olivier Couture**, toujours cool et curieux
- A **Jeff**, Mister thérapie du cerveau
- A **Khadija**, notre mère à tous. Eduquer, c'est répéter… Merci pour tout !
- A **Alex**, l'homme multi fonction du labo qui a toujours une solution à tout
- A **Philippe**, ses pièces, ses vidéos et ses indispensables coup de main
- A **Thu-Mai**, toujours souriante.
- A **Marion**, j'espère une future collègue médecin !!
- A **Line**, aussi tarée que sympa !
- A **Marc** et son torse velu, précieux pour nos manips en tout genre.
- A **Elodie**, et ton petit bébé.
- A **Gioia**, qui nous a quittés un peu trop vite !
- A **Manu**, supporter de Caen, qui un jour comprendra que l'OM c'est beaucoup mieux
- A **Julie Piquet**, qu'est ce que j'aurais fait sans toi au PARCC à l'HEGP… ? Merci !
- A **Bijan Ghalet,** un plaisir de bosser avec toi et tes équipes.
- A **Thibaud Damy**, il arrive notre papier sur l'amylose, promis !

A mes potes, pour la plupart embarqués dans de sales histoires…:

A **Adrien (dit « Gros »),** mon meilleur ami. On ne lâchera jamais rien mon pote et dans 40 ans, on sera toujours là l'un pour l'autre (toi toujours à me demander un peu de blé pour passer le cap…).
A **Natacha (dit « Nata »),** que j'ai souvent eu envie de prendre dans mes bras cette année (désolé Gros, le prends pas perso).
A **Victor (dit « Pouchet »)**, l'auteur de « Pourquoi les oiseaux meurent ». Tu as publié en français, allemand, espagnol, chinois, peut-être même un jour en martien. Mais avant tout, tu es le parrain de ma fille Romy. Je suis fier de toi mon pote, je t'aime.
A **Marianne,** qui m'a donné des cours d'anglais et à qui en échange je donnais des cours d'histoire de littérature indienne.
A **Gilles (dit « Gitoun même si on comprend pas le lien entre ce surnom et lui »).** Durant ma thèse, tu as décroché un taf, tu t'es marié, tu es devenu un mec sans intérêt en fait. Réagis ma poule, je ne serais peut-être pas toujours là pour toi.
A **Manon (dit « Gitoun, son surnom depuis qu'elle est toute petite »)**. Promis, ma prochaine thèse portera sur ta maladie générale encore inexpliquée. On va trouver !
A **Gagey (dit « Antoine »)**, que je trouve particulièrement stylé en jeune papa. Je suis fier de toi mon pote, ta fille est belle dans tes bras.
A **Mélanie (dit « Mééééél, assieds-toi, faut que je te parle »)**. Bon courage avec Gagey, plus que 53 ans à tirer…
A **Vassili (dit « Vass »)**. Ma thèse de science a permis de nous retrouver sur le terrain de foot, à l'EFCAP. C'était bon de te revoir me faire des passes pour que je dribble toute l'équipe et que je plante le but de la victoire.
A **Elodie (dit « Elo »)**, que j'aimerais voir un peu plus. On te voit moins !

A **Zak (dit « ma Teub », dit également « mon amant-ami-frèrot-collègue »)**. Putain ma poule dire que tout a commencé dans le Social Club… Tant de souvenir avec toi, avant et pendant cette thèse. Les Etoiles ma Teub, les Etoiles… Merci pour ton soutien et ton amitié indéfectible depuis notre rencontre.
A **Elsa (dit « Elso »)**. Votre mariage restera pour moi un moment gravé à vie. Tu étais belle, tu étais forte, tu étais toi !

A **Karim (dit « Bény », dit « l'Homme le plus malsain du XXIème siècle, si on exclut Bol le pote de Zak »)**. Merci d'être devenu ce type infréquentable, complètement déséquilibré et à haute probabilité de mourir bientôt lors d'un règlement de compte pour affaire de mœurs. Je t'aime mon pote.
A **Mansour (dit « Kara ? Mais tu es de la famille de… »)**. Dans quelques années, c'est moi qui viendrai écouter ta soutenance de thèse et je me dirai qu'on aura fait du bon chemin ensemble… RDV dans 10 ans ma poule, pour des projets encore plus fous.
A **Arnaud (dit « le sosie d'Edouard Philippe »)**, mon pote d'enfance. On se voit tous les 6 mois mais on se connait par cœur. Ça fait 30 ans qu'on se connait ma poule ! Tu es le numéro un.
A **Bigy et JM (dit « Guillaume et Jean Mathieu »)**. Rien que de penser à vous, je me marre…
A **Nico Deville**, que je ne désespère pas à recruter pour la saison 2018-2019. Le Neymar du pauvre en fait…
A **Jérèm et Cam**, loin des yeux, près du cœur, et surtout tellement stylés à LA !
A **Yann (dit « Bog' »)**, qui clairement en a rien à branler de ma thèse de science…
A **Aldric (dit « Al' »)** et à sa **Cam (dit « la meuf un peu hypochondriaque mais ça va encore »)**. On vous kiffe vous deux ! Je reste encore hyper surpris qu'Al soit arrivé à te chopper Cam, tu vaux tellement mieux…
Aux potes du Cap, **Schaeff, Naill, Vince, le Porc du Port, et j'en passe**… On ne se voit pas assez les gars, mais quand on se voit c'est toujours du lourd bordel.

A mes co-chefs de clinique, devenu mes amis. A **Meriem (dit « Dr Kara »)**, tu vas me manquer toi en novembre. Le jour de ma soutenance, tu ne seras plus à Necker… ça craint ça. Tu es au top meuf. A **Mathilde (dit « la sexopathe refoulée (mais pas tant refoulée que ça) »)**, meuf je voulais te dire que j'étais hyper heureux de continuer l'aventure avec toi à Necker. **A Véro (dit « la psychopathe incomprise du grand public »)**, tu es une tornade niveau 5/5 mais à mon contact j'ai l'impression que tu t'es un peu calmée… Nan je déconne ça n'a rien changé du tout tu es toujours aussi tarée. Et à **Suzanne**, que je vois deux fois moins que ce que j'aimerais ! ;)

A **Younes (dit « Boss »)**, parti loin prendre un peu l'air, qui a toujours été bienveillant et un soutien pour moi. Notre boulot sur l'élastographie hépatique aura été un succès, j'aurais tellement aimé faire pleins d'autres trucs avec toi… Peut-être plus tard !

A **Hugues et Alex**, mes potes de Martinique. Vous me manquez les gars. C'était quand même hyper bon ces six mois ensemble chez vous.

Les potes de ma meuf, que j'ai eu le malheur d'apprendre à connaitre : **Clarisse et son pauvre mec** (vous êtes bons tous les deux quand même), **Constance et Guillaume** (les kiffeurs de New-York), **Coco et son mec que je kiffe** (Bakayoko transféré à Chelsea !), **Luigy et Victoire** (qui s'est grave calmée depuis que c'est une daronne) et Charles, **Lolo et sa meuf** (bon vent en Belgique, j'espère que ça va le faire, vous le méritez !), **Pierre et Eloise** (que j'adorerais mieux connaitre)

Enfin, aux cochons, brebis, lapins, rats, souris, babouins et parfois humains qui m'ont accompagné durant ces projets de recherche…

Merci à tous

Liste des Abréviations

2-D : 2-Dimensations
3-D : 3-Dimensations
BNP : brain natriuretic peptide
CMH : cardiomyopathie hypertrophique
dB : décibel
ECG : électrocardiogramme
EWI : electromechanical wave imaging
FC : fréquence cardiaque
HIFU : high-intensity focused ultrasound (ultrasons focalisés de haute intensité)
I_{SPTA} : spatial peak temporal average intensity
IC : insuffisance cardiaque
IC-FEp: insuffisance cardiaque à fraction d'éjection préservée
IC-FEr: insuffisance cardiaque à fraction d'éjection reduite
MI : mechanical index
NT-proBNP: N-terminal pro-brain natriuretic peptide
PVC : pression veineuse centrale
RAC : rétrécissement aortique calcifié
RF : radiofréquence
RH : rigidité hépatique
SVD : singular value decomposition
TAVI : transaortic valve implantation
TVI : tissue velocity doppler
SWE : shear wave elastography (élastographie par onde de cisaillement)

Table des matières

1. Introduction……p.14
   1.1. Etat de l'art de l'échocardiographie
   1.2. Echographie conventionnelle et ultrarapide
   1.3. Possibles effets des ultrasons sur les tissus biologiques
   1.4. Objectifs du travail de thèse

2. Elastographie myocardique……p.20
   2.1. Introduction et Objectifs
   2.2. Travaux fondamentaux
      2.2.1. **Manuscrit** "*Ultrafast harmonic coherent compound (UHCC) imaging for high frame rate echocardiography and shear wave elastography"*
      2.2.2. **Manuscrit** "*Validation of a non-invasive Myocardial Shear Wave Elastography device for clinical applications in cardiology"*
   2.3. Applications chez l'enfant
      2.3.1. Présentation du travail
      2.3.2. **Manuscrit** "*Myocardial stiffness assessment using shear wave imaging in heathy children and hypertrophic cardiomyopathy"*
   2.4. Applications chez l'adulte
      2.4.1. Présentation du travail
      2.4.2. **Manuscrit** "*Myocardial stiffness and aging: non-invasive shear wave imaging evaluation in healthy and hypertrophic cardiomyopathy adults"* (In review)
      2.4.3. **Manuscrit** "*Myocardial stiffness in cardiac amyloidosis and heart failure*" (In preparation)
   2.5. Perspectives

3. Elastographie hépatique……..…….……p.117
   3.1. Introduction et Objectifs
   3.2. **Manuscrit** "*Towards non-invasive assessment of central venous pressure using real time and quantitative liver stiffness estimation"*
   3.3. Perspectives

4. Imagerie des fibres myocardiques par ultrasons……...p.154
   4.1. Introduction et Objectifs
   4.2. **Manuscrit** "*Imaging the dynamics of cardiac fiber orientation in vivo using 3D Ultrasound Backscatter Tensor Imaging*"
   4.3. Perspectives

5. Imagerie des flux coronaires par ultrasons…….p.168
   5.1. Introduction et Objectifs
   5.2. **Manuscrit** "*Non-invasive imaging of the coronary vasculature using ultrafast ultrasound*" **+ Editorial Comment**
   5.3. Perspectives

6. Couplage électromécanique……..p.188
   6.1. Introduction et Objectifs
   6.2. **Manuscrit** "*Electromechanical wave imaging in human foetus*" (In preparation) et Perspectives

7. Thérapie par ultrasons focalisés……...…p.198
7.1. Introduction et Objectifs
7.2. Section de cordage valvulaire
7.2.1. Présentation du travail
7.2.2. **Manuscrit** "*Pulsed cavitational ultrasound for non-invasive chordal cutting guided by real-time 3D echocardiography"* **+ Editorial Comment**
7.3. Valve calcifiée
7.3.1. Présentation du travail
7.3.2. **Manuscrit** "*Pulsed Cavitational Ultrasound Softening: a new non-invasive therapeutic approach of calcified bioprosthetic valve stenosis"* **+ Editorial Comment**
7.4. Perspectives

8. Perspectives générales…...……..p.237

9. Conclusions……..p.240

10. Références bibliographiques (autres que celles incluses dans les manuscrits)……..p.242

11. Résumé du travail scientifique……..p.249

1. Introduction

1.1. Etat de l’art de l’échocardiographie

Il est devenu coutumier de commencer tout travail sur l’imagerie cardiaque en rappelant que « les maladies cardiovasculaires sont la première cause de mortalité dans le monde ». Mais on oublie parfois de rappeler que la prise en charge optimale d’une maladie commence par un diagnostic précis et fiable. Et pour être précis et fiable, il faut voir les choses, les comprendre et pouvoir les analyser. L’imagerie cardiaque, quel que soit la technique utilisée (ultrasons, rayon X, résonnance magnétique voire imagerie nucléaire), est l’outil de première ligne du cardiologue pour faire un bon diagnostic, donc une bonne prise en charge. L’amélioration de nos outils d’imagerie cardiaque est donc devenue un enjeu majeur de santé publique, nécessitant une recherche fondamentale innovante poussée vers des applications utiles aux patients.

Les ultrasons dans le domaine médical (l’échographie) sont utilisés depuis plus de 40 ans. Cette méthode d'imagerie est non-invasive, facile à utiliser, relativement portable, sûre, non dispendieuse, et des acquisitions peuvent être faites en temps réel. Dans le domaine cardiovasculaire, par exemple, l'échographie est devenue l'un des principaux systèmes d'imagerie médicale et est utilisée dans pratiquement tous les hôpitaux et cliniques pour le diagnostic des maladies cardiovasculaires.

L'échographie est basée sur le principe pulse-écho. Une onde ultrasonore est transmise (impulsion) par un transducteur fait de cristaux piézo-électriques ou un transducteur micro-usiné capacitif (CMUT), qui oscille lorsqu'un signal électrique lui est appliqué. Ce signal électrique est ainsi converti en une onde cinétique ou mécanique, l'ultrason. Cette onde ultrasonore lorsqu’elle interagit avec les tissus biologiques, peut être réfléchie et/ou diffusée en fonction des propriétés acoustiques du tissu, et ce processus va former un écho. Cet écho peut être reçu par le transducteur ultrasonore, et on pourra alors former une image, en convertissant l'énergie mécanique en énergie électrique, et à l’aide d’un post-traitement de l'information. Les ultrasons ne peuvent pas passer à travers les os ou les poumons, qui sont pleins d'air. Par conséquent, pour l'imagerie cardiaque non invasive l'utilisation de sondes « phased-array » est essentielle (figure 1), car elles pourront être positionnées dans de petites fenêtres d’imagerie (entre les côtes, etc…). Diverses méthodes de transmission, de réception et de post-traitement des ondes ultrasonores ont donné lieu à des techniques d'échographie distinctes qui permettent d'analyser de façon différente l’interaction des échos dans les tissus biologiques. Les techniques d’ultrasons conventionnelles et ultrarapides en sont deux exemples.

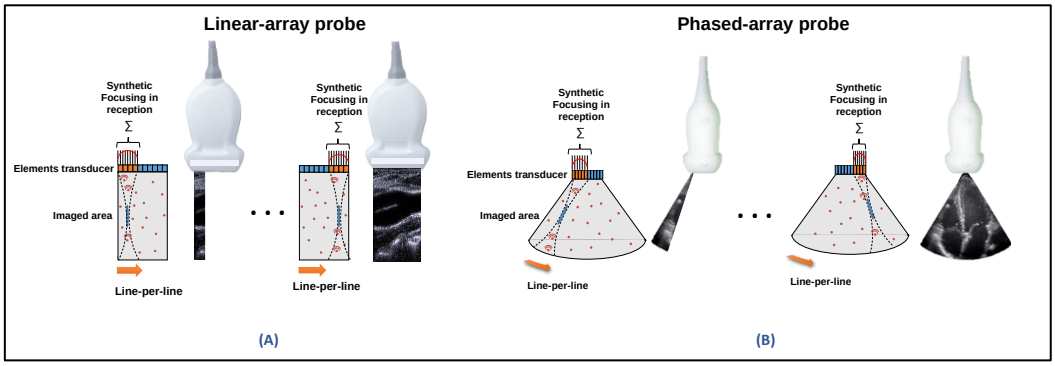

Figure 1 : Sondes « linear-array » et sondes « phased array »

1.2. Echographie conventionnelle et ultrarapide (figure 2)

L'imagerie conventionnelle est basée sur le scan ligne par ligne du milieu en utilisant des faisceaux focalisés. Ces faisceaux focalisés sont construits grâce à des lois de retards appliquées sur l'onde émise par chaque élément du transducteur. Les hétérogénéités du milieu le long de la ligne balayée reflètent le faisceau focalisé, puis les échos rétrodiffusés sont reçus par le transducteur. En ajustant la loi de retard en réception, les ondes sont focalisées en réception également, et chaque ligne de l'image peut être reconstruite (focalisation en synthétique). Pour reconstruire une image complète, il est nécessaire de répéter ce processus pour toutes lignes et temps, ce qui signifie que l'on doit effectuer plus d'une centaine de répétitions. Avec cette méthode, il est possible d'imager le corps humain en temps réel, avec des fréquences d'imagerie allant jusqu'à 100 images/s. Différents types d'imagerie ultrasonore conventionnelle, utilisant l'effet Doppler, sont utilisés en pratique clinique pour étudier les flux sanguins.

Au contraire de l'imagerie dite « conventionnelle », l'imagerie ultrarapide est basée sur l'insonification du milieu par les ondes planes ou divergentes, à la place des faisceaux focalisés décrits précédemment, ce qui permet l'augmentation de la cadence d'imagerie jusqu'à 20.000 images/s. Les ondes planes et divergentes sont générées en appliquant une loi de retard plane ou circulaire sur les éléments du transducteur. Dans les deux cas, il est possible de reconstruire toute une image avec une seule émission, ce qui n'est pas possible pour l'imagerie ultrasonore conventionnelle. En revanche, la résolution et le contraste de ces images sont dégradées. Une façon de surmonter cette limitation est la somme cohérente des

échos rétrodiffusés. La première application médicale de l'imagerie ultrarapide a été l'imagerie de la rigidité des tissus mous, grâce à l'élastographie par des ondes de cisaillement ou palpation à distance par force de radiation acoustique. Cette technique se montre notamment très pertinente pour accéder à des changements de rigidité tissulaire (comme dans une tumeur). L'imagerie Doppler ultrarapide a été également développée pour l'imagerie du cerveau et sa sensibilité a été augmentée par le filtre spatiotemporel SVD (décomposition sur des valeurs singulières) développé au sein de l'Institut Langevin. Récemment, l'imagerie ultrarapide en trois dimensions a été aussi étendue grâce au développement d'un prototype d'échographe ultrarapide avec 1024 voies électroniques (en matrice 32x32), permettant l'extension de nouvelles méthodes d'imagerie en trois dimensions, notamment l'élastographie et l'imagerie Doppler.

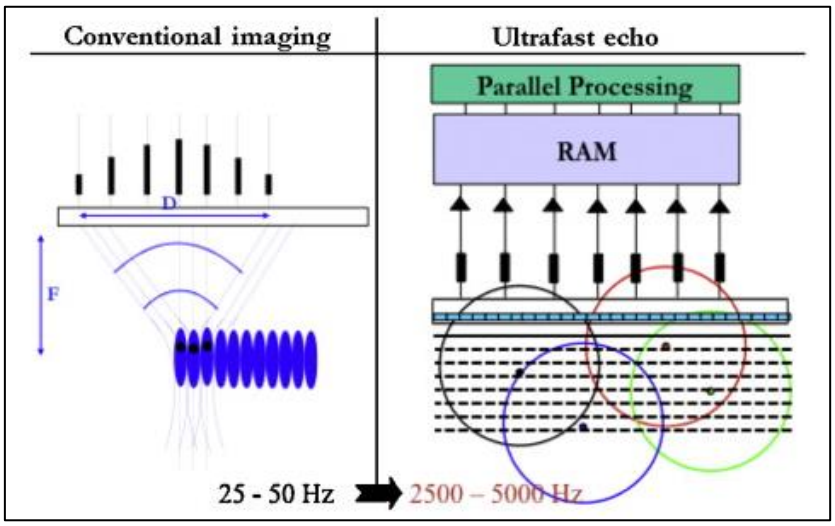

Figure 2 : Imagerie ultrasonore en conventionnel et en ultrarapide

1.3. Possibles effets des ultrasons sur les tissus biologiques

C'est grâce aux travaux de Paul Langevin que le premier générateur d'ultrasons sous forme de sonar a été créé pendant la première guerre mondiale, faisant usage pour la première fois de la piézoélectricité. Les effets biologiques des ultrasons ont été rapportés dès les années 1920 par les chercheurs américains Alfred Lee Loomis et Robert W. Wood (Tempany et al. 2011). Par la suite, les ultrasons focalisés de haute intensité, plus connus sous les initiales anglaises HIFU (high intensity focused ultrasound) ont été étudiés pour la première fois en 1942 pour l'ablation de tissus biologiques, par le Dr John G. Lynn (Jenne

and et al 2012). Les frères Fry, Francis et William, ont développé cette technique entre les années 1950 et 1960 et ont mené les premiers tests cliniques sur la maladie de Parkinson traitée par HIFU (Bailey et al. 2003). Depuis, de nombreuses applications médicales ont été imaginées puis mises en oeuvre, donnant lieu à de nombreux dispositifs ultrasonores différents.

L'échographie interventionnelle, c'est-à-dire l'utilisation d'ultrasons à haute intensité ou/et basse fréquence afin d'avoir un impact physique sur les tissus, existe grâce à deux principaux phénomènes biophysiques : la dissipation thermique et la cavitation. A l'heure actuelle, en application médicale, il existe quatre principaux types d'application à l'échographie interventionnelle : l'ablathermie, la lithotripsie, la sonothrombolyse et l'histotripsie. Chacune de ces applications exploite un des deux phénomènes biophysiques, voire les deux.

A titre d'exemple, l'ablathermie utilise exclusivement l'effet thermique des ultrasons focalisés. L'échauffement localisé, typiquement de plus de 60°, est provoqué par une exposition prolongée (ou continue) d'HIFU en un point. Cet échauffement entraine la coagulation des vaisseaux et la mort cellulaire (nécrose ou apoptose selon l'énergie ultrasonore délivrée) (REF).

A contrario, l'histotripsie utilise exclusivement l'effet mécanique des ultrasons focalisés, aussi appelé phénomène de cavitation. C'est l'application d'impulsions (ou « pulse ») ultrasonores de très courte durée (1-2 ms par exemple) à très haute intensité (> 10.000 W/cm2) qui crée des variations de pressions (positive et négative) au sein de la tâche focale, et l'apparition du phénomène de cavitation (Plesset 1949). D'un point de vue plus général, le phénomène de cavitation est la formation d'une cavité au sein d'un tissu ou d'un solide. Le changement brutal de pression, étant la résultante d'impulsions ultrasonores de très haute intensité, crée cette cavité et force le gaz dissous dans le tissu ou le liquide à se rassembler, et donc à former un nuage de bulles. Si ces impulsions sont répétées, à fréquence donnée (de l'ordre de 20 Hz à 1 kHz), ce nuage sera excité en permanence et les bulles continueront à osciller en se réorganisant continuellement de manière aléatoire. Ce mouvement de gaz et ces variations de pressions vont engendrer une fragmentation purement mécanique des tissus biologiques adjacents. Cependant, même si cette activité énergétique parait aléatoire, il est tout de même possible de réaliser des lésions de taille reproductible avec des frontières bien définies (Tzu-Yin Wang et al. 2011). Les bulles ne peuvent être générées que dans un périmètre bien défini par la tache focale du transducteur et son champ de pression rayonné.

Il est intéressant d'observer que la géométrie de la tache focale est définie par la géométrie du transducteur en lui-même (diamètre et distance à la tache focale) et par la longueur d'onde (ou la fréquence) de l'impulsion émise (figure 3). Pour faire simple, à géométrie donnée, plus la fréquence sera élevée, plus la tache focale sera petite et précise. Mais plus la fréquence sera élevée, plus l'atténuation énergétique du tissu traversé avant d'arriver à la tache focale sera importante, et donc plus difficile il sera d'obtenir les pressions négatives nécessaires pour déclencher le phénomène de cavitation. C'est à travers cet « équilibre » entre précision et puissance que les possibles applications cliniques devront être discutées.

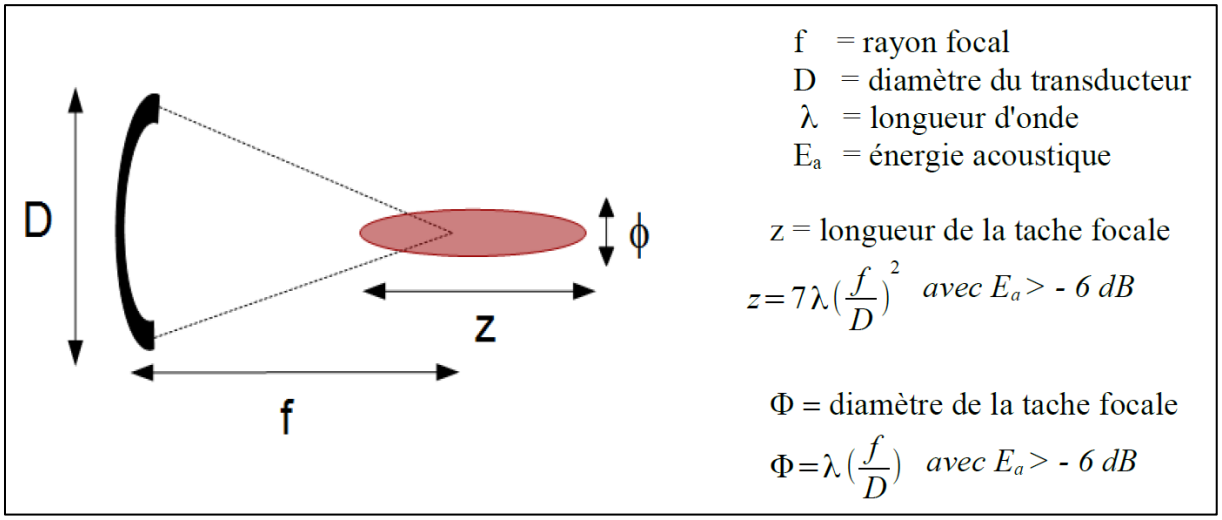

Figure 3 : Tache focale d'un transducteur sphérique mono-élément

1.4. Objectifs du travail de thèse

Cette thèse avait pour but d'élargir le champ d'application des ultrasons en cardiologie, dans le domaine de l'imagerie et dans le domaine de la thérapie. C'est donc la translation de nouvelles technologies ultrasonores vers des applications cliniques en cardiologie qui a motivé et guidé ce travail de thèse.

2. Elastographie myocardique

2.1. Introduction et Objectifs

Le cœur est l'organe musculaire responsable de la perfusion sanguine dans le corps humain. La paroi du cœur est divisée en trois couches musculaires différentes, et le myocarde en est le principal composant. L'évaluation de la rigidité myocardique pourrait aider l'évaluation de plusieurs maladies cardiaques associées aux changements d'élasticité, telles que l'ischémie, les cardiomyopathies et l'insuffisance cardiaque. Cependant, jusqu'à aujourd'hui, la rigidité du myocarde ne peut pas être mesurée de manière non invasive en pratique clinique. Au cours des dernières années, des techniques d'élastographie par ultrasons ou par l'imagerie par résonance magnétique ont été proposées et mises au point pour évaluer les propriétés de rigidité des tissus. Ces techniques permettent la cartographie de la propagation des ondes mécaniques dans le tissu. Plus spécifiquement, des ondes de cisaillement à basse fréquence peuvent être induites et suivies afin d'estimer leur vitesse de propagation (qui se situe généralement entre 1 et 10 m/s), qui est directement liée à la rigidité du tissu par le module de cisaillement (μ), défini par l'équation :

$$\mu = \rho\,(Vc)^2$$

avec ρ correspondant à la masse volumique et Vc correspondant la vitesse d'onde de cisaillement.

L'élastographie par onde de cisaillement est la méthode choisie et développée pendant cette thèse, et présentée dans ce chapitre. L'élastographie par onde de cisaillement consiste à 1) générer une poussée en utilisant la force de radiation acoustique, 2) imager la propagation des ondes de cisaillement résultantes à des cadences élevées grâce à l'imagerie ultrarapide et 3) cartographier la vitesse locale de l'onde de cisaillement, qui peut être utilisée pour déterminer la rigidité locale des tissus à l'aide de modèles rhéologiques. Généralement, l'imagerie ultrasonore ultrarapide, qui permet de suivre la propagation d'une onde de cisaillement, utilise l'émission d'ondes planes par des sondes linéaires. Cependant, les champs de vue obtenus sont limités par la taille de la sonde ultrasonore. Par ailleurs, pour l'application cardiaque transthoracique (non-invasif et à travers les côtes) l'utilisation de ces sondes et de ce type d'émissions ne sont pas adaptés. Pour augmenter les champs de vue pour application cardiaque, l'utilisation de sondes appelées « phased-array » et d'émission d'ondes divergentes est normalement préférable.

Pour l'imagerie ultrarapide par ondes divergentes, qui utilise la sommation cohérente de plusieurs insonifications, le concept de sources virtuelles doit être envisagé. Une onde divergente transmise est définie par l'application d'une loi de retard circulaire (créée par une source virtuelle unique placée à l'arrière du transducteur) sur les éléments d'émission. Différentes ondes divergentes peuvent être transmises et sommées de façon cohérente, pour recréer un point focal synthétique et améliorer la qualité de l'image, en contraste et en résolution. Cependant, le nombre de sources virtuelles et leurs positions respectives peuvent conduire à des résultats variables en termes de qualité d'image et de cadence, et ces paramètres doivent être adaptés à chaque application d'imagerie spécifique.

Cependant, l'élastographie par onde de cisaillement pour l'application cardiaque et en particulier en transthoracique reste difficile in vivo pour de multiples raisons. Tout d'abord, la présence de bruit de « clutter », les aberrations de phase et les réverbérations réduisent la qualité d'image à cause de la distorsion des impulsions émises. Deuxièmement, l'atténuation des ultrasons réduit le rapport signal-bruit des vitesses de déplacement des tissus, qui sont utilisées pour suivre l'onde de cisaillement. Des études récentes ont montré, de façon indépendante, que l'imagerie harmonique et la sommation cohérente pourraient pallier à ces deux questions.

Sur la base de ces travaux, nous introduisons une nouvelle technique : «l'imagerie par sommation cohérente harmonique ultrarapide», travail principalement conduit par le Dr Mafalda Correia et auquel j'ai pu participer. Cette méthode combine la sommation cohérente avec l'imagerie harmonique. Elle utilise une approche d'inversion de pulse en fenêtre glissante, avec l'objectif d'améliorer l'imagerie ultrarapide transthoracique du cœur. Ce type d'imagerie a été testé et appliqué dans deux cas : l'élastographie d'onde de cisaillement cardiaque et l'imagerie mode-B ultrarapide. Pour cette application, nous avons utilisé un échographe ultrarapide (Aixplorer, Supersonic Imagine, France) et une sonde « phased-array » (XP5-1, Supersonic Imagine, France) à la fréquence de 2.75 MHz.

Des expériences visant à quantifier la qualité de notre technique d'élastographie ont été réalisées dans un fantôme de graisse de porc et gélatine-agar, avec deux configurations différentes. Dans la première configuration, un absorbeur de polyuréthane a été recouvert d'une couche de gélatine-agar pour créer un fantôme qui imite un tissu mou homogène idéal. Dans la seconde, un morceau de peau de ventre de porc avec de la graisse sous-cutanée a été positionné au-dessus de la gélatine-agar. Cette couche a permis la génération d'aberrations ultrasonores comparables à celles causées in vivo. Lors de ces expériences, deux séquences d'élastographie par onde cisaillement ont été effectuées : une par

sommation cohérente des images fondamentales et l'autre par sommation cohérente de l'imagerie harmonique (notre technique).

Pour ces expériences, notamment pour la première configuration, nos résultats ont montré que l'imagerie fondamentale présente un meilleur rapport signal à bruit que l'imagerie harmonique. Par contre pour la deuxième configuration, l'imagerie harmonique et la sommation cohérente présentent des meilleurs rapports signal à bruit (de 2 dB) que l'équivalent en imagerie fondamentale. Nos résultats ont montré l'intérêt d'utiliser l'imagerie harmonique pour des applications cardiaques en transthoraciques humain, car exposées à gros effets d'aberrations.

La faisabilité in vivo a été évaluée en effectuant l'élastographie d'onde cisaillement et le mode-B par sommation cohérente de l'imagerie harmonique en cardiaque et en transthoracique chez six volontaires sains. L'élastographie d'onde cisaillement a été possible pour tous les volontaires et la vitesse d'onde de cisaillement moyenne calculée a été de 1.27 ± 0.29 m/s. Par rapport à l'imagerie en mode-B, le contraste a été toujours plus grand que l'imagerie fondamentale équivalente. Plus précisément, une diminution du bruit de « clutter » de 6,3 dB a été trouvée pour une onde divergente et de 13,8 dB pour 40 ondes divergentes par rapport à l'imagerie fondamentale avec le même nombre d'ondes émises.

Tous ces résultats prometteurs ont montré le potentiel de cette technique pour réaliser l'élastographie d'onde de cisaillement cardiaque en transthoracique et améliorer l'imagerie ultrarapide de mode-B du cœur humain. Pour étendre cette étude in vivo préclinique à grande échelle clinique, et évaluer la réelle performance/reproductibilité de la technique dans un vrai contexte clinique, nous avons décidé d'appliquer cela à une population de volontaires sains et une population caractéristique de malades, atteint de cardiomyopathie hypertrophique (CMH). La cardiomyopathie hypertrophique est définie par une hypertrophie plus ou moins importante du muscle cardiaque. Dans cette maladie, la structure normale du tissu musculaire cardiaque est perturbée. Concernant la fonction cardiaque, c'est principalement une dysfonction diastolique qui résulte de cette anomalie structurelle (Maron and Maron 2013). En l'état actuel des choses, il est difficile d'évaluer avec précision et de manière quantitative la fonction diastolique chez les patients atteint d'une CMH. L'élastographie myocardique par onde de cisaillement pourrait permettre cela. Nous avons décidé de réaliser deux études cliniques prospectives, chez l'enfant à l'hôpital Necker-Enfants maladies (NCT02619825) et chez l'adulte à l'hôpital Henri-Mondor et à l'Hôpital Européen Georges Pompidou (NCT02537041).

De plus, une troisième étude prospective a également été réalisée chez l'adulte à

l'hôpital Henri-Mondor et à l'Hôpital Européen Georges Pompidou, avec pour objectif de comparer différentes situations pathologiques : 1) l'insuffisance cardiaque à fraction d'éjection réduite, 2) l'insuffisance cardiaque à fraction d'éjection conservée, et 3) l'amylose cardiaque. L'objectif principal était d'apporter de nouvelles informations sur l'intérêt et les limites de l'élastographie myocardique en clinique.

Pour mettre en place ces trois essais cliniques, nous avons développé une interface graphique (GUI, pour graphical user interface) basée sur l'environnement Matlab (logiciel). Ce GUI a assuré l'autonomie du cardiologue pour effectuer de l'élastographie cardiaque par onde de cisaillement. En effet, le GUI permet au médecin d'intégrer en une seule acquisition des informations sur le patient, de choisir et d'adapter la profondeur de la poussée et le déclenchement de l'ECG (trigger selon le cycle cardiaque, en télé-diastole), et enfin d'acquérir les données. Les séquences utilisées pour chaque patient/volontaire ont été : l'élastographie d'onde de cisaillement et le mode-B harmonique pour deux coupes échographiques différentes, coupe parasternal petit-axe et parasternal grand-axe.

2.2. Travaux fondamentaux

2.2.1. Manuscrit "*Ultrafast harmonic coherent compound (UHCC) imaging for high frame rate echocardiography and shear wave elastography*"

Ce travail a été publié dans IEEE Trans Ultrason Ferroelectr Freq Control en 2016 (M. Correia et al. 2016).

Il a permis de présenter l'imagerie par sommation cohérente harmonique ultrarapide (imagerie non-linéaire) qui avait des résultats prometteurs pour nos futures applications cliniques d'élastographie myocardique.

Ultrafast Harmonic Coherent Compound (UHCC) Imaging for High Frame Rate Echocardiography and Shear-Wave Elastography

Mafalda Correia, Jean Provost, Simon Chatelin, Olivier Villemain, Mickael Tanter, and Mathieu Pernot

***Abstract*—Transthoracic shear-wave elastography (SWE) of the myocardium remains very challenging due to the poor quality of transthoracic ultrafast imaging and the presence of clutter noise, jitter, phase aberration, and ultrasound reverberation. Several approaches, such as diverging-wave coherent compounding or focused harmonic imaging, have been proposed to improve the imaging quality. In this study, we introduce ultrafast harmonic coherent compounding (UHCC), in which pulse-inverted diverging waves are emitted and coherently compounded, and show that such an approach can be used to enhance both SWE and high frame rate (FR) B-mode Imaging. UHCC SWE was first tested in phantoms containing an aberrating layer and was compared against pulse-inversion harmonic imaging and against ultrafast coherent compounding (UCC) imaging at the fundamental frequency. *In vivo* feasibility of the technique was then evaluated in six healthy volunteers by measuring myocardial stiffness during diastole in transthoracic imaging. We also demonstrated that improvements in imaging quality could be achieved using UHCC B-mode imaging in healthy volunteers. The quality of transthoracic images of the heart was found to be improved with the number of pulse-inverted diverging waves with a reduction of the imaging mean clutter level up to 13.8 dB when compared against UCC at the fundamental frequency. These results demonstrated that UHCC B-mode imaging is promising for imaging deep tissues exposed to aberration sources with a high FR.**

***Index Terms*—Cardiac stiffness, coherent compounding, pulse-inversion (PI) harmonic imaging, shear-wave elastography (SWE), ultrafast imaging.**

I. Introduction

MYOCARDIAL stiffness evaluation could help to assess and diagnose several pathologies associated with elasticity changes, such as ischemia, cardiomyopathies, and heart failure. However, as of today, myocardial stiffness cannot be measured noninvasively in clinical practice. In the past decades, ultrasound [1]–[7] and magnetic resonance [8]–[10] elastography imaging techniques have been proposed and developed to evaluate tissue stiffness properties. Techniques are typically based on the mapping of the propagation of mechanical waves in tissue; more specifically, low-frequency shear waves are induced and tracked to estimate their propagation speed (which typically lies between 1 and 10 m/s). Specifically, ultrasound shear-wave elastography (SWE) consists in: 1) generating a push using acoustic radiation force; 2) image the resulting shear-wave propagation; and 3) map the local velocity of the shear wave, which can be used to determine the local stiffness of tissues using rheological models of varying complexities.

Recent advances in the elastography techniques have allowed for stiffness measurements in deep organs, such as the heart [11]–[16]. Indeed, several *in vivo* SWE studies have shown in open-chest animals that local stiffness measurements, during one cardiac cycle, are feasible and clinically relevant [17]–[19]. A high imaging frame rate (FR) is required, i.e., typically above 1000 frames/s, to track shear waves induced in the human heart. Different approaches were proposed to achieve such FRs, such as, ECG gated [20], [21], and ultrafast imaging with unfocused transmit waves [22]–[26]. However, transthoracic shear-wave imaging remains challenging *in vivo* for multiple reasons. First, the presence of clutter noise, jitter, phase aberrations, and ultrasound reverberation reduce the imaging quality due to distortion of the transmitted pulses. Second, ultrasound attenuation reduces the signal-to-noise ratio (SNR) of the tissue velocities used to track the shear wave. Recent studies have shown, independently, that harmonic imaging [27] and coherent compounding [28] could palliate these two issues.

Harmonic imaging uses the nonlinear propagation of ultrasound wave to improve image quality [29]. Indeed, many factors, such as, e.g., the presence of fat, skin layer thickness, and hydration level result in the progressive distortion of ultrasound waves as they propagate into the tissue. This distortion leads to imaging artifacts, such as, e.g., clutter noise, jitter, phase aberration, and ultrasound reverberation. Harmonic imaging provided a reduction of these artifacts using a lower frequency in transmit but without compromising on contrast and resolution [30]. The nonlinear propagation of ultrasound waves, in biological tissues, generates harmonic frequencies that are multiple integers of the fundamental transmitted-wave frequency. To perform harmonic imaging, one must isolate the higher harmonic signals contained in the backscattered ultrasound echoes,

Manuscript received December 18, 2015; accepted February 11, 2016. Date of publication February 15, 2016; date of current version March 11, 2016. This work was supported by the European Research Council under the European Union's Seventh Framework Program (FP/2007-2013)/ERC Grant 311025.

M. Correia, J. Provost, O. Villemain, M. Tanter, and M. Pernot are with the Ecole Supérieure de Physique et Chimie Industrielles (ESPCI) ParisTech, Langevin Institute, PSL Research University, CNRS UMR7587, INSERM U979, Paris Diderot University, Paris 75005, France (e-mail: mafalda.correia@espci.fr).

S. Chatelin was with the Ecole Supérieure de Physique et Chimie Industrielles (ESPCI) ParisTech, Langevin Institute, PSL Research University, CNRS UMR7587, INSERM U979, Paris Diderot University, Paris 75005, France. He is currently with the Institute of Image-Guided Surgery, IHU, ICube Laboratory, 67412 Illkirch, France.

Digital Object Identifier 10.1109/TUFFC.2016.2530408

0885-3010 © 2016 IEEE. Translations and content mining are permitted for academic research only. Personal use is also permitted, but republication/redistribution requires IEEE permission. See http://www.ieee.org/publications_standards/publications/rights/index.html for more information.

and different methods typically based on filtering and pulse inversion have been proposed to do so [30]. Indeed, a bandpass filter [31] can be directly applied onto the baseband signals to isolate the second harmonic content. In pulse-inversion (PI) techniques [32], two identical pulses of opposite polarity are sequentially transmitted. Their respective received signals are then summed, which result in the cancellation of linear and odd harmonic components and in the doubling of the even harmonic components. The PI method is often preferred as it has the advantage of cancelling harmonic content generated by the electronics. However, since two pulses are summed to form a single image, PI divides the imaging FR by 2.

While harmonic imaging techniques have been used extensively for B-mode and contrast imaging, their application to SWE is relatively recent. Song *et al.* [27] proposed a PI harmonic sequence with unfocused emissions for SWE, using a phased-array transducer to improve transthoracic cardiac shear-wave measurements. Also, Doherty *et al.* [33] proposed a fully sampled sliding-window PI harmonic technique that decreases jitter and does not divide by half the imaging FR, to arterial acoustic radiation force impulse imaging improvement. Both works showed an improvement of the tissue velocity estimation, indicating that harmonic imaging for cardiac transthoracic applications can contribute to improve shear-wave tracking and, as a consequence, myocardial stiffness measurements.

Approaches based on the coherent compounding of successive backscattered echoes, such as, e.g., as synthetic aperture imaging [34] and plane-wave coherent compounding [35], have been proposed to improve image quality and motion estimation. For instance, in plane-wave coherent compounding, the backscattered echoes from successive tilted plane waves transmitted at high FR are coherently compounded to restore a synthetic focus in transmit. Recently, this principle was extended to diverging waves [28] to achieve larger fields-of-view using ultrafast ultrasound imaging in cardiac applications. This approach is similar to synthetic aperture imaging when a small number of virtual sources positioned behind the probe are used [36].

Based on [28], we propose to combine the coherent compounding approach with harmonic imaging, using a sliding-window PI approach, with the objective of improving transthoracic ultrafast imaging of the heart. In this study, we demonstrate that by combining the two techniques, larger SNR and reduced clutter and aberration noise can be obtained.

Specifically, we propose two implementations of ultrafast harmonic coherent compound (UHCC) imaging: one for cardiac SWE, and another for high FR B-mode imaging. UHCC SWE was designed for enhanced shear-wave propagation tracking and thus is performed at a very high FR. We showed herein that UHCC SWE improves the SNR of shear-wave velocity mapping, when compared against ultrafast coherent compound (UCC) imaging at the fundamental frequency [28] and sliding-window PI harmonic (UH) imaging [33] in a pork-belly gelatin–agar phantom. The *in vivo* feasibility of UHCC SWEI was evaluated on the heart, by measuring the diastolic myocardial stiffness transthoracically of six healthy volunteers. UHCC B-mode imaging was designed to improve imaging quality at large field-of-view and high FR, and evaluated *in vivo* in healthy volunteers. We showed that UHCC B-mode imaging is more efficient for clutter noise reduction than UCC B-mode imaging at the fundamental frequency.

II. Materials and Methods

An Aixplorer system (Supersonic Imagine, Aix-en-Provence, France) and a 2.75-MHz linear phased-array transducer (Vermon S.A., Tours, France, 96 elements, 0.2-mm pitch) were used for B-mode and SWE acquisitions. Two sequences based on ultrafast imaging [28] were designed: a first sequence dedicated to SWE imaging, and a second to perform B-mode imaging. The two sequences were built with similar transmit patterns and were adapted according to the constraints of each imaging mode.

A. Imaging Sequences

The imaging sequences developed herein are based on the emission of diverging waves. Diverging waves are defined by a virtual source located behind the probe and are associated with an emission subaperture. These diverging waves emanating from different virtual sources can then be coherently summed, and image quality can be improved (see [28] for details).

For each imaging mode, a different diverging-waves' transmission sequence was designed. SWE requires a high FR for the tracking of the propagation of shear waves. Hence, a small number of virtual sources were used in SWE sequences. To increase the relatively limited SNR associated with a small number of virtual sources, the virtual sources can be positioned farther behind the probe to increase the radius of the diverging wave, which allows for a larger number of elements contributing to the emission and limits the geometrical attenuation. The tradeoff, however, is a reduced field-of-view. In the case of B-mode imaging, a large number of virtual sources positioned near the probe were used to achieve a large field-of-view and high contrast imaging, at the cost of a reduced FR.

To perform harmonic imaging, the emission associated with each virtual source was performed twice, with opposite polarities.

1) UHCC Imaging: A shear wave was generated using a push beam with a 2.75-MHz central frequency with full aperture, i.e., using all the 96 elements of the probe. Immediately after generating the shear wave, the UHCC imaging sequence was launched. In this sequence, N virtual sources were used with a full aperture, i.e., with all 96 elements). The set of N diverging waves was transmitted (center frequency = 1.9 MHz and pulse duration = 2 cycles) by organizing the virtual sources (indicated by $i = 1, \ldots, N$ in Fig. 1) in a virtual array with a pitch equal to 96/N elements (see Fig. 1), and at a 30-mm distance behind the probe. For each virtual source, diverging waves of opposite polarity were emitted sequentially and the backscattered RF signals associated with both polarities were recorded and summed using a sliding window [33]. Finally, by coherently recombining each harmonic data set associated with different virtual sources, compounded harmonic images were produced with an FR equal to the pulse

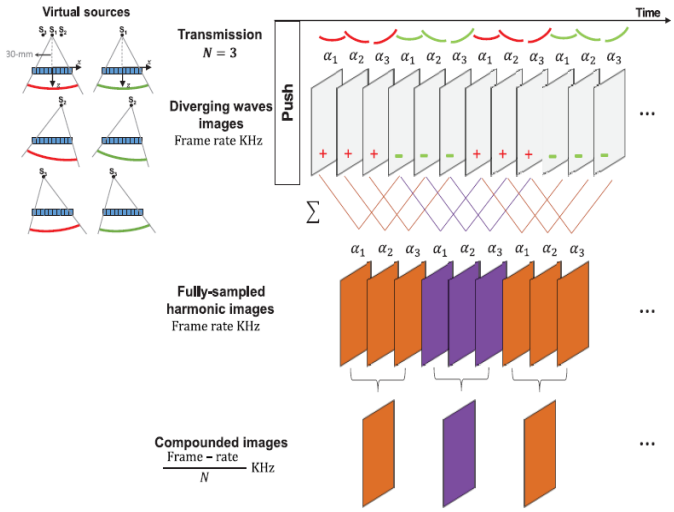

Fig. 1. UHCC SWE sequence principle. Example of implementation of a sliding-window PI harmonic technique and three coherently compounded diverging waves.

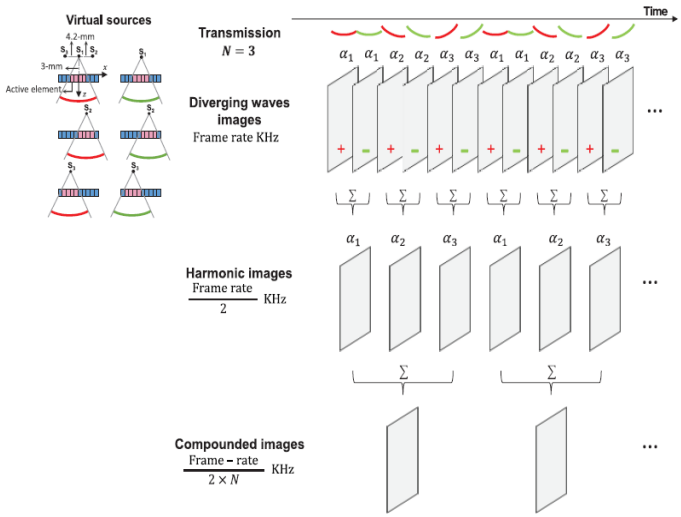

Fig. 2. UHCC B-mode sequence principle. Example of implementation of a conventional PI harmonic technique with three coherently compounded diverging waves.

repetition frequency. From these images, 2-D axial tissue displacements' maps were obtained using a table–sum 1-D RF cross correlation with cosine interpolation applied onto RF data [37], [38]. After compounding of the images associated with each virtual source, the resulting FR was, therefore, given by

$$\mathrm{FR} = \frac{\mathrm{PRF}}{N} \tag{1}$$

where PRF is the pulse repetition frequency and N is the number of coherently compounded diverging waves. The FR achieved was therefore equal to the one in the UCC imaging sequence [28].

The time sequence of an UHCC SWE acquisition is summarized in Fig. 1, in which an example using three diverging waves is provided. In this study, the UHCC was compared against other previously published techniques, which correspond to UHCC without the use of either pulse inversion (UCC) or coherent compounding (UH), respectively.

2) UHCC B-Mode Imaging: For B-mode imaging, a set of N diverging waves was transmitted (center frequency = 1.9 MHz and pulse duration = 2 cycles) using a 21-element subaperture. The virtual sources were arranged in a virtual 1-D array by positioning each virtual source ($i = 1, \ldots, N$) at the center of a (96/21)-element subaperture (Fig. 2), i.e., 4.2-mm distance space, and at a 3-mm distance behind the ultrasound probe. For each virtual source, diverging waves of opposite polarity were emitted sequentially and backscattered RF signals from each polarity were received and summed. Unlike UHCC SWE sequence no sliding-window sum was applied. By coherently recombining each N-harmonic data set, compounded images were produced. The resulting FR is given by

$$\mathrm{FR} = \frac{\mathrm{PRF}}{2 \times N} \tag{2}$$

where PRF is the pulse repetition frequency and N is the number of coherently compounded diverging waves. The B-mode UHCC imaging sequence is summarized in Fig. 2, using a three diverging-waves' example.

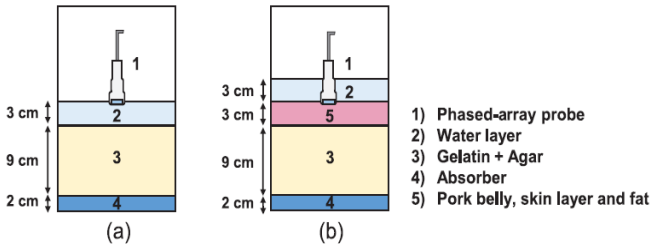

Fig. 3. *In vitro* experimental apparatus. (a) Gelatin–agar phantom configuration. (b) Pork-belly gelatin–agar phantom configuration.

B. In Vitro Experimental Setup

1) Pork-Belly Gelatin–Agar Phantom Fundamental and Harmonic Coherently Compounded Diverging-Waves' SWE Studies: Experiments to quantify the image quality of UHCC SWE were performed in a pork-belly gelatin–agar phantom (7% gelatin, 2% Agar, and 1% propanol), with two different experimental apparatuses.

In the first experimental apparatus, an absorber made of polyurethane (NPL, UK) was covered with a gelatin–agar layer to create a gelatin–agar phantom [Fig. 3(a)] that mimics an ideal homogeneous soft tissue.

In the second one, a fresh piece of pork-belly skin with fat was positioned above the gelatin–agar [Fig. 3(b)]. The pork-belly skin layer allowed us to generate ultrasound aberrations similar to the ones caused *in vivo*. In both experimental apparatus, the probe was positioned on top of the phantoms immersed in a layer of water to guarantee good acoustic coupling.

In all the *in vitro* experiments, a shear wave was generated using a 300-μs-long, 2.75-MHz push beam focused at 65 mm below the center of the transducer. Six different sequences to track the shear wave during 7 ms were compared in the two phantom configurations. Specifically, three different sequences with $N = 1$, 2, and 3 coherently compounded diverging waves were designed, with and without pulse inversion, i.e., UHCC and UCC sequences. The imaging depth was fixed to 90 mm and the *PRF* to 5924 Hz. For the fundamental sequences

TABLE I
PARAMETERS FOR *In Vitro* UCC AND UHCC IMAGING

Imaging sequences parameters	UCC SWE imaging				UHCC SWE imaging			
	Push	UCC			Push	UHCC		
Center frequency (MHz)	2.75	2.75			2.75	1.9		
Number of pushes	$N = 1$	–			$N = 1$	–		
Number of diverging-waves transmitted (N)	–	1–3			–	2–6		
Virtual sources axial position (mm)	–	30			–	30		
Subapertures length (mm)	19.2	19.2			19.2	19.2		
Pulse-repetition-frequency (PRF)	–	5924 Hz			–	5924 Hz		
Frame rate (FR)	–	$N = 1$ 5924 Hz	$N = 2$ 2962 Hz	$N = 3$ 1975 Hz	–	$N = 2$ 5924 Hz	$N = 4$ 2962 Hz	$N = 6$ 1975 Hz
Acquisition duration	300 µs	20 ms max			300 µs	20 ms max		

(i.e., without pulse inversion), a 2.75-MHz center frequency was used. In the case of harmonic sequences, a 1.9-MHz center frequency was used in transmit and a 3.8-MHz frequency was used in receive. Each sequence was repeated five times. Additionally, prior to the shear-wave imaging sequence, a UHCC B-mode image was obtained using 10 coherently compounded diverging waves. Table I shows the UCC and UHCC SWE imaging parameters used in *in vitro*.

C. In Vivo Human Heart Experimental Setup

The *in vivo* feasibility was assessed by performing transthoracic human heart SWE and B-mode imaging in six healthy volunteers. All volunteers signed an informed consent and the research study was performed within the clinical investigation protocol no. 2015-A00187-42 approved by the CPP (Comité de Protection des Personnes), Ile de France VI, France. The acoustic output of the sequences used *in vivo* was measured using a calibrated interferometer in water. The ultrasonic sequences complied with the Food and Drug Administration (FDA) requirements (510 k Track 3, FDA) regarding the mechanical index (MI) and the spatial-peak time average (I_{SPTA}) with the derating factor of 0.3 dB cm^{-1} MHz^{-1}. In the SWE imaging sequence, the $\mathrm{MI}_{0.3}$ was limited by the pressure at the focus of the push beam and it was set to 1.8. The $I_{\mathrm{SPTA0.3}}$ was 154 mW/cm^2, assuming a repetition time of 1 s. For the unfocused transmits (80 diverging waves), the $\mathrm{MI}_{0.3}$ and $I_{\mathrm{SPTA0.3}}$ were 0.6 and 2.2 mW/cm^2, respectively, assuming a repetition time of 1 s. For both imaging acquisitions, $\mathrm{MI}_{0.3}$ and $I_{\mathrm{SPTA0.3}}$ values were inferior to $\mathrm{MI}_{0.3} = 1.90$ and $I_{\mathrm{SPTA0.3}} =$ 720 mW/cm^2, limits imposed by the FDA. The temperature at the probe surface was also measured and remained stable for the transmission of one SWEI (20-ms duration) and B-mode imaging (15-ms duration) sequences repeated every second. The increased temperature was inferior to temperature uncertainty of the measurement system (± 0.1 °C) during the sequences' tests.

The experiments were conducted and performed by a trained cardiologist. A parasternal short-axis view was used for all the acquisitions. The time between each acquisition was 1 min. Repeatability was assessed in one volunteer by performing five successive acquisitions separated by 1 min.

1) Transthoracic UHCC SWE Study: A push beam of 2.75-MHz central frequency and 300-µs duration was induced in the center of the anteroseptal myocardial wall of the left ventricle. The focal depth was adjusted for each patient between 45 and 75 mm to position the focal zone at the midwall location of the anteroseptal wall. The UHCC SWE sequences were set to one, two, and three diverging-waves' transmission with a PRF of 6849 Hz. They were synchronized with the ECG signal to generate and detect shear-wave motion at end diastole.

A prior to the UHCC SWE acquisition, a UHCC B-mode imaging was also obtained with the following parameters: 15 diverging waves, at a 120-mm depth, and an FR equal to 153 frames/s (PRF = 4608 Hz).

2) UHCC and UCC B-Mode Imaging—Diverging Waves Coherently Compounded Number Evaluation: To evaluate the imaging quality in terms of SNR and contrast, experiments were performed using a UHCC B-mode imaging sequence and compared against the performances of UCC. For both sequences, i.e., UHCC and UCC, the transmission was performed using 1–40 coherently compounded diverging waves, at a 100-mm depth and with a PRF equal to 5319 Hz. The imaging FR varied between 5319 and 133 frames/s for the UCC sequence. For the same number of coherently compounded diverging waves, the FR was divided by two for UHCC. Table II shows the parameters used for UHCC SWEI and UHCC B-mode imaging in the *in vivo* experiments.

D. Postprocessing Analysis

Beamforming of radio-frequency (RF) signals was performed using a conventional delay-and-sum algorithm implemented on the GPU.

1) Shear-Wave Propagation Tracking and Speed Estimation: Tissue axial velocity images were obtained using 1-D cross correlation of successive frames with cosine interpolation applied on the beamformed RF signals [37], [38]. A 1.5-mm kernel size with a 97.5-% overlap was used for all sequences. Tissue velocity images were then scan converted. Spatiotemporal tissue velocity data were then computed and shear-wave speeds in the $-x$- and $+x$-directions were assessed using a linear least-squares estimation on temporal 1-D cross correlation with different lateral spatial lags (lags range: 0.2–1.8-mm) [39].

TABLE II
PARAMETERS FOR *In vivo* UHCC SWEI AND UCC/UHCC B-MODE IMAGING

Imaging sequences parameters	SWE imaging				B-mode imaging			
	Push	UHCC			UCC		UHCC	
Center frequency (MHz)	2.75	1.9			2.75		1.9	
Number of pushes	$N = 1$	–			–		–	
Number of diverging-waves tran smitted (N)	–	2 to 6			1 to 40		2 to 80	
Axial position of virtual sources (mm)	–	30			3		3	
Subapertures length (mm)	19.2	19.2			4.2		4.2	
Pulse-repetition-frequency (PRF)	–	6849 Hz			5319 Hz		5319 Hz	
Frame rate (FR)	–	$N = 2$ 6849 Hz	$N = 4$ 3425 Hz	$N = 6$ 1975 Hz	$N = 1$ 5319 Hz	… $N = 40$ 133 Hz	$N = 2$ 2660 Hz	… $N = 80$ 67 Hz
Acquisition duration	300 µs	20 ms max			15 ms max		15 ms max	

For the *in vitro* experiments, the shear-wave speed was estimated using the spatiotemporal tissue velocity data that were averaged within depths of 3-mm around the push location.

In these experiments, the SNR was evaluated quantitatively around the push region for UCC and UHCC SWE studies. SNR maps were calculated as follows:

$$\mathrm{SNR_{dB}} = 10\log_{10}\frac{\sum_{t=0}^{T} S(x,y,z)^2}{\sigma_{xz}^2} \tag{3}$$

where S is the tissue velocity image, σ_{xz} is the tissue velocity standard deviation in the absence of shear-wave propagation, and T is the acquisition time. The averaged SNR values were evaluated within a region-of-interest around the push location. The percentage of area within these regions-of-interest with an SNR above a threshold of 25 dB was quantified. This threshold was determined by Deffieux *et al.* [40] as an acceptable SNR for the reconstruction of shear velocity maps with a standard deviation of 10%.

For the *in vivo* acquisitions, the average myocardial wall motion was subtracted before the tissue velocity images scan conversion, since the natural myocardial wall has a low-frequency content [41], [42] and acts as a noise source in the detection of the shear-wave propagation. Also, the anteroseptal wall was segmented to using a B-mode image reference acquired.

Then, the shear-wave speed in the $-x$- and $+x$-directions was estimated, through spatiotemporal tissue velocity data that were averaged within depths of 3-mm around the push location in the anteroseptal wall. Shear-wave speeds were assessed and the adjusted coefficient of determination ($\bar{R}^2$) of the least-squares fit results was calculated. The adjusted coefficient of determination was used as an exclusion criterion for the shear-wave speed estimation. Values with an adjusted coefficient of larger than 80% of the shear-wave speed estimation were excluded and no shear-wave propagation was considered in those cases.

2) UHCC and UCC B-Mode Imaging: The B-mode image quality was assessed on the final images, i.e., after beamforming, coherent summation, scan conversion, and log compression, with a 60-dB dynamic range. Then, to evaluate imaging quality in a function of the number of diverging-waves' emitted, a mean clutter level analysis in regions-of-interest was performed, for both UHCC and UCC sequences. These regions-of-interests (5×6 mm^2) were chosen and positioned arbitrarily in the anterior and posterior wall, and in the left ventricle cavity at approximately the same depth to evaluate the contrast of the image. For each region-of-interest, the absolute intensity values of ultrasound images were averaged over the region of interest. Finally, the mean clutter level for UHCC and UCC was determined by the ratio of the average intensity in the cardiac cavity and in the tissue.

III. RESULTS

A. Gelatin–Agar/Pork-Belly Gelatin–Agar Phantoms Fundamental and Harmonic Coherently Compounded Diverging-Waves' SWE Studies

Fig. 4 presents the results acquired for the gelatin–agar phantom. Acquisitions provided an image quality that was sufficiently high for the estimation of the shear-wave speed, regardless of the number of compounded diverging waves or of the use of pulse inversion.

Fig. 5 shows the results obtained with this pork-belly gelatin–agar phantom.

Shear-wave propagation tracking was possible for all acquisitions. However, in this case, due to the skin and fat layer, which causes ultrasound aberrations, the UHCC sequence resulted in a qualitatively larger SNR. Indeed, one can observe that the waveform is better defined with respect to the background noise and especially at larger propagation distances when using UHCC.

Figs. 6 and 7, and Table III provide a systematic and quantitative analysis of this observation. The percentage of area with an SNR above a threshold of 25 dB was quantified and is showed as well in Table III.

Fig. 6 shows that the SNR is relatively similar when using the UCC and UHCC sequences in the gelatin–agar phantom configuration. We also note that the SNR increases with the number of compounded diverging waves, as was demonstrated previously in [28].

Fig. 7, on the other hand, shows that in the presence of an aberrating layer such as a pork-belly layer and for a fixed number of compounded diverging waves, the SNR associated with UHCC is larger than the SNR associated the UCC sequence.

Table III summarizes these results using the spatial average of the SNR maps of the regions-of-interest shown in Figs. 6 and 7. Interestingly, in the absence of an aberrating layer (i.e., when using the gelatin–agar phantom), the SNR associated with

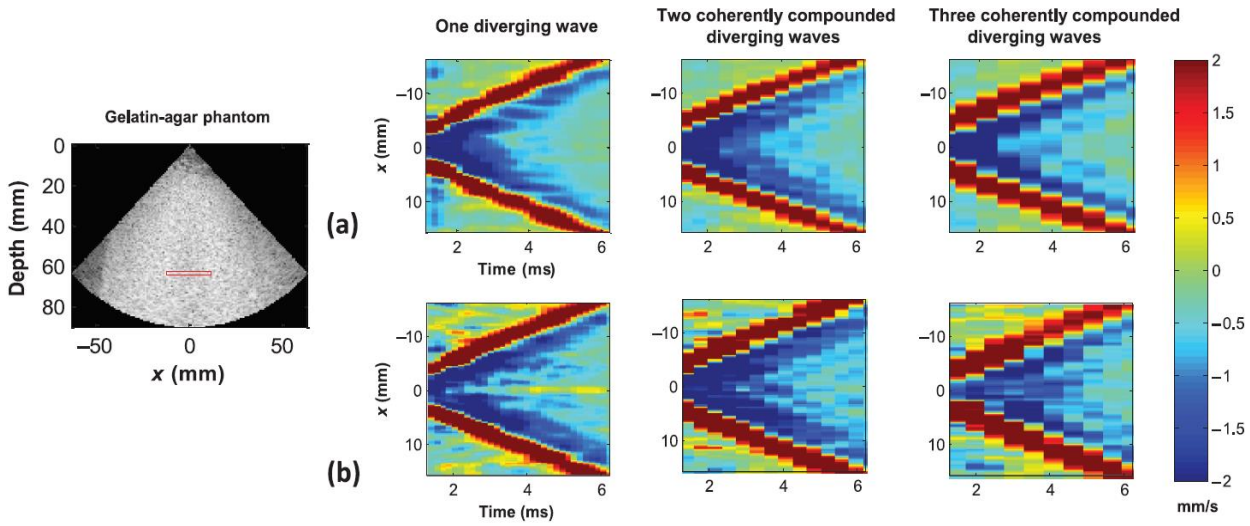

Fig. 4. Gelatin–agar phantom configuration results. An UHCC B-mode image using 10 diverging waves, spatiotemporal tissue velocity images of the shear-wave propagation (push depth equal to 65 mm) for (b) UHCC and (a) UCC SWE using one to three coherently compounded diverging waves. Tissue velocities were averaged axially within a 3-mm region.

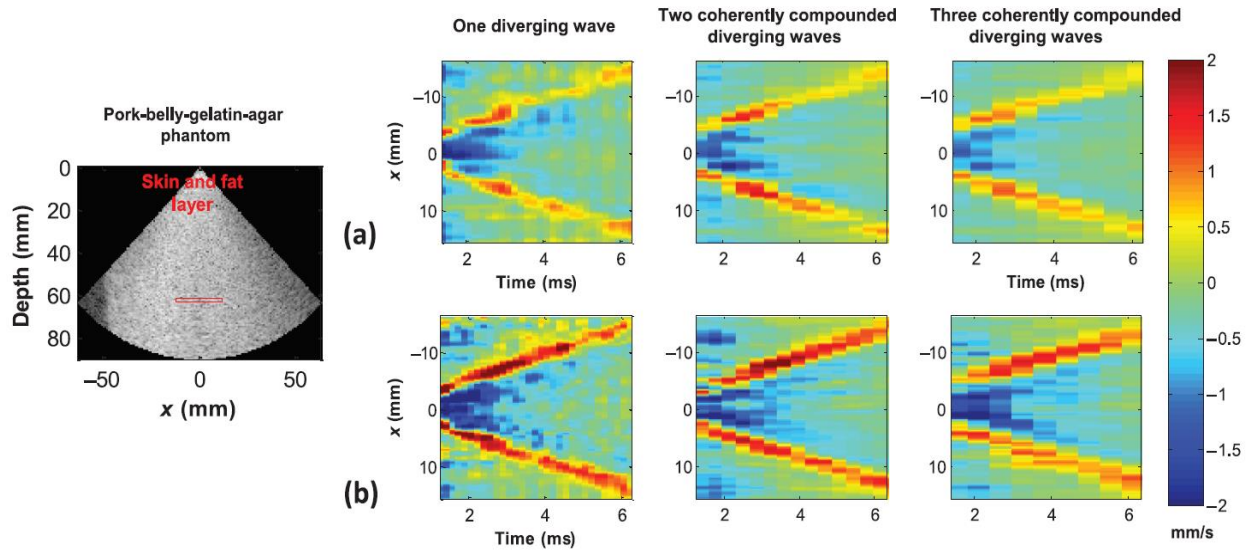

Fig. 5. Pork-belly gelatin–agar phantom configuration results. A B-mode ultrafast harmonic using 10 diverging waves and spatiotemporal tissue velocity images of the shear wave propagation (push depth 65 mm) for (a) UCC and (b) UHCC. SWE using one to three coherently compounded diverging waves. Tissue velocities were averaged axially within a 3-mm region.

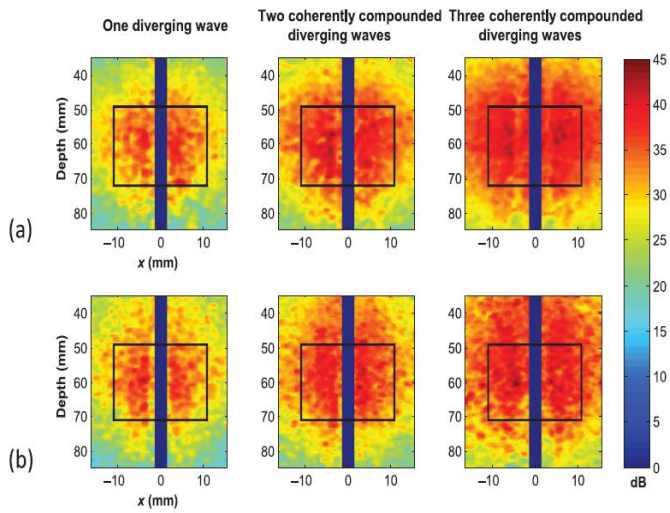

Fig. 6. SNR maps of gelatin–agar phantom configuration for (a) UCC and (b) UHCC imaging. The blue boxes represent the push region and the black rectangles represent the SNR regions-of-interest.

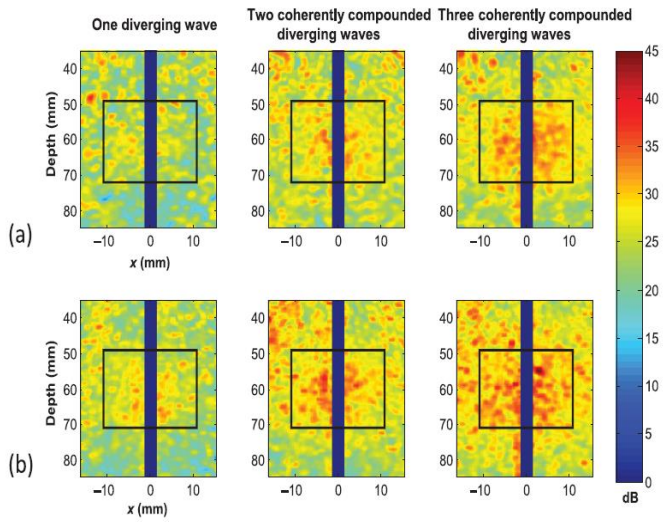

Fig. 7. SNR maps of pork-belly gelatin–agar phantom configuration for (a) UCC and (b) UHCC imaging. The blue boxes represent the push region and the black rectangles represent the SNR regions-of-interest.

TABLE III
MEAN SNR OF UHCC AND UCC AND SNR PERCENTAGE ABOVE 25 dB IN THE REGIONS-OF-INTEREST FOR DIFFERENT NUMBER OF DIVERGING WAVES IN THE TWO PHANTOM CONFIGURATIONS

		One diverging-wave		Two diverging-waves		Three diverging-waves	
		SNR (dB)	Area % > = 25 dB	SNR (dB)	Area % > = 25 dB	SNR (dB)	Area % > = 25 dB
Gelatin-agar phantom	Fundamental	33.7	100.0	37.2	100.0	38.7	100.0
	Harmonic	33.7	95.6	36.5	100.0	38.0	100.0
Pork-belly-gelatin-agar phantom	Fundamental	25.7	47.1	28.4	88.4	30.2	95.9
	Harmonic	27.1	69.2	30.0	96.3	32.0	99.9

the UHCC sequence was relatively equivalent with the SNR associated with the UCC sequence, albeit by a small value (0.7 dB when using two and three coherently compounded diverging waves). Also, the area above 25 dB was almost 100% using both UHCC and UCC. In contrast, the UHCC sequence provided a consistent improvement in SNR in the presence of an aberrating layer, i.e., pork-belly gelatin–agar phantom. This improvement was larger in absolute difference of SNR when increasing the number of diverging waves, but the relative improvement was approximately constant (approx. 30.6% SNR improvement when compared against UCC for a fixed number of compounded diverging waves). The SNR surface area percentage above 25 dB was higher for UHCC than UCC and increased consistently with two and three coherently compounded diverging waves.

B. In Vivo Acquisitions

1) Transthoracic UHCC SWE in the Human Heart: UHCC SWE was evaluated *in vivo* at high FRs (> 1500 frames/s), using one to three diverging waves. The spatiotemporal axial tissue displacements' images, averaged within 3-mm depth around the myocardial wall center are shown in Fig. 8 for the six volunteers.

Without coherent compounding, shear-wave imaging the shear-wave propagation was detected in volunteers 1 (in both directions), 2 (in both directions), and 6 (in $+x$-direction). Using two compounded diverging waves, the shear-wave propagation was detected in all volunteers in at least one direction. Using three diverging waves, shear waves were detected in all acquisitions in both directions, except in volunteer 6, where no shear wave was detected.

The shear-wave speed was estimated for all the acquisitions where shear waves could be tracked in at least one direction.

After the applicability of the exclusion criteria, shear-wave propagation speeds were estimated in all cases, with the exception of the volunteers 4 (in $-x$-direction) and 6 (in $-x$-direction). These results are shown in Table IV.

Repeatability tests were performed in one volunteer. The UHCC sequence was repeated five times for one to three compounded diverging and shear waves were tracked for both $-x$ and $+x$-directions. In each acquisition, spatiotemporal images were computed, averaged within a 3-mm deep region, and centered in the left-ventricle anterior-septal midwall. Arithmetic means and standard deviations are presented in Table V.

2) Transthoracic B-Mode Human Heart Study: UHCC B-mode imaging was evaluated using 1–40 coherently compounded diverging-waves' transmission, and compared against UCC B-mode. Fig. 9 shows the imaging quality improvement of the UCC and UHCC B-mode images with an increasing number of diverging waves. As indicated by [43], increasing the number of compounded diverging waves resulted in improvements in terms of SNR, lateral resolution, and contrast when compared with a single diverging-wave image.

The mean clutter value in the cardiac cavity (regions-of-interest represented by red boxes) was also evaluated and the results are presented in Fig. 9.

The contrast of UHCC B-mode imaging was consistently larger than UCC B-mode imaging. Specifically, a clutter level decrease of 6.3 dB was found for one diverging wave and 13.8 dB for 40 diverging waves compared against UCC imaging with the same number of transmitted waves.

IV. DISCUSSION

This paper investigated the potential of a hybrid ultrafast imaging sequence based on the combination of pulse inversion and coherent compound imaging. Two sequences were designed and implemented *in vivo*: UHCC SWE and UHCC B-mode imaging. The main aim of this study was to assess the potential of UHCC as a means to improve shear-wave tracking in transthoracic cardiac applications that suffer from different noise sources.

UHCC SWE was first evaluated in an *in vitro* study. Harmonic imaging alone was shown to improve the shear-wave tracking in the presence of an aberrating layer composed of porcine fat-and-skin. Combining the coherent compounding approach allowed for a larger SNR. The feasibility of UHCC SWE was assessed in transthoracic imaging of the human heart. Experiments were performed in six healthy volunteers during end diastole in the left-ventricle anteroseptal wall. The acquisitions were performed during end diastole, i.e., when the myocardium is relatively soft and the shear-wave

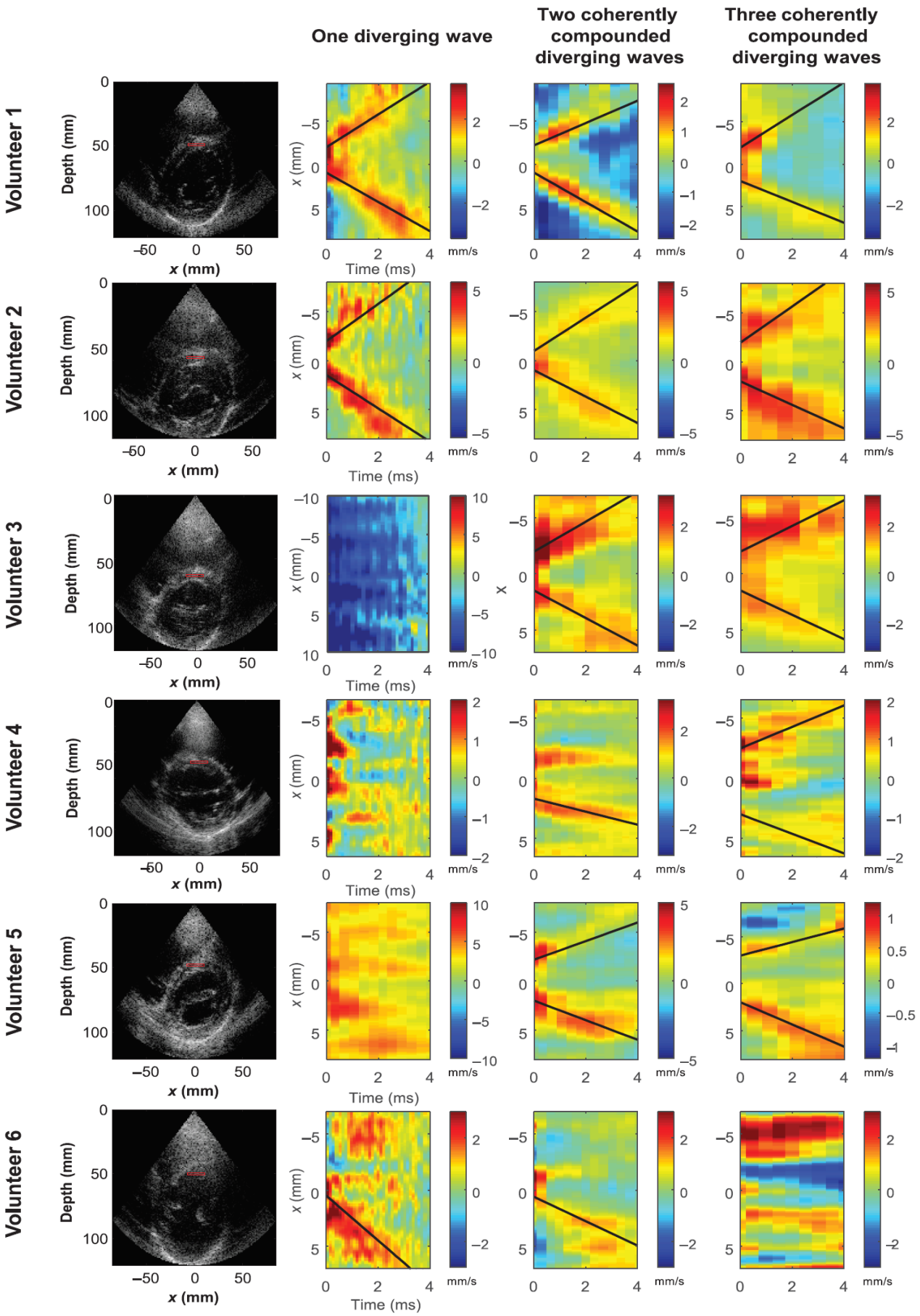

Fig. 8. *In vivo* transthoracic UHCC SWE in the human heart of six volunteers at end diastole. Left column: UHCC B-mode images acquired 5 ms before the SWE acquisition. Right column: spatiotemporal tissue velocity maps of the shear-wave propagation and averaged within 3-mm depth at the center of the myocardial wall for one (i.e., no coherent compound applied), two, and three diverging waves. The black lines represent the tracked shear-wave propagation path. Its slope corresponds to the shear-wave speed.

TABLE IV
SHEAR-WAVE SPEED ESTIMATION FOR THE SIX VOLUNTEERS

Shear wave speed ± std* (m/s)	One diverging-wave				Two diverging-waves				Three diverging-waves			
	$-x$ direction	R^2	$+x$ direction	R^2	$-x$ direction	R^2	$+x$ direction	R^2	$-x$ direction	R^2	$+x$ direction	R^2
Volunteer 1	1.65 ± 0.42	0.83	1.11 ± 0.36	0.85	1.71 ± 0.22	0.91	1.15 ± 0.26	0.89	1.92 ± 0.13	0.95	1.13 ± 0.24	0.90
Volunteer 2	1.70 ± 0.37	0.85	1.26 ± 0.51	0.80	1.75 ± 0.17	0.93	1.17 ± 0.35	0.86	1.95 ± 0.14	0.95	1.11 ± 0.39	0.84
Volunteer 3	–	–	–	–	1.34 ± 0.33	0.86	1.23 ± 0.19	0.89	1.15 ± 0.32	0.86	1.09 ± 0.16	0.93
Volunteer 4	–	–	–	–	–	–	0.54 ± 0.19	0.92	0.81 ± 0.24	0.90	0.89 ± 0.27	0.89
Volunteer 5	–	–	–	–	0.95 ± 0.13	0.84	1.39 ± 0.48	0.80	0.72 ± 0.30	0.87	1.18 ± 0.23	0.91
Volunteer 6	–	–	1.86 ± 0.38	0.84	–	–	1.09 ± 0.38	0.84	–	–	–	–

*Std denotes for standard deviation of the least-squares fit. Values with an adjusted R^2 inferior to 0.80 were excluded.

TABLE V
REPEATABILITY TEST OF SHEAR-WAVE VELOCITY MEASUREMENTS ON ONE VOLUNTEER

Shear wave speed mean ± std* (m/s)	One diverging-wave		Two diverging-waves		Three diverging-waves	
	$+x$ direction	$-x$ direction	$+x$ direction	$-x$ direction	$+x$ direction	$-x$ direction
	1.88 ± 0.51	1.64 ± 0.30	1.44 ± 0.17	1.16 + 0.20	1.59 ± 0.44	1.31 ± 0.22

*Std denotes for standard deviation of the arithmetic mean.

speed is typically in the range of 1–2 m/s. The reproducibility of the presented technique was assessed in one volunteer by performing five acquisitions. Results showed that shear-wave tracking is possible by the combination of harmonic imaging and coherent compound imaging with diverging waves. Up to three diverging waves were used. Variations between $+x$- and $-x$-directions were also found, as expected, due to the complexity and anisotropy of myocardium tissue in the anteroseptal wall, composed of an arrangement of fibers from left and right ventricles.

In this study, UHCC was shown to improve SWE in phantoms and it was feasible *in vivo* in most of the cases. However, UHCC SWE remains challenging *in vivo*, as shear-wave velocity estimation was not possible for all acquisitions. Therefore, further investigation is required to determine the ideal number of diverging-waves' transmission and to apply such technique in clinical practice routine.

The maximum number of coherently compounded diverging waves is indeed limited by the shear-wave speed. The tradeoff between the number of coherently compounded diverging waves and the temporal sampling in SWE depends on many parameters including the tissue stiffness and the probe parameters and is complex to quantify. This study suggests that for shear-wave speeds of a few meters per second, three pulse-inverted coherently compounded diverging waves (i.e., corresponding to six emissions) can be used for diastolic shear-wave propagation tracking. For a PRF of 5924 frames/s, this corresponds to an FR of 1916 frames/s.

In systole, the heart contracts and, as a result, the shear-wave speed is comparatively higher. To estimate the systolic shear-wave speed, higher FRs are required, or, equivalently, a smaller number of coherently compounded diverging waves should be used, which, in turn, reduces the SNR. The twisting of the heart during systole could also exacerbate artifacts associated with out-of-plane motion. The *in vivo* SWE studies in open-chest animals [17]–[19] have shown that shear-wave speed in systole is at least three times higher compared against the diastolic shear-wave speed (shear-wave speed in the range of 5–6 m/s). Consequently, for a PRF of 5924 frames/s, the FR necessary to track shear-wave speed in systole could reach 5924 frame/s, which corresponds to one diverging-wave transmission.

When using such a small number of emissions, it can be shown [28] that the influence of fast cardiac tissue motion degrades the coherence of the compound operation only in a limited and for most practical aspects, negligible. However, for a larger number of compounded diverging waves, a motion correction factor should be considered, as proposed previously [44].

It should also be noted that even if all the acquisitions were performed by a trained cardiologist differences between acquisitions could occurred due to patient breathing or sonographer's motion.

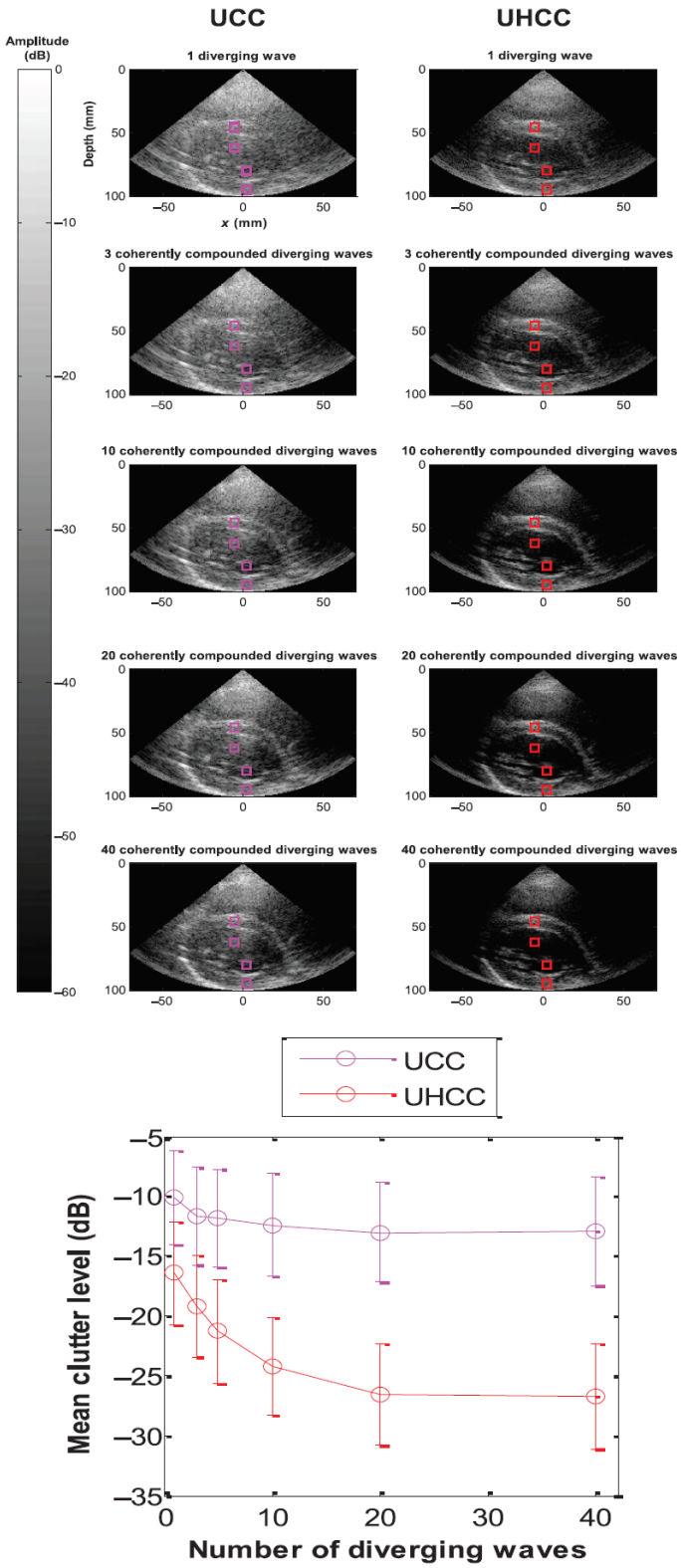

Fig. 9. UCC and UHCC B-mode images. Comparison using different number of diverging waves. The average clutter signal level was evaluated in the anterior and posterior myocardium wall and left ventricle cavity (represented by the magenta and red boxes, for UCC and UHCC, respectively).

This study was focused on the challenging application of myocardial SWE. However, UHCC could benefit and be applied to other applications that have limited imaging quality due to attenuation and aberrations, such as in liver SWE. These sequences could also be implemented in conventional linear arrays by replacing the emission of diverging waves with plane waves.

UHCC B-mode imaging was also implemented and evaluated *in vivo*. A comparison of the technique against UCC was performed to assess differences in contrast, SNR and axial resolution.

Regarding clutter noise reduction, contrast increase, and axial resolution improvement, the combination of harmonic imaging with UCC imaging allowed for a strong increase in image quality when compared against the fundamental imaging. In this method, no sliding window was applied to privilege the PI effect instead of imaging FR, unlike in the UHCC SWE sequence. Using coherent compounding, the tradeoff between FR and image quality can be adjusted at no expense in terms of field-of-view. B-mode images with good image quality can be obtained at an FR of 270 frames/s for 10 coherently compounded diverging waves and for 10 cm of depth. These results are promising for imaging deep tissues exposed to aberration sources in cardiac applications but also for the imaging of the liver in patients with high body mass index.

V. Conclusion

In this study, we combined harmonic imaging and coherent compounding ultrafast imaging and applied it to cardiac SWE and high FR B-mode imaging. The sequences were implemented on an ultrasound scanner and experiments were performed with a phased-array probe. Image quality and shear-wave propagation detection was evaluated by comparing the technique with the fundamental approach. Experiments performed through an aberrating layer, showed that shear-wave propagation tracking was improved by both harmonic imaging and coherent compounding and even more by the combination of both techniques, with UHCC imaging. Improvements in SNR were quantified and consistent in all *in vitro* experiments. *In vivo* feasibility was shown in the human heart to measure noninvasively shear-waves' speeds of the left ventricle wall and to evaluate B-mode image quality improvement. This technique could be used to perform shear-wave imaging and to improve B-mode imaging in the human heart.

References

[1] M. Fatemi and J. F. Greenleaf, "Vibro-acoustography: an imaging modality based on ultrasound-stimulated acoustic emission," in *Proc. Nat. Acad. Sci. USA*, vol. 96, no. 12, pp. 6603–6608, Jun. 1999.

[2] S. Catheline, J. Thomas, F. Wu, and M. A. Fink, "Diffraction field of a low frequency vibrator in soft tissues using transient elastography," *IEEE Trans. Ultrason., Ferroelectr., Freq. Control*, vol. 46, no. 4, pp. 1013–1019, Jul. 1999.

[3] L. Sandrin *et al.*, "Transient elastography: A new noninvasive method for assessment of hepatic fibrosis," *Ultrasound Med. Biol.*, vol. 29, no. 12, pp. 1705–1713, Dec. 2003.

[4] A. P. Sarvazyan, O. V Rudenko, S. D. Swanson, J. B. Fowlkes, and S. Y. Emelianov, "Shear wave elasticity imaging: A new ultrasonic technology of medical diagnostic," *Ultrasound Med. Biol.*, vol. 24, no. 9, pp. 1419–1435, 1998.

[5] K. Nightingale, M. S. Soo, R. Nightingale, and G. Trahey, "Acoustic radiation force impulse imaging: in vivo demonstration of clinical feasibility," *Ultrasound Med. Biol.*, vol. 28, no. 2, pp. 227–235, Feb. 2002.

[6] J. Bercoff, M. Tanter, and M. Fink, "Supersonic shear imaging: a new technique for soft tissue elasticity mapping," *IEEE Trans. Ultrason., Ferroelectr., Freq. Control*, vol. 51, no. 4, pp. 396–409, Apr. 2004.

[7] P. Song, H. Zhao, A. Manduca, M. W. Urban, J. F. Greenleaf, and S. Chen, "Comb-push ultrasound shear elastography (CUSE): a novel method for two-dimensional shear elasticity imaging of soft tissues," *IEEE Trans. Med. Imag.*, vol. 31, no. 9, pp. 1821–1832, Sep. 2012.

[8] R. Muthupillai, D. Lomas, P. Rossman, J. Greenleaf, A. Manduca, and R. Ehman, "Magnetic resonance elastography by direct visualization of propagating acoustic strain waves," *Science*, vol. 269, no. 5232, pp. 1854–1857, Sep. 1995.

[9] J. Rump, D. Klatt, J. Braun, C. Warmuth, and I. Sack, "Fractional encoding of harmonic motions in MR elastography," *Magn. Reson. Med.*, vol. 57, no. 2, pp. 388–395, Feb. 2007.

[10] K. J. Glaser, A. Manduca, and R. L. Ehman, "Review of MR elastography applications and recent developments," *J. Magn. Reson. Imag.*, vol. 36, no. 4, pp. 757–774, Oct. 2012.

[11] S. J. Hsu, R. R. Bouchard, D. M. Dumont, P. D. Wolf, and G. E. Trahey, "In vivo assessment of myocardial stiffness with acoustic radiation force impulse imaging," *Ultrasound Med. Biol.*, vol. 33, no. 11, pp. 1706–1719, Nov. 2007.

[12] C. Pislaru, M. W. Urban, I. Nenadic, and J. F. Greenleaf, "Shearwave dispersion ultrasound vibrometry applied to in vivo myocardium," in *Proc. Int. Conf. IEEE Eng. Med. Biol. Soc.*, Jan. 2009, pp. 2891–2894.

[13] M. Pernot, M. Couade, P. Mateo, B. Crozatier, R. Fischmeister, and M. Tanter, "Real-time assessment of myocardial contractility using shear wave imaging," *J. Amer. Coll. Cardiol.*, vol. 58, no. 1, pp. 65–72, Jun. 2011.

[14] A. Kolipaka *et al.*, "MR elastography as a method for the assessment of myocardial stiffness: Comparison with an established pressure-volume model in a left ventricular model of the heart," *Magn. Reson. Med.*, vol. 62, no. 1, pp. 135–140, Jul. 2009.

[15] I. Sack, J. Rump, T. Elgeti, A. Samani, and J. Braun, "MR elastography of the human heart: Noninvasive assessment of myocardial elasticity changes by shear wave amplitude variations," *Magn. Reson. Med.*, vol. 61, no. 3, pp. 668–677, Mar. 2009.

[16] B. Robert, R. Sinkus, J.-L. Gennisson, and M. Fink, "Application of DENSE-MR-elastography to the human heart," *Magn. Reson. Med.*, vol. 62, no. 5, pp. 1155–1163, Nov. 2009.

[17] R. R. Bouchard, S. J. Hsu, M. L. Palmeri, N. C. Rouze, K. R. Nightingale, and G. E. Trahey, "Acoustic radiation force-driven assessment of myocardial elasticity using the displacement ratio rate (DRR) method," *Ultrasound Med. Biol.*, vol. 37, no. 7, pp. 1087–1100, Jul. 2011.

[18] M. Couade *et al.*, "In vivo quantitative mapping of myocardial stiffening and transmural anisotropy during the cardiac cycle," *IEEE Trans. Med. Imag.*, vol. 30, no. 2, pp. 295–305, Feb. 2011.

[19] C. Pislaru, M. W. Urban, S. V Pislaru, R. R. Kinnick, and J. F. Greenleaf, "Viscoelastic properties of normal and infarcted myocardium measured by a multifrequency shear wave method: comparison with pressure-segment length method," *Ultrasound Med. Biol.*, vol. 40, no. 8, pp. 1785–1795, Aug. 2014.

[20] M. Pernot, K. Fujikura, S. D. Fung-Kee-Fung, and E. E. Konofagou, "ECG-gated, mechanical and electromechanical wave imaging of cardiovascular tissues in vivo," *Ultrasound Med. Biol.*, vol. 33, no. 7, pp. 1075–1085, Jul. 2007.

[21] J. Provost, W.-N. Lee, K. Fujikura, and E. E. Konofagou, "Electromechanical wave imaging of normal and ischemic hearts in vivo," *IEEE Trans. Med. Imag.*, vol. 29, no. 3, pp. 625–635, Mar. 2010.

[22] J.-Y. Lu and J. F. Greenleaf, "Pulse-echo imaging using a nondiffracting beam transducer," *Ultrasound Med. Biol.*, vol. 17, no. 3, pp. 265–281, Jan. 1991.

[23] L. Sandrin, S. Catheline, M. Tanter, X. Hennequin, and M. Fink, "Time-resolved pulsed elastography with ultrafast ultrasonic imaging," *Ultrason. Imag.*, vol. 21, no. 4, pp. 259–272, Oct. 1999.

[24] L. Tong, H. Gao, H. F. Choi, and J. D'hooge, "Comparison of conventional parallel beamforming with plane wave and diverging wave imaging for cardiac applications: A simulation study," *IEEE Trans. Ultrason., Ferroelectr., Freq. Control*, vol. 59, no. 8, pp. 1654–1663, Aug. 2012.

[25] I. K. Ekroll, A. Swillens, P. Segers, T. Dahl, H. Torp, and L. Lovstakken, "Simultaneous quantification of flow and tissue velocities based on multi-angle plane wave imaging," *IEEE Trans. Ultrason., Ferroelectr., Freq. Control*, vol. 60, no. 4, pp. 727–738, Apr. 2013.

[26] M. Couade *et al.*, "Ultrafast imaging of the heart using circular wave synthetic imaging with phased arrays," in *Proc. IEEE Int. Ultrason. Symp.*, 2009, pp. 515–518.

[27] P. Song *et al.*, "Improved shear wave motion detection using pulse-inversion harmonic imaging with a phased array transducer," *IEEE Trans. Med. Imag.*, vol. 32, no. 12, pp. 2299–2310, Dec. 2013.

[28] C. Papadacci, M. Pernot, M. Couade, M. Fink, and M. Tanter, "High-contrast ultrafast imaging of the heart.," *IEEE Trans. Ultrason., Ferroelectr., Freq. Control*, vol. 61, no. 2, pp. 288–301, Feb. 2014.

[29] T. A. Whittingham, "Tissue harmonic imaging," *Eur. Radiol.*, vol. 9, no. Suppl. 3, pp. S323–S326, Jan. 1999.

[30] F. Tranquart, N. Grenier, V. Eder, and L. Pourcelot, "Clinical use of ultrasound tissue harmonic imaging," *Ultrasound Med. Biol.*, vol. 25, no. 6, pp. 889–894, 1999.

[31] T. Christopher, "Finite amplitude distortion-based pulse echo ultrasonic imaging," *IEEE Trans. Ultrason., Ferroelectr., Freq. Control*, vol. 44, no. 1, pp. 125–139, Jan. 1997.

[32] Q. Ma, Y. Ma, X. Gong, and D. Zhang, "Improvement of tissue harmonic imaging using the pulse-inversion technique," *Ultrasound Med. Biol.*, vol. 31, no. 7, pp. 889–894, Jul. 2005.

[33] J. R. Doherty, J. J. Dahl, and G. E. Trahey, "Harmonic tracking of acoustic radiation force-induced displacements," *IEEE Trans. Ultrason., Ferroelectr., Freq. Control*, vol. 60, no. 11, pp. 2347–2358, Nov. 2013.

[34] J. A. Jensen, S. I. Nikolov, K. L. Gammelmark, and M. H. Pedersen, "Synthetic aperture ultrasound imaging," *Ultrasonics*, vol. 44, no. Suppl. 1, pp. e5–15, Dec. 2006.

[35] G. Montaldo, M. Tanter, J. Bercoff, N. Benech, and M. Fink, "Coherent plane-wave compounding for very high frame rate ultrasonography and transient elastography," *IEEE Trans. Ultrason., Ferroelectr., Freq. Control*, vol. 56, no. 3, pp. 489–506, Mar. 2009.

[36] S. I. Nikolov, J. Kortbek, and J. A. Jensen, "Practical applications of synthetic aperture imaging," in *Proc. IEEE Int. Ultrason. Symp.*, 2010, pp. 350–358.

[37] J. Luo and E. Konofagou, "A fast normalized cross-correlation calculation method for motion estimation," *IEEE Trans. Ultrason., Ferroelectr., Freq. Control*, vol. 57, no. 6, pp. 1347–1357, Jun. 2010.

[38] J. Provost, A. Gambhir, J. Vest, H. Garan, and E. E. Konofagou, "A clinical feasibility study of atrial and ventricular electromechanical wave imaging," *Heart Rhythm*, vol. 10, no. 6, pp. 856–862, Jun. 2013.

[39] J. McLaughlin and D. Renzi, "Using level set based inversion of arrival times to recover shear wave speed in transient elastography and supersonic imaging," *Inverse Prob.*, vol. 22, no. 2, pp. 707–725, 2006.

[40] T. Deffieux, J.-L. Gennisson, B. Larrat, M. Fink, and M. Tanter, "The variance of quantitative estimates in shear wave imaging: Theory and experiments," *IEEE Trans. Ultrason., Ferroelectr., Freq. Control*, vol. 59, no. 11, pp. 2390–2410, Nov. 2012.

[41] E. E. Konofagou and J. Provost, "Electromechanical wave imaging for noninvasive mapping of the 3D electrical activation sequence in canines and humans in vivo," *J. Biomech.*, vol. 45, no. 5, pp. 856–864, Mar. 2012.

[42] H. Kanai, "Propagation of spontaneously actuated pulsive vibration in human heart wall and in vivo viscoelasticity estimation," *IEEE Trans. Ultrason., Ferroelectr., Freq. Control*, vol. 52, no. 11, pp. 1931–1942, Nov. 2005.

[43] C. Papadacci, M. Pernot, M. Couade, M. Fink, and M. Tanter, "Shear Wave Imaging of the heart using a cardiac phased array with coherent spatial compound," in *Proc. IEEE Int. Ultrason. Symp.*, Oct. 2012, pp. 2023–2026.

[44] B. Denarie, T. A. Tangen, I. K. Ekroll, N. Rolim, H. Torp, and T. Bjåstad, "Coherent plane wave compounding for very high frame rate ultrasonography of rapidly moving targets," *IEEE Trans. Med. Imag.*, vol. 32, no. 7, pp. 1265–1276, Jul. 2013.

Mafalda Correia was born in Lisbon, Portugal, on October 1989. She received the B.Sc. and M.Sc. degrees in biomedical engineering from Faculdade De Ciências E Tecnologia (FCT)—Nova University of Lisbon, Lisbon, Portugal, in 2010 and 2012, respectively, and the M.Sc. degree in medical imaging from Telecom ParisTech School, Paris, France, in 2013. She is currently working at the Institut Langevin, in Paris, pursuing the Ph.D. degree, focusing on 2-D and 3-D ultrafast imaging, specifically, on cardiac shear wave elastography.

Jean Provost was born in Montreal, QC, Canada, in 1983. In 2006 and 2009, he completed his undergraduate and graduate studies at Ecole Polytechnique de Montreal, Canada, and Ecole Centrale Paris and Universite Paris-Sud, France, before obtaining the Ph.D. degree in biomedical engineering from Columbia University in New York in 2012.

He is currently a Researcher with the Institut Langevin, Paris, France, and the National Center for Scientific Research (CNRS), Paris, France. His research interests include high-frame-rate ultrasound imaging, tissue motion and blood flow mapping, and multiwave imaging techniques.

Simon Chatelin was born in Orléans, France, in October 1984. He received the Engineer degree in biophysics from Telecom Physics Strasbourg, Strasbourg, France, in 2007, and the Ph.D. degree in biomechanics from the University of Strasbourg, Strasbourg, France, in 2010, for his work on the coupling of biomechanics and medical imaging for the investigation of the intracerebral traumatic brain injuries.

He was a Postdoctoral Fellow with the Center for Research on Inflammation (Inserm-APHP), Paris, France, from 2011 to 2013, and with the Institut Langevin (ESPCI, Inserm), Paris, France, from 2013 to 2015, where he focused on the development of magnetic resonance elastography (MRE) to investigate the cerebral effects of the cannabinoids and on the application of ultrasound shear-wave elastography to muscular and cardiac soft tissues. In March 2015, he joined the Institute of Image-Guided Surgery of Strasbourg (IHU, ICube Laboratory), Strasbourg, France, working on the development of MRE in the field of the numerical simulations dedicated to computer-assisted surgery.

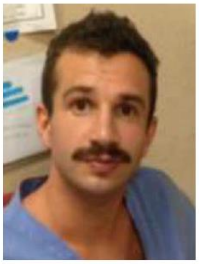

Olivier Villemain was born in Paris, France, in June 1985. He received the M.D. degree in cardiology and the M.Sc. degree in cardiovascular physiology from the University of Paris V, Paris, France, in 2014 and 2015, respectively. He is currently pursuing the Ph.D. degree from the French National Institute of Health and Medical Research (INSERM), Langevin Institute, Paris, France.

His research interests include ultrasound imaging, shear-wave elasticity imaging, and medical ultrasound therapy, specifically on cardiac applications.

Mickael Tanter received an engineering degree in 1994 from Supelec and the Ph.D. degree in physics in 1999 from the Paris 7 University. He is a Research Professor with the French National Institute for Health and Medical Research (INSERM), Langevin Institute, Paris, France. For eight years, he was the Head of the Inserm Laboratory U979, Wave Physics for Medicine, Langevin Institute, ESPCI Paris, France. In 2006, he cofounded Supersonic Imagine, Aix-en-Provence, France, with M. Fink, J. Souquet, and C. Cohen-Bacrie, which is an innovative French company positioned in the field of medical ultrasound imaging and therapy. He is the author of more than 160 peer-reviewed papers and book chapters and holds 24 world patents in the field of ultrasound. His research interests include the development of new approaches in wave physics for medical imaging and therapy, also a wide range of topics: elastography using supersonic shear-wave imaging, ultrafast ultrasound imaging, HIFU, and, more recently, the concept of fUtrasound (functional ultrasonic imaging of brain activity).

Prof. Tanter is an Associate Editor of the IEEE TRANSACTIONS ON ULTRASONICS, FERROELECTRICS, AND FREQUENCY CONTROL, and a member of the Technical Program Committee of the IEEE International Ultrasonics Symposium and the Administrative Committee of the IEEE UFFC Society. He was the recipient of ten scientific awards, including the Frederic Lizzi Early Career Award of the International Society of Therapeutic Ultrasound, the Montgolfier Prize of the French National Society for Industry Valorization, the Leon Brillouin Prize of the Institute of Electrical and Electronics Engineers (IEEE) and SEE Society, the Yves Rocard Prize of the French Society of Physics (SFP), the Sylvia Sorkin Greenfield Award of the American Association of Physicists in Medicine for the Best Paper published in Medical Physics in 2011, the Grand Prize of Medicine and Medical Research of the City of Paris, the Honored Lecture of the Radiology Society of North America in 2012, and the prestigious European Research Council (ERC) Advanced Grant to develop fUltrasound applications.

Mathieu Pernot received an engineering degree in 2001 from the ESPCI in Paris and the Ph.D. degree in physics in 2004 from the Paris 7 University. He is a Research Scientist with the French National Health Institute (INSERM), Paris, France, and a Permanent Member of the Wave Physics for Medicine and Biology team, Institut Langevin, Paris, France, since 2007. He cofounded the French startups Cardiawave, Paris, France, in 2014, and Neuroflows in 2016. He has authored/coauthored about 70 papers in international peer reviewed journals and has filed 17 patents in the field of ultrasound imaging and therapy. His research interests include the development of ultrafast ultrasound imaging and therapeutic ultrasound with a special interest on cardiovascular applications.

Dr. Pernot, as a Principal Investigator, has raised over 3 million euros from the European Research Council, the French National Research Agency, and the French Innovation Program in ultrasound imaging and therapy. He received a prestigious award from the European Research Council (1.5 M€ ERC Starting Grant) in 2012 for his research on ultrafast imaging of the human heart and early diagnosis of heart failure.

2.2.2. Manuscrit "*Validation of a non-invasive Myocardial Shear Wave Elastography device for clinical applications in cardiology" (In press)*

Ce travail a été accepté pour publication dans Innovation and Research in BioMedical Engineering (IRBM, In Press).

Le but principal de ce travail était de présenter les limites d'applications cliniques de l'élastographie myocardique, notamment en termes d'épaisseur du myocarde et de rigidité maximale estimable de manière quantitative. De plus, cela nous a poussés à décrire les méthodes d'acquisition (GUI, graphical user interface) et le post-processing permettant l'autonomisation progressive du clinicien.

Les principaux résultats ont été de montrer qu'une épaisseur de tissu < 5 mm et/ou un module de cisaillement > 25 kPa exposaient l'utilisation de notre outil (selon les paramètres utilisés) à des biais importants, donc à des limites d'applications cliniques.

Cela a permis de mieux programmer et concevoir les études cliniques.

IRBM - Your Submission

IRBM **<eesserver@eesmail.elsevier.com>**

À mafalda.correia, ilyapod, olivier.villem., jerome.baranger, mickael.tanter, mathieu.pernot

Ms. Ref. No.: IRBM-D-17-00066R1
Title: Non-invasive Myocardial Shear Wave Elastography device for clinical applications in cardiology
IRBM - Innovation and Research in BioMedical Engineering

Dear Mafalda,

I am pleased to confirm that your paper "Non-invasive Myocardial Shear Wave Elastography device for clinical applications in cardiology" has been accepted for publication in IRBM - Innovation and Research in BioMedical Engineering.

Comments from the Editor and Reviewers can be found below.

Thank you for submitting your work to this journal.

With kind regards,

David Melodelima, Ph.D.
Deputy Editor
IRBM - Innovation and Research in BioMedical Engineering

Validation of a non-invasive Myocardial Shear Wave Elastography device for clinical applications in cardiology

Mafalda Correia[1], Ilya Podetti[1], Olivier Villemain[1], Jerome Baranger[1], Mickael Tanter[1] and Mathieu Pernot[1]

[1]Institut Langevin, ESPCI Paris, PSL Research University, CNRS UMR7587, INSERM U979, Paris 6 University and Paris 7 University

17, Rue Moreau
75012 Paris
France

Abstract

Ultrasound Shear Wave Elastography has been widely used in clinical practice to access tissues' stiffness non-invasively. However, the application of this technique to access myocardial stiffness clinically and non-invasively was yet not demonstrated. In this study, we introduce a new prototype for clinical application purposes, the Myocardial Shear Wave Elastography imaging (MSWEi) device. The device lays on an ultrafast ultrasound scanner, a dedicated sequence of Shear Wave Elastography and unfocused emissions at very high frame rate for myocardial stiffness evaluation, and a dedicated graphical user interface for physicians use in clinical settings. The prototype was evaluated and validated in-vitro using calibrated mimicking tissue phantoms, providing accurate and robust measurements for tissues' stiffness up to 25kPa. The device was also validated for stiffness estimation on thin layers for thickness superior to 5-mm. The in-vivo and non-invasive application of the prototype was also evaluated on a patient. The results demonstrated that feasibility of MSWEi by a trained echocardiographist to access myocardial stiffness non-invasively in a clinical setting.

Introduction

In the past decades, Elastography techniques, based on ultrasound imaging, have been introduced to assess the elastic properties of soft tissues non-invasively (consult Gennisson et al. 2013 for a review of the principles and techniques). Shear Wave Elastography (SWE) is a quantitative ultrasound-based elastography technique, based on ultrafast frame rate imaging of mechanical shear waves propagation in the tissue (propagation velocities typically varies between 1 and 10 m/s) induced through the application of a time varying external force. Specifically, SWE consists in (1) the generation of a push-beam within the tissue of interest using acoustic radiation force, (2) imaging the resulting shear-wave propagation and (3) estimating the local velocity of the shear wave propagation, which can be used to determine the local stiffness of tissues varying complexities (Bercoff et al. 2004), e.g., the cardiac muscle, i.e. the myocardium. The myocardium is a complex three-dimensional network of particularly organized, specific and elastic fibers with physical properties that change in time and spatially. The evaluation of the myocardial stiffness could help the diagnosis of several conditions allied to stiffness changing, e.g. heart failure. Different studies have shown the feasibility of quantifying myocardial stiffness in-vivo in open chest animals (Hsu et al. 2007; Pislaru et al. 2009; Pernot et al. 2011; Bouchard et al. 2011; Pernot et al. 2016). Recent studies have demonstrated that non-invasive transthoracic myocardial stiffness measurements is feasible in few normal subjects at high temporal resolution (Song et al. 2013; Papadacci et al. 2014; Correia et al. 2016).

However, myocardial stiffness measured non-invasively in clinical practice on patients with cardiac disease was yet not demonstrated. In this study, we introduce a clinical implementation of Myocardial Shear Wave Elastography using ultrafast imaging at very high frame rates, a device for clinical evaluation purposes. Furthermore, we validate this implementation on in-vitro calibrated isotropic phantoms which mimic the myocardial thickness and stiffness.

Material and Methods

1. Myocardial Shear Wave Elastography Imaging (MSWEi) device for clinical purposes

A 2.75-MHz linear phased-array probe (96 elements, 0.2-mm pitch, Vermon S.A., Tours, France) connected to an ultrafast ultrasound scanner (Aixplorer, Supersonic Imagine, Aix-en-Provence, France) was used to perform the acquisitions. An electrocardiograph (ECG) system (AccuSync 42, AccuSync Medical Research Corporatio, CT, USA) was used to trigger and measured ECG signals in real time, which was recorded by a data acquisition board (USB-201 model, MC Measurement Computing, MA, USA). A dedicated software with a graphical user interface (Matlab 2015a, MathWorks, Natick, MA, USA) was developed for this application and used on a tablet (Surface Pro 3, Microsoft Corporation, Redmond, Washington, USA), Figure 1, to run and perform the acquisitions.

The imaging sequences were designed to 1) perform a primary ultrafast harmonic B-mode image (Correia et al. 2016) followed by 2) Shear Wave Elastography acquisition (Papadacci et al. 2014; Correia et al. 2016). The imaging sequences developed and used in this study were based on the emission of unfocused ultrasound beams, i.e., diverging-waves. For details on diverging-waves transmission concept and formation, see (Papadacci et al. 2014).

1.1. B-mode and Myocardial Shear Wave Elastography Imaging

Prior to Myocardial Shear Wave Elastography, a B-mode image was acquired for anatomical landmark purposes. This B-mode image was based on Ultrafast Harmonic Coherent Compound Imaging, presented by (Correia et al. 2016), using 15 diverging-waves transmission at 2.1-MHz.

After B-mode imaging, Shear Wave Elastography was launched with ECG-trigger synchronization. To induce a shear wave propagation within the tissue, a push-beam, through acoustic radiation force, was transmitted at 3-MHz, 300-µs duration and at a push-depth of interest. Immediately after generating the shear wave, ultrafast imaging was launched at frame rates superior to 1000 images/s. Ultrafast imaging

sequence consisted on the successive transmission of 2 diverging-waves at 3-MHz (Papadacci et al. 2014). The acoustic output of Myocardial Shear Wave Elastography imaging sequences were measured using a calibrated interferometer in water. The sequences fulfilled the Food and Drug Administration (FDA) requirements (510k track 3, FDA) defined by the mechanical index (MI) and the spatial-peak time average (I_{SPTA}) with a derating factor of 0.3 dB cm^{-1} MHz^{-1}. The $MI_{0.3}$ was set to 1.8 ($MI_{0.3}$<1.9 by FDA) and the I_{SPTA} was set to 157 mW cm^{-2} ($I_{SPTA\ 0.3}$<720 mW cm^{-2} by FDA), with a repetition time of 1 second.

In what concerns in-vivo human imaging experimentation, informed consents were obtained within the clinical investigation protocol n° 2015-A00187-42 approved by the CPP (Comité de Protection des Personnes), Ile de France VI, France.

1.2. Graphical User Interface

The graphical user interface was developed with the purpose of allowing complete independence between the physician and the ultrafast ultrasound scanner and perform Shear Wave Elastography for myocardial stiffness measurements application. Parameters as the main information of the patient in study, the choice of the push focusing depth and ECG trigger timing within the cardiac cycle were integrated, as it is showed in Figure 1.

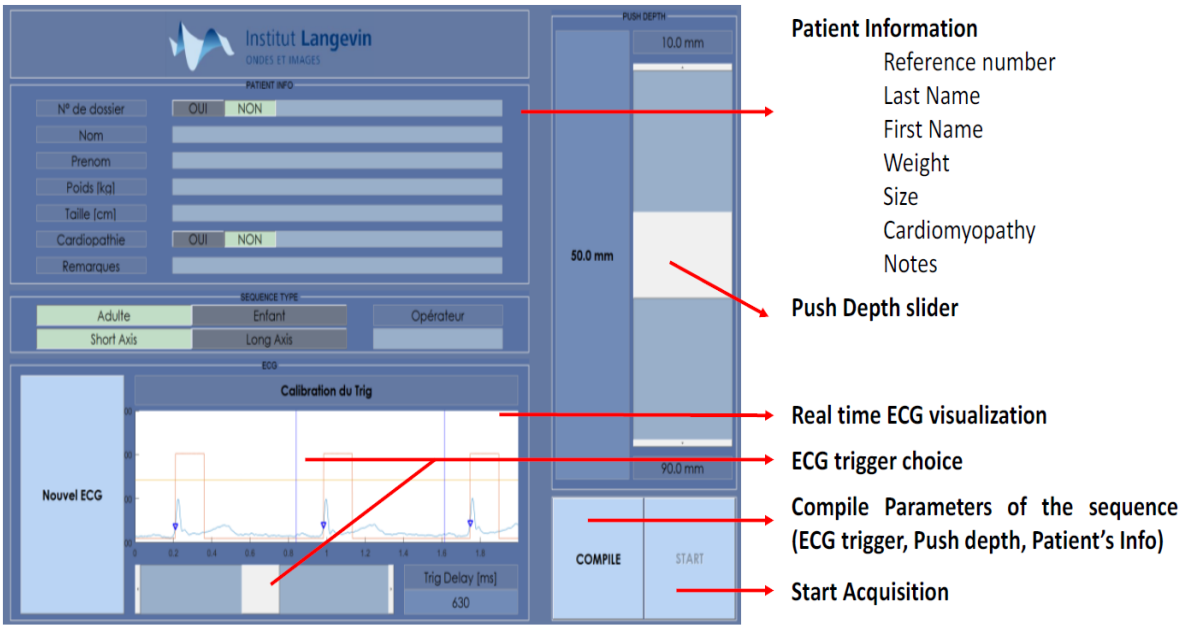

FIGURE 1 : GRAPHICAL USER INTERFACE FOR CLINICAL MYOCARDIAL SHEAR WAVE ELASTOGRAPHY IMAGING.

1.3. Post-processing analysis: shear wave propagation velocity measurements

The radio-frequency (RF) signals of the acquisition were first backup in the tablet. The RF data were processed off-line with a Matlab (2015a, The MathWorks Inc., Natick, MA, USA) interface. The RF-data

were then reconstructed offline using a conventional delay-and-sum beamforming algorithm, implemented in a graphical processing unit (K600, NVidia, Santa Clara, CA, USA).

Tissue velocity images were attained using 1-D cross-correlation of successive beamformed images with cosine interpolation (1.5-mm kernel size and 97.5-% overlap), (Bonnefous et al. 1986; Sandrin et al. 1999; McLaughlin & Renzi 2006), followed by scan-conversion. Subsequently, spatiotemporal tissue velocity data were computed and shear wave propagation velocities in the lateral direction were calculated using linear least-squares estimation on temporal 1-D cross-correlation with different lateral spatial lags (lags range: 0.2 to 1.8-mm) (McLaughlin & Renzi 2006; Correia et al. 2016). Finally, the shear modulus (μ) can be calculated by the followed relationship (Equation 1):

EQUATION 1: $$\mu = {v_s}^2 \rho$$

where the v_s corresponds to the shear wave propagation velocity and ρ the tissue's density. The shear modulus is linked to a measure of stiffness, through the Hooke's law.

2. Evaluation and validation on in-vitro calibrated phantoms

Isotropic Polyvinyl alcohol (PVA) hydrogels have been largely used as tissue mimicking models for Shear Wave Elastography imaging due to their elastic mechanical properties. In this study, we investigated the performance of our device to provide accurate stiffness on various PVA hydrogels of different thickness and different stiffness. First, we developed soft isotropic models with different thicknesses to mimic the in-vivo anatomical differences of the myocardial thickness (e.g. normal against hypertrophic or dilated myocardium), and soft isotropic models with different stiffness to evaluate and validate the limits of our technique to assess myocardial stiffness.

In the first model configuration, eight different samples were created and constituted by 10-% PVA solution (molecular weight 89 000–98 000, 99+% hydrolyzed, Sigma-Aldrich, St Louis, US), 1-% cellulose (20 µm in diameter, S3504 Sigmacell, Sigma-Aldrich, St Louis, US) and 89-% distilled water. Samples were transferred into a parallelepiped PVC mold (80 x 50 x 50-mm3) and underwent two isotropic freezing/unfreezing cycles (i.e. approximately 20°C during 12-h followed by -18°C during 12-h). Then, the samples were cut in slices with different thickness, i.e. from 1.8 to 18 mm thick (Figure 2). The purpose of this experimental configuration was to evaluate the tissue thickness effect under the same tissue stiffness.

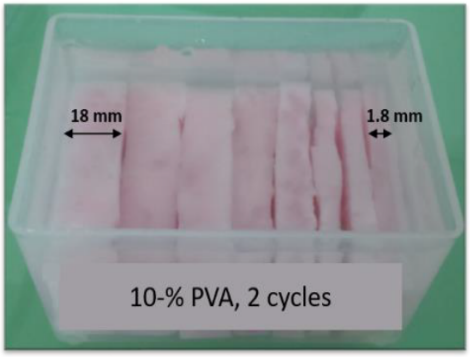

FIGURE 2: THE FIRST SOFT ISOTROPIC MODEL CONFIGURATION. EIGHT DIFFERENT SAMPLES OF DIFFERENT TICKNESSES (FROM 1.8 TO 13 MM THICK).

In the second model configuration, twenty different samples were created and they were divided equally in five groups of different PVA percentages, i.e. different media stiffness. Therefore, they were divided in: (1) 5-% PVA solution, 1-% cellulose and 94-% distilled water; (2) 7.5-% PVA solution, 1-% cellulose and 91.5-% distilled water; (3) 10-% PVA solution, 1-% cellulose and 89-% distilled water; (4) 12.5-% PVA solution, 1-% cellulose and 86.5-% distilled water; and (5) 15-% PVA solution, 1-% cellulose and 84-% distilled water. All samples were transferred into a parallelepiped PVC mold (80 x 50 x 50-mm3). For each group, each sample underwent 2 to 5 isotropic freezing/unfreezing cycles (i.e. approximately 20°C during 12-h followed by -18°C during 12-h) to induce elastic property changings, e.g. media stiffness changings.

For all configurations, the experimental setup included an absorber (Polyurethane, NPL, UK) covered by the PVA samples, immersed in water to guarantee good acoustic coupling. The experimental setup is presented in Figure 3 with the phased-array probe positioned at 5-mm distance of the each sample.

To evaluate the results given by the MSWEi device imaging, as presented in the last section, four acquisitions were performed for each PVA sample for reproducibility purposes and they were compared with the Aixplorer ultrasound scanner, using the clinical system and a 10-2-MHz linear-array probe, which was considered as the gold-standard measurements. A comparison in function of tissue stiffness and thickness was evaluated. The tissue stiffness comparison was made using linear regression and the Bland-Altman analysis.

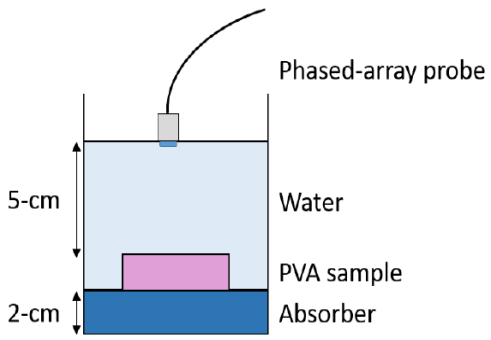

FIGURE 3: THE IN-VITRO EXPERIMENTAL SETUP.

Results

1. Evaluation and validation on in-vitro calibrated phantoms

For the in-vitro acquisitions, shear wave propagation velocities were calculated through the post-processing analysis as presented in the last section. For each PVA sample, four acquisitions were performed using the commercial SWE mode of the Aixplorer ultrasound scanner system, as gold-standard measurements, and the Myocardial Shear Wave Elastography imaging device. A comparison between the imaging device and the gold-standard was evaluated in terms of shear wave velocity measurements and the corresponding results are presented in Figure 4.

In Figure 4(A), the Myocardial Shear Wave Elastography imaging device measurements as a function of the PVA sample thicknesses are presented with the corresponding averaged and standard-deviation reproducibility values. The corresponding gold-standard measured value, i.e. a shear wave velocity of 3 m/s, by the Aixplorer ultrasound scanner is also represented. These results showed that the shear velocity decreases when the sample gets thin. For thicknesses inferior to 5-mm, the shear wave velocities measured by the MSWEi device present a bias superior to 15-% when compared to the gold-standard.

Figure 4(B) and (C) show the correlation and the Bland-Altman analysis between MSWEi device and the gold-standard measurements. Results showed a strong correlation between both, corroborated by a Bland-Altman plot. Very good agreement was found for shear velocities less 5 m/s than whereas the absolute errors increases at high velocities.

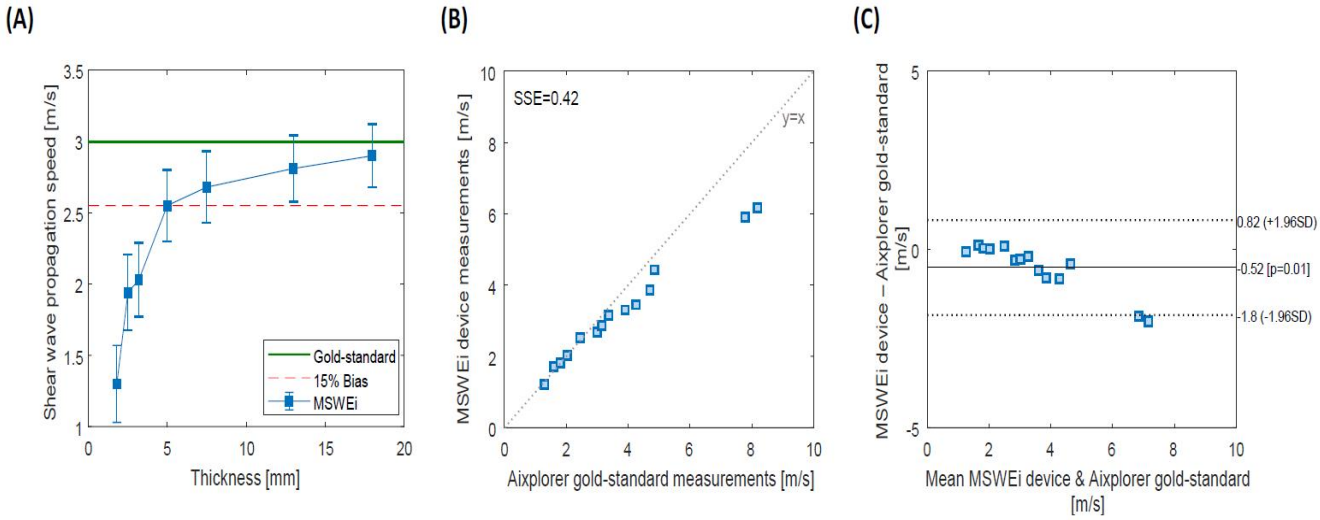

FIGURE 4: SHEAR WAVE PROPAGATION VELOCITY IN FUNCTION OF THICKNESS AND COMPARISON WITH THE CORRESPONDING GOLD-STANDARD SHEAR WAVE VELOCITY VALUE (A), CORRELATION BETWEEN THE MYOCARDIAL SHEAR WAVE ELASTOGRAPHY IMAGING DEVICE AND THE AIXPLORER GOLD-STANDARD MEASUREMENTS (B), AND BLAND-ALTMAN ANALYSIS OF MYOCARDIAL SHEAR WAVE ELASTOGRAPHY IMAGING DEVICE AND THE AIXPLORER GOLD-STANDARD MEASUREMENTS (C).

2. Myocardial Shear Wave Elastography imaging device application for clinical purposes

Figure 5 presents the Myocardial Shear Wave Elastography Imaging device application in clinical practice and an example of an in-vivo transthoracic myocardial shear wave propagation. Figure 5(B) shows an example of a possible shear wave propagation tracking in-vivo transthoracically in a long-axis view. When shear wave propagation tracking is possible, the shear wave propagation velocity can be calculated through the post-processing analysis presented.

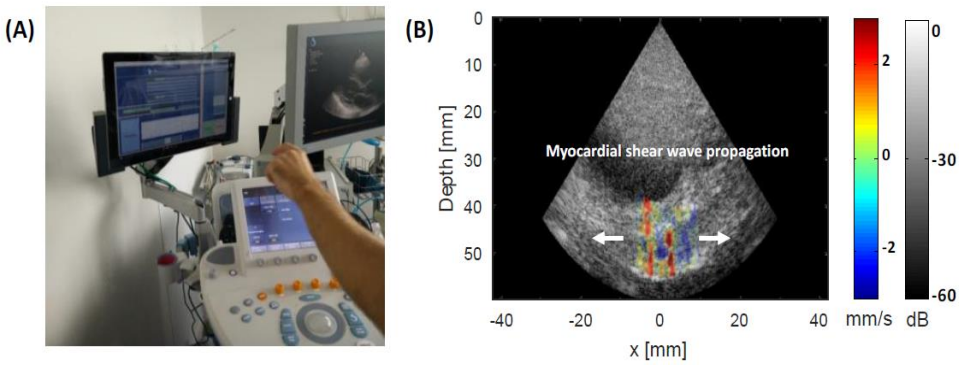

FIGURE 5: CLINICAL MYOCARDIAL SHEAR WAVE ELASTOGRAPHY IMAGING APPLICATION EXAMPLE. (A) CORRESPONDS TO THE CLINICAL SETUP AND (B) A TISSUE VELOCITY IMAGE OF THE MYOCARDIAL SHEAR WAVE PROPAGATION IN A TRANSTHORACIC LONG-AXIS VIEW.

Discussion

In this study, we evaluated and validated a new device to perform non-invasive Myocardial Shear Wave Elastography for the purpose of future clinical studies. This prototype consisted on an ultrafast ultrasound

scanner, dedicated ultrasound sequences for myocardial shear wave elastography (Papadacci et al. 2014; Correia et al. 2016) and a dedicated graphical user interface that enables the physician to perform the acquisition in a clinical setting. The prototype was evaluated and validated in-vitro using calibrated mimicking tissue phantoms and an example of in-vivo application was also presented.

We tested the performances of the prototype on various calibrated hydrogels of different thickness and stiffness. The shear wave velocity was found to decrease slightly with thickness between 5 and 18-mm and then suddenly dropped for thicknesses inferior to 5 mm. This effect was expected and is mainly due to guided waves propagation when the thickness and the shear wavelength become on the same order of magnitude (Thu-Mai Nguyen et al. 2011). Consequently, the measured shear velocity is underestimated for thickness smaller than 5-mm, with a shear wave velocity bias superior to 15%. These results also show that Shear Wave velocity can be accurately measured in tissues with thicknesses superior to 5-mm, with a shear wave velocity bias up to 15%. Therefore, the application of Shear Wave Elastography in clinical practice for myocardial stiffness assessment may be limited on very thin myocardium in specific pathologies, which are characterized by a reduction of the myocardial wall thickness (Mcmurray et al. 2012).

In what concerns the evaluation of different tissues' stiffness and the prototype measurements robustness, the results showed that measurements acquired by MSWEi and the clinical system of the Aixplorer ultrafast ultrasound scanner, i.e. the considered gold-standard, are in good agreement. The Bland-Altman statistical analysis shows that MSWEi measurements are robust up to 5 m/s (i.e. a shear modulus of 25 kPa). For higher shear wave velocities, i.e. stiffer tissues, the MSWEi lacks to track and estimate properly the shear wave propagation velocity. This fact is mainly related to the imaging frame limitation (2000 images/s) due to the large imaging depth required for the heart and imaging quality to track the shear wave propagation. Therefore, the application of the Myocardial Shear Wave Elastography imaging device, as presented, is considered to be limited to a maximum of 5 m/s, i.e. a shear modulus of 25kPa. We expect this range to be large enough since normal myocardial shear velocity is around 1.5m/s and very stiff pathological myocardium around 4 m/s (Villemain et al. n.d.).

Finally, the application of the prototype was evaluated clinically by trained echocardiographists. The presented results showed that the acquisition can be performed very easily by the physician within a 10 minute examination, but also that myocardial shear wave propagation can be tracked in-vivo, non-invasively and clinically.

Conclusion

In this study, we presented a novel Myocardial Shear Wave Elastography imaging device to evaluate myocardial stiffness non-invasively using an ultrafast ultrasound scanner in a clinical setting. The imaging setup was evaluated in-vitro and the in-vivo application was also showed. The in-vitro results showed that the Shear Wave Elastography prototype provides accurate and robust measurement in tissue mimicking phantoms for stiffness up to 25kPa.

Acknowledgements

This work was supported from European Research Council grant under the European Union's Seventh Framework Program (FP/2007–2013) / ERC Grant Agreement n°311025.

Bibliography

Bercoff, J., Tanter, M. & Fink, M., 2004. Supersonic shear imaging: a new technique for soft tissue elasticity mapping. *IEEE Transactions on Ultrasonics, Ferroelectrics and Frequency Control*, 51(4), pp.396–409. Available at: http://ieeexplore.ieee.org/articleDetails.jsp?arnumber=1320804 [Accessed March 29, 2014].

Bonnefous, O., Pesque, P. & Bernard, X., 1986. A new velocity estimator for color flow mapping. In *Proc. IEEE Ultrason. Symp.* IEEE, pp. 855–860.

Bouchard, R.R. et al., 2011. Acoustic radiation force-driven assessment of myocardial elasticity using the displacement ratio rate (DRR) method. *Ultrasound in medicine & biology*, 37(7), pp.1087–100. Available at: http://www.sciencedirect.com/science/article/pii/S030156291100202X [Accessed August 21, 2014].

Correia, M. et al., 2016. Ultrafast Harmonic Coherent Compound (UHCC) imaging for high frame rate echocardiography and Shear Wave Elastography. *IEEE Transactions on Ultrasonics, Ferroelectrics, and Frequency Control*, pp.1–1. Available at: http://ieeexplore.ieee.org/lpdocs/epic03/wrapper.htm?arnumber=7407422.

Gennisson, J.-L. et al., 2013. Ultrasound elastography: principles and techniques. *Diagnostic and interventional imaging*, 94(5), pp.487–95. Available at: http://www.ncbi.nlm.nih.gov/pubmed/23619292 [Accessed September 9, 2014].

Hsu, S.J. et al., 2007. In vivo assessment of myocardial stiffness with acoustic radiation force impulse imaging. *Ultrasound in medicine & biology*, 33(11), pp.1706–19. Available at: http://www.sciencedirect.com/science/article/pii/S0301562907002530 [Accessed August 13, 2014].

McLaughlin, J. & Renzi, D., 2006. Using level set based inversion of arrival times to recover shear wave speed in transient elastography and supersonic imaging. *Inverse Problems*, 22(2), pp.707–725.

Mcmurray, J.J. V et al., 2012. ESC Guidelines for the diagnosis and treatment of acute and chronic heart failure 2012. *European Journal of Heart Failure*, 14(8), pp.803–869.

Papadacci, C. et al., 2014. High-contrast ultrafast imaging of the heart. *IEEE transactions on ultrasonics,*

ferroelectrics, and frequency control, 61(2), pp.288–301. Available at: http://www.ncbi.nlm.nih.gov/pubmed/24474135 [Accessed April 15, 2014].

Pernot, M. et al., 2011. Real-time assessment of myocardial contractility using shear wave imaging. *Journal of the American College of Cardiology*, 58(1), pp.65–72. Available at: http://www.ncbi.nlm.nih.gov/pubmed/21700091 [Accessed April 11, 2014].

Pernot, M. et al., 2016. Shear Wave Imaging of Passive Diastolic Myocardial Stiffness: Stunned Versus Infarcted Myocardium. *JACC. Cardiovascular imaging*. Available at: http://www.sciencedirect.com/science/article/pii/S1936878X16302273 [Accessed May 31, 2016].

Pislaru, C. et al., 2009. Shearwave dispersion ultrasound vibrometry applied to in vivo myocardium. *Conference proceedings : ... Annual International Conference of the IEEE Engineering in Medicine and Biology Society. IEEE Engineering in Medicine and Biology Society. Conference*, 2009, pp.2891–4. Available at: http://www.ncbi.nlm.nih.gov/pubmed/19964051 [Accessed August 21, 2014].

Sandrin, L. et al., 1999. Time-Resolved Pulsed Elastography with Ultrafast Ultrasonic Imaging. *Ultrasonic Imaging*, 21(4), pp.259–272. Available at: http://uix.sagepub.com/content/21/4/259.abstract [Accessed October 24, 2014].

Song, P. et al., 2013. Improved Shear Wave Motion Detection Using Pulse-Inversion Harmonic Imaging with a Phased Array Transducer. *IEEE transactions on medical imaging*, (c). Available at: http://www.ncbi.nlm.nih.gov/pubmed/24021638.

Thu-Mai Nguyen et al., 2011. Assessment of viscous and elastic properties of sub-wavelength layered soft tissues using shear wave spectroscopy: Theoretical framework and in vitro experimental validation. *IEEE Transactions on Ultrasonics, Ferroelectrics and Frequency Control*, 58(11), pp.2305–2315. Available at: http://ieeexplore.ieee.org/document/6071049/ [Accessed May 26, 2017].

Villemain, O. et al., Myocardial stiffness assessment using shear wave imaging in pediatric hypertrophic cardiomyopathy (in review).

2.3. Applications chez l'enfant

2.3.1. Présentation du travail

Après avoir présenté la nouvelle technique d'imagerie dédiée à l'application humaine de l'élastographie myocardique (l'imagerie par sommation cohérente harmonique ultrarapide), puis avoir présenté nos modalités d'acquisition et de post-traitement ainsi que les limites attendues en clinique, l'enjeu était à présent de réaliser la « preuve de concept » chez l'humain en pratique clinique. Pour cela, il fallait concevoir une étude réalisable chez l'humain, permettant de montrer la fiabilité et la reproductibilité de la technique, tout en montrant un intérêt clinique fort.

Cette étude a été promue par la Société Française de Cardiologie, après avoir obtenu l'accord du Comité de Protection des Personnes de Paris VI (2015-A00438-41) et une déclaration à l'ANSM (DMDPT-DAIG/MM/2015-A00438-41). De plus, cette étude a été déclarée au registre international d'études cliniques (ClinicalTrials.gov; NCT02619825).

2.3.2. Manuscrit "*Myocardial stiffness assessment using shear wave imaging in heathy children and hypertrophic cardiomyopathy*"

Ce travail a été accepté pour publication dans JACC Cardiovascular Imaging. Il est actuellement sous presse.

JIMG052417-0656-TR Decision Letter

jimg@msubmit.net

À olivier.villem., moi

"Myocardial stiffness assessment using shear wave imaging in pediatric hypertrophic cardiomyopathy"

Dear Dr. Villemain:

On behalf of the American College of Cardiology, we are pleased to accept your above referenced manuscript for publication.

PLEASE ALSO NOTE THE FOLLOWING PENDING ITEMS, WHICH MUST BE RECEIVED BEFORE WE CAN SCHEDULE YOUR ARTICLE FOR PUBLICATION. ALL ITEMS SHOULD BE EMAILED TO US AT: jaccimg@acc.org

1. Per the editors and statistical reviewer, the following change was made on p. 3: "high specificity and sensibility" was changed to "high specificity and sensitivity." You do not need to resend your manuscript.

NOTE ABOUT ACCEPTED PAPERS:

In order to add or remove any authors after acceptance of their paper, all listed authors at the time of acceptance need to provide written approval to the JACC Journals' editorial office (jaccimg@acc.org) prior to the scheduling and publication of the paper.

Thank you for your contribution to JACC: Cardiovascular Imaging.

Sincerely,

Thomas H. Marwick, M.B.B.S., Ph.D., M.P.H.
Deputy Editor
JACC: Cardiovascular Imaging

Y. Chandrashekhar, MD, FACC
Editor-in-Chief
JACC: Cardiovascular Imaging
Heart House, 2400 N Street NW, Washington, DC, 20037
Ph: 202-375-6136
Fax: 202-375-6819
Email: jaccimg@acc.org

Myocardial stiffness assessment using shear wave imaging in pediatric hypertrophic cardiomyopathy

Authors: O. Villemain, MD,[1,2] M. Correia, PhD,[2] D. Khraiche, MD,[1] I. Podetti,[2] M. Meot, MD,[1] A. Legendre, MD,[1] M. Tanter, PhD,[2] D. Bonnet, MD, PhD,[1*] / M. Pernot, PhD,[2*]

[1]**M3C-Necker Enfants malades, AP-HP, Université Paris Descartes, Sorbonne Paris Cité, Paris, France**

[2]**Institut Langevin, ESPCI, CNRS, Inserm U979, PSL Research University, 17 rue Moreau, 75012 Paris, France**

* Co-last authors. Mathieu Pernot and Damien Bonnet contributed to this work equally

Corresponding Author: Olivier Villemain, MD

M3C-Necker Enfants malades, AP-HP, Université Paris Descartes, Sorbonne Paris Cité, Paris, France

Telephone: (33) 1 44 49 43 44. Fax: (33) 1 44 49 43 40

E-mail : olivier.villemain@inserm.fr

COMPETING INTERESTS: Dr. Tanter is co-founder of SuperSonic Imagine. The other authors have nothing to disclose.

Word count: 5422

ABSTRACT

Background. The pathophysiology of hypertrophic cardiomyopathy (HCM) is characterized by an increase of ventricular stiffness in most patients. However, myocardial stiffness (MS) cannot be measured non-invasively by the existing techniques.

Purpose. The goal of our study was to investigate the potential of Myocardial Shear Wave Imaging (SWI), to quantify the diastolic MS non-invasively in a pediatric population of HCM.

Methods. We prospectively included 28 patients with HCM and 28 healthy controls matched for age (range: 5-18 years) and sex. A standard echocardiography and a SWI were performed. 21 HCM patients underwent a cardiopulmonary exercise test. SWI was performed using an ultrafast ultrasound system (Aixplorer, Supersonic Imagine, France) and a phased-array probe (2.75 MHz). SWI acquisitions were performed on the antero-septal basal segment during the end-diastole, in two orthogonal views. Fractional anisotropy (FA) estimated by shear wave speed was also evaluated.

Results. The median MS in the control group was 1.7 (CI95%, 1.3-1.8) kPa. MS was significantly higher in the HCM (7.9 [7.2-10.5] kPa), $p<0.01$. The FA was lower in HCM (0.084 [0.058-0.130]) compared to controls (0.138 [0.086-0.222]), $p=0.01$. Based on ROC curves analysis, no unique echocardiographic parameter could predict a MS>4 kPa with a high specificity and sensibility. Strong correlations were found between the MS and peak oxygen uptake ($r=-0.752$; $p<0.01$) or peak oxygen pulse ($r=-0.773$; $p<0.01$). Among the seven HCM patients who had MS > CI95% (>10.5 kPa), six had an echocardiographic restrictive profile assessed by LAVI >48 ml/m², E/A >2, E-wave DT <150 ms, and e' medial <6 cm/s.

Conclusion. Non-invasive SWI evaluation of diastolic myocardial stiffness is a valuable adjunct to characterize diastolic function of the left ventricle in pediatric HCM. Additional studies are needed to evaluate its role as a predictor of outcome and as a therapeutic target. (Non-Invasive Evaluation of Myocardial Stiffness by Elastography in Pediatric Cardiology: NCT02619825)

Key Words: myocardial stiffness • echocardiography • pediatric • myocardium • cardiomyopathy

ABRREVIATIONS:

ASB: antero septo basal

BSA: body surface area

CPET: cardiopulmonary exercise test

ECG: electrocardiogram

DT: deceleration time

FA: fractional anisotropy

GS: global strain

HCM: hypertrophic cardiomyopathy

HF: heart failure

HFpEF: heart failure with preserved ejection function

HV: healthy volunteer

IVRT: isovolumic relaxation time

LAVI: left atrium volume index

LVEF: left ventricle ejection fraction

LVEDD: left ventricle end-diastolic diameter

LVESD: left ventricle end-systolic diameter

MS: myocardial stiffness

PV S/D ratio: pulmonary veins velocities

SD: standard deviation

SWI: shear wave imaging

TV: theoretical value

Vp: transmitral flow propagation velocity

INTRODUCTION

Echocardiographic diagnosis of HCM is usually simple and based on an anatomical definition[1]. One of the major difficulties is the assessment of the left ventricle diastolic function in this condition, while it is one of the main prognostic parameter for the children or the adults with HCM[1-2]. Diastolic dysfunction in HCM is related to the alteration of the myocardial passive stiffness (MS) that modifies left ventricle relaxation[3]. The alteration of MS is supposed to be caused by the myocardial architectural modification with "multiple intercellular connections often arranged on chaotic alignment and with expanded interstitial (matrix) collagen"[4].

In a general view, the assessments of diastolic function can be divided between those that reflect the process of active/auxotonic relaxation (depending on filling load and afterload) and those that reflect passive stiffness (independent of load conditions)[5]. However, the evaluation of diastolic function in HCM still remains challenging[6]. Indeed, the conventional echocardiographic parameters used for the evaluation of the diastolic function[7] are difficult to apply to children, mostly because the use of these parameters does not seem to be applicable with robustness to children with cardiomyopathy[8]. Today, we lack reproducible quantitative tools independent of loading conditions and anthropometric parameters to evaluate diastolic left ventricular function in children with HCM.

Having access to such a quantitative non-invasive reproducible parameter could have three main interests: (1) evaluating the potential role of this parameter as predictor of cardiovascular events in this population; (2) assessing the impact of medical and / or surgical treatments on this parameter; (3) developing interventions that could use this parameter as a therapeutic target.

Shear wave imaging (SWI) by ultrafast imaging is an ultrasound-based technique for quantitative, local, and non-invasive mapping of soft tissue elastic properties. This technique has proved to be clinically efficient in evaluating tissue stiffness in numerous organs. The technological validation of MS by SWI has previously been reported[9]. In addition, it has been

compared with invasive gold standard parameters for left ventricle diastolic function[10]. The clinical feasibility has been demonstrated in adults[11] and children[11]. Nevertheless, no clinical studies have been reported yet to determine the interest and the contribution of this technology to the assessment of diastolic function in pediatric HCM.

The purpose of our study was to quantify the diastolic MS non-invasively using myocardial SWI in pediatric hypertrophic cardiomyopathy (HCM) patients compared to an age and sex matched control group of healthy children.

METHODS

Study population and design

This was a prospective study performed at the Necker-Enfants Malades Hospital, Paris, France. HCM patients were identified according to the guidelines of the European Society of Cardiology[1,12], using a specific inclusion criterion: wall thickness ≥ 2 standard deviation (SD) in one or more LV myocardial segments. We included both familial and sporadic cases of HCM. Healthy controls were recruited from our clinic. All healthy controls had normal clinical examination and normal echocardiography with no personal history of cardiac anomaly. None had familial history of HCM or other inherited cardiac disease.

Exclusion criteria included systolic blood pressure (BP) ≥ 90 percentile or/and diastolic BP ≥ 90 percentile, any persistent cardiac arrhythmia, more than moderate valvular disease, any relevant coronary artery diseases, and anechogenicity.

All subjects included in the study had clinical examination, ECG, echocardiography and cardiac SWI. All tests were performed on the same day. Twenty-one patients of the HCM group had cardiopulmonary exercise test.

The study was approved by the local ethics committee, and all patients gave written informed consent (Non-Invasive Evaluation of Myocardial Stiffness by Elastography in Pediatric Cardiology; this trial is registered with ClinicalTrials.gov, NCT02619825).

Study paraclinical investigations

Echocardiography

Echocardiographic studies were performed on a Vivid 9 system (General Electric Healthcare, Chalfont St. Giles, Great Britain). Mitral valve inflow pattern (E and A velocity), E-wave deceleration time (E-wave DT), isovolumic relaxation time (IVRT estimated on mitral valve inflow pattern), septal and lateral mitral valve annular tissue Doppler velocities (e' and a'), left atrial volume index (LAVI), as well as pulmonary veins S-wave on D-wave ratio (PV S/D ratio) were recorded in an apical 4-chamber view, to assess the parameters of diastolic function according to American Society of Echocardiography guidelines[13]. Data were analyzed from stored images by an experienced operator (D.K.), who was unaware of other tests results. Measurements were made in three cardiac cycles; the mean value was used for statistical analysis.

Myocardial stiffness measured by shear wave imaging (figure 1 and online video)

SWI is based on the remote generation of shear waves in soft tissue by acoustic radiation force combined with ultrasonic ultrafast imaging of the shear wave propagation (5000 images/s), using the same ultrasonic transducer[14]. A short push (300 μs) of focused ultrasound was transmitted by a diagnostic ultrasonographic probe (phased array, 2.75-MHz central frequency; SuperSonic Imagine, Aix-en-Provence, France) to induce micrometric tissue displacements in a small zone of the myocardium by acoustic radiation force. The push was generated in the left ventricular endocardium. In response to that transient mechanical excitation, a shear wave was generated in the low–kHz-frequency range and propagated in the myocardium at velocities from 1 to 10 m/s, depending upon the intrinsic tissue stiffness. Tissue velocity maps were computed offline for each frame by using in-phase quadrature frame to frame cross-correlation. Myocardial wall motion was removed by subtraction of the average wall motion during the acquisition, bringing to light tissue motion induced solely by the shear wave. Shear wave velocity was computed at the depth of the mid-wall myocardium using spatiotemporal data from shear wave propagation. Finally, the shear modulus μ (i.e., stiffness) was derived using the equation:

$$\mu = \rho c^2 \text{ (kPa)} \qquad \text{(Equation 1)}$$

where c is the shear wave velocity, and ρ is the volume mass of the tissue.

The explored myocardial segment was the antero septo basal segment (ASB segment). It was evaluated in two orthogonal axes (short- and long-axis views, see figure 1). All acquisitions were performed at end-diastole and triggered by an electrocardiogram (ECG). Data were interpreted by two experienced readers (O.V. and M.C.) who were unaware of the subjects' clinical information and the results of other diagnostic tests.

Fractional Anisotropy

Like any fiber-composed muscular tissue, the myocardium presents a significant anisotropy of its elastic properties. Consequently, MS is expected to be higher when measured along the fibers, which are mainly oriented along the circumferential direction in the mid-wall layer. In order to evaluate the degree of anisotropy in the myocardium, the fractional anisotropy (FA) was computed. FA was defined using two shear wave speed (SWS) measurements performed in orthogonal propagation directions (long axis and short axis views) using the formula published by Lee et al[15] in 2011:

$$FA_{SWI} = \sqrt{2}\,\frac{\sqrt{(SWSsa-SWSm)^2+(SWSla-SWSm)^2}}{\sqrt{SWSsa^2+SWSla^2}} \qquad \text{(Equation 2)}$$

where SWSsa and SWSla were respectively the shear wave speed in short axis and in long axis, and SWSm was the mean shear wave speed.

Cardiopulmonary exercise test (CPET)

Cardiopulmonary exercise tests were performed to assess maximal exercise capacity by means of a cycle ergometer (Ergoline®, Bitz, Germany). Patients were encouraged to continue exercising until dyspnea or fatigue forced them to stop. The workload was increased by 5 to 10 W, depending on the predicted maximum exercise capacity, and in such

a way that maximal effort was attained within ~8–12 min. Oxygen uptake and carbon dioxide output were measured breath-by-breath using an automated system (Sensor Medics system 290; Anaheim, California, United States of America). The exercise test was considered as maximal if the patient achieved a respiratory exchange ratio >1.1 and/or maximal heart rate >90% of the theoretical maximal heart rate and/or as oxygen uptake reaching a plateau. Measured cardiopulmonary exercise test parameters (peak oxygen uptake [VO_2/Kg] and peak oxygen pulse [O2P]) were expressed in percentage of predicted theoretical value (TV) published by Cooper et al[16]. The system calibration was performed before every test according to the manufacturer's specifications.

Statistical analysis

Data for continuous variables are presented as mean ± SD, if normally distributed, or as median and interquartile range [25%-75%] if non-normally distributed. Continuous variables were compared with unpaired Student t tests or the nonparametric Mann-Whitney U test where appropriate. Correlation of continuous variables was examined with simple linear regression analysis. Receiver operating characteristic (ROC) curves and area under the curve (AUC) were computed to assess the effectiveness of mean diastolic echocardiographic parameters (LAVI, E/A, e', E/e', e'/a', PV S/D ratio) to predict MS (> 4 kPa), and to assess the effectiveness of the MS to predict the type of HCM (HCM without restrictive profile or RCM-HCM). The intra- and interoperator reproducibilities were evaluated on four successive series of measurements using the standardized coefficient of variation (CV)[17]. Kruskal–Wallis tests were performed to find possible significant (p 0.05) differences among the acquisition series (same or different operator). All analyzes were conducted using *Medcalc* (MedCalc Software, Mariakerke, Belgium).

RESULTS

Population characteristics

A total of 60 subjects (30 HCM and 30 controls) were prospectively screened for inclusion into the study. Two patients from the control group had exclusion criteria (2 congenital heart disease: atrial septal defects). In HCM group, two patients had exclusion criteria (1 systemic arterial hypertension, 1 poor echogenicity). Finally, 56 subjects were included: HCM (n=28) and control group (n=28).

Patients' and controls' clinical characteristics and echocardiographic results are shown in table 1.

Myocardial stiffness results (figure 2)

Healthy controls group

The median MS in the control group was 1.7 (range: 1.3-1.8) kPa. There was no correlation between age and MS (p=0.63, R^2=0.009).

HCM group

The median MS of the HCM group was 7.9 (CI95%, 7.2-10.5) kPa. There was no correlation between age and MS (p=0.44, R^2=0.114).

Comparison between MS healthy and MS HCM group

There was a significant statistical difference between the MS healthy group and the global HCM group (p<0.01). Based on the ROC curve analysis, the optimal cut-off value of MS for detection of HCM was 4 kPa (Se=100%, Sp=100%). The AUC of MS to differentiate healthy patients from HCM patients was 1.000 (95% CI 0.936 to 1.000; p<0.01).

ROC curves and Correlation of MS with measures of diastolic function by echocardiography (table 2 and Figure 3)

Positive correlations were found between MS and conventional parameters in echocardiography (table 2). The strongest correlated parameters with MS were: LAVI (r=0.744, p<0.01), e' septal (r=-0.709, p<0.01), LV GS (r=0.633, p<0.01), e'/a' septal (r=-0.602, p<0.01).

Based on the ROC curve analysis, the optimal cut-off values and the AUC of the mean diastolic echocardiographic parameters (LAVI, E/A, e', E/e', e'/a', PV S/D ratio) for detection

of MS > 4 kPa are summarized in figure 3. E/e' ratio was the strongest parameter for detection of MS>4 kPa (E/e'>7.2: AUC=0.816, Se=91%, Sp=68%), E/A was the one with the highest specificity (E/A<1.58: AUC=0.666, Se=51.6%, Sp=81.8%), and e'/a' was the one with the highest sensitivity (e'/a'<2.2: AUC=0.759, Se=95.6%, Sp=47.8%).

Cardiopulmonary exercise test (figure 4)

21 HCM patients had CPET. Seven HCM patients did not have CPET: 5 patients had contra-indications (NYHA ≥III; history of ventricular arrhythmia), 2 patients were too young (age <6 years). Strong correlations were found between MS and peak VO_2/Kg % of theoretical value (r=-0.752; p<0.01) or peak O_2P % of theoretical value (r=-0.773; p<0.01).

Fractional anisotropy results (figure 5)

The mean fractional anisotropy of the control group (median=0.138 [0.086-0.222]) is higher than that of the HCM group (median=0.084 [0.058-0.130]), p=0.01.

Characteristics of patients with MS > CI95% (>10.5 kPa)

7/28 HCM patients had MS >10.5 kPa.

HCM Patients' baseline characteristics including clinical characteristics and echocardiographic results are shown in table 3. LAVI (p<0.01), E/A ratio (p=0.01), E-wave DT (p<0.01), IVRT (p<0.01), and PV S/D ratio (p<0.01) were statistically significantly different between HCM without MS <10.5 kPa (n=21) and HCM with MS >10.5 kPa (n=7).

Seven patients of the HCM group had conventional echocardiographic parameters suggesting a restrictive physiology. These were defined according to the recent update from the American Society of Echocardiography and the European Association of Cardiovascular Imaging[18] : enlargement of left atrium [LAVI >48 ml/m²] and impaired ventricular filling with restrictive physiology [E/A >2; E-wave DT <150 ms; e' medial <6 cm/s])[19-20-21]. Following this definition, 6/7 HCM patients (86%) who had MS > 10.5 kPa had a restrictive profile.

There was no statistical difference in fractional anisotropy between the HCM without MS <10.5 kPa (median=0.084 [0.056-0.134]) and those with MS >10.5 kPa (median=0.074 [0.066-0.098]), p=0.71.

Intra- and interoperator reproducibility

The intra- and interoperator reproducibilities of the MS measurement were studied in 10 HV and 10 HCM. There was no significant difference between the four successive series of measurements made by the same operator (Kruskal–Wallis test). The intraoperator standardized CV was 5.2% over the studied population and varied from 1% to 16%. There was no significant difference between the four successive series of measurements made by the two different operators (Kruskal–Wallis test) and the corresponding CV was 4.7%.

DISCUSSION

Our study is the first to propose a quantitative non-invasive measure of MS in children. Values of MS in healthy children were remarkably identical at different ages. Larger series are necessary to confirm this finding. We also show that MS is higher in children with HCM. In addition, MS can be proposed as a valuable tool to identify a restrictive profile in this group of children with HCM. Finally, the estimation of fractional anisotropy that provides information on myocardial structure is different between controls and HCM. This new non-invasive parameter could also be used in other conditions, in congenital heart diseases or for different cardiac structures such as the right ventricle.

It is well recognized that symptoms in HCM are mainly the consequence of diastolic dysfunction related to increased chamber stiffness[4]. Nevertheless, there is no reliable biological or imaging tool to assess myocardial stiffness in clinical practice. Recently, Kitzman et al. recalled that the evaluation of diastolic function is a key criterion for understanding the prognosis of patients with HCM[22]. Consequently, the recent European

guidelines for HCM indicate that the assessment of LV filling pressures is helpful in the evaluation of symptoms and disease staging. These guidelines also report that the classical echocardiographic parameters to evaluate diastolic dysfunction are often contradictory[1,23]. Some commonly used Doppler-derived parameters such as E/Vp or the E/e' ratios have been considered to give a good estimate of the LV filling pressures in HCM[24]. Still, Geske et al reported that the correlation of these parameters with invasive measure of left atrial pressure[25] was poor (r=0.28, p=0.07). In pediatric HCM, the use of Doppler-derived parameters to estimate diastolic function is challenging, particularly because of the poor interoperator agreement[8].

In this study, we show that SWI, which has already provided numerous evidences of clinical interests on other organs such as liver[26,27] or breast[28], can be used to estimate MS. Comparison of MS and invasive measure of passive relaxation by pressure-volume loops has demonstrated that the intrinsic stiffness of the LV impacted on the left atrial pressure[29]. Therefore, we think that measurement of MS can be used to evaluate left ventricle passive relaxation.

Indeed, we found a significant correlation between the MS, the peak E-wave, e', e'/a' and LAVI parameters. It is interesting to note that these parameters are related to the passive filling, mainly dependent on the LV intrinsic stiffness. In parallel, we found a weak correlation with A-duration, peak A-wave, and a ', related to atrial systole and atrioventricular coupling. In addition, we show here that very high MS is associated with the classical echocardiographic parameters of restrictive physiology in HCM. This potential role of MS in stratifying patients for the risk of subsequent cardiac events is important[30,31,32]. The role of MS, and particularly of high MS values, in predicting outcomes has to be evaluated in larger series of children with HCM.

Beyond the evaluation of cardiac function, myocardial stiffness allows assessing the fractional anisotropy. Cardiac magnetic resonance imaging (CMR) using diffusion tensor imaging was the first clinical imaging technique used to analyze the myocardium orientation fibers[33,34]. Lee et al introduced the concept of elastic tensor imaging (ETI)[15,35] to obtain the

same information but using ultrasound, based on the SWI. In 1991, Factor et al showed that pathological fibrosis and myocardial architecture disorganization in HCM may contribute to increased ventricular chamber stiffness and impaired relaxation in this disease[36]. Moreover, Ho et al demonstrated that myocardial fibrosis was probably one of the earliest manifestations of the HCM[37]. Here, the fractional anisotropy was found to be different in HV and in pediatric HCM. The role of this measure as a predictor of outcome has yet to be determined.

We found a correlation between MS and O2P in pediatric HCM. As O2P is reduced in any condition that reduces left ventricular stroke volume response during a sustained effort, this correlation may reflect poor adaptation of stroke volume during exercise in part related to impaired passive relaxation[38]. This is in line with the findings of Nihoyannopoulos et al who showed that the exercise capacity of HCM patients was directly correlated with exercise symptoms and diastolic function evaluated by echocardiography[39].

Limitations

The gold standard of MS assessment remains an invasive measurement with a conductance catheter. Ethically, it was not possible to perform this invasive measure on healthy volunteers or on children with HCM recruited exclusively for this study. However, previous studies on animal models have shown strong correlation between MS estimated by SWI and MS estimated through the end-diastolic strain-stress relationship[9,10].

The second limitation of our study is the local evaluation of MS by the SWI. Indeed, we compared global functional parameters of diastolic function of the LV with a segmental parameter (myocardial stiffness of the ASB segment).

The last limitation concerns the technique itself. Indeed, the estimation of the tissue stiffness by SWI is dependent on certain ultrasonic parameters and the tissue characteristics, in particular its thickness. Nguyen et al showed that for low thicknesses of the ventricular wall, the thickness of the wall must be taken into account in order to derive a quantitative MS[40].

With the ultrasonic parameters used in our study, myocardial thicknesses of less than 4 mm could not be evaluated with certainty. This is why we have included a population over 5 years of age.

Perspectives

The last ESC Guidelines on HF[41] specified that "no treatment has yet been shown, convincingly, to reduce morbidity or mortality in patients with HFpEF". This is due to the fact that the physiopathology of this disease is still misunderstood, but also because we lack quantitative and reproductive tools to evaluate the HFpEF, specifically for the HCM. We believe that the MS estimated by SWI may be an interesting predictor of outcome and may help to stratify patients for the evaluation of treatment strategies. In addition, it might be interesting to evaluate the effect of drugs currently used in HCM on MS values. If any positive effect is seen in association with changes in outcomes, MS could be used as a surrogate or as a therapeutic target in future trials.

CONCLUSION

In this study, we quantitatively assessed the diastolic MS in children using SWI in healthy volunteers and pediatric HCM. MS was high in children with HCM, and even higher in those with a restrictive physiology. In addition, the fractional anisotropy obtained by SWI could help giving additional information on the myocardial structure.

Our study remains descriptive but it offers the perspective to evaluate this new non-invasive marker as a potential predictor of outcome and as a potential therapeutic target.

COMPETING INTERESTS: Dr. Tanter is co-founder of SuperSonic Imagine.

FUNDING: This study was supported by European Research Council (ERC) under the European Union's Seventh Framework Program (FP/2007–2013)/ERC grant agreement 311025 and by the French Society of Cardiology.

TABLES

Table 1. Population characteristics (n=56)

	Healthy volunteer (n=28)	**HCM (n=28)**	**p**
Age (years)	11.5±3.4	12.3±4.2	0.61
Sex (M/F)	17/11	17/11	1.00
Weight (kg)	42.5±16.0	45.7±23.7	0.32
Height (cm)	145.5±21.0	149.4±25.7	0.57
BMI (kg/m²)	20.0±3.7	18.9±5.1	0.88
NYHA I	28	20	**<0.01**
NYHA II	0	5	
NYHA III-IV	0	2	
Echocardiography parameters			
LA surface (4 chambers view, cm²)	10.5±4.1	16.5±7.0	**<0.01**
LAVI (ml/m²)	21.8±9.9	39.6±26.8	**0.03**
LVEF (%)	63.6±4.7	71.8±9.4	**0.02**
LVEDD	41.8±7.1	38.3±6.8	0.11
LVESD	25.4±5.2	16.2±4.7	**0.04**
LV Mass / BSA (g/m²)	80.9±21.5	110±36.6	**0.02**
LV GS (%)	-19.2±1.4	-13.2±2.9	**<0.01**
ASB segment GS (%)	-17.9±1.4	-8.3±3.3	**<0.01**
ASB segment end diastolic thickness (mm)	8.1±1.7	16.5±5.2	**<0.01**
SD ASB segment end diastolic thickness	0.2±1.1	8.1±4.9	**<0.01**
Maximal end diastolic thickness (mm)	9.2±1.8	18.0±5.5	**<0.01**

SD maximal end diastolic thickness	0.7±0.9	10.1±4.6	**<0.01**
Peak E-wave (cm/s)	96.0±16.1	74.5±27.6	**<0.01**
Peak A-wave (cm/s)	54.0±12.1	47.2±14.0	0.80
E/A	1.9±0.6	1.6±0.5	**0.04**
E-wave DT (ms)	155±32	146±70	0.82
A duration (ms)	117±17	114±31	0.90
e' septal (cm/s)	14.9±2.5	6.2±3.1	**<0.01**
a' septal (cm/s)	6.6±1.9	5.9±1.8	0.44
E/e'	6.0±2.1	15.7±12.7	**<0.01**
e'/a' septal	2.5±0.8	1.1±0.6	**<0.01**
IVRT (ms)	62.4±10.1	92.2±18.2	**<0.01**
PV S/D ratio	0.79±0.23	1.23±0.68	**<0.01**

A: late diastolic peak (pulsed-wave doppler); **a':** late diastolic mitral annular velocity by doppler tissue imaging; **ASB:** antero septo basal; **BSA:** body surface area; **DT:** deceleration time; **E:** early diastolic peak (pulsed-wave doppler); **e':** early diastolic mitral annular velocity by Doppler tissue imaging; **GS:** global strain; **IVRT:** isovolumic relaxation time; **LA:** left atrium; **LAVI:** left atrium volume index; **LVEF:** left ventricle ejection fraction; **LVEDD:** left ventricle end-diastolic diameter; **LVESD:** left ventricle end-systolic diameter; **PV S/D ratio :** pulmonary veins velocities; **SD:** standard deviation; **Vp:** transmitral flow propagation velocity;

Table 2. Correlations between myocardial stiffness and echocardiographic parameters (all the population, n=56)

	r	p
Echocardiography		
LA surface (4 chambers view, cm²)	0.509	**<0.01**
LAVI (ml/m²)	0.744	**<0.01**
LVEF (%)	0.318	0.13
LVEDD	0.269	0.29
LVESD	0.308	0.21
LV Mass / BSA (g/m^2)	0.330	0.06
LV GS (%)	0.633	**<0.01**
ASB segment GS (%)	0.599	**<0.01**
ASB segment end diastolic thickness (mm)	0.520	**<0.01**
SD ASB segment end diastolic thickness	0.544	**<0.01**
Peak E-wave (cm/s)	-0.500	**<0.01**
Peak A-wave (cm/s)	-0.296	**0.04**
E/A	-0.218	0.13
E-wave DT (ms)	-0.192	0.18
A duration (ms)	-0.058	0.70
e' septal (cm/s)	-0.709	**<0.01**
a' septal (cm/s)	-0.092	0.54
E/e'	0.225	0.09
e'/a' septal	-0.602	**<0.01**
IVRT (ms)	-0.416	**0.01**
PV S/D ratio	0.373	**0.04**

ASB: antero septo basal

Table 3. Characteristics of HCM patients with or without MS > 10.5 kPa

	HCM with MS < 10.5 kPa (n=21)	**HCM with MS > 10.5 kPa (n=7)**	**p**
Age (years)	13,5±3,2	9,1±4,9	**<0.01**
Sex (M/F)	12/9	5/2	0.32
Weight (kg)	51.6±22.2	28.2±18.1	**<0.01**
Height (cm)	157.1±19.3	127.1±29.2	**<0.01**
BMI (kg/m²)	19.9±5.2	15.7±3.7	**0.02**
NYHA I	17	3	**0.03**
NYHA II	4	2	
NYHA III-IV	0	2	
Echocardiography parameters			
LA surface (4 cavities view, cm²)	15.2±5.5	20.1±10.4	0.14
LAVI (ml/m²)	28.2±12.1	68.8±31.5	**<0.01**
LVEF (%)	72.3±9.6	70.3±7.6	0.72
LVEDD	45±7.4	38.3±6.6	0.25
LVESD	27.8±5.6	23.4±6.1	0.43
LV Mass / BSA (g/m²)	116.8±30.1	92.6±19.5	**0.05**
LV GS (%)	-13.4±3.2	-12.4±1.5	0.59
ASB segment GS (%)	-9.1±3.0	-7.7±2.3	0.42
ASB segment end diastolic thickness (mm)	17.7±4.8	13.2±6.1	**0.04**
SD ASB segment end diastolic thickness	8.8±4.9	6.1±4.5	0.21
Maximal end diastolic thickness (mm)	19.1±4.6	14.4±5.9	**0.03**
SD maximal end	10.7±4.8	6.7±2.8	**0.01**

diastolic thickness			
Peak E-wave (cm/s)	78.5±26	56.7±29.7	0.11
Peak A-wave (cm/s)	50.4±9.6	24.3±13.7	**<0.01**
E/A	1.6±0.6	2.4±0.5	**0.01**
E-wave DT (ms)	167±66	75±21	**<0.01**
A duration (ms)	118±32	98±23	0.22
e' septal (cm/s)	6.6±3.3	3.8±1.5	0.17
a' septal (cm/s)	6.0±1.8	5.4±1.8	0.64
E/e'	15.7±13.4	16.1±6.1	0.88
e'/a' septal	1.2±0.7	0.9±0.2	0.69
IVRT (ms)	106.5±20.7	52.8±22.3	**<0.01**
PV S/D ratio	1.71±0.48	0.88±0.44	**<0.01**

ASB: antero septo basal

REFERENCES

1. Elliott PM, Anastasakis A, Borger MA, et al. 2014 ESC Guidelines on diagnosis and management of hypertrophic cardiomyopathy: The Task Force for the Diagnosis and Management of Hypertrophic Cardiomyopathy of the European Society of Cardiology (ESC). *Eur Heart J*. 2014;35(39):2733-2779..
2. Spirito P, Chiarella F, Carratino L, Berisso MZ, Bellotti P, Vecchio C. Clinical Course and Prognosis of Hypertrophic Cardiomyopathy in an Outpatient Population. *N Engl J Med*. 1989;320(12):749-755.
3. Zile MR, Baicu CF, S. Ikonomidis J, et al. Myocardial Stiffness in Patients With Heart Failure and a Preserved Ejection Fraction: Contributions of Collagen and Titin. *Circulation*. 2015;131(14):1247-1259..
4. Maron BJ. Hypertrophic Cardiomyopathy. *JAMA*. 2002;287(10):1-18.
5. Zile MR, Brutsaert DL. New Concepts in Diastolic Dysfunction and Diastolic Heart Failure: Part I. *Circulation*. 2002;105(11).
6. McMahon CJ, Nagueh SF, Pignatelli RH, et al. Characterization of Left Ventricular Diastolic Function by Tissue Doppler Imaging and Clinical Status in Children With Hypertrophic Cardiomyopathy. *Circulation*. 2004;109(14).
7. Nagueh SF, Appleton CP, Gillebert TC, et al. Recommendations for the Evaluation of Left Ventricular Diastolic Function by Echocardiography. *J Am Soc Echocardiogr*. 2009;22(2):107-133.
8. Dragulescu A, Mertens L, Friedberg MK. Interpretation of Left Ventricular Diastolic Dysfunction in Children With Cardiomyopathy by EchocardiographyClinical Perspective. *Circ Cardiovasc Imaging*. 2013;6(2).
9. Pernot M, Couade M, Mateo P, Crozatier B, Fischmeister R, Tanter M. Real-time assessment of myocardial contractility using shear wave imaging. *J Am Coll Cardiol*. 2011;58(1):65-72.
10. Pernot M, Lee W-N, Bel A, et al. Shear Wave Imaging of Passive Diastolic Myocardial Stiffness: Stunned Versus Infarcted Myocardium. *JACC Cardiovasc Imaging*. 2016;9(9):1023-1030.
11. Song P, Bi X, Mellema DC, et al. Quantitative Assessment of Left Ventricular Diastolic Stiffness Using Cardiac Shear Wave Elastography: A Pilot Study. *J Ultrasound Med*. 2016;35(7):1419-1427.
12. Ponikowski P, Voors AA, Anker SD, et al. 2016 ESC Guidelines for the diagnosis and treatment of acute and chronic heart failure. *Eur Heart J*. 2016.
13. Nagueh SF, Smiseth OA, Appleton CP, et al. *Recommendations for the Evaluation of*

Left Ventricular Diastolic Function by Echocardiography: An Update from the American Society of Echocardiography and the European Association of Cardiovascular Imaging. Vol 29.; 2016.

14. Bercoff J, Tanter M, Fink M. Supersonic shear imaging: a new technique for soft tissue elasticity mapping. *IEEE Trans Ultrason Ferroelectr Freq Control*. 2004;51(4):396-409.
15. Lee W-N, Larrat B, Pernot M, Tanter M. Ultrasound elastic tensor imaging: comparison with MR diffusion tensor imaging in the myocardium. *Phys Med Biol*. 2012;57(16):5075-5095.
16. Cooper DM, Weiler-Ravell D, Whipp BJ, Wasserman K. Growth-related Changes in Oxygen Uptake and Heart Rate during Progressive Exercise in Children. *Pediatr Res*. 1984;18(9):845-851.
17. Glüer C-C, Blake G, Lu Y, Blunt1 BA, Jergas1 M, Genant1 HK. Accurate assessment of precision errors: How to measure the reproducibility of bone densitometry techniques. *Osteoporos Int*. 1995;5(4):262-270.
18. Nagueh SF, Smiseth OA, Appleton CP, et al. Recommendations for the Evaluation of Left Ventricular Diastolic Function by Echocardiography: An Update from the American Society of Echocardiography and the European Association of Cardiovascular Imaging. *J Am Soc Echocardiogr*. 2016;29(4):277-314.
19. Maron BJ, Towbin JA, Thiene G, et al. Contemporary Definitions and Classification of the Cardiomyopathies. *Circulation*. 2006;113(14).
20. Webber SA, Lipshultz SE, Sleeper LA, et al. Outcomes of Restrictive Cardiomyopathy in Childhood and the Influence of Phenotype: A Report from the Pediatric Cardiomyopathy Registry. *Circulation*. 2012.
21. Lipshultz SE, Orav EJ, Wilkinson JD, et al. Risk stratification at diagnosis for children with hypertrophic cardiomyopathy: an analysis of data from the Pediatric Cardiomyopathy Registry. *Lancet (London, England)*. 2013;382(9908):1889-1897.
22. Kitzman DW, Little WC. Left Ventricle Diastolic Dysfunction and Prognosis. *Circulation*. 2012;125(6).
23. Sorajja P, Nishimura RA, Ommen SR, et al. Use of echocardiography in patients with hypertrophic cardiomyopathy: clinical implications of massive hypertrophy. *J Am Soc Echocardiogr*. 2006;19(6):788-795.
24. Nagueh SF, Lakkis NM, Middleton KJ, Spencer WH, Zoghbi WA, Quiñones MA. Doppler Estimation of Left Ventricular Filling Pressures in Patients With Hypertrophic Cardiomyopathy. *Circulation*. 1999;99(2).
25. Geske JB, Sorajja P, Nishimura RA, Ommen SR. Evaluation of Left Ventricular Filling Pressures by Doppler Echocardiography in Patients With Hypertrophic Cardiomyopathy. *Circulation*. 2007;116(23).

26. Wong VW-S, Vergniol J, Wong GL-H, et al. Diagnosis of fibrosis and cirrhosis using liver stiffness measurement in nonalcoholic fatty liver disease. *Hepatology*. 2010;51(2):454-462.
27. Villemain O, Sitefane F, Pernot M, et al. Toward Noninvasive Assessment of CVP Variations Using Real-Time and Quantitative Liver Stiffness Estimation. *JACC Cardiovasc Imaging*. April 2017. doi:10.1016/j.jcmg.2017.01.018.
28. Evans A, Whelehan P, Thomson K, et al. Invasive Breast Cancer: Relationship between Shear-wave Elastographic Findings and Histologic Prognostic Factors. *Radiology*. 2012;263(3):673-677.
29. Pak PH, Maughan WL, Baughman KL, Kass DA. Marked Discordance Between Dynamic and Passive Diastolic Pressure-Volume Relations in Idiopathic Hypertrophic Cardiomyopathy. *Circulation*. 1996;94(1).
30. Lipshultz SE, Orav EJ, Wilkinson JD, et al. Risk stratification at diagnosis for children with hypertrophic cardiomyopathy: an analysis of data from the Pediatric Cardiomyopathy Registry. *Lancet (London, England)*. 2013;382(9908):1889-1897.
31. Kubo T, Gimeno JR, Bahl A, et al. Prevalence, Clinical Significance, and Genetic Basis of Hypertrophic Cardiomyopathy With Restrictive Phenotype. *J Am Coll Cardiol*. 2007;49(25):2419-2426.
32. Kushwaha SS, Fallon JT, Fuster V. Restrictive Cardiomyopathy. *N Engl J Med*. 1997;336(4):267-276.
33. Scollan DF, Holmes A, Winslow R, Forder J. Histological validation of myocardial microstructure obtained from diffusion tensor magnetic resonance imaging. *Am J Physiol - Hear Circ Physiol*. 1998;275(6).
34. Le Bihan D, Mangin J-F, Poupon C, et al. Diffusion tensor imaging: Concepts and applications. *J Magn Reson Imaging*. 2001;13(4):534-546.
35. Lee W-N, Pernot M, Couade M, et al. Mapping myocardial fiber orientation using echocardiography-based shear wave imaging. *IEEE Trans Med Imaging*. 2012;31(3):554-562.
36. Factor SM, Butany J, Sole MJ, Wigle ED, Williams WC, Rojkind M. Pathologic fibrosis and matrix connective tissue in the subaortic myocardium of patients with hypertrophic cardiomyopathy. *J Am Coll Cardiol*. 1991;17(6):1343-1351.
37. Ho CY, López B, Coelho-Filho OR, et al. Myocardial Fibrosis as an Early Manifestation of Hypertrophic Cardiomyopathy. *N Engl J Med*. 2010;363(6):552-563.
38. Suga H, Sagawa K. Instantaneous pressure-volume relationships and their ratio in the excised, supported canine left ventricle. *Circ Res*. 1974;35(1):117-126.
39. Nihoyannopoulos P, Karatasakis G, Frenneaux M, McKenna WJ, Oakley CM. Diastolic function in hypertrophic cardiomyopathy: Relation to exercise capacity. *J Am Coll*

Cardiol. 1992;19(3):536-540.

40. Nguyen T-M, Couade M, Bercoff J, Tanter M. Assessment of viscous and elastic properties of sub-wavelength layered soft tissues using shear wave spectroscopy: theoretical framework and in vitro experimental validation. *IEEE Trans Ultrason Ferroelectr Freq Control*. 2011;58(11):2305-2315.

41. Ponikowski P, Voors AA, Anker SD, et al. 2016 ESC Guidelines for the diagnosis and treatment of acute and chronic heart failure. *Eur J Heart Fail*. 2016;18(8):891-975.

FIGURES

Figure 1: Myocardial Shear Wave Elastography

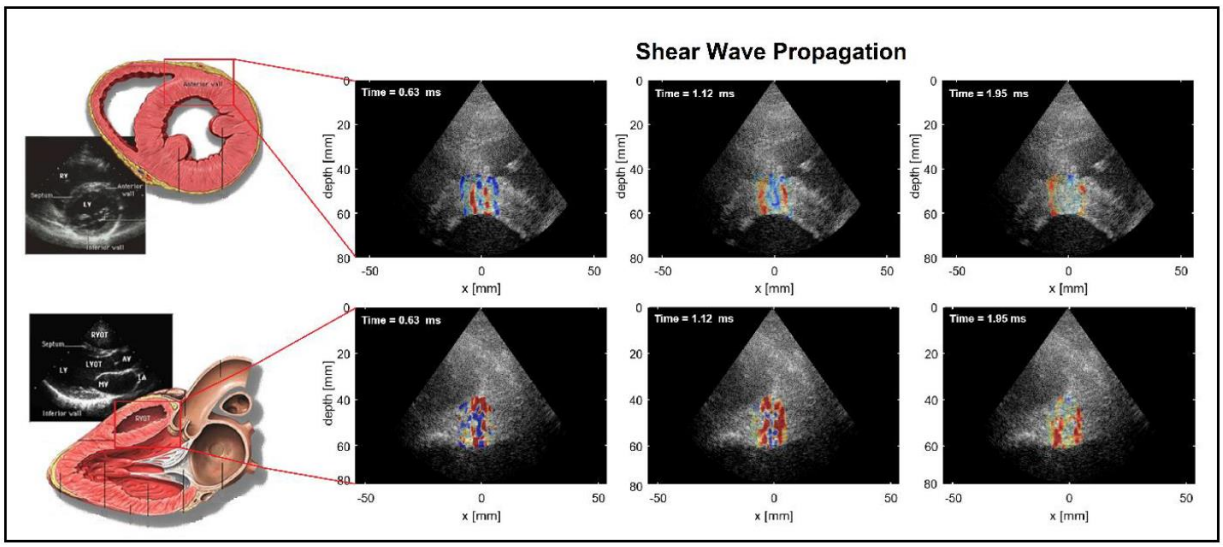

Legend figure 1: B-mode and Shear wave elastography imaging examples of a Hypertrophic Cardiomyopathy (HCM) patient. Shear wave propagation in short- and long-axis views (Tissue axial velocity images).

Figure 2: Elastography Results

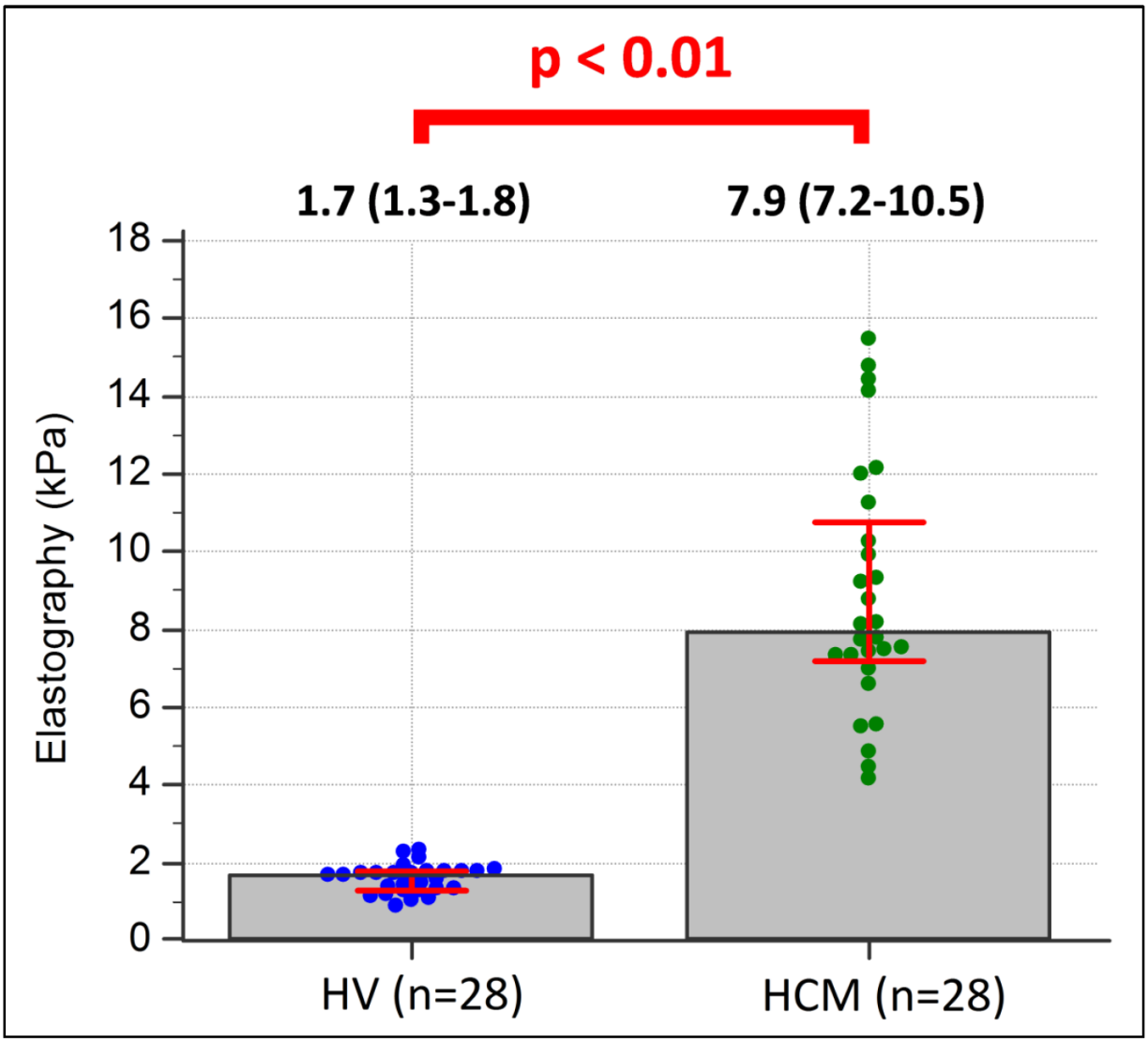

Legend figure 2: **HV,** healthy volunteers; **HCM,** hypertrophic cardiomyopathy

Figure 3: Receiver operating characteristic (ROC) curves of mean diastolic echocardiographic parameters (LAVI, E/A, e', E/e', e'/a', PV S/D ratio) to predict MS (>/< 4 kPa).

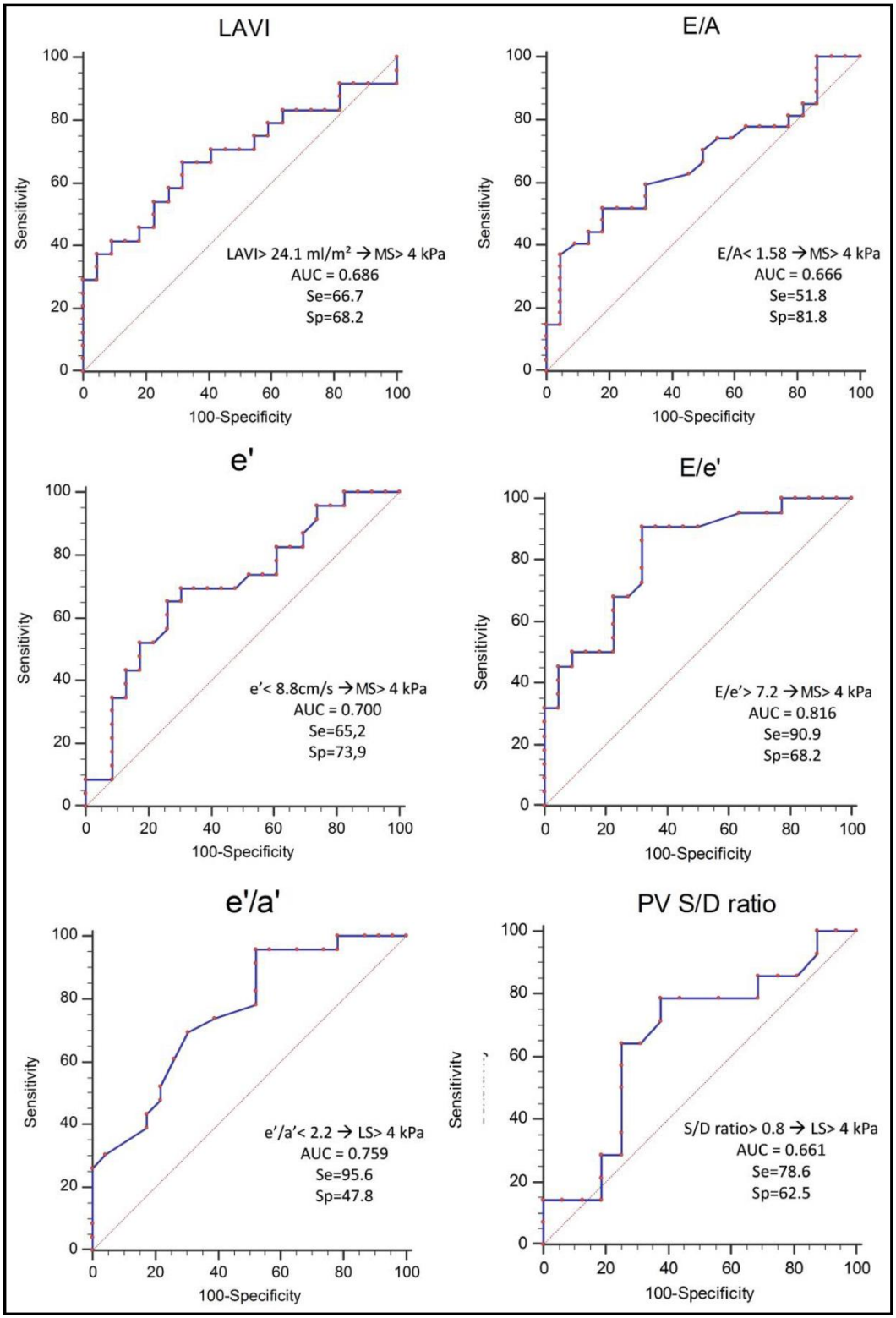

Figure 4: Correlations between MS and peak VO_2/Kg % TV or peak O_2P % TV (n=21).

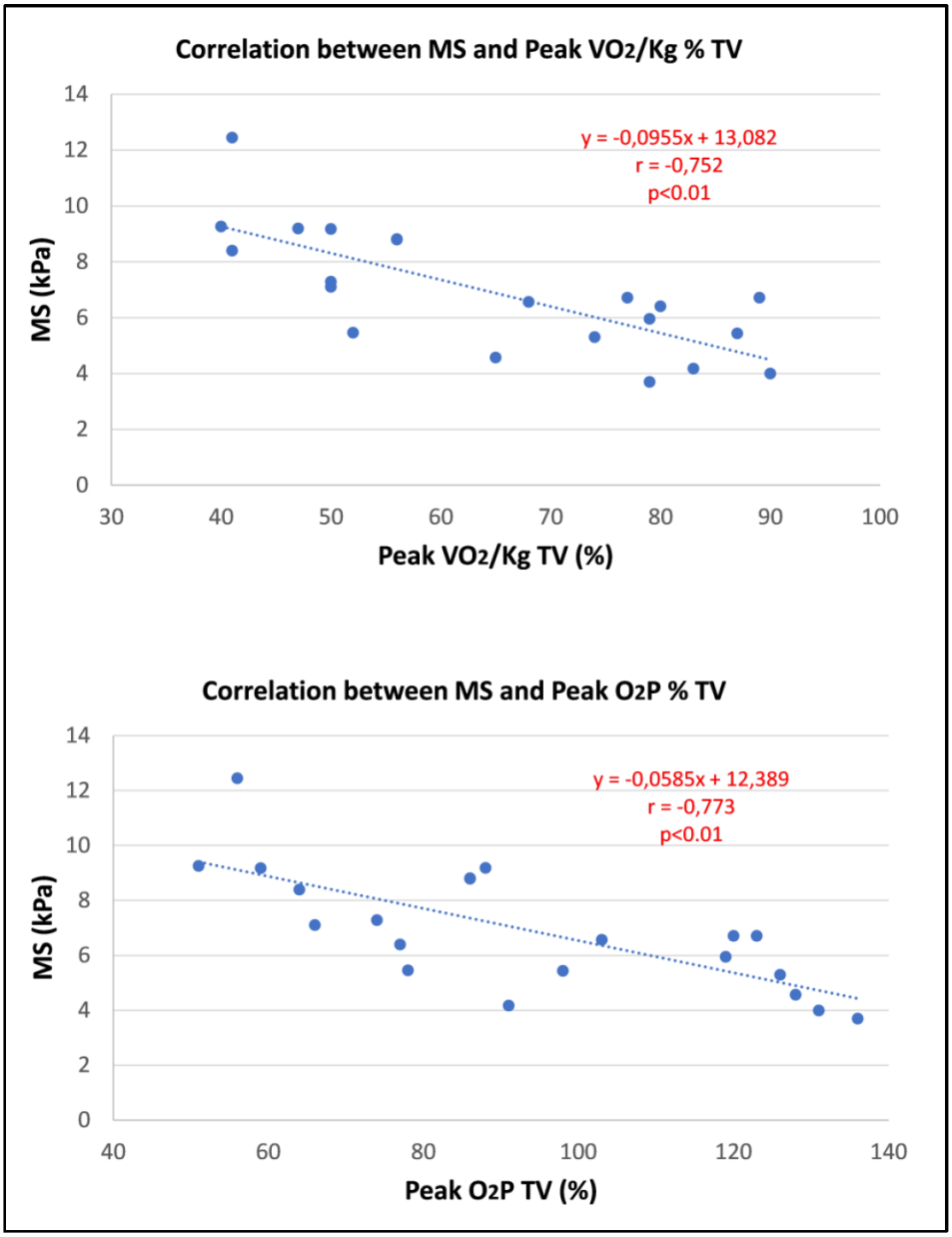

Legends: MS: myocardial stiffness; **O_2P:** oxygen pulse; **VO_2:** oxygen uptake; **TV:** theoretical value

Figure 5: Fractional Anisotropy Results

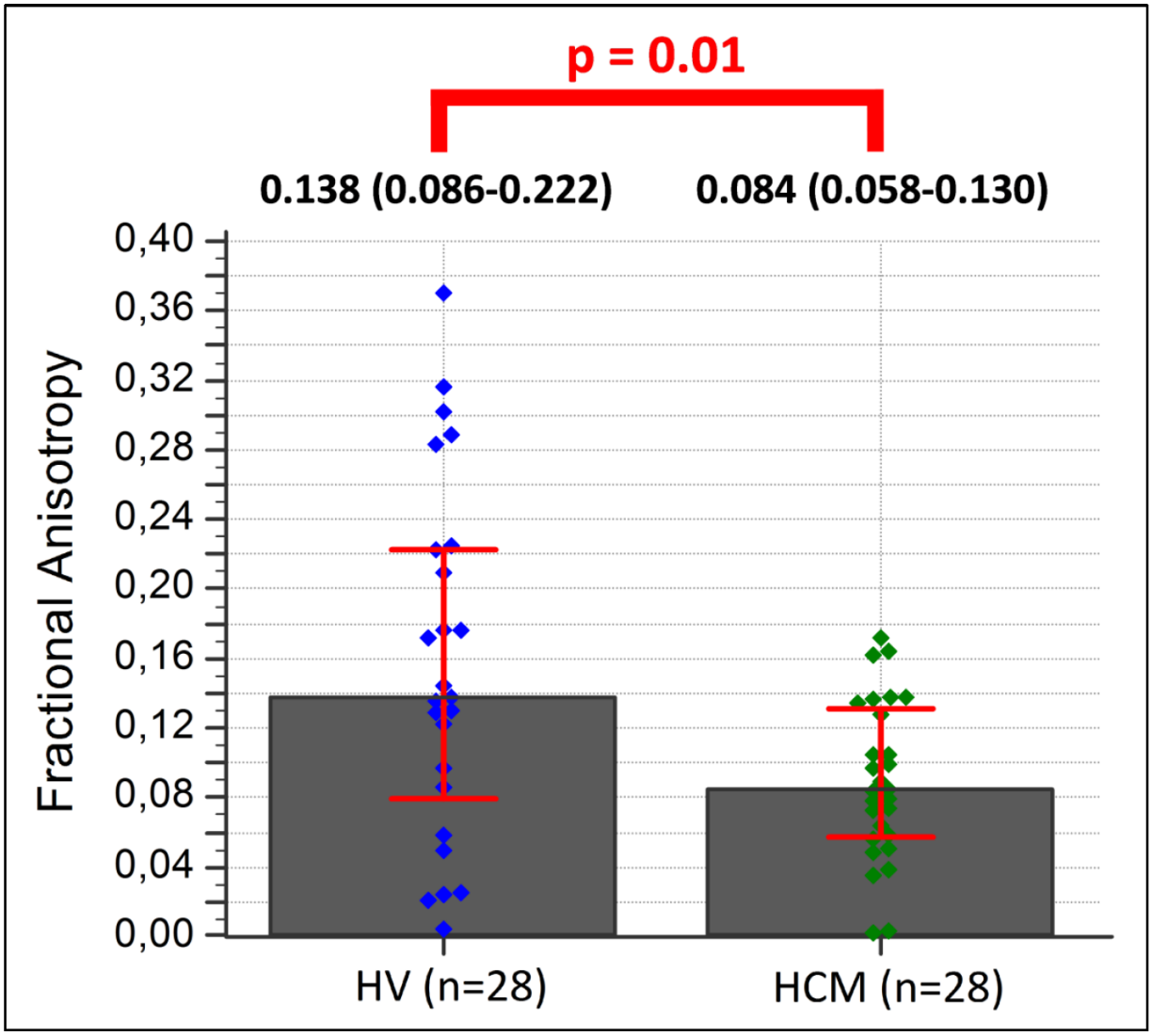

Legend figure 5: **HV,** healthy volunteers; **HCM,** hypertrophic cardiomyopathy;

2.4. Applications chez l'adulte

2.4.1. Présentation du travail

Cette étude présente la même méthodologie que l'étude pédiatrique, avec deux différences importantes : 1) le recrutement de volontaires sains a été plus nombreux afin d'analyser l'évolution physiologique de la rigidité myocardique avec l'âge, 2) l'ajout de l'IRM myocardique comme outil analytique. Cette étude s'est faite en parallèle de l'étude pédiatrique, avec comme objectifs de montrer la faisabilité et la reproductibilité dans une population adulte de volontaires sains et de patients ayant une CMH, et de montrer que cet outil diagnostique pourrait avoir une valeur ajoutée en pratique clinique.

Cette étude, comme l'étude pédiatrique, a été promue par la Société Française de Cardiologie, après avoir obtenu l'accord du Comité de Protection des Personnes de Paris VI (2015-A00187-42) et une déclaration à l'ANSM (DMDPT-DAIG/MM/2015-A00187-42). De plus, cette étude a été déclarée au registre international d'études cliniques (ClinicalTrials.gov; NCT02537041).

2.4.2. Manuscrit "*Myocardial stiffness and aging: non-invasive shear wave imaging evaluation in healthy and hypertrophic cardiomyopathy adults"* (In review)

Ce travail est soumis pour publication et est actuellement en review.

Myocardial stiffness and aging: non-invasive shear wave imaging evaluation in healthy and hypertrophic cardiomyopathy adults

Authors: O. Villemain, MD,*† M. Correia, PhD,* E. Mousseaux, MD, PhD,‡ J. Baranger,* S. Zarka, MD,† I. Podetti,* G. Soulat, MD,‡ T. Damy, MD, PhD,Δ A. Hagège, MD, PhD,† M. Tanter, PhD,* M. Pernot, PhD,*§, E. Messas, MD, PhD,†§

* Institut Langevin, ESPCI, CNRS, Inserm U979, PSL Research University,
† Hôpital Européen Georges Pompidou, Université Paris Descartes, Cardio-Vascular Departement, UMR 970, Paris, France
‡ Hôpital Européen Georges Pompidou, Université Paris Descartes, Département de Radiologie, INSERM U970, Paris, France
Δ Department of Cardiology, AP-HP, Henri Mondor Teaching Hospital, Créteil, France.
§ Co-last authors. Mathieu Pernot and Emmanuel Messas contributed to this work equally

Corresponding Author: Mathieu Pernot, PhD

Institut Langevin, ESPCI, CNRS, Inserm U979, PSL Research University, 17 rue Moreau, 75012 Paris, France

Telephone: (33) 1 80 96 30 86

E-mail: mathieu.pernot@espci.fr

COMPETING INTERESTS: Dr. Tanter is co-founder of SuperSonic Imagine.

Word count: XXXX

ABSTRACT

Background. Myocardial stiffness (MS) is an important prognostic and diagnostic parameter of diastolic function especially in hypertrophic cardiomyopathy. MS is also affected by physiological aging. However, the clinical assessment of MS and the diastolic function remains challenging and limits the study of the relationship between age and myocardial stiffness. A recently introduced ultrasound based technique called Shear wave imaging (SWI) has the potential to provide intrinsic MS noninvasively.

Objectives. The goal of our study was to investigate the potential of Myocardial SWI to quantify the diastolic myocardial stiffness (MS, kPa) noninvasively in healthy adult volunteers (HV) and its variation with age, and in hypertrophic cardiomyopathy populations with heart failure and preserved ejection function (HCM-HFpEF).

Methods. We prospectively included 80 adults: 60 HV (divided into three groups: 20-40 yo (n=20); 40-60 yo (n=20); 60-80 yo (n=20)) and 20 HCM-HFpEF. An echocardiography, a cardiac magnetic resonance imaging (CMR) and a biological exploration were achieved. The MS estimation was performed using an ultrafast ultrasound scanner with cardiac phased array. Fractional anisotropy (FA) of shear wave speed was also estimated.

Results. For 20-40, 40-60, and 60-80 yo group respectively, the mean MS was 2.59±0.58 kPa, 4.70±0.88 kPa, 6.08±1.06 kPa ($p<0.01$ between each group). MS strongly correlated with age ($r=0.88$). For the HCM-HFpEF group (mean MS=12.68±2.91 kPa), the MS was significantly higher than in the healthy volunteer ($p<10^{-4}$), with a cut-off identified at 8 kPa (AUC=0.993, Se=95%, Sp=100%). The FA was lower in HCM-HFpEF (mean=0.133±0.073) than in HV (0.238±0.068), $p<0.01$. Positive correlations were found between the MS and diastolic parameters in echocardiography (E/e', $r=0.783$; E/Vp, $r=0.616$; left atrial volume index, $r=0.623$) and with fibrosis markers in CMR (late gadolinium enhancement, $r=0.804$, myocardial T1 pre-contrast, $r=0.711$).

Conclusion. MS was found to increase significantly with age in healthy adults and was significantly higher in HCM-HFpEF patients. We hope that in the near future that this data will help to better identify HF-pEF patients and to characterize more precisely patients with primitive cardiomyopathy. (Non-Invasive Evaluation of Myocardial Stiffness by Elastography: NCT02537041)

Key Words: echocardiography • myocardial stiffness • myocardium • diastolic function

ABRREVIATIONS:

BNP: brain natriuretic protein

CMR: cardiac magnetic resonance imaging

DBP: diastolic blood pressure

DT: deceleration time

ECG: electrocardiogram

ECV: extracellular volume

FA: fractional anisotropy

HCM: hypertrophic cardiomyopathy

HF: heart failure

HFpEF: heart failure with preserved ejection function

HR: heat rate

HV: healthy volunteer

IVRT: isovolumic relaxation time

LGE: late gadolinium enhancement

MS: myocardial stiffness

SBP: systolic blood pressure

SWI: shear wave imaging

Vp: transmitral flow propagation velocity;

INTRODUCTION

Myocardial stiffness (MS) is known to play a key-role in diastolic left ventricular function[1]. Abnormalities in LV relaxation and MS are one of the key pathophysiological mechanisms[2] in heart failure patients with preserved ejection fraction (HFpEF). Hypertrophic cardiomyopathy is also associated to severe diastolic dysfunction mainly due to fibrosis and fiber disarray[3]. Moreover, MS is also affected by aging due to progressive physiological changes and cellular and extracellular matrix alterations. However, as the clinical assessment of MS and the diastolic function is still challenging[4], the study of the relationship between age and myocardial stiffness has remained limited to invasive explorations[5].

In a general view, the assessments of diastolic function can be divided into those that reflect the process of active/auxotonic relaxation (depending on filling load and afterload) and those that reflect passive stiffness (independent of load conditions)[6]. In clinical practice, biological parameters are correlated with ventricular filling pressures (brain natriuretic protein[7], BNP, for example), echocardiographic parameters are identified to assess the auxotonic relaxation and/or the filling pressure, and cardiac magnetic resonance imaging (CMR) offers tools to evaluate the myocardial fibrosis (late enhancement gadolinium[8], LGE) or the collagen volume fraction (pre-post contrast T1 times (T1 mapping[9]) or extracellular volume fraction[10], ECV). However, noninvasive estimation of MS remains challenging. To date, the cardiac catheterization is the only validated option to assess the MS clinically, through the compliance estimation thanks to the pressure-volume loops[11]. But the risks for the patients, the necessary equipment and the costs of these interventions make this exam unfeasible in daily clinical practice.

Shear wave imaging (SWI) is an ultrasound-based technique for quantitative, local, and noninvasive mapping of soft tissue's stiffness. The clinical impact of SWI has been demonstrated during the last decade in the field of breast lesions[12] and liver[13] imaging. Quantification of MS using SWI has also been investigated extensively on animal models in

previous studies [14]. SWI was compared to invasive gold standard parameters[15] derived from Pressure-Volume loops and was shown to quantify the end-diastolic MS accurately. More recently, the clinical feasibility and reproducibility of SWI was investigated on a small group of healthy volunteer[16]. The next step is to demonstrate the clinical interest and contribution of this technology for the assessment of diastolic myocardial stiffness and its impact on diastolic LV function. Unlike other imaging techniques, echocardiography is inexpensive, rapid and widely available and can be performed in real-time at the patient bedside allowing monitoring of the heart structure and function.

The goals of our study were 1) to quantify MS noninvasively in a healthy adult population in order to establish reference values of MS and its dependence with age, 2) to compare it to severely altered MS in hypertrophic cardiomyopathy (HCM) patients with HFpEF and 3) to investigate the correlation of MS with conventional echocardiography and CMR index of diastolic function.

METHODS

Study patients & design

This was a prospective study conducted at the Hôpital Européen Georges Pompidou, Paris, France. A population of healthy volunteers (HV) was contacted and recruited by the Clinical Investigation Center. Healthy volunteers specific inclusion criteria were: no history of heart failure symptoms, LVEF >50%, E/e' <13, as well as normal values of brain natriuretic protein (BNP, <35 pg/ml). Three age groups were composed within the recruited healthy volunteers: 20 to 39 years old (yo), 40 to 59 yo, 60 to 79 yo. Exclusion criteria included systolic blood pressure (SBP) ≥140mmHg or/and diastolic blood pressure (DBP) ≥90mmHg, any persistent cardiac arrhythmia, more than moderate valvular disease, any relevant coronary artery diseases, any contraindication to cardiac magnetic resonance imaging (CMR), and anechogenicity.

Patients with clinical, genetic and echocardiographic evidence for sarcomeric HCM with HFpEF (HCM-HFpEF group) were included. HCM-HFpEF patients were identified according to the consensus of the European Society of Cardiology[17,18], using specific inclusion criteria: wall thickness ≥ 15 mm in one or more LV myocardial segments; sarcomeric protein gene mutation identified; left ventricular ejection fraction (LVEF) >50%; New York Heart Association functional class ≥II; at least one hospitalization for acute heart failure; and E/e'≥13 or E/e' 8 to 13 combined with elevated BNP (>35 pg/ml).

All subjects included in the study underwent clinical explorations, biological explorations (hematocrit, CRP, BNP), an echocardiography, a CMR and a cardiac SWI. All explorations were performed on the same day. Three months later and if no clinical event was noted (symptoms of heart failure, hospitalization for cardiac cause, modification of weight or BP), a second echocardiography and cardiac SWI were realized to estimate the reproducibility on five patients per HV sub-group, randomly selected (n total = 15).

The study was approved by the local ethics committee, and all patients gave written informed consent (Non-Invasive Evaluation of Myocardial Stiffness by Elastography; this trial is registered with ClinicalTrials.gov, NCT02537041).

Imaging procedures

Echocardiography

Echocardiographic explorations were performed on a Vivid 9 system (General Electric Healthcare, Chalfont St. Giles, Great Britain). Mitral valve inflow pattern (E and A velocity), E-wave deceleration time (E-wave DT), isovolumic relaxation time (IVRT), transmitral flow propagation velocity (Vp), septal mitral valve annular velocities (e' and a'), as well as pulmonary veins S-wave on D-wave ratio (PV S/D ratio) were recorded in an apical 4-chamber view, to assess the markers of diastolic function according to American Society of Echocardiography guidelines[19]. Data were analyzed from stored images by experienced

operators (O.V. and A.H.) who were unaware of other test results. Measurements were made in 3 cardiac cycles; the average was used for statistical analysis.

CMR

The CMR protocol consisted of cine-sequences, T1-weighted spin-echo, and 2-dimensional inversion recovery gradient echo sequences for late enhancement assessment after gadobutrol administration (LGE). Post contrast T1 times (T1 mapping) was performed with a modified Look-Locker inversion recovery sequence with a 3(3)5 scheme before and 15 min after contrast application[20]. Mapping was performed over all available short-axis slices. Extracellular volume fraction (ECV) was calculated on the basis of the combination of pre- and post-contrast T1 mapping data according to the approach proposed by Rommel et al.[10] using the formula:

$$ECV = (\Delta R1_{myocardium}/\Delta R1_{blood}) \times (1 - hematocrit) \qquad \text{(Equation 1)}$$

, where R1 = 1/T1 time.

All acquisitions were consistent with the Society for Cardiovascular Magnetic Resonance published guidelines[21]. Data were interpreted by two experienced readers (E.M. and G.S.) who were unaware of the subjects' clinical information and the results of other diagnostic tests.

Myocardial stiffness measured by shear wave imaging (figure 1 and video online)

SWI is based on the remote generation of shear waves in soft tissue by acoustic radiation force combined with ultrasonic ultrafast imaging of the shear wave propagation (5000 images/s), using the same ultrasonic transducer[22]. A short push (300 µs) of focused ultrasound was transmitted by a diagnostic ultrasonographic probe (phased array, 2.75-MHz central frequency; SuperSonic Imagine, Aix-en-Provence, France) to induce micrometric tissue displacements in a small zone of the myocardium by acoustic radiation force. The push was generated in the left ventricular endocardium. In response to that transient mechanical

excitation, a shear wave was generated in the low–kHz-frequency range and propagated in the myocardium at velocities from 1 to 10 m/s, depending upon the intrinsic tissue stiffness. Tissue velocity maps were computed offline for each frame by using in-phase quadrature frame to frame cross-correlation. Myocardial wall motion was removed by subtraction of the average wall motion during the acquisition, bringing to light tissue motion induced solely by the shear wave. Shear wave velocity was computed at the depth of the mid-wall myocardium using spatiotemporal data from shear wave propagation. Finally, the shear modulus μ (i.e., stiffness) was derived using the equation:

$$\mu = \rho c^2 \text{ (kPa)} \qquad \text{(Equation 2)}$$

where c is the shear wave velocity, and ρ is the volume mass of the tissue.

The explored myocardial segment was the antero septo basal segment (ASB segment). It was evaluated in two orthogonal axes (short- and long-axis views, see figure 1). Short-axis measurements were used to derive the shear modulus, whereas long-axis and short-axis values were used to compute the fractional anisotropy. All acquisitions were performed at end-diastole and triggered by an electrocardiogram (ECG).

Data were interpreted by one experienced reader (O.V.) who was unaware of the subjects' clinical information and the results of other diagnostic tests.

Fractional Anistropy

Like any fiber-composed muscular tissue, the myocardium presents a significant anisotropy of its elastic properties. Consequently MS is expected to be higher when measured along the fibers, which are mainly oriented along the circumferential direction in the midwall layer. In order to evaluate the degree of anisotropy in the myocardium, the fractional anisotropy (FA) was computed. FA was defined using twoshear wave speed (SWS) measurements performed

in orthogonal propagation directions (long axis and short axis views) using the formula published by Lee et al[23] in 2011:

$$FA_{SWI} = \sqrt{2}\,\frac{\sqrt{(SWSsa-SWSm)^2+(SWSla-SWSm)^2}}{\sqrt{SWSsa^2+SWSla^2}} \qquad \text{(Equation 3)}$$

where SWSsa and SWSla were respectively the shear wave speed in short axis and in long axis, and SWSm was the mean shear wave speed.

Statistical analysis

Data for continuous variables are presented as mean ± SD, if normally distributed, or as median and interquartile range if non-normally distributed. Categorical variables are presented as frequencies and percentages. Comparisons between groups were made using chi-square tests for categorical variables. Continuous variables were compared with unpaired Student t tests or the nonparametric Mann-Whitney U test where appropriate. Univariate and stepwise multivariate linear regression analyses were performed to identify predictors of r (standardized coefficient of linear regression). Receiver operating characteristic (ROC) curves and area under the curve (AUC) were computed to assess the effectiveness of MS to predict healthy or pathologic subjects. Reproducibility of MS estimation (three months after the first estimation) was tested by the Bland-Altman limits of agreement. The reproducibility coefficient was calculated as 1.96 x the SD of the differences, as proposed by Bland and Altman[24]. All the analyses were conducted using *Medcalc* (MedCalc Software, Mariakerke, Belgium).

RESULTS

Population characteristics

A total of 93 subjects (69 HV and 24 HCM-HFpEF) were prospectively screened for inclusion into the study (see figure 2, Flowchart). Eight patients of the HV group were excluded based on the exclusion criteria (1 congenital heart disease and 1 valvulopathy on echocardiography, 1 doubt on infract scar on CMR, 6 anechoic). Two patients of the HCM-HFpEF group were excluded based on the exclusion criteria (2 infarct scars seen on CMR, 2 anechoic). Finally, 80 subject were included: HCM-HFpEF group (n=20), HV 20-39 yo group (n=20), HV 40-59 yo group (n=20), HV 60-79 yo group (n=20). See the flowchart in figure 2.

The molecular genetic causes of HCM-HFpEF group were: 8 mutations of MYH7, 6 mutations of MYBPC3, 2 mutations of TNNT2, 1 mutation of TPM1, 1 mutation of TNNI3, 1 mutation of MYL3, 1 mutation of MYL2.

Subjects' baseline characteristics including clinical characteristics, laboratory data, echocardiographic results, and CMR results are shown in table 1.

There is no statistical difference between the HV group and the HCM-HFpEF group in terms of age (p=0.22), BMI (p=0.74), and BP (systolic, p=0.41; diastolic, p=0.47).

Concerning the HCM-HFpEF group, 6 patients (30%) had a NYHA functional class ≥III (4=III, 2=IV). 20 patients (100%) had a BNP >35 pg/ml. Regarding echocardiographic results, LV mass index was significantly higher than the HV group (125±34 versus 70.6±20, p<0.01), the ASB segment was significantly thicker than the HV group (20.8±5.1 versus 5.9±1.4, p<0.01), with a segment strain lower than the HV group (-6.4±3.6 versus -16.9±2.2, p<0.01). All the main diastolic function parameters were significantly different (p<0.01) than those of the HV group (E/A; e'; E/e'; E-wave DT; IVRT; Vp; E/Vp, PV S/D ratio). Regarding CMR results, 16/20 (80%) had a LGE on the ASB segment (p<0.01). There was a difference between healthy volunteer and HCM-HFpEF groups concerning myocardial T1 post-contrast (p=0.02) and ECV (p<0.01).

Myocardial stiffness results

HV group (figure 3)

The mean MS concerning the HV group was 4.47±1.68 kPa. No HV people had a MS estimation over 8 kPa. The mean MS was 2.59±0.58 kPa for the 20-39 yo HV group, 4.70±0.88 kPa for the 40-59 yo HV group, and 6.08±1.06 kPa for the 60-79 yo HV group. There was a statistical significant difference between all age group ($p<0.01$).

Myocardial stiffness dependence on age

A strong increase in MS with age was found (Figure 3). The correlation between age (x) and MS (y) values was robust ($y=0.087x+0.1248$, $r^2=0.77$, $p<0.01$). A multivariate linear regression analysis (including sex, age, BMI, HR, SBP, DBP) showed age was the only clinical parameter correlated with the MS (age, $p<0.01$; sex, $p=0.77$; BMI, $p=0.98$; HR, $p=0.88$; SBP, $p=0.33$; DBP, $p=0.63$). The correlation of echocardiographic parameters and age was lower: E/A, $r^2=0.30$; E/e', $r^2=0.23$; E/Vp $r^2=0.01$ (see online figure A).

HCM-HFpEF group

The mean MS of the HCM-HFpEF group was 12.68±2.91 kPa. Only two patients had a MS estimation under 8 kPa (6.46 and 7.97 kPa). The correlation between age and MS values for this pathological group was low ($r^2=0.14$, $r=0.37$, $p<0.01$). We found no difference between MYH7 and MYBPC3 mutation subgroups ($p=0.34$).

Comparison between MS healthy and MS HCM-HFpEF groups (figure 4)

There was a significant statistical difference between the MS healthy group and the MS HCM-HFpEF group ($p<0.01$). Based on the ROC curve analysis, the optimal cut-off value of MS for detection of HCM-HFpEF was 8 kPa (AUC=0.993, Se=95%, Sp=100%).

Correlation of MS with measures of diastolic function (figure 5) and myocardial fibrosis

Positive correlations were found between the MS and parameters in echocardiography (Figure 5; E/e', $r=0.783$, $p<0.01$; E/Vp, $r=0.616$, $p<0.01$; left atrial volume index, $r=0.623$, $p<0.01$) and CMR (late gadolinium enhancement, $r=0.804$, $p<0.01$; myocardial T1 pre-contrast, $r=0.711$,

p<0.01; myocardial T1 post-contrast, r=0.595, p=0.01; extracellular volume fraction, r=0.447, p=0.03).

Reproducibility

On fifteen HV patients reevaluated three months later, the mean MS was 4.26±1.36 kPa (no statistical difference with the initial assessment, p=0.67). Moreover, Bland-Altman analysis demonstrated good agreement between measurements: MS +0.08 kPa (upper limit of agreement [ULA]: +0.89 kPa; lower limit of agreement [LLA]: -0.73 kPA), see online figure B.

Fractional anisotropy results (figure 6)

The mean fractional anisotropy of the HV group (0.238±0.068) was higher than that of the HCM-HFpEF group (0.133±0.073, p<0.01). 18/20 (90%) patients in HCM-HFpEF group had a fractional anisotropy under 0.155 while 56/60 (93%) HV had a fractional anisotropy over this cut-off (AUC=0.891, Sensibility=90%, Specificity=91.2%).

DISCUSSION

In this study, MS was assessed quantitatively using SWI in healthy volunteers and HCM patients with HFpEF. To our knowledge, this is the first study to assess MS quantitatively and noninvasively in both HV and pathological cases (HCM-HFpEF). The main results of the study were: 1) SWI allowed us to establish the reference values of MS in a healthy volunteer population; 2) MS was found to increase strongly with age in the normal heart; 3) there was a large difference in myocardial stiffness between healthy volunteers and HCM-HFpEF (cut-off =8 kPa). Jan D'hooge and Frank Rademakers recently raised the question of whether SWI by ultrafast imaging could be the "remedy for the Achilles' Heel of echocardiography"[25]. In this editorial comment, they reminded the fact that echocardiography, although being the first line exploration in cardiology, does not provide any quantitative information on (local) ventricular

compliance or stiffness, and issued the assumption that SWI could be the solution to this situation.

The first major result of this study is the observation of the myocardial stiffness aging. Thanks to the NORRE Study[26], Caballero et al also found a gradual change with age of the main echocardiographic parameters to assess diastolic function. In this study, which analyzed 449 healthy volunteer echocardiographs, it is interesting to note that the E/e' ratio goes from an average of 6.9 ± 1.6 in 20-40 yo subjects to an average of 9.7 ± 2.8 in 60-75 yo subjects, a change of approximately 50% with a fairly linear evolution. This myocardial aging was also evaluated by CMR on human population[27] or by invasive estimation on animal study[28]. In 1991, Weger et al have well demonstrated that the age-induced physiological myocardial fibrosis impacts on the cardiac function[29], including the ability of the ventricle to relax during the diastolic filling (auxotonic relaxation). Regarding healthy volunteers who participated in our study, we also found a linear evolution of myocardial stiffness, allowing to establish the first reference ranges of MS based on age.

The second interest of our study was to demonstrate a myocardial stiffness difference between HV and HCM-HFpEF noninvasively. Zile et al have showed on myocardial histologic explorations of HFpEF patients[30] that an increase in passive myocardial stiffness is due to an architectural modification (increase of collagen and titin). Moreover, in a systematic review on HCM[3] published in 2002, Barry J. Maron noted that the "LV myocardial architecture is disorganized […] with multiples intercellular connections often arranged on chaotic alignment and with expanded interstitial (matrix) collagen", which is supported by previous work which tried to link myocardial histological explorations and myocardial stiffness[31]. Our study shows that the abnormal myocardial stiffness of this characteristic pathological group (HCM-HFpEF) can be estimated noninvasively. In addition, the analysis of fractional anisotropy revealed a tissue architecture difference between the two groups of our study, with a decrease of the physiological anisotropy in the HCM-HFpEF group. SWI could not only provide the myocardial stiffness noninvasively but also information on the myocardial architecture.

Beyond the analysis of viscoelastic properties and of tissue structure, the comparison of MS with the recommended ultrasound parameters used to assess the diastolic function seems to show that this quantitative parameter could help to distinguish patients with diastolic dysfunction from others. Obviously, the diastolic function analysis remains complex and it would be unrealistic to think that one quantitative parameter could define the left ventricular diastolic function. For example, LAVI >34ml/m² is one of the key structural alteration allowing the definition the diagnostic of HFpEF[18], but Caballero et al[26] have also clarified that 15.1% of heathy people have a LAVI >34ml/m² while only 0.5% have a E/e' ratio >15. Nevertheless, the MS assessment of patients with HFpEF has clearly helped tounderstand this disease better[32]. Being able to perform it noninvasively would refine our diagnostic capabilities and probably would help us to understand disease "at the bedside" better, with a noninvasive approach.

Beyond the diagnostic contribution that the evaluation of MS by SWI could represent, the prospects of therapeutic follow-up could be interesting. The current finding is that there is no specific medical treatment of diastolic dysfunction in HCM. This is probably due to the fact that there is as yet no medical treatment with a high expected efficacy in HFpEF, as recalled in the recent European guidelines: "No treatment has yet been shown, convincingly, to reduce morbidity or mortality in patients with HFpEF"[18]. Noninvasive MS assessment could be a major tool for the development of novel treatments of HCM and/or HFpEF.

Finally, we have observed a good reproducibility of the MS assessment. Despite the small size of this analysis group (n=15), which limits its interpretation, these results indicate that this technique could be used to evaluate a patient through a longitudinal follow up. We did not reevaluate the reproducibility of this technique on HCM-HFpEF groups for two reasons: 1) it is still difficult to estimate the impact of the disease evolution on the MS results, 2) the treatment of these patients were modified after the initial evaluation and could modify their diastolic function (and maybe their myocardial structure).

Limitations

The gold standard of MS assessment remains an invasive measurement with a conductance catheter. From a regulatory point-of-view, this exploration could not be achieved on healthy volunteers recruited exclusively for this study, notably because of the risks inherent to this invasive exploration. However, previous work on animal model had shown a strong correlation between MS estimated by SWI and MS estimated through the end-diastolic strain-stress relationship[15,14]. Concerning the HCM-HFpEF group, no catheterization was provided in the management of these patients during the time of the study. The second limitation of our study is the local evaluation of MS by the SWI. Indeed, we compared global functional parameter (E/e', E/Vp or LAVI) with a segmental parameter (myocardial stiffness of the ASB segment). Nonetheless, the same segment was analyzed for all people included in the study.

CONCLUSION

In this study, we quantitatively assessed the end-diastolic myocardial stiffness in humans using SWI in healthy volunteers and sarcomeric hypertrophic cardiomyopathies with HFpEF patients. The myocardial stiffness was found to increase with age and a cut-off of 8 kPa allowed differentiating clearly these two groups. The fractional anisotropy obtained by SWI reflected the underlying tissue structure modifications.

Thanks to this ultrasound technology, the noninvasive assessment of myocardial stiffness enables a new diagnostic option in cardiology. In the future, further studies will aim to evaluate other heart diseases, as isolated HFpEF, HFrEF or other cardiomyopathies in order to specify the impact of this parameter in clinical practice.

ACKNOWLEDGEMENTS: We thank the team of the Clinical Investigation Center (Centre d'Investigation Clinique, INSERM) and the Clinical Research Unity (Unité de Recherche Clinique, URC-HEGP) for their contribution in this work.

COMPETING INTERESTS: Dr. Tanter is co-founder of SuperSonic Imagine.

FUNDING: This study was supported by European Research Council (ERC) under the European Union's Seventh Framework Programme (FP/2007–2013)/ERC grant agreement 311025 and by the French Society of Cardiology.

REFERENCES

1. Kass DA, Bronzwaer JGF, Paulus WJ. What Mechanisms Underlie Diastolic Dysfunction in Heart Failure? *Circ Res*. 2004;94(12).
2. Westermann D, Kasner M, Steendijk P, et al. Role of Left Ventricular Stiffness in Heart Failure With Normal Ejection Fraction. *Circulation*. 2008;117(16).
3. Maron BJ. Hypertrophic Cardiomyopathy. *JAMA*. 2002;287(10):1-18. doi:10.1001/jama.287.10.1308.
4. Flachskampf FA, Biering-Sørensen T, Solomon SD, Duvernoy O, Bjerner T, Smiseth OA. Cardiac Imaging to Evaluate Left Ventricular Diastolic Function. *JACC Cardiovasc Imaging*. 2015;8(9):1071-1093. doi:10.1016/j.jcmg.2015.07.004.
5. Fujimoto N, Hastings JL, Bhella PS, et al. Effect of ageing on left ventricular compliance and distensibility in healthy sedentary humans. *J Physiol*. 2012;590(8):1871-1880. doi:10.1113/jphysiol.2011.218271.
6. Zile MR, Brutsaert DL. New Concepts in Diastolic Dysfunction and Diastolic Heart Failure: Part I. *Circulation*. 2002;105(11).
7. Lubien E, DeMaria A, Krishnaswamy P, et al. Utility of B-Natriuretic Peptide in Detecting Diastolic Dysfunction. *Circulation*. 2002;105(5).
8. Moon JC., Reed E, Sheppard MN, et al. The histologic basis of late gadolinium enhancement cardiovascular magnetic resonance in hypertrophic cardiomyopathy. *J Am Coll Cardiol*. 2004;43(12):2260-2264. doi:10.1016/j.jacc.2004.03.035.
9. Iles L, Pfluger H, Phrommintikul A, et al. Evaluation of Diffuse Myocardial Fibrosis in Heart Failure With Cardiac Magnetic Resonance Contrast-Enhanced T1 Mapping. *J Am Coll Cardiol*. 2008;52(19):1574-1580. doi:10.1016/j.jacc.2008.06.049.
10. Rommel K-P, von Roeder M, Latuscynski K, et al. Extracellular Volume Fraction for Characterization of Patients With Heart Failure and Preserved Ejection Fraction. *J Am Coll Cardiol*. 2016;67(15):1815-1825. doi:10.1016/j.jacc.2016.02.018.
11. Suga H, Sagawa K. Instantaneous Pressure-Volume Relationships and Their Ratio in the Excised, Supported Canine Left Ventricle. *Circ Res*. 1974;35(1).
12. Evans A, Whelehan P, Thomson K, et al. Invasive Breast Cancer: Relationship between Shear-wave Elastographic Findings and Histologic Prognostic Factors. *Radiology*. 2012;263(3):673-677. doi:10.1148/radiol.12111317.
13. Wong VW-S, Vergniol J, Wong GL-H, et al. Diagnosis of fibrosis and cirrhosis using liver stiffness measurement in nonalcoholic fatty liver disease. *Hepatology*. 2010;51(2):454-462. doi:10.1002/hep.23312.
14. Pernot M, Couade M, Mateo P, Crozatier B, Fischmeister R, Tanter M. Real-time

assessment of myocardial contractility using shear wave imaging. *J Am Coll Cardiol*. 2011;58(1):65-72. doi:10.1016/j.jacc.2011.02.042.

15. Pernot M, Lee W-N, Bel A, et al. Shear Wave Imaging of Passive Diastolic Myocardial Stiffness: Stunned Versus Infarcted Myocardium. *JACC Cardiovasc Imaging*. 2016;9(9):1023-1030. doi:10.1016/j.jcmg.2016.01.022.
16. Song P, Bi X, Mellema DC, et al. Quantitative Assessment of Left Ventricular Diastolic Stiffness Using Cardiac Shear Wave Elastography: A Pilot Study. *J Ultrasound Med*. 2016;35(7):1419-1427. doi:10.7863/ultra.15.08053.
17. Elliott PM, Anastasakis A, Borger MA, et al. 2014 ESC Guidelines on diagnosis and management of hypertrophic cardiomyopathy. *Eur Heart J*. 2014.
18. Ponikowski P, Voors AA, Anker SD, et al. 2016 ESC Guidelines for the diagnosis and treatment of acute and chronic heart failure. *Eur Heart J*. 2016.
19. Nagueh SF, Smiseth OA, Appleton CP, et al. *Recommendations for the Evaluation of Left Ventricular Diastolic Function by Echocardiography: An Update from the American Society of Echocardiography and the European Association of Cardiovascular Imaging*. Vol 29.; 2016. doi:10.1016/j.echo.2016.01.011.
20. Messroghli DR, Plein S, Higgins DM, et al. Human Myocardium: Single-Breath-hold MR T1 Mapping with High Spatial Resolution—Reproducibility Study. *Radiology*. 2006;238(3):1004-1012. doi:10.1148/radiol.2382041903.
21. Kramer CM, Barkhausen J, Flamm SD, et al. Standardized cardiovascular magnetic resonance (CMR) protocols 2013 update. *J Cardiovasc Magn Reson*. 2013;15(1):91. doi:10.1186/1532-429X-15-91.
22. Bercoff J, Tanter M, Fink M. Supersonic shear imaging: a new technique for soft tissue elasticity mapping. *IEEE Trans Ultrason Ferroelectr Freq Control*. 2004;51(4):396-409. doi:10.1109/TUFFC.2004.1295425.
23. Lee W-N, Larrat B, Pernot M, Tanter M. Ultrasound elastic tensor imaging: comparison with MR diffusion tensor imaging in the myocardium. *Phys Med Biol*. 2012;57(16):5075-5095. doi:10.1088/0031-9155/57/16/5075.
24. Martin Bland J, Altman D. Statistical methods for assessing agreement between two methods of clinical measurement. *Lancet*. 1986;327(8476):307-310. doi:10.1016/S0140-6736(86)90837-8.
25. D'hooge J, Rademakers F. A Remedy for the Achilles' Heel of Echocardiography? *JACC Cardiovasc Imaging*. 2016;9(9):1031-1033. doi:10.1016/j.jcmg.2015.12.019.
26. Caballero L, Kou S, Dulgheru R, et al. Echocardiographic reference ranges for normal cardiac Doppler data: results from the NORRE Study. *Eur Hear J - Cardiovasc Imaging*. 2015.
27. Hollingsworth KG, Blamire AM, Keavney BD, MacGowan GA. Left ventricular torsion,

energetics, and diastolic function in normal human aging. *Am J Physiol - Hear Circ Physiol*. 2012;302(4).

28. Pacher P, Mabley JG, Liaudet L, et al. Left ventricular pressure-volume relationship in a rat model of advanced aging-associated heart failure. *Am J Physiol - Hear Circ Physiol*. 2004;287(5).
29. Weber KT, Brilla CG, Janicki JS. Myocardial fibrosis: functional significance and regulatory factors. *Cardiovasc Res*. 1993;27(3).
30. Zile MR, Baicu CF, Ikonomidis J, et al. Myocardial Stiffness in Patients with Heart Failure and a Preserved Ejection Fraction: Contributions of Collagen and Titin. *Circulation*. 2015.
31. Factor SM, Butany J, Sole MJ, Wigle ED, Williams WC, Rojkind M. Pathologic fibrosis and matrix connective tissue in the subaortic myocardium of patients with hypertrophic cardiomyopathy. *J Am Coll Cardiol*. 1991;17(6):1343-1351. doi:10.1016/S0735-1097(10)80145-7.
32. Zile MR, Baicu CF, Gaasch WH. Diastolic Heart Failure — Abnormalities in Active Relaxation and Passive Stiffness of the Left Ventricle. *N Engl J Med*. 2004;350(19):1953-1959. doi:10.1056/NEJMoa032566.

FIGURES

Figure 1: Myocardial Shear Wave Imaging

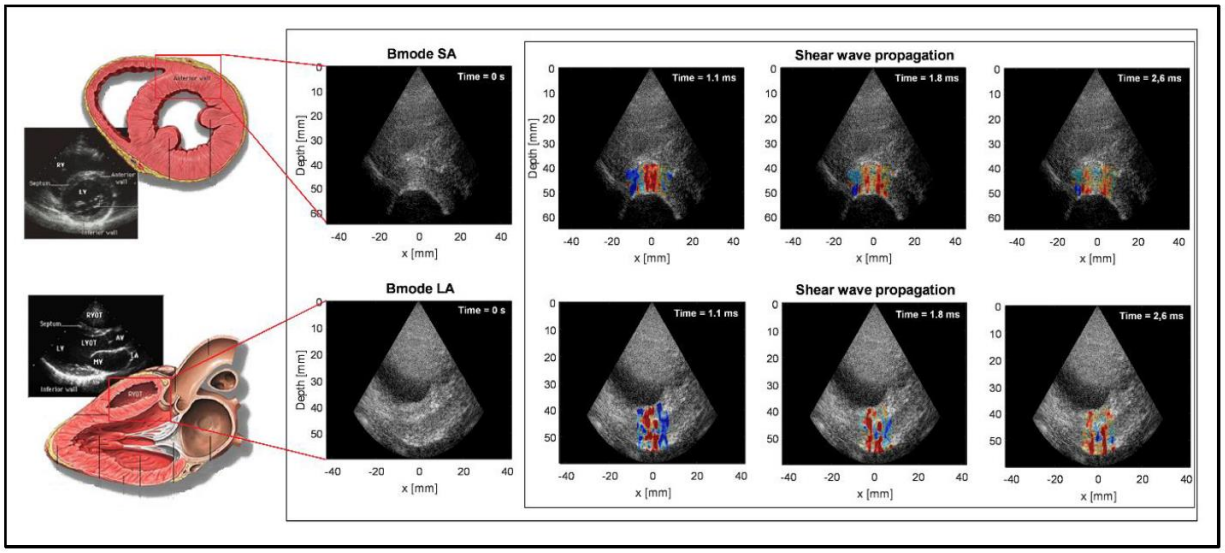

Legend figure 1: B-mode and Shear wave elastography imaging examples of a Healthy Volunteer (HV). Shear wave propagation in short- and long-axis views of a HV (Tissue axial velocity images).

Figure 2: Study Flowchart

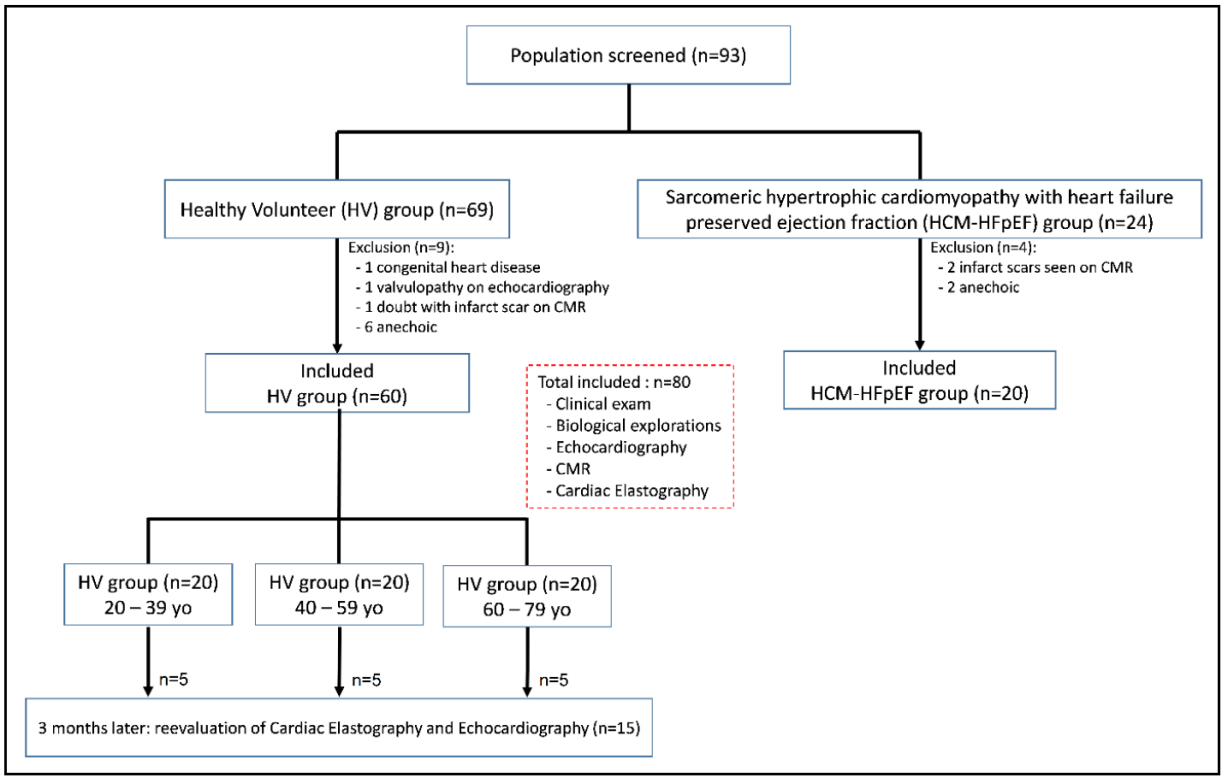

Figure 3: Myocardial Stiffness for Healthy Volunteer

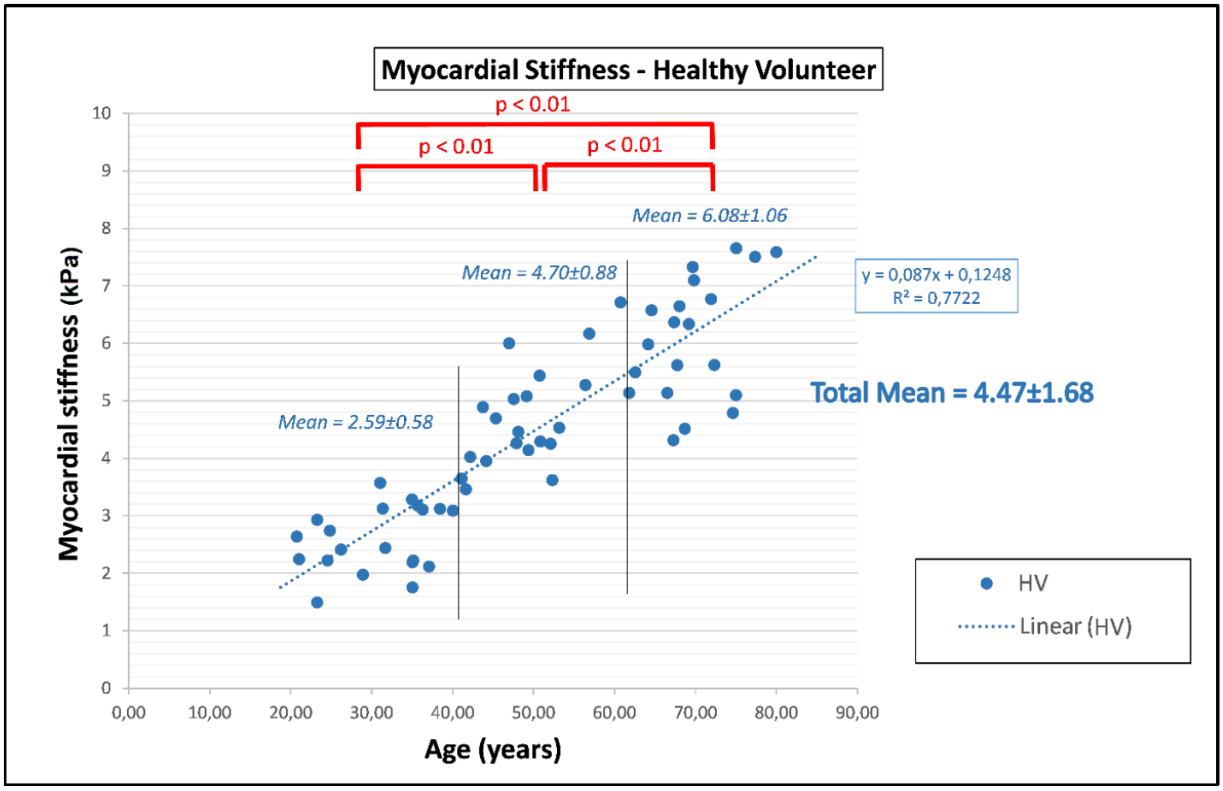

Figure 4: Comparison of Myocardial Stiffness between healthy volunteer group (HV) and hypertrophic cardiomyopathy with HFpEF group (HCM group)

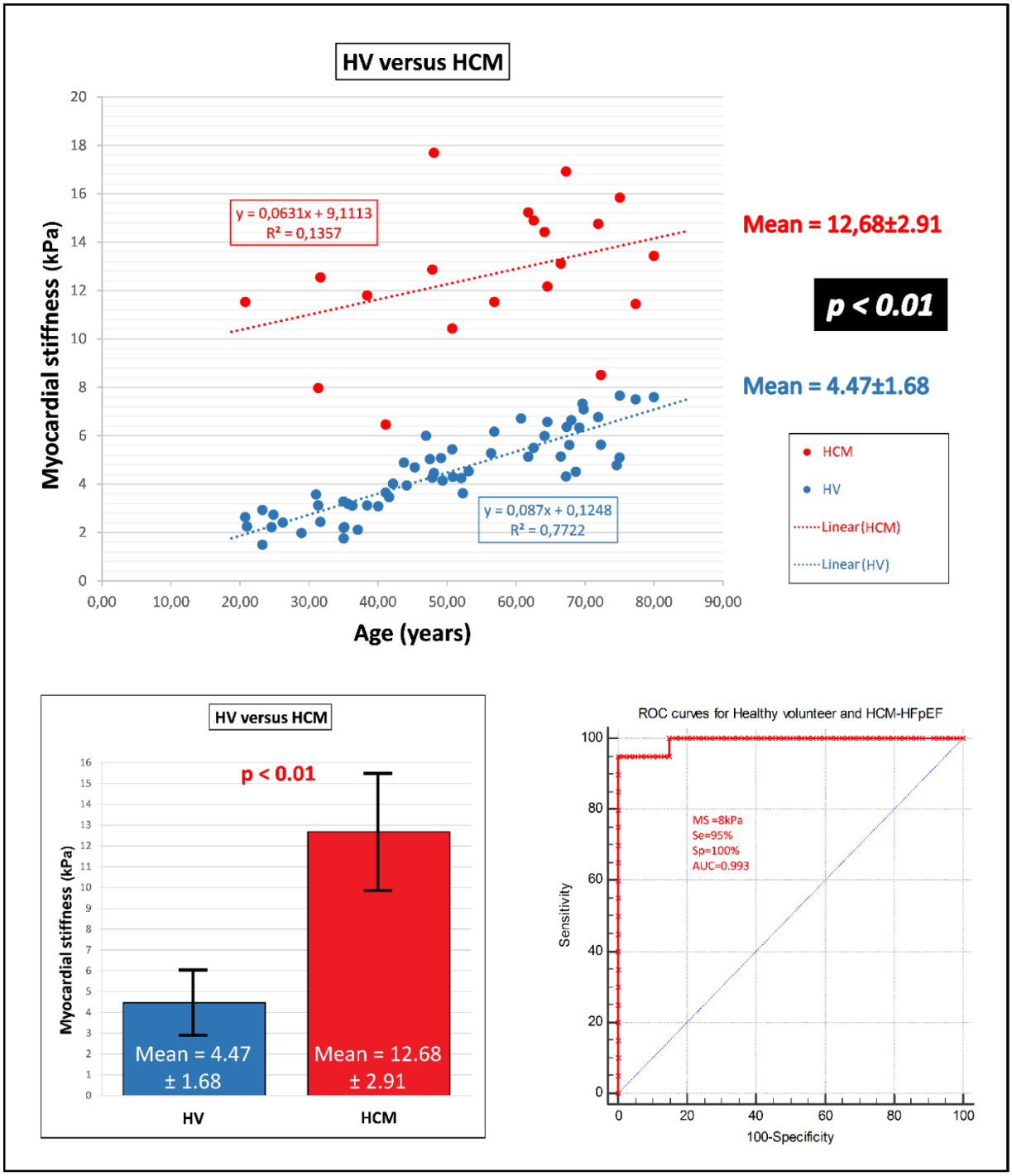

Figure 5: Correlations between Myocardial Stiffness and E/e', E/Vp, and LAVI on the study population.

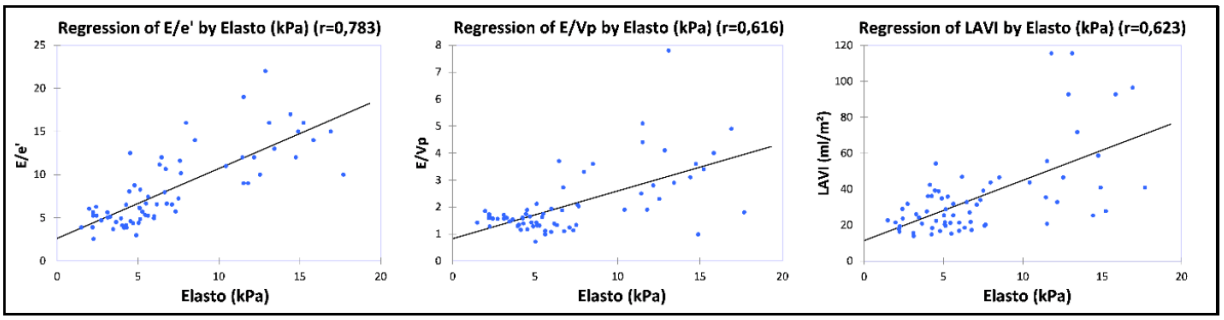

Figure 6: Comparison of Fractional Anisotropy between healthy volunteer group (HV) and hypertrophic cardiomyopathy with HFpEF group (HCM group)

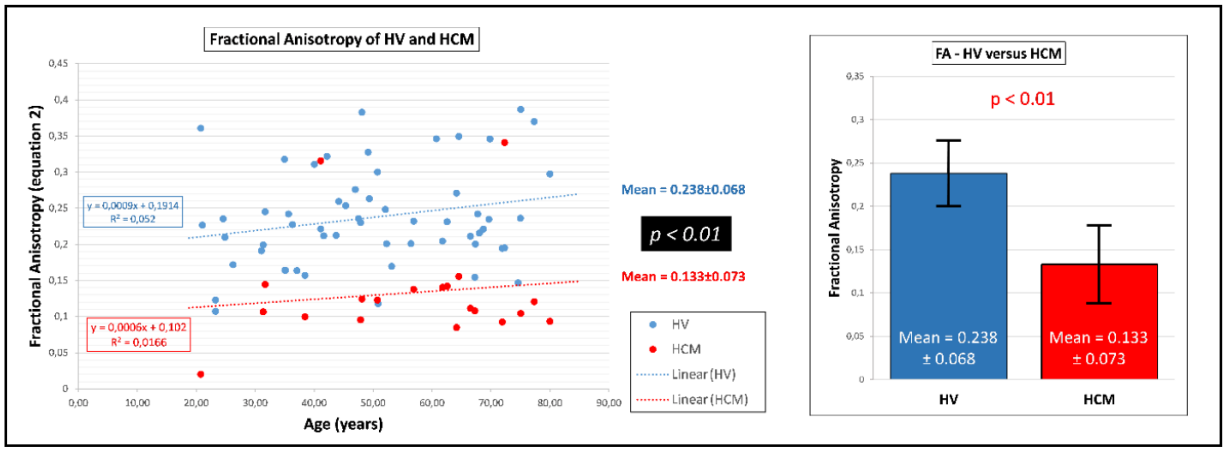

TABLES

Table 1. Population characteristics

	Healthy volunteer (n=60)	**HCM-HFpEF (n=20)**	**p**
Age (years)	50.6±16.9	57±17.5	0.22
Sex (M/F)	31/29	17/3	**<0.01**
BMI (kg/m²)	23.6±2.9	24.8±3.6	0.74
Systolic BP, mmHg	117±10	115±11	0.41
Diastolic BP, mmHg	70±7	75±6	0.47
NYHA I	52	0	**<0.01**
NYHA II	8	14	**<0.01**
NYHA III-IV	0	6	**<0.01**
Biology (blood explorations)			
CRP (mg/l)	1.4±1.1	1.9±0.8	0.55
BNP (pg/ml)	16 [<5-29]	365 [183-512]	**<0.01**
Hemotacrit (%)	43 (41-45)	40 (38-42)	**0.03**
Echocardiography parameters			
LA surface (4 cavities view, cm²)	16.1±4	29.3±7.1	**<0.01**
LAVI (ml/m²)	25.9±8.7	43.3±18.6	**<0.01**
LAVI >34ml/m²	12/60 (20%)	15/20 (75%)	**<0.01**
LVEF (%)	68±9.9	66±7.9	0.67
LVEDD	45.9±4.8	49.9±5.7	0.47
LVESD	28.3±4.8	24.6±3.2	0.22
LV Mass / BSA (g/m²)	70.6±20	125±34	**<0.01**
LV GS (%)	17.4±2.4	14.6±3.1	**<0.01**
ASB segment GS (%)	16.9±2.2	6.4±3.6	**<0.01**
ASB segment end diastolic thickness (mm)	5.9±1.4	20.8±5.1	**<0.01**
Peak E-wave (cm/s)	74.8±17.6	88.3±30.2	**<0.01**

E/A	1.4±0.5	1.1±0.4	**<0.01**
e' septal (cm/s)	13.8±4.1	5.8±1.9	**<0.01**
E/e'	5.9±2.4	16.1±6.5	**<0.01**
e'/a' septal	1.6±0.8	1.3±0.9	0.29
E-wave DT (ms)	179±60	238±62	**<0.01**
IVRT (ms)	94±17	144±31	**<0.01**
Vp (cm/s)	50.4±7.4	29.2±5.5	**<0.01**
E/Vp	1.3±0.3	3.4±1.5	**<0.01**
PV S/D ratio	1.2±0.3	0.7±0.3	**<0.01**
Cardiac Magnetic Resonance			
ASB segment end diastolic thickness (mm)	5.7±1.4	18.3±3.4	**<0.01**
LV mass / LVED volume (g/ml)	0.75±0.17	2.1±0.51	**<0.01**
Myocardial T1 pre-contrast (ms)	1217±49	1299±80	**<0.01**
Blood T1 pre-contrast (ms)	1738±102	1694±67	0.17
Myocardial T1 post-contrast (ms)	440±52	395±60	**0.02**
Blood T1 post-contrast (ms)	247±41	230±50	0.08
Focal LGE present (ASB segment)	0/60 (0%)	16/20 (80%)	**<0.01**
Extracellular volume fraction (%)	24.5±3.7	27.2±4.1	**<0.01**

A: late diastolic peak (pulsed-wave doppler); **a':** late diastolic mitral annular velocity by doppler tissue imaging; **ASB:** antero septo basal; **BSA:** body surface area; CRP: **DT:** deceleration time; **E:** early diastolic peak (pulsed-wave doppler); **e':** early diastolic mitral annular velocity by doppler tissue imaging; **GS:** global strain; **IVRT:** isovolumic relaxation time; **LA:** left atrium; **LAVI:** left atrium volume index; **LVEF:** left ventricle ejection fraction; **LVEDD:** left ventricle end-diastolic diameter; **LVESD:** left ventricle end-systolic diameter; **NTproBNP:** N-terminal pro brain natriuretic peptide ; **PV S/D ratio :** pulmonary veins velocities **Vp:** transmitral flow propagation velocity;

ONLINE APPENDIX FIGURE

Figure A: Correlation between echocardiographic parameters (E/A, E/e', E/Vp) and age on heathy volunteers

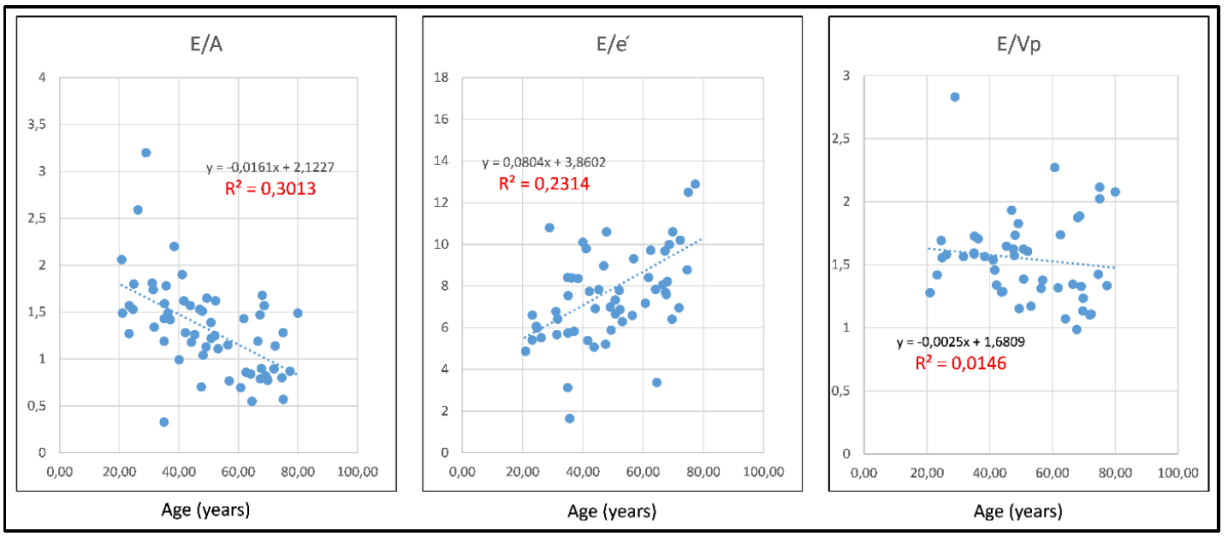

Figure B: Bland-Altman-Plots for myocardial stiffness analysis

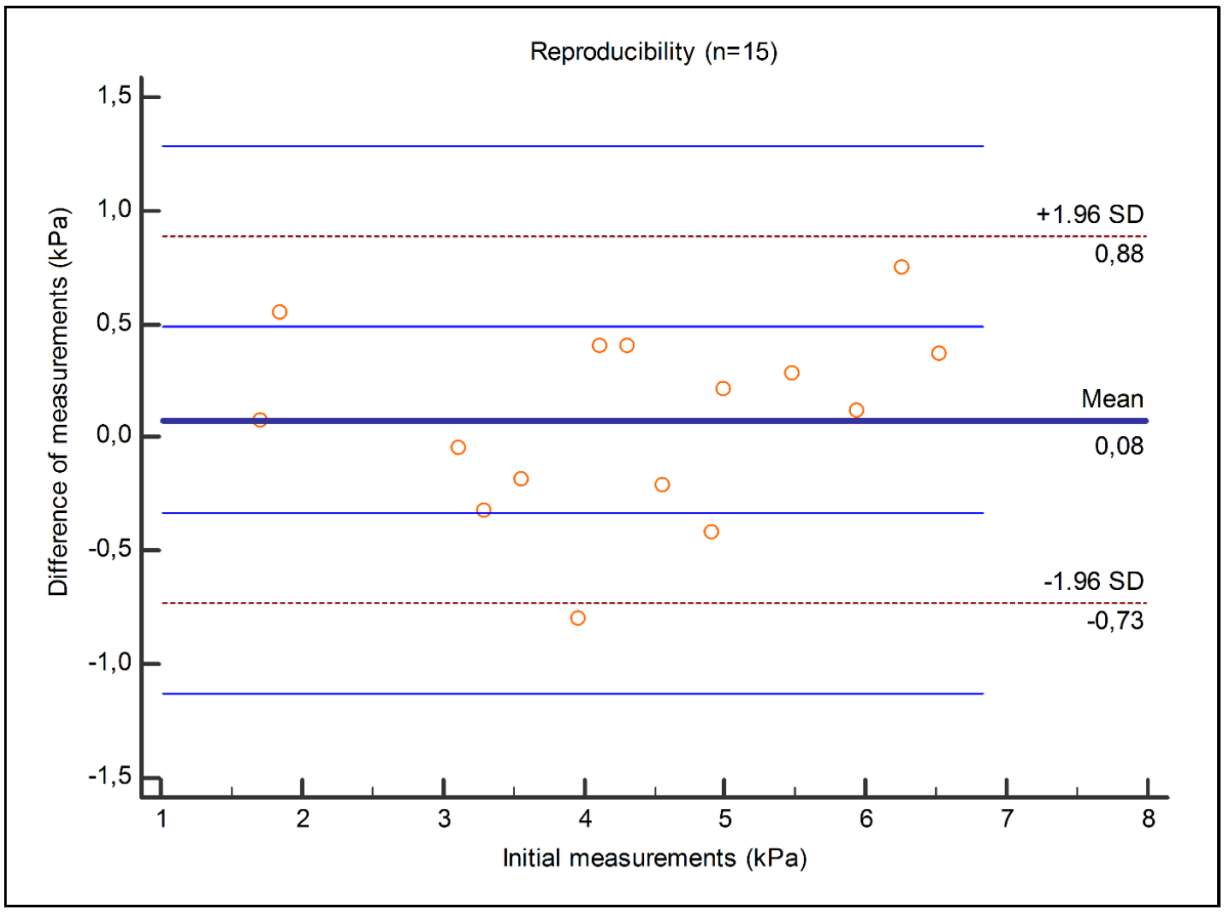

Legend of figure B (online): Bland-Altman-Plots with mean difference of measurements (three months later) and limits of agreement for the HV sub-group (n=15). The mean difference is equal to +0.08 kPa (upper limit of agreement [ULA]: +0.89 kPa; lower limit of agreement [LLA]: -0.73 kPA).

2.4.3. Manuscrit "*Myocardial stiffness in cardiac amyloidosis and heart failure*" (In preparation)

Les études pédiatriques et adultes sur populations saines et patients ayant une CMH ont permis de montrer : 1) la faisabilité et la reproductibilité de la technique d'imagerie, 2) sa capacité à différencier un cœur sain d'un cœur malade (par élastographie et par estimation de la fraction d'anisotropie), et 3) d'estimer quantitativement un paramètre directement lié à la fonction diastolique (la rigidité myocardique).

L'étape suivante était donc de montrer, dans des situations pathologiques cliniques bien identifiées, que l'élastographie myocardique avait une valeur ajoutée diagnostique. Pour cela, nous avons inclus de manière prospective 60 patients entre février et octobre 2016, sur deux centres (l'hôpital Henri-Mondor, à Créteil, et à l'Hôpital Européen Georges Pompidou, à Paris), divisés en 3 groupes (n total=60) :

1) <u>l'insuffisance cardiaque à fraction d'éjection réduite [IC-FEr] (n=20)</u>

   Critères d'inclusion pour le groupe IC-FEr :

   - Sujet ayant reçu une information sur la recherche et signé le formulaire de consentement
   - Bénéficiaire d'un régime de sécurité sociale
   - Adulte ≤ 90 ans
   - Diagnostic d'IC systolique selon Guidelines ESC 2012 (Mcmurray et al. 2012): la présence de symptômes d'insuffisance cardiaque droits ou gauches, la présence de signes physiques d'insuffisance cardiaque, FEVG < 45%.

   Critères d'exclusion pour le groupe IC systolique :

   - Grossesse
   - Arythmie atriale permanente
   - Anéchogénéicité
   - Allergie au gel d'échocardiographie
   - Refus ou incapacité linguistique ou psychique de signer le consentement éclairé
   - Allergie au gadolinium

2) <u>l'insuffisance cardiaque à fraction d'éjection préservée [IC-FEp] (n=20)</u>

   Critères d'inclusion pour le groupe IC-FEp :

   - Sujet ayant reçu une information sur la recherche et signé le formulaire de

consentement

- Bénéficiaire d'un régime de sécurité sociale
- Adulte ≤ 90 ans,
- Hospitalisation en cardiologie pour oedème aigu pulmonaire (OAP) hémodynamique sur poussée d'ICD.
- FEVG >45% (pas de dysfonction systolique)
- BNP > 500 pg/mL
- Absence de pathologie pulmonaire associée
- Pas d'autre cardiopathie connue (valvulaire, ischémique ou rythmique).

Critères d'exclusion pour le groupe ICD isolée :

- Grossesse
- Arythmie atriale permanente
- Trouble cinétique segmentaire à l'échographie.
- Anéchogénéicité,
- Allergie au gel d'échocardiographie.
- Refus ou incapacité linguistique ou psychique de signer le consentement éclairé
- Allergie au gadolinium

3) <u>l'amylose cardiaque (n=20)</u>

Critères d'inclusion pour le groupe Amylose :

- Sujet ayant reçu une information sur la recherche et signé le formulaire de consentement
- Bénéficiaire d'un régime de sécurité sociale
- Age > 18 ans
- Diagnostic d'amylose AL (confirmé par la réalisation d'électrophorèse des protides, de l'immunofixation, du dosage des chaînes libres sériques et de la recherche de protéinurie de Bence Jones) ou diagnostic d'amylose TTR héréditaire ou sénile
- Diagnostic d'amylose confirmé par l'examen anatomopathologique et la réalisation de biopsie
- Hypertrophie biventriculaire (SIV>12mm)
- FEVG >45% (pas de dysfonction systolique)
- Pas d'autre cardiopathie connue (valvulaire, ischémique ou rythmique).

Critères d'exclusion pour le groupe Amylose :

- Grossesse
- Arythmie atriale permanente
- Anéchogénéicité
- Allergie au gel d'échographie
- Refus ou incapacité linguistique ou psychique de signer le consentement éclairé
- Allergie au gadolinium

Concernant la méthodologie de l'élastographie myocardique, le mode d'acquisition, de recueil de données et de post-traitement a été le même que celui des études portant sur la cardiomyopathie hypertrophique (cf chapitre 2.4.1 et 2.4.2).

Les données échocardiographiques recueillies sur l'ensemble de la population de l'étude (n=60) ont été :

- Imagerie 3D : Volumes ventriculaires de la FE et de l'index de sphéricité.
- Imagerie 2D : VTD, VTS, FEVG (Simpson 4 cavités et 2 cavités), Masse VG, épaisseur TD SIV et Parois postérieures, Volume OG, globale longitudinale strain (2D speckle tracking)
- Imagerie TM: TM trans-ventriculaire classique avec tous les paramètres [épaisseurs, Masse VG et FEVG]
- Doppler : E/A, E/Em, E/Vp, TRIV, flux VP si possible, Flux veineux sus hépatique

Aucune IRM cardiaque dédiée à cette étude n'a été réalisée.

Résultats

Les résultats de cette étude sont encore en cours d'analyse et d'interprétation.

Le tableau 1 résume les caractéristiques épidémiologiques, échographiques et élastographiques (résultats partiels) de la population (n=60)

Tableau 1 : Caractéristiques de la population de l'étude « *Myocardial stiffness in cardiac amyloidosis and heart failure* »

	IC-FEr (n=20)	**IC-FEp (n=20)**	**Amylose (n=20)**	**p**
Age	68.8 [63.0-72.6]	49.8 [38.3-56.6]	69.3 [60.3-78.4]	0.01
Sexe ratio (M/F)	15/5	15/5	18/2	0.34
Poids (kg)	76 [68-82]	75 [65-80]	69 [62-83]	0.22
Taille (cm)	171 [160-177]	174 [165-179]	173 [162-177]	0.67
IMC	26.0±3.3	24.7±2.9	23±2.9	0.24
Echocardiographie				
Surface OG (4 cavités, cm²)	24.3 [20.3-29.4]	29.5 [24.8-34.0]	37.4 [31.9-44.3]	<0.01
Volume OG indexé (ml/m²)	32.1 [25.7-38.2]	40.6 [32.4-57.4]	48.2 [38.4-56.6]	<0.01
Volume OG indexé >34ml/m²	7/20 (35%)	13/20 (65%)	19/20 (95%)	<0.01
FE VG (%)	35 [30-41]	73 [65-77]	62 [51-69]	<0.01
DTD VG (mm)	57 [52-61]	53 [48-56]	48 [42-50]	0.08
DTS VG (mm)	48 [41-50]	26 [23-31]	30 [27-34]	<0.01
Masse VG / SC (g/m^2)	99 [84-108]	81 [69-92]	119 [107-143]	0.04
VG GS (%)	9.9 [8.5-10.8]	15 [13-17]	11 [8-16]	0.02
ASB segment GS (%)	8.7 [7.8-9.6]	16 [14-19]	7.7 [5.9-8.9]	<0.01
Epaisseur télédiastolique ASB segment (mm)	10 [8-11]	6 [5.5-9.5]	13 [13-15]	0.01
Pic onde E (cm/s)	57 [40-72]	58 [50-83]	146 [128-158]	<0.01
E/A	0.76 [0.62-1.01]	1.0 [0.72-1.23]	3.4 [2.4-4.9]	<0.01
e' septal (cm/s)	5 [4-6]	5 [4-7]	5 [5-9]	0.61
E/e'	11 [9.4-15.8]	11.3 [8.7-15.1]	12.2 [5.6-15.9]	0.77
TD onde E (ms)	187 [121-247]	232 [180-264]	161 [146-218]	0.06
TRIV (ms)	65 [45-86]	96 [80-123]	78 [67-100]	0.10

Vp (cm/s)	37 [25-52]	41.5 [33.5-49]	36 [32-42]	0.41
E/Vp	1.35 [1.20-2.93]	1.46 [1.26-1.79]	1.95 [1.54-2.47]	0.44
S/D ratio (veines pulmonaires)	1.31 [1.05-1.44]	1.06 [0.75-1.18]	0.57 [0.51-0.70]	0.03
Élastographie				
Élastographie (kPa)	En attente	En attente	Non-estimable quantitativement	

Les valeurs sont exprimées en médianes, avec [IQ25%-IQ75%].
ASB : antéro-septo-basal ; DTD : diamètre télédiastolique ; DTS : diamètre télésystolique ; FE : fraction d'éjection ; GS : global strain ; OG : oreillette gauche ; TD : temps de décélération ; TRIV : temps de relaxation isovolumique ; VG : ventricule gauche ; Vp : vitesse de propagation

Concernant les patients ayant une amylose cardiaque, tous les patients avaient une élastographie non estimable quantitativement car ayant une onde de cisaillement trop rapide.

Discussion du travail en cours, de ses limites et de ses perspectives

A travers des résultats encore intermédiaires de cette étude clinique, un résultat nous semble déjà intéressant. En effet, les patients ayant une amylose cardiaque ont une rigidité qui n'est pas analysable de manière quantitative selon notre technique, car trop élevée. En effet, notre travail portant sur les limites de notre technique (cf paragraphe 2.2.2, Manuscrit *Validation of a non-invasive Myocardial Shear Wave Elastography device for clinical applications in cardiology*) a montré qu'une vitesse d'onde de cisaillement supérieure à 5m/s rendaient sa visualisation difficile, ce qui se passe dans ce sous-groupe clinique.

Malgré tout, cette étude, qui reste en cours d'analyse, pourrait présenter certaines difficultés. La première concerne la méthodologie d'inclusion et le fait qu'il n'y ait pas eu d'appareillement par l'âge lors de des inclusions. Effectivement, nous avons conçu et débuté l'étude en même temps que celle portant sur les volontaires sains et les CMH. Etant donné que ces études avaient pour but d'apporter une preuve de concept clinique pour l'élastographie myocardique, nous n'avions aucune donnée de référence disponible, notamment aucune idée préconçue sur l'évolution physiologique de la rigidité myocardique en fonction de l'âge. Malgré certaines études fondamentales chez l'humain sain (Fujimoto et al. 2012), nous avions décidé d'inclure les patients sans appareillement statistique spécifique. Au regard de nos résultats chez les volontaires sains, cela pourrait constituer un biais dans l'analyse et l'interprétation de nos nouveaux résultats. La seconde difficulté concerne l'interprétation de la non visualisation de l'onde de cisaillement chez les patients du

groupe amylose. En effet, l'analyse des datas brutes a été reprise chez les 20 patients de ce groupe, et malgré la visualisation du push dans le myocarde et l'excellente échogénicité de ces patients, l'onde de cisaillement n'était pas observable. La seule interprétation possible est que l'onde de cisaillement est trop rapide donc que le myocarde est trop rigide. Nous restons encore prudents sur l'exactitude de cette conclusion et peut-être que des travaux in vitro sur des myocardes explantés (atteints d'amylose cardiaque), permettant des cadences d'images supérieures, donc des visualisation d'onde de cisaillement plus rapides, pourraient être pertinents pour confirmer notre conclusion.

2.5. Perspectives

A travers ces travaux, nous avons apporté la preuve clinique que l'élastographie myocardique était réalisable et reproductible, chez l'enfant comme chez l'adulte. Nous avons également montré que cette nouvelle technique d'imagerie pouvait différencier des cœurs sains de cœurs malades, tout en ayant un résultat quantitatif qui permettrait de mieux caractériser la fonction diastolique en pratique clinique. De plus, nous avons apporté des réponses aux limites ainsi qu'aux perspectives d'amélioration de cette technique.

Pour la suite, l'enjeu va être de montrer que l'élastographie myocardique a une valeur ajoutée pour « soigner des malades », donc pour mieux suivre et analyser les prises en charge thérapeutiques de certaines cardiopathies. Les perspectives d'application sont donc particulièrement nombreuses. A titre d'exemple, nous pourrions évoquer l'évaluation d'un traitement spécifique pour une cardiomyopathie bien identifiée (type maladie de Pompe avec introduction par alpha-glucosidase), ou l'évaluation d'un traitement général pour une situation cardiologique spécifique (par exemple l'efficacité en aigue du traitement immunosuppresseur pour un transplanté cardiaque), ou enfin l'évaluation d'un traitement général pour une situation cardiologique générale (type traitement par Digoxine ou Cordarone chez des patients ayant une IC-FEp). A titre personnel, je pense que la prochaine étape de l'élastographie myocardique dans notre pratique clinique devra passer un de ces protocoles thérapeutiques cliniques, afin de montrer que l'élastographie myocardique permet d'améliorer la prise en charge (et le suivi) de ces malades. L'enjeu sera donc de bien choisir le protocole à mettre en place aussi bien chez l'enfant que chez l'adulte, d'avoir les moyens matériels et humains adéquats pour le réaliser, puis d'apporter un résultat clair sur l'apport de l'élastographie myocardique dans la situation choisie. A ce moment-là, nous aurons tous les arguments pour être convaincants sur l'importance de disposer de ce nouvel outil d'imagerie en pratique clinique courante.

3. Elastographie hépatique

3.1. Introduction et Objectifs

L'insuffisance cardiaque (IC) est la principale cause de morbidité et de mortalité chez les patients cardiaques et peut provoquer des dysfonctionnements d'organes multiples en raison de diverses interactions. Une dysfonction cardiaque droite peut induire des signes de cœur congestif droit en raison de l'augmentation des pressions de remplissage, avec des répercussions directes sur le foie (congestion hépatique). À l'heure actuelle, l'estimation indirecte des pressions de remplissage du cœur droit est obtenue grâce à l'examen clinique, à un paramètres biologique (le BNP ou le NT-proBNP) et grâce à certains paramètres échographiques. Le cathéter cardiaque droit est le « gold standard » pour mesurer la pression veineuse centrale (PVC), mais il est invasif, coûteux et risqué.

L'élastographie du foie a d'abord été développée pour analyser les propriétés tissulaires de cet organe, en particulier pour le classement de la cirrhose. Il est important de noter que la congestion altère la rigidité intrinsèque du foie. Pour cette raison, des études récentes ont démontré que la rigidité hépatique (RH) et la PVC sont corrélées. Malgré tout jusqu'à maintenant, ces études ont eu des limitations techniques et l'utilisation potentielle de la mesure de la RH par ultrasons comme substitut fiable et quantitatif de l'estimation de la PVC en pratique clinique nécessite des preuves supplémentaires.

Il existe plusieurs techniques d'échographie pour évaluer la RH (cf figure 5). Les principaux étant l'élastographie impulsionnelle (par exemple Fibroscan®) et l'impulsion de force de rayonnement acoustique (ARFI) avec une estimation qualitative (par exemple, Siemens Virtual Touch Quantification®) ou avec une estimation de quantification absolue par Shear Wave Elastography (SWE). Le SWE est le seul à permettre une estimation en temps réel avec une image quantifiée absolue. Plusieurs études sur les animaux ont montré l'intérêt de SWE pour corréler l'estimation de la rigidité et la congestion des organes, en particulier pour le rein. À notre connaissance, aucune étude clinique n'avait été menée sur des humains pour lier le PVC et la RH estimée par le SWE en temps réel.

Nous cherchions ici à déterminer si la RH estimée par SWE pouvait estimer de manière fiable la mesure de PVC lors du cathétérisme cardiaque droit. En outre, nous avons regardé si les changements aigus de la PVC étaient corrélés avec les changements dans la RH.

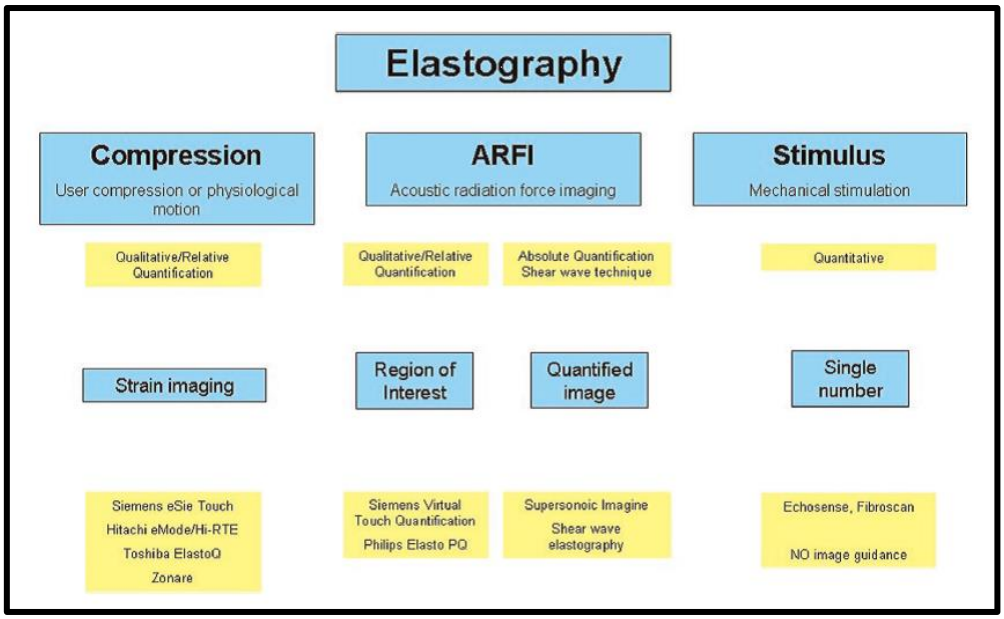

Figure 5 : Méthodes d'élastographie par ultrason

3.2. Manuscrit "*Towards non-invasive assessment of central venous pressure using real time and quantitative liver stiffness estimation"*

Ce travail est publié dans JACC : Cardiovascular Imaging, sous forme de Letter to the Editor (Villemain, Sitefane, et al. 2017).

Le manuscrit complet fait suite à la publication.

JACC: CARDIOVASCULAR IMAGING
VOL. ■, NO. ■, 2017
© 2017 BY THE AMERICAN COLLEGE OF CARDIOLOGY FOUNDATION
ISSN 1936-878X/$36.00
PUBLISHED BY ELSEVIER

iMAIL

LETTER TO THE EDITOR

Toward Noninvasive Assessment of CVP Variations Using Real-Time and Quantitative Liver Stiffness Estimation

Heart failure is the main cause of morbidity and mortality in cardiac patients, and may cause the dysfunctions of multiple organs as a result of various interactions. A right heart dysfunction can induce signs of congestive right heart due to the increase of filling pressures, with direct repercussions on the liver (hepatic congestion). Currently, the indirect estimation of filling pressures of the right heart is achieved through clinical examination and ultrasound parameters. Right heart catheterization (RHC) is the gold standard to measure central venous pressure (CVP) (1) but it is invasive, costly, and cannot be repeated for close follow-up, particularly on children.

Liver elastography was initially developed to analyze the tissue properties of this organ, especially for the grading of cirrhosis. It is important to note that congestion alters the intrinsic rigidity of the liver (2). For this reason, recent studies have demonstrated that liver stiffness (LS) and CVP are correlated (3,4). Until now, however, these studies have had technical limitations and the potential usefulness of LS measurement using shear wave elastography (SWE) as a reliable and quantitative surrogate of CVP in clinical practice needs further developments. To our knowledge, no clinical studies have been conducted on humans to link the CVP and the LS estimated by SWE in real time.

Here we sought to determine whether LS estimated by SWE could reliably estimate the measurement of CVP during RHC. In addition, we investigated whether acute changes in CVP paralleled changes in LS.

A total of 103 children (6.8 ± 5.5 years of age) referred to our institution for diagnostic or interventional RHC were prospectively enrolled. CVP and LS were measured simultaneously at baseline and after 15 ml/kg of volume loading. Inferior vena cava diameter and pulsed-Doppler profile of hepatic veins were also evaluated. Plasma level of N-terminal pro-B-type natriuretic peptide was assayed during the RHC.

SWE was used to image LS with the Aixplorer ultrasound imaging system (Aixplorer, Supersonic Imagine, Aix-en-Provence, France) with an abdominal curved probe (SC6-1), during the RHC procedure. These acquisitions were performed at 2 moments during the procedure, before and after the rapid saline loading (at the same time of the pre-CVP and post-CVP measurements). The physicians performing the LS measurement were unaware of the CVP results.

At baseline RHC, the mean CVP was 7.4 ± 2.9 mm Hg (range 3 to 16 mm Hg) and the mean LS was 9.0 ± 5.8 kPa (range 4 to 46.1 kPa). After volume loading, the mean CVP increased significantly to 10.0 ± 3.3 mm Hg (range 3 to 18 mm Hg) ($p < 10^{-4}$) and the mean LS increased significantly to 14.4 ± 9.1 kPa (range 4.3 to 72 kPa) ($p < 10^{-4}$). LS strongly correlated with CVP, pre-loading ($r = 0.86$; $p < 10^{-4}$) and post-loading ($r = 0.87$; $p < 10^{-4}$) (**Figure 1**).

All patients who had an increasing CVP also had an increasing LS (93 of 103 patients). In addition, all patients who had a decreasing CVP also had a decreasing LS (10 of 103 patients).

Optimal cutoff value of LS for detection of CVP >10 mm Hg was 10.8 kPa (sensibility = 89.3%, specificity = 86.0%), with an area under the curve of 0.946 (95% confidence interval: 0.920 to 0.971; $p = 0.01$). Beyond this correlation, LS is sufficient to provide an indirect and reliable measurement of quantitative CVP variations ($r = 0.86$, $\rho = 0.756$, $p < 10^{-4}$; multivariate model). Inferior vena cava diameter ($r = 0.40$, $\rho = -0.408$, $p = 0.01$), pulsed-Doppler profile of hepatic veins ($r = 0.19$, $\rho = 0.078$, $p = 0.483$), and N-terminal pro-B-type natriuretic peptide ($r = 0.10$, $\rho = 0.038$, $p = 0.736$) were less robust than LS to estimate CVP.

The intraoperator and interoperator reproducibility of the LS measurement technique were studied in 20 patients, and we found no significant statistical difference.

For children with congenital heart disease and no argument for tissue liver anomalies, noninvasive and quantitative estimation of filling pressures can be very difficult to perform. The paradox is that the filling pressures (and specifically CVP) have been recognized as a major predictive parameter of adverse events. The management of the acute heart failure at the child's bedside depends on the evaluation of volume or pressure overload (5). That is why a quantitative and real-time parameter as LS by SWE could be clinically necessary.

Here, we show that LS measurement using SWE is a reliable surrogate of quantitative estimation of the CVP. It can also be used to measure CVP changes in real time. LS could potentially be a useful noninvasive tool for evaluation and follow-up of acute and chronic right heart failure.

FIGURE 1 Results

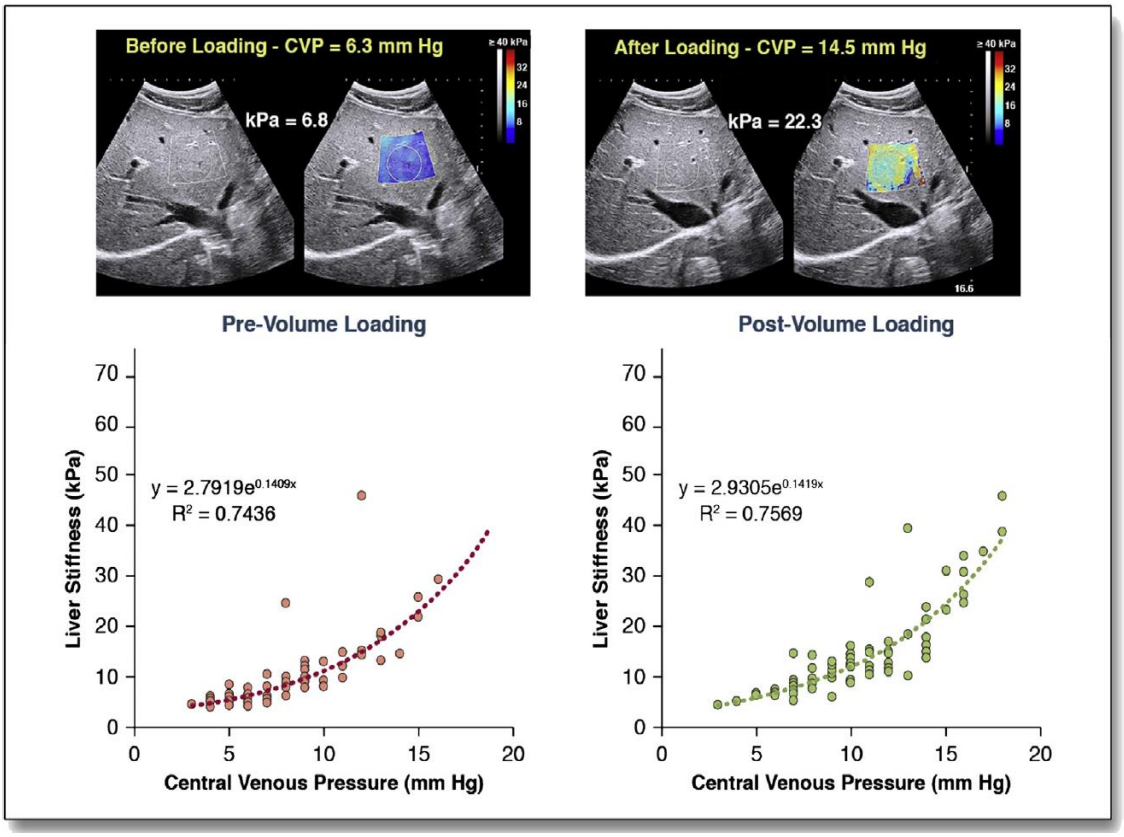

Correlation between liver stiffness and central venous pressure (CVP), pre- and post-volume loading, with an example of evaluation of liver stiffness by shear wave elastography (kPa).

Olivier Villemain, MD*
Fidelio Sitefane, MD
Mathieu Pernot, PhD
Sophie Malekzadeh-Milani, MD
Mickael Tanter, PhD
Damien Bonnet, MD, PhD
Younes Boudjemline, MD, PhD

*M3C-Necker Enfants malades
AP-HP, Université Paris Descartes
Sorbonne Paris Cité
Cardio-Vascular Department
149 rue de Sèvres
Paris 75015
France
E-mail: olivier.villemain@inserm.fr

http://dx.doi.org/10.1016/j.jcmg.2017.01.018

Please note: Dr. Tanter is cofounder of SuperSonic Imagine. All other authors have reported that they have no relationships relevant to the contents of this paper to disclose.

REFERENCES

1. Nagueh SF, Kopelen HA, Zoghbi WA. Relation of mean right atrial pressure to echocardiographic and Doppler parameters of right atrial and right ventricular function. Circulation 1996;93:1160–9.

2. Millonig G, Friedrich S, Adolf S, et al. Liver stiffness is directly influenced by central venous pressure. J Hepatol 2010;52:206–10.

3. Taniguchi T, Sakata Y, Ohtani T, et al. Usefulness of transient elastography for noninvasive and reliable estimation of right-sided filling pressure in heart failure. Am J Cardiol 2014;113:552–8.

4. Jalal Z, Iriart X, De Lédinghen V, et al. Liver stiffness measurements for evaluation of central venous pressure in congenital heart diseases. Heart 2015;101:1499–504.

5. Hsu DT, Pearson GD. Heart failure in children: part II: diagnosis, treatment, and future directions. Circ Hear Fail 2009;2:490–8.

Towards Non-Invasive Assessment of Central Venous Pressure Variations using Real Time and Quantitative Liver Stiffness Estimation

Brief Title:

Estimation of Central Venous Pressure Variations by Liver Elastography

Authors: O. Villemain[1-2], F. Sitefane[1], M. Pernot[2], S. Malekzadeh-Milani[1], M. Tanter[2], D. Bonnet[1], Y. Boudjemline[1]

[1]**M3C-Necker Enfants malades, AP-HP, Université Paris Descartes, Sorbonne Paris Cité, Paris, France**

[2]**Institut Langevin, ESPCI, CNRS, Inserm U979, PSL Research University, Paris, France**

Corresponding Author: Olivier Villemain, MD

M3C-Necker Enfants malades, AP-HP, Université Paris Descartes, Sorbonne Paris Cité, Paris, France

Telephone: (33) 1 44 49 43 44

Fax: (33) 1 44 49 43 40

Word count: 5907

Abstract

Objectives. The main purpose of this study was to assess the correlation between the liver stiffness (LS) estimated by shear wave elastography (SWE) and the central venous pressure (CVP) during hemodynamic variations in a cohort of children with heart disease.

Background. SWE has been shown and used as a non-invasive, quantitative and reproducible approach to assess LS. LS has been reported to be associated with fibrosis but there is also a potential dependence of LS with the CVP.

Methods. 103 children (6.8±5.5 years) referred to our institution for diagnostic or interventional right heart catheterization (RHC) were prospectively enrolled. CVP and LS were measured simultaneously at baseline and after 15 ml/kg of volume loading. Inferior vena cava (IVC) diameter and pulsed-Doppler profile of hepatic veins were also evaluated. Plasma level of NT-pro-BNP was assayed during the RHC.

Results. At baseline RHC, the mean CVP was 7.4±2.9 mm Hg [range 3–16] and the mean LS was 9.0±5.8 kPa [4–46.1]. After volume loading, the mean CVP increased significantly to 10±3.3 mm Hg [3-18] ($p<10^{-4}$) and the mean LS increased significantly to 14.4±9.1 kPa [4.3-72] ($p<10^{-4}$). LS strongly correlated with CVP, pre-loading ($r=0.86$, $p<10^{-4}$) and post-loading ($r=0.87$, $p<10^{-4}$)]. Optimal cut-off value of LS for detection of CVP > 10 mmHg was 10.8 kPa (Se=89.3%, Sp=86.0%), with an area under the curve of 0.946 (95% CI 0.920 to 0.971; p=0.01). Beyond this correlation, LS is sufficient to provide an indirect and reliable measurement of quantitative CVP variations ($p<10^{-4}$, multivariate model). IVC diameter, pulsed-Doppler profile of hepatic veins and NT-pro-BNP were less robust than LS to estimate CVP.

Conclusions. Here, we show that LS measurement using SWE is a reliable surrogate of quantitative estimation of the CVP. It can also be used to measure CVP changes in real time. LS could potentially be a useful non-invasive tool for evaluation and follow-up of acute and chronic right heart failure.

Key words: noninvasive diagnostic heart failure; ultrasound; heart failure; pressure; liver

CONDENSED ABSTRACT:

The purpose of this study was to assess the correlation between the liver stiffness (LS) estimated by shear wave elastography (SWE) and the central venous pressure (CVP) during hemodynamic variations in a prospective cohort of 103 children with heart disease.

All the patients underwent a right heart catheterization with CVP measurement associated with LS estimation by SWE and biological/echocardiographic parameters, before and after saline loading (15ml/kg). LS by SWE offered the most robust and reliable parameters to estimate the CVP in real time.

LS could potentially be a useful non-invasive tool for evaluation and follow-up of acute and chronic right heart failure.

ABBREVIATIONS LIST

ARFI: acoustic radiation force impulse

BMI: body mass index

CVP: central venous pressure

HF: heart failure

IVC: inferior vena cava

LS: liver stiffness

NT-proBNP: N-terminal pro-brain natriuretic peptide

RCH: right heart catheterization

SWE: shear wave elastography

TTE: transthoracic echography

Vs, Vd, and Var: maximal velocities of the systolic, diastolic, and atrial reversal waves, respectively

INTRODUCTION

Heart failure (HF) is the main cause of morbidity and mortality in cardiac patients, and may cause the dysfunctions of multiple organs as a result of various interactions[1,2]. In particular, liver dysfunctions are closely associated with HF[3], an interaction referred to as cardiohepatic syndrome. A right heart dysfunction can induce signs of congestive right heart due to the increase of filling pressures, with direct repercussions on the liver (hepatic congestion). Currently, the indirect estimation of filling pressures of the right heart is achieved through clinical examination, and ultrasound parameters[4]. Right heart catheterization is the gold standard to measure central venous pressure (CVP)[5] but it is invasive, costly and cannot be repeated for close follow-up particularly on children.

Liver elastography was initially developed to analyze the tissue properties of this organ, especially for the grading of cirrhosis[6]. It is important to note that congestion alters the intrinsic rigidity of the liver[7]. For this reason, recent studies have demonstrated that liver stiffness (LS) and CVP are correlated[8,9]. Until now, however, these studies have had technical limitations and the potential usefulness of LS measurement using ultrasound as a reliable and quantitative surrogate of CVP in clinical practice needs further developments.

There are several ultrasound techniques to assess LS[10]. The main ones being the transient elastography (for instance Fibroscan®) and the acoustic radiation force impulse (ARFI) with qualitative estimation (e. g. Siemens Virtual Touch Quantification®) or with absolute quantification estimation by Shear Wave Elastography (SWE). The SWE is the only one allowing a real-time estimate with an absolute quantified image. Several animal studies have shown the interest of SWE to correlate the stiffness estimation and the organ congestion, particularly for the kidney[11]. To our knowledge, no clinical studies have been conducted on humans to link the CVP and the LS estimated by SWE in real time.

Here we sought to determine whether LS estimated by SWE could reliably estimate the measurement of CVP during right heart catheterization. In addition, we investigated whether acute changes in CVP paralleled changes in LS.

METHODOLOGY

This prospective study was conducted from July 2015 to March 2016 in Hôpital Necker-Enfants Malades, Paris, France. The study was approved by the local ethics committee. Children were included in the study after written informed consent was obtained from the parents.

All children (1) referred for diagnostic or interventional right heart catheterization (RHC) and (2) without chronic liver disease (based on medical records including history, clinical examination, viral serology status, and liver echography) were eligible for the study. Patients with acute decompensated heart failure, ascites, or severe obesity (BMI ≥ 120% of the 95th percentile) were excluded.

All patients underwent a unique procedure conducted by different physicians blinded to each other's results. The procedure was performed in the cath lab, and the following data were collected: (1) Routine blood sampling -including N-terminal pro-brain natriuretic peptide (NT-proBNP) measurement-, (2) LS measurements (LS), (3) transthoracic echocardiography (TTE) and (4) hemodynamic results during RHC. Blood samples were taken at the beginning of the procedure.

Cardiac catheterization

All procedures were performed either under general anesthesia, endotracheal intubation and ventilation (FiO2=0.21) or under local anesthesia. RHC was performed using a 5-French Cordis special JR3.5 catheter (Cordis, USA) inserted through the right femoral vein. Pressure measurements were calibrated before the study from the midaxillary line. Measurements of median right atrial, superior and inferior vena cava pressures were averaged during three to

five cycles to obtain CVP value. Two CVP measurements were performed: at the beginning of the procedure (CVPpre), and at the end of the procedure after a 15 ml/kg rapid saline loading (CVPpost).

The physician performing the cardiac catheterization was unaware of LS results.

Liver stiffness measurements by Shear Wave Elastography (SWE)

SWE was used to image LS with the Aixplorer ultrasound imaging system (Aixplorer, Supersonic Imagine, Aix-en-Provence, France) with an abdominal curved probe (SC6-1), during the RHC procedure. Five acquisitions were obtained on the right lobe of the liver, free of large vascular structures, using the shear wave elastography imaging mode (SWE™) of the Aixplorer scanner in the 'penetration' setting. A "QBox™" region of interest (mean diameter 30 mm) was positioned inside the elasticity image after each acquisition to obtain a mean stiffness value. In accordance with the guidelines[12], the liver stiffness measurement by SWE was defined in this study as the median of five successive stiffness values using the QBox. These acquisitions were performed at two moments during the procedure, before and after the rapid saline loading (at the same time of the CVPpre and CVPpost measurements).

The physicians performing the LS measurement was unaware of the CVP results.

Echocardiography

TTE was performed using Vivid 7 (GE Vingmed Ultrasound A.S., Horten, Norway). As described previously[13-14], non-invasive CVP was estimated from the dimensions of the inferior vena cava and its respiratory motion with the collapsibility index [Minimal diameter/(Maximal diameter + Minimal diameter)], and from the hepatic veins pulsed Doppler (with Vs, Vd, and Var, maximal velocities of the systolic, diastolic, and atrial reversal waves, respectively).

Statistical analysis

Clinical, biological, LS and RHC data were expressed as mean (standard deviation, SD) or median (range) for continuous variables or as a proportion (per cent) for categorical variables. Non-parametric Mann-Whitney test for quantitative variables and Fisher's exact test for qualitative variables were used to assess differences between groups when appropriate. At baseline, correlations (ρ, Spearman's rank coefficient) and multiple regression test for the multivariate model were used to assess the association between LS or CVP values and other variables (CVP or LS, IVC collapsibility, Vs/(Vs+Vd), and NT-proBNP). Receiver operating characteristic (ROC) curves and areas under the curve (AUC) were computed to assess the effectiveness of SWE to predict CVP elevation. A CVP of >10 mm Hg was considered as clinically significant. Statistical significance was set at $p<0.05$. Grubbs' test ($\alpha=0.05$, Z-score >2/<-2) defined an outlier patient[15]. The intra- and interoperator reproducibility were evaluated over the studied population using the standardized coefficient of variation (CV)[16]. Kruskal–Wallis tests were performed to find possible significant (p 0.05) differences among the acquisition series (same or different operator). Analysis was conducted using *Medcalc* (MedCalc Software, Mariakerke, Belgium).

RESULTS

Population characteristics

A total of 111 patients were prospectively screened for inclusion into the study. Five patients had exclusion criteria (2 architectural anomalies on liver echocardiography, 2 acute decompensated heart failures, 1 severe obesity). In addition, three other patients were excluded because they were anechoic. Finally, 103 patients were included.

Patients' baseline clinical characteristics including the type of congenital heart defects, and laboratory data are shown in Table 1.

The indications and characteristics of catheterization procedures are summarized in Table 2.

The median duration of the procedure (time between CVP/LS pre and CVP/LS post) was 27 ± 11 minutes [range 7-89].

Hemodynamic parameters, LS and Doppler parameters before and after loading (Table 3)

We did not observe any changes in heart rate or aortic blood pressure during the procedure (see table 3).

At baseline, the CVPpre was 7.4±2.9 mmHg [3-16] and the LSpre was 9.0±5.8 kPa [4–46.1].

After loading, the CVPpost increased to 10±3.3 mmHg [3-18] ($p<10^{-4}$) and the LSpost also increased to 14.4±9.1 kPa [4.3-72] ($p<10^{-4}$) (Figure 1).

93/103 patients had increased (or stabilized) CVP following volume loading. In this subgroup, the CVP increased (or stabilized) from 7.0±2.5 mmHg [3-14] to 9.7±3.1 mmHg [3-18] ($p<10^{-4}$). In parallel, the LS increased (or stabilized) also from 8.5±5.4 kPa [4-46] to 14.7±10.2 [4-72]. All patients who had an increasing CVP also had an increasing LS (Figure 2).

10/103 patients had decreased CVP following volume loading. The indications of catheterization procedures were: aortopulmonary window closure (2 patients), atrial septal defect closure (2 patients), pulmonary arterial hypertension diagnostic RHC (2 patient), coarctation stenting (1 patient), patent ductus arteriosus closure (1 patient), transcatheter implantation of a pulmonary valve (1 patient), and pre-transplantation (1 patient). The CVP decreased from 11.3±3.4 mmHg [6-16] to 8.1±4.2 mmHg [3-15] (p=0.03). In parallel, the LS decreased also from 15.2±7.9 kPa [7-29] to 10.4±6.2 [4-23] (p=0.04). All patients who had a decreasing CVP also had a decreasing LS (Figure 2).

There was no statistical difference between the IVC diameters (p=0.60 for maximal diameter; p=0.13 for minimal diameter) or IVC collapses (p=0.13) before and after loading.

The hepatic vein pulsed doppler showed a significant statistical difference for Vd (p=0.001) and Vs/(Vs+Vd) (p=0.001) before and after loading.

Correlations between CVP, LS and others parameters

The correlation between CVP and LS values was robust, before volume loading (r^2=0.74, r=0.86, $p<10^{-4}$) and after volume loading (r^2=0.76, r=0.87, $p<10^{-4}$), Figure 3.

The AUC of LS for identification of CVP >10 mm Hg was 0.946 (95% CI 0.920 to 0.971; p=0.01). Based on the ROC curve analysis, the optimal cut-off value of LS for detection of CVP >10 mm Hg was 10.8 kPa (sensitivity= 89.3%, specificity=86.0%, positive predictive value=77.9%, negative predictive value=93.6%, accuracy= 94.8%, Figure 4).

A correlation analysis at the baseline between CVP and the other parameters showed that LS (ρ=0.756, r=0.86, $p<0.10^{-4}$) was the most reliable parameter to determine the CVP. The Figure 5 summarizes the complete results. Concerning the correlation at the baseline between LS and the others parameters, the results were: CVP (ρ=0.756, r=0.86, $p<10^{-4}$); IVC collapsibility (ρ=-0.470, r=0.47, p=0.02), Vs/(Vs+Vd) (ρ=-0.110, r=0.26, p=0.33), and NT-proBNP (ρ=-0.053, r=0.06, p=0.634).

The multivariate analysis to determine the CVP at the baseline showed the LS as the only reliable parameter ($p<10^{-4}$) in comparison with the others [IVC collapsibility, p=0.177; VS/(Vs+Vd), p=0.097; NT-proBNP, p=0.054).

Intra- and interoperator reproducibility

The intra- and interoperator reproducibility of the LS measurement technique were studied in 20 patients. There was no significant difference between the five successive series of measurements made by the same operator (Kruskal–Wallis test). The intraoperator standardized CV was 4.1% over the studied population and varied from 1% to 13%. There was no significant difference between the five successive series of measurements made by the two different operators (Kruskal–Wallis test) and the corresponding CV was 3.7%.

Outliers

Three patients had discordant results according to the correlation found between LS and CVP values. Two patients (8.4 and 10 years old) had a single ventricle physiology and the indication

of their catheterization was the Fontan fenestration closure. The third patient (14 years old) was hospitalized for a chronic pericarditis (due to a camptodactyly-arthropathy-coxa vara-pericarditis syndrome, CACP syndrome) and needed a catheterization for pericardiocentesis and cardiac hemodynamic evaluation. Concerning these three patients, their biological explorations (especially NT-proBNP < 300 pg/ml and CRP < 5 mg/l) and their liver echography were normal. Characteristics of discordant cases are displayed in table 4.

DISCUSSION

Our study shows that LS estimated by SWE is strongly correlated with the simultaneous measure of the CVP. It appears more correlated to CVP than other echo parameters such as IVC collapsibility or hepatic Doppler profile. Beyond this correlation, the accuracy of LS estimated by SWE in quantifying liver stiffness is sufficient to provide an indirect and reliable measurement of quantitative CVP variations. We show here that acute changes in CVP during saline loading are paralleled by LS changes. This was also true for patients with decrease of CVP during the procedure that also translated into decrease in LS.

Realizing the whole procedure during cardiac catheterization in cath lab, we were able to evaluate simultaneously the LS and the CVP with an unchanged patient positioning. The patient position plays a crucial role in the accuracy of the assessment of the CVP. Jalal and al discussed this bias in their work[9] (where the measures were not carried out at the same time), making it more difficult to correlate CVP and LS estimated by transient elastography (Fibroscan®). Jugul et al, on their series of five hundred patients[17], showed a 50% difference between CVP recorded in supine position (as in catheterization lab) and Fowler position (45-60 degrees sitting), from 7.3±3.6 to 10.5±3.4 mmHg. Moreover, in 2014, Taniguchi et al had already shown a link between CVP and LS by transient elastography while specifying that their estimations were spaced three hours, on thirty-one patients in acute heart failure[8]. Our results showed that the change in real-time estimations was significant on a shorter period (27 ± 11

minutes between [CVP / LS] pre and [CVP / LS] post measurements), as Millonig et al had shown on an animal model[7]. It therefore seemed essential to correlate these parameters to achieve all these estimations in stable conditions simultaneously.

Assessing a pediatric population maximized our chances to have healthy livers[18] and having a congenital heart disease population broadened the range of initial CVP[19].

Finally, in the pediatric population, the hemodynamic response to the filling is less systematic, particularly in congenital heart disease[20]. This made possible an evaluation of heterogeneous situations and also explained the differences in the results of CVP changes (and LS). Therefore, this population seems to be appropriate to show the correlation between CVP and LS in real time.

Comparison of usual paraclinical parameters (IVC, hepatic veins pulsed Doppler, NT-proBNP) and LS by SWE to estimate CVP

The filling pressures of the right heart in the pediatric population are very complicated to estimate noninvasively in clinical practice[21]. The evolution of the anatomical relationships (and size) during the child's growth makes the index and the estimation criteria difficult to validate[22]. The parameters used in pediatric cardiology come directly from adult cardiology, for lack of anything better. No specific and reproducible tool has been validated in this specific population to estimate CVP noninvasively.

For children and adults, the clinical correlation between CVP and the IVC collapsibility index is still debated, mainly because of the intra- and inter-operator variability[23] of IVC collapsibility and because of its relatively low correlation with CVP[24]. This parameter is simple to estimate which still allows the clinician to utilize it. The hepatic veins pulsed Doppler can be difficult to perform in clinical practice[25]. Nevertheless, these parameters are clinically used because ultrasound is still a tool that potentially could provide a rapid and patient's bed side means of gauging preload. In the end, Ommen et al[26] showed that when faced with the limitations of these assessment techniques, it could be better to use a combination of these noninvasive

parameters to estimate the CVP. In clinical practice, the CVP assessment remains complicated with this approach.

Concerning the biological parameters, NT-proBNP remains an expensive examination, requiring a blood sampling and variations of result according to the age[27]. The role of BNP and N-terminal pro BNP in the diagnosis and management of children with heart failure remains controversial. Nir et al have tried to prove the value of this biological parameter for clinical practice, especially for the evaluation of volume or pressure overload in patients with lesions that cause left-to-right shunt[27]. Other studies have found correlation between BNP and adverse cardiovascular events in pediatric outpatients with chronic left ventricular systolic dysfunction[28] or between NT-proBNP and specific population (anthracycline-treated children)[29]. However, to our knowledge, no study has been done to correlate specifically the CVP with the NT-proBNP in a pediatric population.

In parallel, it is clear that LS estimated by ultrasound seems to be a reliable tool to estimate noninvasively the CVP. However, the different ultrasound techniques need to be discussed and compared. In 2009, Lupsor et al[30] have shown that unidimensional transient elastography and shear wave elastography had globally the same accuracy to diagnose chronic hepatitis C. Still, previous studies have shown that there can also be a variability of ultrasound LS estimation depending on the patient position[31] and the probe position[32]. Based on our opinion, the advantage of the LS estimated by SWE compared to other techniques is twofold: it provides a quantitative result in real time and it allows the clinician to have the real-time associated imagery (B-Mode) to locate anatomically his evaluation. In our experience, the LS by SWE is a very easy method to be applied clinically to correlate the CVP and the LS. Naturally, the comparison between the different ultrasound techniques to estimate CVP in real time needs to be realized in a future specific study.

Clinical Applications

For children with congenital heart disease and no argument for tissue liver anomalies, non-invasive and quantitative estimation of filling pressures can be very difficult to perform. The paradox is that the filling pressures (and specifically CVP) have been recognized as a major predictive parameter of adverse events. Ghaferi et al have shown that chronic passive congestion after Fontan procedure increased risk of cirrhosis, hepatic adenoma, and hepatocellular carcinoma[33], and the VAST study concerning Fontan patients had confirmed these results[34]. Concerning the patients with surgically repaired tetralogy of Fallot, Aboulhon et al have stated that the RV diastolic dysfunction is associated with major adverse risks (ventricle tachycardia, hypertension, diabetes mellitus, reoperations), while specifying that the parameters of diastolic function of RV in children were difficult to determine[35]. Concerning pediatric pulmonary hypertension, it is clear that a reliable noninvasive tool to estimate their right filling pressures could have an impact on their management. As a matter of fact, all these clinical situations suffer from a lack of means to assess and monitor the CVP. Similarly, the management of the acute heart failure at the child's bedside depends on the evaluation of volume and/or pressure overload[36]. That is why a quantitative and real-time parameter as LS by SWE could be clinically necessary.

For adults specifically, the main limit to the immediate application of this noninvasive approach to estimate the CVP is to know the patient's liver status. Given the correlation in real time between LS and CVP (whether decrease or increase) shown in our study, we believe it should be relevant to evaluate this in the case of the management of a cardiac decompensation in adults. For example, concerning the role of the diuretic in front of a congestive acute heart failure, the ESC Guidelines precise that "the optimum dose and route of administration (bolus or continuous) are uncertain"[2]. This is probably because the real-time assessment (and monitoring) capabilities of fillings pressures at patient's bedside are limited. The estimation of the CVP by LS finds tis place in this context.

Limits

To allow quantitative estimation of a correlation between LS and CVP (Eq. 3), we must have a population with a "healthy" liver. As we know that the LS varies with the variations of hepatic tissue characteristics, the change in LS (and therefore CVP) needs to be explained only by the loading. Despite biological assessments and liver echography, it is difficult to argue that the livers of patients in the study showed no peculiarity.

Three patients presented inconsistent results from the rest of the study population. We believe that this variability is likely due to the liver status of these patients. Despite the fact that the hepatic explorations were unremarkable (biology and liver ultrasound), the two patients having single ventricle physiology and the patient having a systemic syndrome probably suffer from a disturbed liver architecture. More extensive explorations (MRI type or liver histology[37]) would be necessary to ensure the hepatic status of our population.

CONCLUSION

The LS by SWE seems to be the most reliable surrogate of quantitative estimation of the CVP noninvasively in real time. Through this study, we have shown a strong correlation between the LS by SWE and the CVP. This correlation has proven to work whether the CVP increases or decreases.

The LS by SWE could be the tool used by the clinician during his evaluation to estimate the CVP. It would allow him to monitor quantitatively and reliably the CVP, which is a major predictive parameter of adverse events in many patients with a congenital heart disease. Similarly, its uses in relation to acute heart failure as well as its management, need now to be evaluated.

ACKNOWLEDGEMENTS: The authors thank Isabelle Szezepanski and Marine Venot (Necker-Enfants Malades) for their collaboration.

FUNDING: None

COMPETING INTERESTS: Dr. Tanter is cofounder of SuperSonic Imagine.

REFERENCES

1. Yancy CW, Jessup M, Bozkurt B, et al. 2013 ACCF/AHA Guideline for the Management of Heart Failure. *J Am Coll Cardiol*. 2013;62(16):e147-e239.
2. McMurray JJ V, Adamopoulos S, Anker SD, et al. ESC guidelines for the diagnosis and treatment of acute and chronic heart failure 2012: The Task Force for the Diagnosis and Treatment of Acute and Chronic Heart Failure 2012 of the European Society of Cardiology. Developed in collaboration with the Heart. *Eur J Heart Fail*. 2012;14(8):803-69.
3. Allen LA, Felker GM, Pocock S, et al. Liver function abnormalities and outcome in patients with chronic heart failure: data from the Candesartan in Heart Failure: Assessment of Reduction in Mortality and Morbidity (CHARM) program. *Eur J Heart Fail*. 2009;11(2):170-177.
4. Iwamoto Y, Tamai A, Kohno K, Masutani S, Okada N, Senzaki H. Usefulness of Respiratory Variation of Inferior Vena Cava Diameter for Estimation of Elevated Central Venous Pressure in Children With Cardiovascular Disease. *Circ J*. 2011;75(5):1209-1214.
5. Nagueh SF, Kopelen HA, Zoghbi WA. Relation of Mean Right Atrial Pressure to Echocardiographic and Doppler Parameters of Right Atrial and Right Ventricular Function. *Circulation*. 1996;93(6):1160-1169.
6. Foucher J, Chanteloup E, Vergniol J, et al. Diagnosis of cirrhosis by transient elastography (FibroScan): a prospective study. *Gut*. 2006;55(3):403-408.
7. Millonig G, Friedrich S, Adolf S, et al. Liver stiffness is directly influenced by central venous pressure. *J Hepatol*. 2010;52(2):206-210. doi:10.1016/j.jhep.2009.11.018.
8. Taniguchi T, Sakata Y, Ohtani T, et al. Usefulness of transient elastography for noninvasive and reliable estimation of right-sided filling pressure in heart failure. *Am J Cardiol*. 2014;113(3):552-8.

9. Jalal Z, Iriart X, De Lédinghen V, et al. Liver stiffness measurements for evaluation of central venous pressure in congenital heart diseases. *Heart*. 2015;101(18):1499-1504.

10. Stenzel M, Mentzel H-J. Ultrasound elastography and contrast-enhanced ultrasound in infants, children and adolescents. *Eur J Radiol*. 2014;83(9):1560-1569.

11. Gennisson J-L, Grenier N, Combe C, Tanter M. Supersonic Shear Wave Elastography of In Vivo Pig Kidney: Influence of Blood Pressure, Urinary Pressure and Tissue Anisotropy. *Ultrasound Med Biol*. 2012;38(9):1559-1567.

12. Ferraioli G, Filice C, Castera L, et al. WFUMB Guidelines and Recommendations for Clinical Use of Ultrasound Elastography: Part 3: Liver. *Ultrasound Med Biol*. 2015;41(5):1161-79.

13. Rudski LG, Lai WW, Afilalo J, et al. Guidelines for the echocardiographic assessment of the right heart in adults: a report from the American Society of Echocardiography endorsed by the European Association of Echocardiography, a registered branch of the European Society of Cardiology, and t. *J Am Soc Echocardiogr*. 2010;23(7):685-713-8.

14. Nagueh SF, Kopelen HA, Zoghbi WA. Relation of Mean Right Atrial Pressure to Echocardiographic and Doppler Parameters of Right Atrial and Right Ventricular Function. *Circulation*. 1996;93(6):1160-1169.

15. Grubbs FE. Procedures for Detecting Outlying Observations in Samples. *Technometrics*. 1969;11(1):1-21.

16. Glüer C-C, Blake G, Lu Y, Blunt1 BA, Jergas1 M, Genant1 HK. Accurate assessment of precision errors: How to measure the reproducibility of bone densitometry techniques. *Osteoporos Int*. 1995;5(4):262-270.

17. Tugrul M, Camci E, Pembeci K, Al-Darsani A, Telci L. Relationship between peripheral and central venous pressures in different patient positions, catheter sizes, and insertion sites. *J Cardiothorac Vasc Anesth*. 2004;18(4):446-450.

18. Squires RH. Acute liver failure in children. *Semin Liver Dis*. 2008;28(2):153-66.

19. Haddad F, Doyle R, Murphy DJ, Hunt SA. Right ventricular function in cardiovascular disease, part II: pathophysiology, clinical importance, and management of right

ventricular failure. *Circulation*. 2008;117(13):1717-31.

20. Burrows FA, Williams WG, Teoh KH, et al. Myocardial performance after repair of congenital cardiac defects in infants and children. Response to volume loading. *J Thorac Cardiovasc Surg*. 1988;96(4):548-56.

21. Hsu DT, Pearson GD. Heart failure in children: part I: history, etiology, and pathophysiology. *Circ Heart Fail*. 2009;2(1):63-70.

22. Kampmann C, Wiethoff CM, Wenzel A, et al. Normal values of M mode echocardiographic measurements of more than 2000 healthy infants and children in central Europe. *Heart*. 2000;83(6):667-672.

23. De Lorenzo RA, Morris MJ, Williams JB, et al. Does a Simple Bedside Sonographic Measurement of the Inferior Vena Cava Correlate to Central Venous Pressure? *J Emerg Med*. 2012;42(4):429-436.

24. Prekker ME, Scott NL, Hart D, Sprenkle MD, Leatherman JW. Point-of-Care Ultrasound to Estimate Central Venous Pressure. *Crit Care Med*. 2013;41(3):833-841.

25. Babcock DS, Patriquin H, LaFortune M, Dauzat M. Power doppler sonography: basic principles and clinical applications in children. *Pediatr Radiol*. 1996;26(2):109-15.

26. Ommen SR, Nishimura RA, Hurrell DG, Klarich KW. Assessment of Right Atrial Pressure With 2-Dimensional and Doppler Echocardiography: A Simultaneous Catheterization and Echocardiographic Study. *Mayo Clin Proc*. 2000;75(1):24-29.

27. Nir A, Nasser N. Clinical Value of NT-ProBNP and BNP in Pediatric Cardiology. *J Card Fail*. 2005;11(5):S76-S80.

28. Price JF, Thomas AK, Grenier M, et al. B-type natriuretic peptide predicts adverse cardiovascular events in pediatric outpatients with chronic left ventricular systolic dysfunction. *Circulation*. 2006;114(10):1063-9.

29. Aggarwal S, Pettersen MD, Bhambhani K, Gurczynski J, Thomas R, L'Ecuyer T. B-type natriuretic peptide as a marker for cardiac dysfunction in anthracycline-treated children. *Pediatr Blood Cancer*. 2007;49(6):812-816.

30. Lupsor M, Badea R, Stefanescu H, et al. Performance of a new elastographic method

(ARFI technology) compared to unidimensional transient elastography in the noninvasive assessment of chronic hepatitis C. Preliminary results. *J Gastrointestin Liver Dis*. 2009;18(3):303-10.

31. Ferraioli G, Tinelli C, Zicchetti M, et al. Reproducibility of real-time shear wave elastography in the evaluation of liver elasticity. *Eur J Radiol*. 2012;81(11):3102-3106.
32. Ingiliz P, Chhay KP, Munteanu M, et al. Applicability and variability of liver stiffness measurements according to probe position. *World J Gastroenterol*. 2009;15(27):3398-404.
33. Ghaferi AA, Hutchins GM. Progression of liver pathology in patients undergoing the Fontan procedure: Chronic passive congestion, cardiac cirrhosis, hepatic adenoma, and hepatocellular carcinoma. *J Thorac Cardiovasc Surg*. 2005;129(6):1348-1352.
34. Elder RW, McCabe NM, Hebson C, et al. Features of portal hypertension are associated with major adverse events in Fontan patients: The VAST study. *Int J Cardiol*. 2013;168(4):3764-3769.
35. Aboulhosn JA, Lluri G, Gurvitz MZ, et al. Left and Right Ventricular Diastolic Function in Adults With Surgically Repaired Tetralogy of Fallot: A Multi-institutional Study. *Can J Cardiol*. 2013;29(7):866-872.
36. Hsu DT, Pearson GD. Heart Failure in Children: Part II: Diagnosis, Treatment, and Future Directions. *Circ Hear Fail*. 2009;2(5):490-498.
37. Colli A, Cocciolo M, Riva C, et al. Abnormalities of Doppler waveform of the hepatic veins in patients with chronic liver disease: correlation with histologic findings. *AJR Am J Roentgenol*. 1994;162(4):833-7.

FIGURES LEGENDS

Figure 1. Example of evaluation of liver stiffness by shear wave elastography (kPa) with results of central venous pressure (CVP), before and after loading.

Figure 2. Positive and negative variations of liver stiffness and central venous pressures (CVP), before and after loading.

Figure 3. Correlation between liver stiffness and central venous pressure (CVP), pre and post-volume loading

Figure 4. Estimation of the best liver elastography cut-off to estimate a central venous pressure over 10 mmHg, with receiver operating characteristic (ROC) curve.

Figure 5. Correlation between central venous pressure and clinical parameters

TABLES

Table 1. Characteristics of the population

	All patients (n=103)
Age (years)	6.8 ± 5.5 [0.02-18.2]
Sex (M/F)	45 (44%) / 58 (56%)
BMI (kg/m^2)	16.3 ± 2.6 [11.9-25.7]
Congenital heart defect	
- Single ventricle physiology	16
- Pulmonary arterial hypertension	16
- Atrial septal defect	15
- Patent arterial duct	13
- Pulmonary stenosis/atresia with IVS	10
- Pulmonary atresia with VSD	6
- Transposition of the great arteries	4
- Cardiac transplantation	4
- Aortic coarctation	3
- Aortopulmonary window	3
- Tetralogy of Fallot	2
- Common arterial trunk	2
- Anomalous pulmonary venous return	2
- Others (valves diseases, cardiomyopathies, coronary artery diseases, chronic pericarditis)	7
Laboratory characteristics (median [range])	
NT-proBNP level (pg/ml)	248 [10-2810]
AST level (IU/L)	36 [17-83]
ALT level (IU/L)	24 [9-88]
ALP level (IU/L)	216 [60-547]
GGT level (IU/L)	15 [8-224]
Total bilirubine (µmol/L)	7 [2-48]
Prothrombon time (%)	85 [27-126]
Serum protein (g/L)	69 [54-92]
Platelet count (10^3/mm^3)	256 [98-582]
Blood hemoglobin concentration (g/dL)	13.3 [8.5-20.4]
CRP (mg/L)	<0.5 [<0.5-187]
Leucocytes (10^3/mm^3)	7.9 [3.3-17.6]

Results are mean±SD (range).
ALP: alkaline phosphatase level; **ALT:** alanine aminotransferase; **AST:** aspartate aminotransferase ; **BMI:** body mass index ; **CRP:** C-reactive protein ; **GGT:** gamma-glutamyl transpeptidase ; **IVS:** intact ventricular septum ; **NT-proBNP:** N-terminal pro b-type natriuretic peptide ; **VSD:** ventricular septal defect

Table 2. Indications and characteristics of catheterization procedures

	All patients (n=103)
General anesthesia	56 (54%)
Time between [CVP/LS]pre and [CVP/LS]post measurements (minutes)	27 ± 11 [7-89]
Indications of catheterization procedures	
Diagnostic catheterization	40
- Pulmonary arterial hypertension assessment	15
- Preoperative assessment of complex congenital defects	7
- Pre-TCPC assessment	6
- Endomyocardial biopsy	5
- Post-banding hemodynamic catheterization	1
- Others (angiography, coronarography, pre-transplantation, pericardiocentesis)	6
Interventional catheterization	63
- Patent arterial duct closure	14
- Atrial septal defect closure	13
- Pulmonary artery dilatation/stenting	13
- TCPC fenestration closure	11
- Aortopulmonary window closure	3
- Pulmonary artery banding dilatation	2
- Transcatheter pulmonary valve replacement	2
- Aortic coarctation stenting	1
- Fontan fenestration enlargement	1
- Superior caval vein stenting	1
- Coronary artery fistulas embolization	1
- Aorto-pulmonary collateral vessels embolization	1

Results are median±SD (range).
CVP: central venous pressure; **LS:** liver stiffness; **TCPC:** total cavopulmonary connection

Table 3. Hemodynamics, IVC, Doppler and LS Parameters

	Before Loading	**After Loading**	P Value
Hemodynamics			
CVP (mmHg)	7.4±2.9 [3-16]	10±3.3 [3-18]	**< 0.0001**
RVP (mmHg)	51±32 [16-137]	74±37 [22-135]	**0.01**
mPAP (mmHg)	17.5±22.2 [9-105]	22.8±21.4 [11-109]	**0.02**
Heart rate (bpm)	108±25 [44-171]	113±22 [47-169]	0.34
SBP (mmHg)	92±19 [49-189]	97±20 [57-191]	0.21
DBP (mmHg)	53±13 [29-92]	54±13 [28-94]	0.82
Inferior Vena Cava			
Maximal Diameter (mm)	9±4 [3-20]	10±6 [3-20]	0.60
Minimal Diameter (mm)	4±4 [0-17]	5±3 [0-18]	0.16
Collapses (%)	61±31 [8-100]	55±28 [7-100]	0.12
Hepatic vein flow			
Vs, cm/s	32±19 [7-109]	30 ±14 [6-69]	0.62
Vd, cm/s	26±15 [6-95]	34±18 [9-102]	**0.001**
Var, cm/s	21±12 [6-69]	24±13 [7-60]	0.38
Vs/(Vs+Vd)	0.53±0.13 [0.26-0.75]	0.46±0.12 [0.2-0.75]	**0.001**
Liver Stiffness, kPa	9.0±5.8 [4–46.1]	14.4±9.1 [4.3-72]	**< 0.0001**

Results are mean±SD (range).
bpm: beats per minute; **SBP:** systolic blood pressure; **DBP:** diastolic blood pressure; **LS:** liver stiffness; **mPAS:** mean pulmonary artery systolic pressure; **Vs, Vd, and Var:** maximal velocities of the systolic, diastolic, and atrial reversal waves, respectively.

Table 4. Outliers. Three patients.

	Patient 1	**Patient 2**	**Patient 3**
Sex	M	M	M
Age (years old)	8.4	10	14
BMI	16.4	18	19.4
Heart	Single ventricle physiology	Single ventricle physiology	Chronic pericarditis (CACP syndrome)
Indications of catheterization procedures	Fontan fenestration closure	Fontan fenestration closure	Pericardiocentesis + Hemodynamic exploration
Time between [CVP/LS]pre and [CVP/LS]post measurements (minutes)	62	51	22
LS pre (kPa)	8.4	46.1	24.8
CVP pre (mmHg)	7	12	8
IVC collapse (%) pre	20	26.6	20
Vs/(Vs+Vd) pre	0.44	0.46	0.36
LS post (kPa)	39.8	72	29
CVP post (mmHg)	13	13	11
IVC collapse (%) post	10	15.4	25
Vs/(Vs+Vd) post	0.59	0.32	0.40

BMI: body mass index; **CACP syndrome:** camptodactyly-arthropathy-coxa vara-pericarditis syndrome; **CVP:** central venous pressure; **IVC:** inferior vena cava; **LS:** liver stiffness; **Vs,** and **Vd:** maximal velocities of the systolic, and diastolic, respectively.

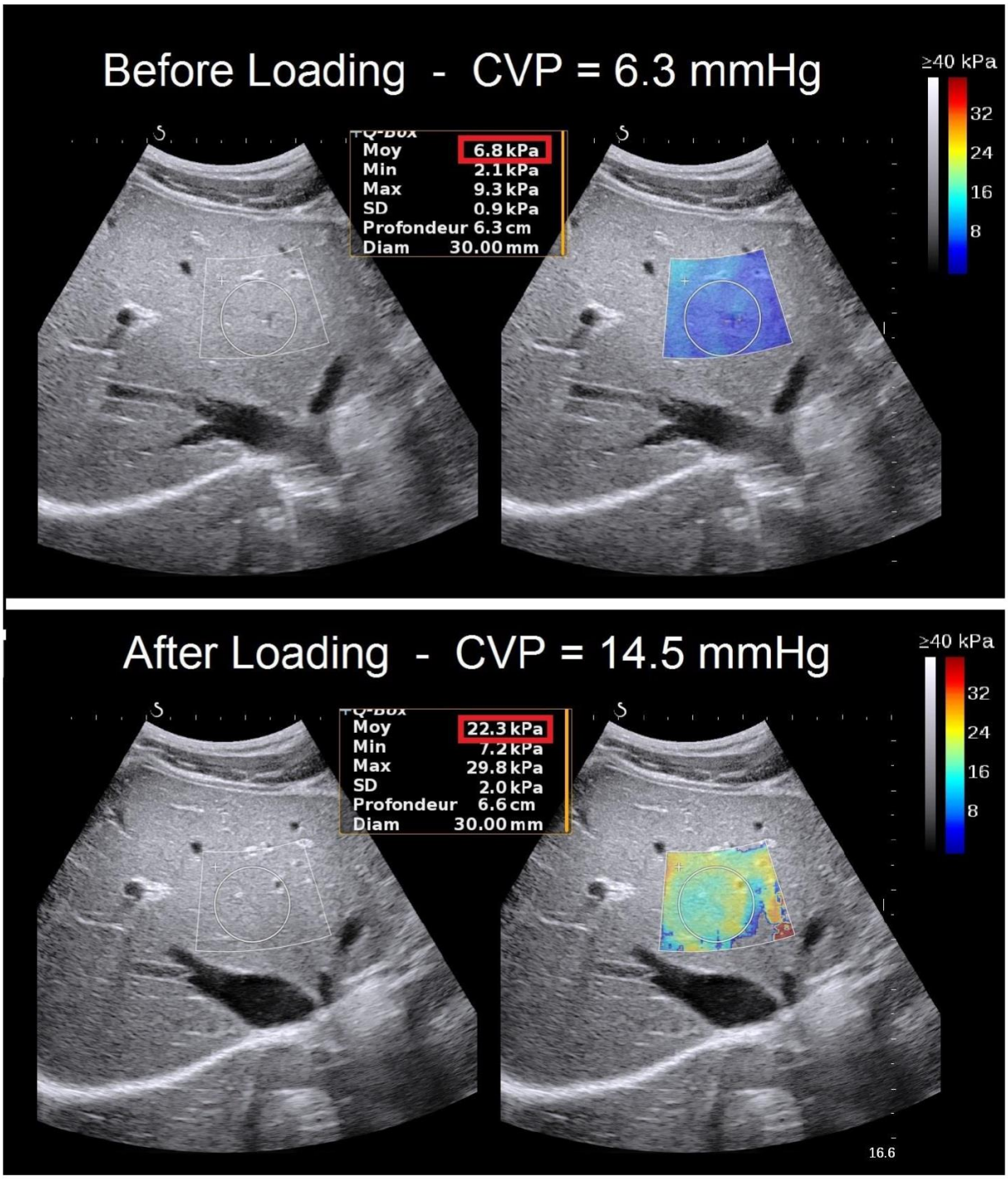
Before Loading - CVP = 6.3 mmHg
≥40 kPa
32
24
16
8
Moy 6.8 kPa
Min 2.1 kPa
Max 9.3 kPa
SD 0.9 kPa
Profondeur 6.3 cm
Diam 30.00 mm
After Loading - CVP = 14.5 mmHg
≥40 kPa
32
24
16
8
Moy 22.3 kPa
Min 7.2 kPa
Max 29.8 kPa
SD 2.0 kPa
Profondeur 6.6 cm
Diam 30.00 mm
16.6

Figure 1

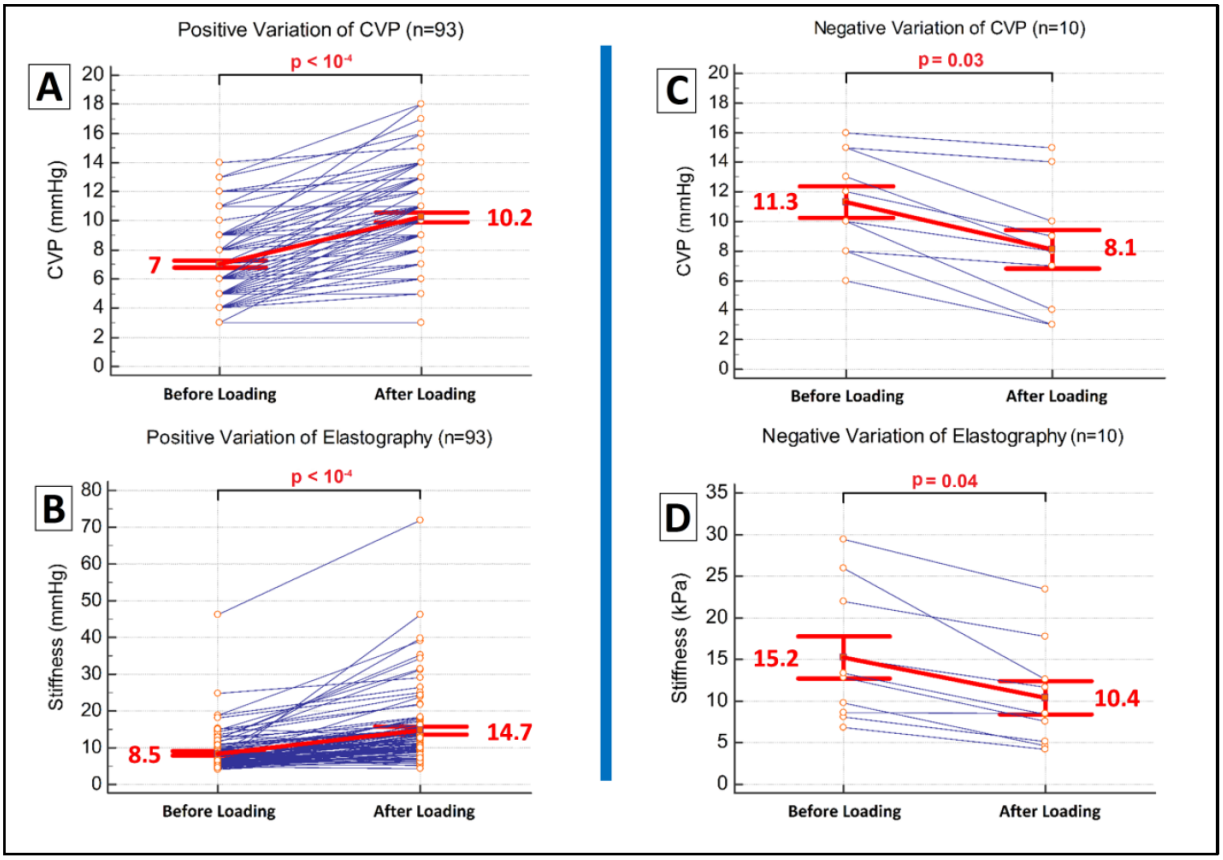
Positive Variation of CVP (n=93)
A
p < 10⁻⁴
CVP (mmHg)
7
10.2
Before Loading
After Loading
Positive Variation of Elastography (n=93)
B
p < 10⁻⁴
Stiffness (mmHg)
8.5
14.7
Before Loading
After Loading
Negative Variation of CVP (n=10)
C
p = 0.03
CVP (mmHg)
11.3
8.1
Before Loading
After Loading
Negative Variation of Elastography (n=10)
D
p = 0.04
Stiffness (kPa)
15.2
10.4
Before Loading
After Loading

Figure 2

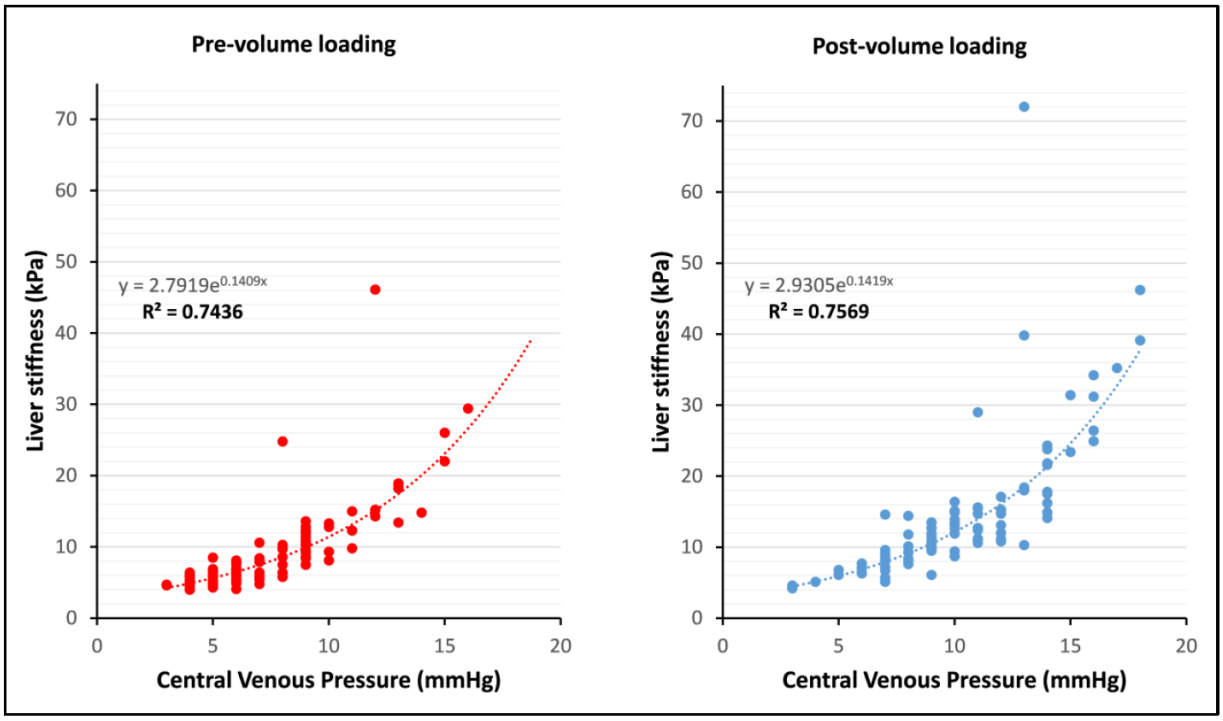
Pre-volume loading
Liver stiffness (kPa)
Central Venous Pressure (mmHg)
y = 2.7919e^0.1409x
R² = 0.7436
Post-volume loading
Liver stiffness (kPa)
Central Venous Pressure (mmHg)
y = 2.9305e^0.1419x
R² = 0.7569

Figure 3

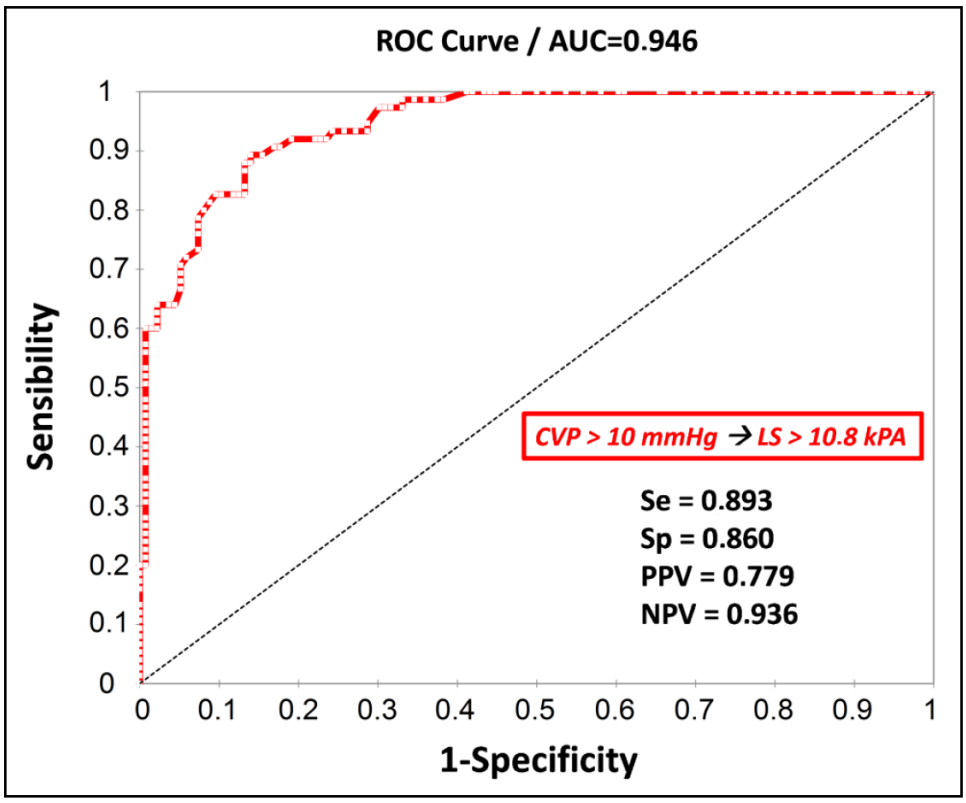
ROC Curve / AUC=0.946
Sensibility
1
0.9
0.8
0.7
0.6
0.5
0.4
0.3
0.2
0.1
0
0
0.1
0.2
0.3
0.4
0.5
0.6
0.7
0.8
0.9
1
1-Specificity
CVP > 10 mmHg → LS > 10.8 kPA
Se = 0.893
Sp = 0.860
PPV = 0.779
NPV = 0.936

Figure 4

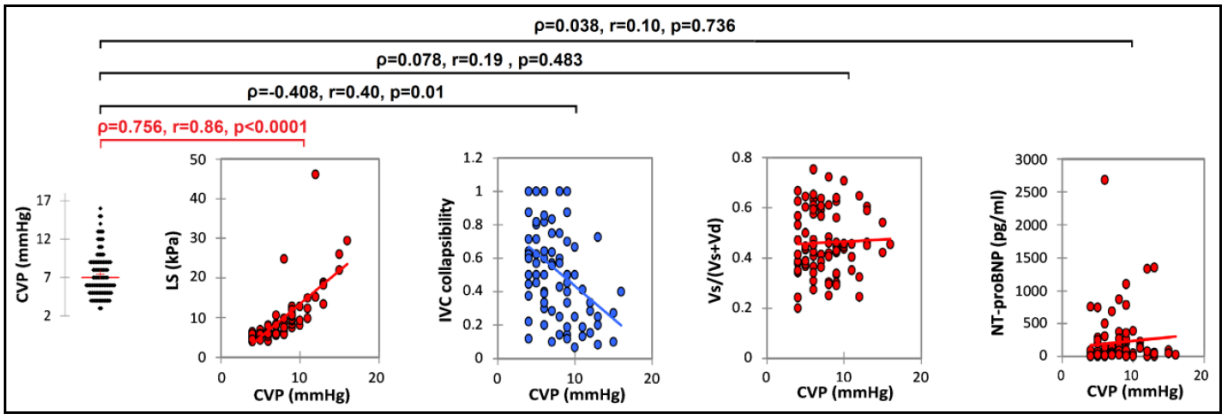
ρ=0.038, r=0.10, p=0.736
ρ=0.078, r=0.19 , p=0.483
ρ=-0.408, r=0.40, p=0.01
ρ=0.756, r=0.86, p<0.0001
CVP (mmHg)
LS (kPa)
IVC collapsibility
Vs/(Vs+Vd)
NT-proBNP (pg/ml)
CVP (mmHg)

Figure 5

3.3. Perspectives

En comparaison de l'élastographie myocardique, l'élastographie hépatique par SWE a cette chance d'être disponible en pratique clinique courante. Ce n'est pas de la recherche fondamentale, les outils (machine d'échographie et sondes) ont le marquage CE.

A la lumière des résultats présentés dans ce travail, l'élastographie hépatique par SWE semble être un outil très fiable et reproductible pour estimer la PVC de manière quantitative et de manière non invasive. De plus, l'évolution en temps réel de cette estimation permet d'imaginer des applications en aigu comme en chronique.

De nombreuses situations cliniques semblent être intéressantes à explorer, notamment en cardiologie pédiatrique et congénitale. Les maladies du cœur droit et leur management (maladie d'Ebstein, dysplasie valvulaire tricuspide, atrésie pulmonaire en stratégie biventriculaire, tétralogie de Fallot réparé avec anneau fendu à titre d'exemples) manquent d'outil non invasif pour estimer les pressions de remplissage du cœur droit. Les cardiomyopathies avec atteinte biventriculaire (dilatée, restrictive, hypertrophique) ainsi que la gestion de leur décompensation aigue pourraient également être une belle population trouvant un intérêt à une application clinique. Enfin, l'ajout de l'élastographie hépatique dans le suivi à long terme des HTAP et l'évaluation de la fonction ventriculaire droite dans ces situations pourraient apporter une valeur ajoutée.

A l'heure actuelle, nous explorons une autre application dans le service de cardiologie pédiatrique à l'hôpital Necker-Enfants malades : l'estimation de pressions pulmonaires dans le montage univentriculaire type Fontan. En effet, une des stratégies chirurgicales visant à augmenter l'espérance de vie de ces cardiopathies très sévères consiste à connecter directement les veines caves aux artères pulmonaires, afin de perfuser les poumons sans utiliser la pompe cardiaque. En définitive, la pression dans les veines caves est égale aux pressions dans les artères pulmonaires. Donc, selon les résultats de notre étude, la rigidité hépatique serait le reflet direct des pressions pulmonaires, qui sont un facteur essentiel de bonne tolérance du montage chirurgical. Les inclusions de ces patients dans une étude prospective sont actuellement en cours, et l'analyse ainsi que l'interprétation de des résultats seront dans la continuité de l'étude "*Towards non-invasive assessment of central venous pressure using real time and quantitative liver stiffness estimation"* (Villemain et al. 2017).

Malgré tout, une des limites encore importante à l'application clinique « tout venant » de cette estimation non invasive de la PVC concerne l'état sous-jacent du foie. Dans notre

étude, nous avons sélectionné une population de patients n'ayant aucun facteur favorisant une anomalie constitutionnelle ou acquise du parenchyme hépatique. Le but était d'éviter ce biais dans la corrélation entre rigidité hépatique et PVC. Lors d'une évaluation clinique d'un patient, il est parfois difficile d'être convaincu de l'absence de pathologie hépatique intrinsèque, qui pourrait modifier le résultat d'élastographie. Il reste donc des travaux à réaliser pour essayer de caractériser la différence entre une élévation de rigidité hépatique exclusivement due à une congestion avec une élévation en partie (ou totalement due) à une atteinte tissulaire du foie. Des analyses multiparamètriques (IRM hépatique, ERM [elastographie par IRM], TDM hépatique + élastographie par SWE) pourraient être intéressantes à explorer.

4. Imagerie des fibres myocardiques par ultrasons

4.1. Introduction et Objectifs

Dans le chapitre 2 de cette thèse, nous avons introduit l'élastographie cardiaque par onde de cisaillement et ses résultats dans trois essais cliniques. Nous avons pu observer qu'en fonction de la coupe échographique, des vitesses d'onde de cisaillement différentes seront mesurées (cf paragraphes 2.3.2 et 2.4.2). C'est essentiellement dû à l'architecture des fibres cardiaques, et à l'anisotropie du myocarde. Le muscle cardiaque humain est en effet un réseau tridimensionnel complexe de fibres élastiques organisées. Le muscle cardiaque est donc un tissu élastique anisotrope, dont les propriétés physiques changent selon les différents axes d'observation, mais également au cours du temps, avec la contraction cardiaque. L'arrangement des fibres est spécifique et directement lié aux propriétés électriques et mécaniques du cœur. Des changements d'architecture des fibres cardiaques et de rigidité peuvent se produire dans de nombreuses maladies cardiaques, et l'évaluation de ces modifications ainsi que leur compréhension de manière non invasive et en temps réel pourraient donc améliorer le diagnostic et le traitement de ces maladies.

Différentes techniques ont été développées, principalement basées sur l'IRM ou l'optique, mais aussi sur les ultrasons pour évaluer la rigidité et/ou l'anisotropie du tissu cardiaque. Comme nous l'avons souligné précédemment, l'imagerie par ultrasons est l'une des principales modalités utilisées en pratique clinique, et plus particulièrement pour l'imagerie cardiaque. Le développement de techniques ultrasonores pour l'évaluation de la rigidité et l'anisotropie cardiaque est donc extrêmement intéressant.

L'orientation des fibres myocardiques est liée aux propriétés mécaniques et électriques du cœur et son étude permettrait de mieux comprendre le développement de pathologies cardiaques. A l'heure actuelle, il n'existe pas de modalités d'imagerie clinique permettant de cartographier l'orientation des fibres cardiaques. Dans l'étude finalisée et présentée ci-dessous, des images du myocarde d'un volontaire sain ont été réalisées par imagerie du tenseur de rétrodiffusion ultrasonore (BTI : Backscatter Tensor Imaging), une nouvelle technologie d'imagerie par ultrasons en 3D qui permet de cartographier les fibres myocardiques en analysant la cohérence spatiale des échos rétrodiffusés à haute cadence d'imagerie. Les applications à l'imagerie de tissus *ex-vivo* de porcs et sur cœur battant de volontaires sains sont présentées.

4.2. Manuscrit "*Imaging the dynamics of cardiac fiber orientation in vivo using 3D Ultrasound Backscatter Tensor Imaging*"

Cette étude a été publiée dans Scientific Reports en 2017 (Papadacci et al. 2017).

SCIENTIFIC REPORTS

OPEN

Imaging the dynamics of cardiac fiber orientation in vivo using 3D Ultrasound Backscatter Tensor Imaging

Received: 3 November 2016
Accepted: 20 March 2017
Published online: 11 April 2017

Clement Papadacci[1], Victor Finel[1], Jean Provost[1], Olivier Villemain[1], Patrick Bruneval[2], Jean-Luc Gennisson[1], Mickael Tanter[1], Mathias Fink[1] & Mathieu Pernot[1]

The assessment of myocardial fiber disarray is of major interest for the study of the progression of myocardial disease. However, time-resolved imaging of the myocardial structure remains unavailable in clinical practice. In this study, we introduce 3D Backscatter Tensor Imaging (3D-BTI), an entirely novel ultrasound-based imaging technique that can map the myocardial fibers orientation and its dynamics with a temporal resolution of 10 ms during a single cardiac cycle, non-invasively and *in vivo* in entire volumes. 3D-BTI is based on ultrafast volumetric ultrasound acquisitions, which are used to quantify the spatial coherence of backscattered echoes at each point of the volume. The capability of 3D-BTI to map the fibers orientation was evaluated *in vitro* in 5 myocardial samples. The helicoidal transmural variation of fiber angles was in good agreement with the one obtained by histological analysis. 3D-BTI was then performed to map the fiber orientation dynamics *in vivo* in the beating heart of an open-chest sheep at a volume rate of 90 volumes/s. Finally, the clinical feasibility of 3D-BTI was shown on a healthy volunteer. These initial results indicate that 3D-BTI could become a fully non-invasive technique to assess myocardial disarray at the bedside of patients.

The myocardial fibers architecture plays a major role in the cardiac function. Fibers orientations vary continuously and smoothly through myocardial walls[1] and this complex organization is closely linked to the mechanical and electrical myocardial function[2–4]. For instance, the helicoidal fiber distribution in the left ventricular walls contributes to the torsional motion of the heart during the ejection phase, which is believed to improve the heart's pumping efficiency[5,6]. The fibers of the heart are also related to its electromechanical properties[7–10]; indeed, the electrical activation propagates preferentially in the direction of myocardial fibers and results in their synchronous contraction. Myocardial fiber disarray is thought to appear in the early stage of many pathologies such as in cardiomyopathies or in fibrosis[11]. The mapping of the fiber architecture, on the one hand, could increase our knowledge of the cardiac function[12], and on the other hand, could potentially enable early diagnosis of cardiomyopathies. Yet, no method to map the fiber architecture is currently used on a regular basis for clinical purposes.

Magnetic Resonance Diffusion Tensor Imaging (MR-DTI)[13,14] is widely used for mapping the structural connectivity of the human brain. However, its application to the heart, while feasible in animals[15] and humans[16], remains challenging *in vivo* due to limited frame rates (and hence long acquisition times) and limited robustness of the MR-DTI signals to tissue motion[11,15,16]. Optical methods such as optical coherence tomography[17] and two-photon microtomy[18] can also map the fiber directions at the microscopic level but remain limited to superficial *ex vivo* tissue and to small regions of interest. In ultrasound imaging, several methods have been proposed to quantify the anisotropy of various physical parameters linked to the fiber orientation, including the ultrasonic attenuation[19,20], the integrated backscattered intensity[19–22] and the myocardial stiffness using Elastic Tensor Imaging (ETI)[23]. However, none of these methods has been yet implemented for the time-resolved, 3D mapping of the myocardial fibers orientation.

[1]Institut Langevin, ESPCI ParisTech, CNRS UMR 7587, INSERM U979, 17 rue Moreau, 75012, Paris, France. [2]Department of Pathology, Hôpital Européen Georges Pompidou, 21, rue Leblanc, 75015, Paris, France. Clement Papadacci and Victor Finel contributed equally to this work. Correspondence and requests for materials should be addressed to M.P. (email: mathieu.pernot@inserm.fr)

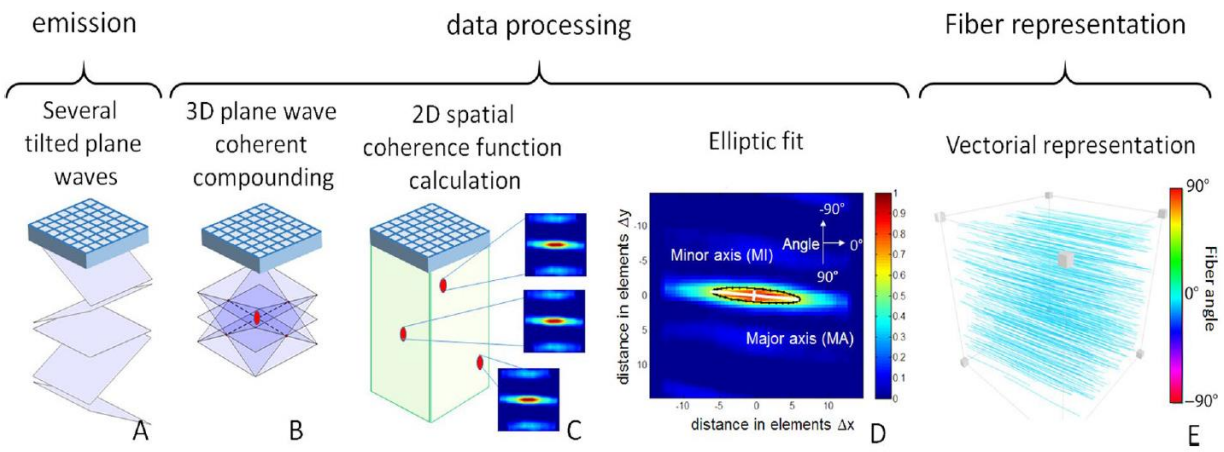

Figure 1. 3D-BTI principle. (**A**) Tilted plane waves are emitted and the associated backscattered echoes are recorded. (**B**) Coherent compounding is applied in postprocessing to synthetically generate voxel-specific focal zones. (**C**) The 2D spatial coherence function is calculated for each voxel and (**D**) an elliptic fit is applied to determine the fibers orientation. (**E**) A vector representation is then achieved to display the fibers orientation in 3D.

In this paper, an entirely novel ultrasound-based imaging technique called Backscatter Tensor Imaging (3D-BTI) is described and evaluated *in vivo* with respect to its capability of mapping the myocardial fibers orientation and its time-resolved dynamics during an entire cardiac cycle. 3D-BTI is based on ultrafast volumetric ultrasound acquisitions, which are used to quantify the spatial coherence of backscattered echoes at each point of the imaged volume at a rate of 90 volumes/s. Spatial coherence is a physical property of backscattered waves that depends on the distribution of scatterers at the subwavelength scale. Ultrasonic spatial coherence has thus the capability to provide statistical information on the tissue microstructure at a scale far below the resolution of ultrasound images. In 3D-BTI, the anisotropy of spatial coherence is analyzed on a 2D matrix probe in order to derive its principal directions and derive the fibers orientation. The link between the anisotropy of spatial coherence and the fibers orientation was previously demonstrated in composite materials and in fibrous soft tissues such as the myocardium and the skeletal muscle[24, 25].

Another key aspect of 3D-BTI is the use of volumetric ultrafast plane wave imaging. We recently developed a 3D fully programmable ultrasound system for volumetric ultrafast plane wave imaging achieving volume rates of up to 5000 volumes/s[26]. By coherent compounding of the backscattered echoes associated with tilted plane wave emissions, the spatial coherence and thus the fibers orientation can be obtained simultaneously in each voxel of the volume at high volume rate.

3D-BTI is hereby found to be capable of mapping the transmural fibers orientation in a beating heart. For the purpose of this validation study, 3D-BTI was compared to histological analysis on *ex vivo* explanted myocardial tissues. An excellent agreement on the transmural fiber orientation was found between 3D-BTI and histology. The *in vivo* feasibility of 3D-BTI on a beating heart was then demonstrated in an open chest ovine model. Finally, transthoracic imaging was performed on a healthy volunteer to show the clinical feasibility of 3D-BTI. To our knowledge, it is the first time that the dynamics of the myocardial fibers are observed non-invasively over an entire cardiac cycle of a single heartbeat in humans.

Results

The general principle of 3D-BTI is illustrated in Fig. 1. First, tilted plane waves (Fig. 1A) are emitted from a 2D matrix array probe connected to a customized, programmable, ultrasound system[26]. For each emitted plane wave, the backscattered echoes received by each element of the matrix probe are recorded and further processed using 3D plane-wave coherent compounding to synthetically generate a voxel-specific focal region (Fig. 1B). The spatial coherence associated to each focal region is then computed at each point of the 3D volume (Fig. 1C) and used to determine the fiber orientation by applying an elliptic fit (Fig. 1D). Finally, a vector representation is used for the visualization of fibers in 3D space (i.e. Fig. 1E).

***Ex vivo* experiments.** To establish the accuracy and precision of 3D-BTI, myocardial samples explanted from the anterior wall of the left ventricle of a porcine heart were imaged using 3D-BTI and further analyzed by histology. Figure 2A shows the 3D grayscale ultrasound image of one myocardial sample and three examples of spatial coherence functions obtained at different depths (Fig. 2B,C,D). At each location, the spatial coherence presents a strong anisotropy with a principal direction that varies with depth. The vector representation (Fig. 2F) of the entire volume shows that fiber orientation varies across the wall. Fiber orientation was found to vary gradually through the ventricular wall, which is consistent with the literature[1]. The transmural orientation was averaged over the volume for the 5 myocardial samples and was found to vary continuously through the wall with an average difference of $98.6° \pm 8.9°$ between endocardium and epicardium. These results were compared against the fiber orientation obtained from histological analysis. Figure 3A and B shows a representative sample studied with both histology and 3D-BTI. Figure 3C shows a Bland-Altman analysis applied to all five samples of this study. A bias of 0.33 degrees and 95-% limits of agreement equal to $-10.1°$ and $10.7°$ were found.

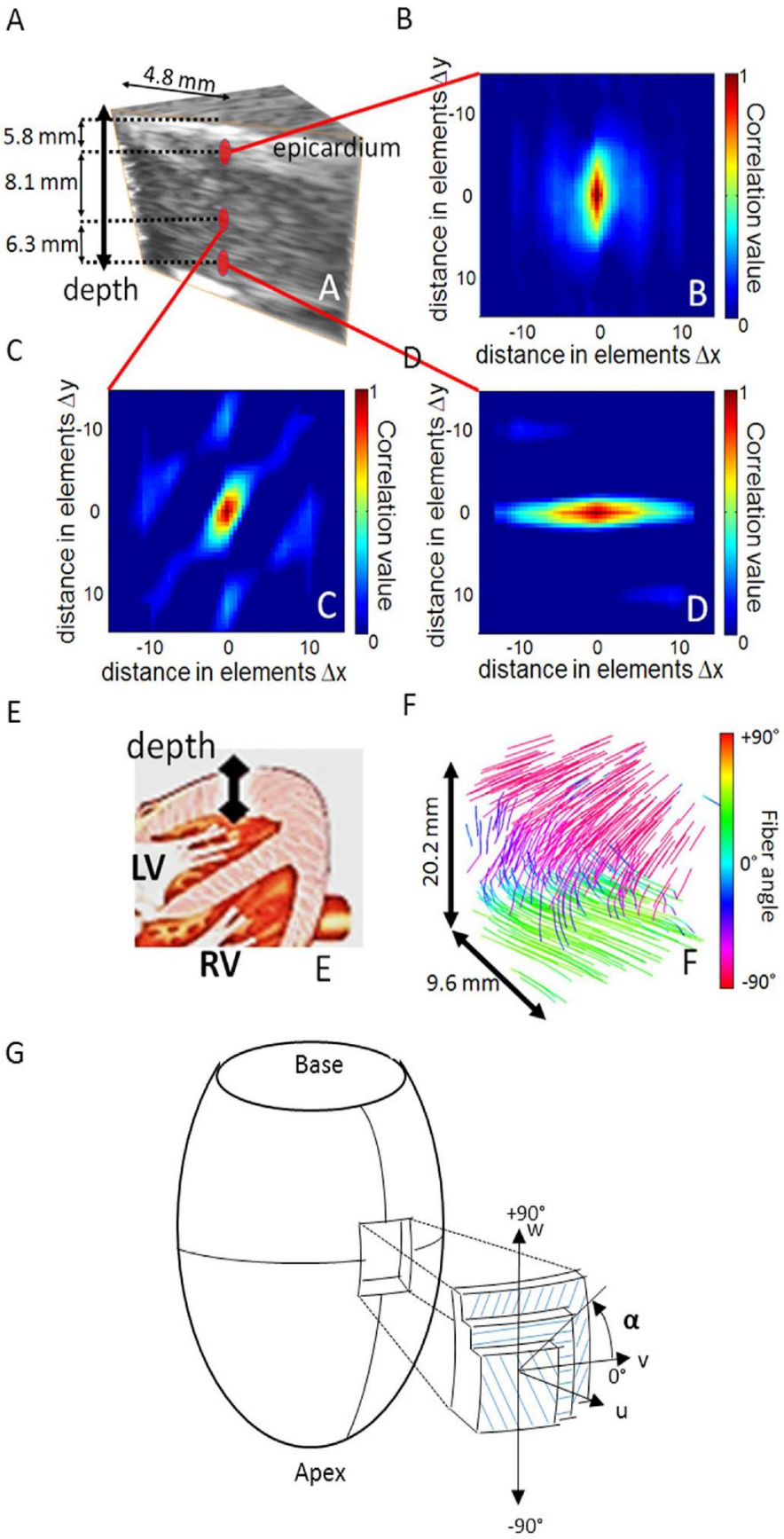

Figure 2. 3D-BTI of one *ex vivo* porcine myocardial sample. (**A**) 3D grayscale ultrasound image of one myocardial sample. (**B**,**C**,**D**) Three examples of spatial coherence functions obtained for different depth locations in the sample. (**E**) Drawing of the heart associated to the ultrasound acquisition location. (**F**) Vector representation used for the visualization of the transmural variation of the fibers in the entire sample. (**G**) Schematic representation of the reference coordinates. Local axes u, v and w are defined by the circumferential and longitudinal directions on the epicardial surface. Fiber angle α, is positive when measured counterclockwise from the v-axis. (Figure adapted from Streeter *et al.*[27]).

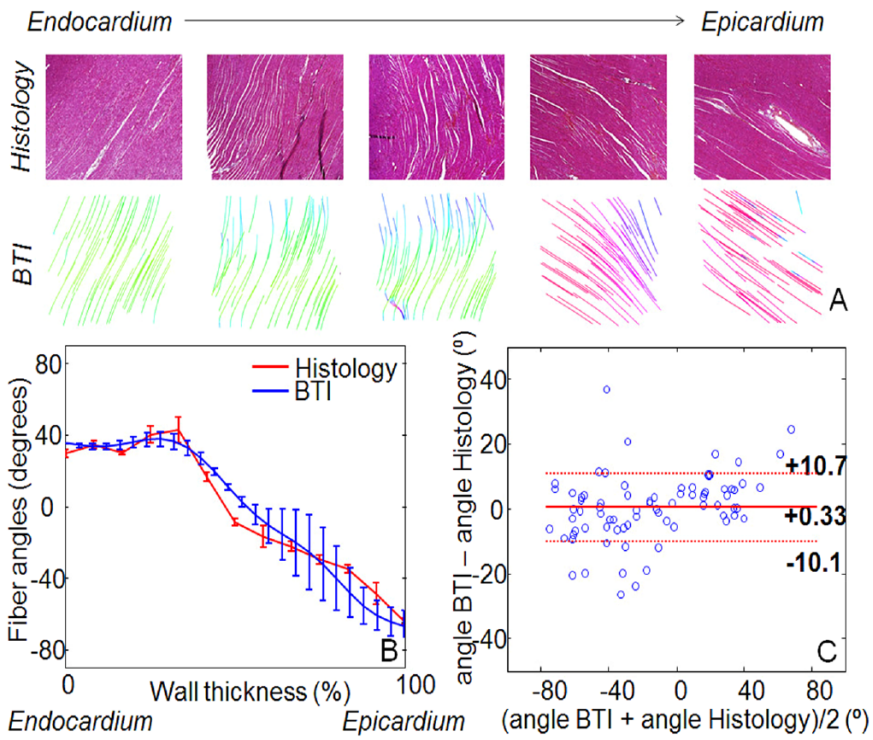

Figure 3. 3D-BTI validation against histology. (**A**) Five histological slices (20X) and associated BTI slices of a left ventricle myocardial sample highlights the transmural angle variation of the fibers. (**B**) An example of the fiber angles variation assessed with histology and with 3D-BTI through the wall thickness (0% endocardium – 100% Epicardium) for the same sample is displayed. (**C**) Bland-Altman plot of the transmural fiber angles estimated by 3D-BTI and histology (n = 5 myocardium samples).

***In vivo* open chest experiments.** The *in vivo* feasibility of 3D-BTI was demonstrated in the beating heart of an open chest sheep. 3D-BTI acquisitions were performed during a complete single cardiac cycle with a volume rate of 90 volumes/s. Figure 4 shows examples of fiber reconstruction at specific times of the cardiac cycle (A Late Diastole, B Early Systole, C Late Systole, D Early Diastole). It demonstrates the feasibility of following the fiber orientation during an entire cardiac cycle at high frame rate (the complete cine-loop is shown in Supplemental Movie 1). The transmural fiber distribution at one location as a function of time is shown in Fig. 5. Fiber angles were found to vary as a function of depth with an absolute difference of 96° from the epicardium to the endocardium.

***In vivo* transthoracic BTI of the human heart.** Finally, the feasibility of 3D-BTI on the human heart was shown on a healthy volunteer in a realistic clinical transthoracic imaging setting. Transthoracic conventional gray-scale imaging was used to position the probe on the parasternal view. 3D-BTI was then performed with a total imaging depth of 60 mm. Figure 6 shows the helicoidal fiber distribution imaged in the left ventricle anterior wall at mid-level both in systole and in diastole. Fiber angles were found to vary transmurally with an absolute difference of 104 ± 9° from the epicardium to the endocardium.

Discussion

In this study, we have introduced 3D-BTI, a novel ultrasound-based technique for the mapping of the fibers orientation in myocardial tissues. The objectives were to determine the accuracy and precision of 3D-BTI in mapping the fibers structure and to demonstrate its feasibility on beating hearts. The accuracy and precision of 3D-BTI were validated in 5 *ex vivo* porcine left ventricular myocardial samples. The fibers angles distribution of each sample was obtained within volumes of 3 cm^3 and the transmural angle variations of each sample were compared to histology. An excellent agreement was found against histology, therefore demonstrating the accuracy and precision of 3D-BTI.

The *in vivo* feasibility of 3D-BTI was then demonstrated in a beating sheep heart. The fibers distribution of the left ventricular free wall was successfully imaged during one entire cardiac cycle at a volume rate of 90 volumes/s. To our knowledge, this is the first time that the dynamics of the myocardial fibers were mapped during an entire cardiac cycle at high frame rate. The transmural fiber variation was found to be 96° in diastole and did not change significantly during the systolic phase despite a 56% increase in wall thickness. This small variation over the cardiac cycle confirms the results of several studies that have investigated the fibers orientation in diastole and in systole using histology[27]. Finally, the feasibility of BTI in a realistic clinical transthoracic imaging setup was shown on a healthy volunteer and allowed for the mapping of the myocardial fibers orientation of the human heart both in systole and in diastole.

3D-BTI could not only bring new insights in the knowledge of the cardiac mechanics but it could also become a major tool to non-invasively detect fiber disorders linked to cardiac diseases in early stages. Myocardial fiber

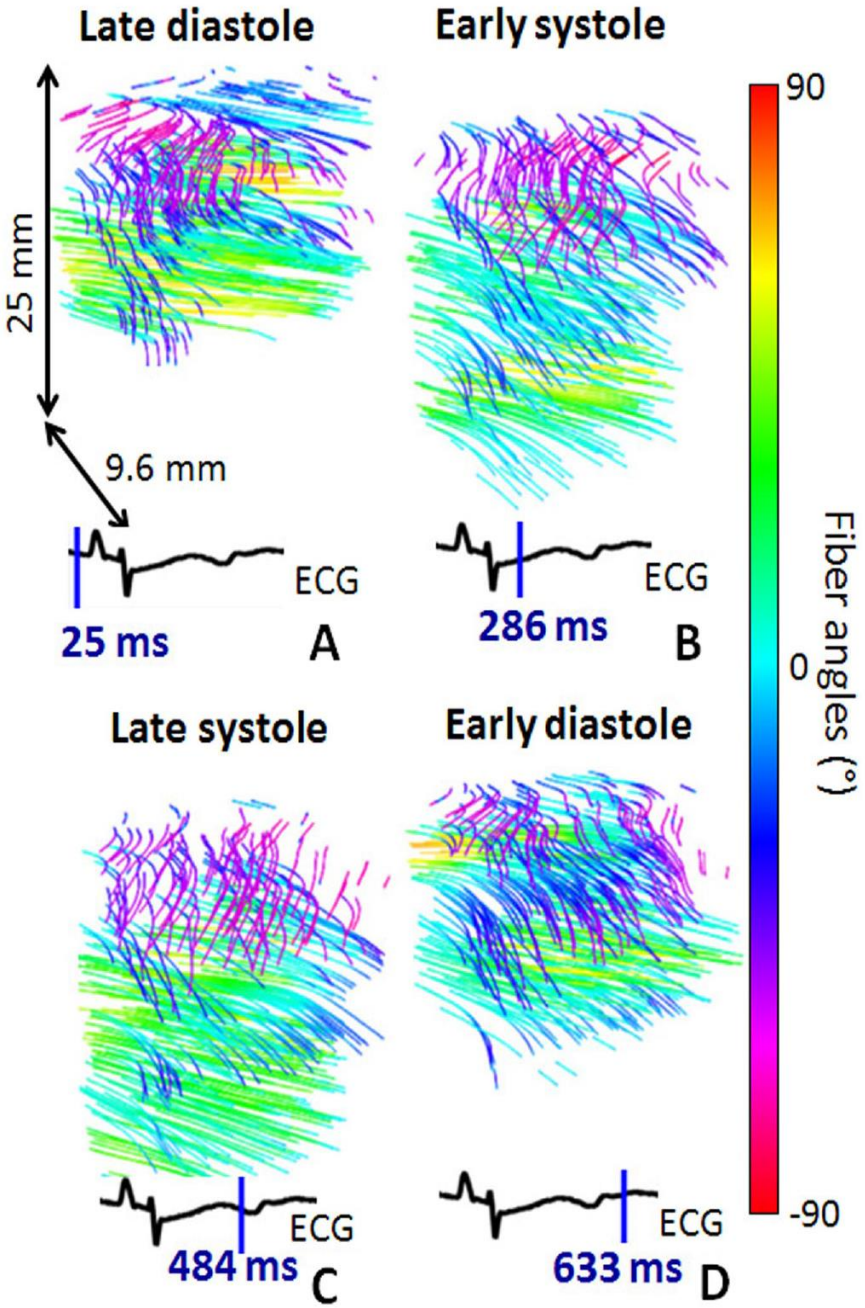

Figure 4. *In vivo* 3D-BTI. 3D representation of fibers orientation in the left ventricle of an open-chest sheep at four different moments of the cardiac cycle (i.e. (**A**) Late Diastole, (**B**) Early Systole, (**C**) Late Systole, (**D**) Early Diastole).

disarray has been shown in post-infarct remodeling of the left ventricle as well as in hypertrophic cardiomyopathy. 3D-BTI may be used to quantify disarray in the fiber angles but also to map the fractional anisotropy in order to quantify collagen infiltration and fibrosis content. Fractional anisotropy provides a measure of the level of anisotropy and can be obtained using the coherence values along and across the fibers.

3D-BTI presents a number of advantages as it can be performed non-invasively at high frame rate, and *in vivo* in beating hearts. In contrast to shear wave imaging based techniques, 3D-BTI is based on low energy emissions and thus can be performed continuously to provide the complete description of the fiber dynamics at high frame rate. Moreover, while the present study focused on the use of plane waves for the generation of synthetic foci, diverging waves[28, 29], which can achieve even larger fields of view and image the entire heart in 3D[26], could also be used to improve 3D-BTI. The use of diverging waves would, however, result in a non-uniform spatial resolution. This is a limitation that needs to be evaluated in more detail.

3D-BTI is robust to motion as a result of the use of ultrafast volumetric acquisitions, which enabled the mapping of the coherence functions in entire 3D volumes using a limited number of transmits. For example, while 49 plane wave emissions were sufficient to perform 3D-BTI in each voxel, performing the equivalent acquisition using standard focusing would have required 64*64*500 emissions, which would corresponds to a few minutes per volume instead of a few milliseconds in the case of plane wave imaging.

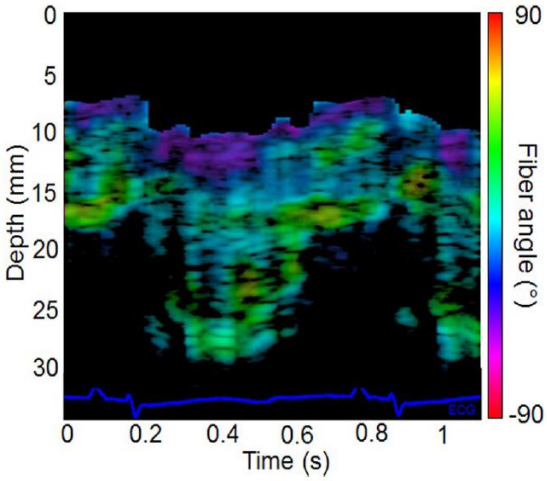

Figure 5. Fiber orientation temporal variation. *In vivo* fiber angle variation in the left ventricular wall within a cardiac cycle as a function of depth and time. The color scale represents the value of the fiber angle superimposed onto a standard M-mode of the left ventricle. The associated ECG is displayed at the bottom of the figure.

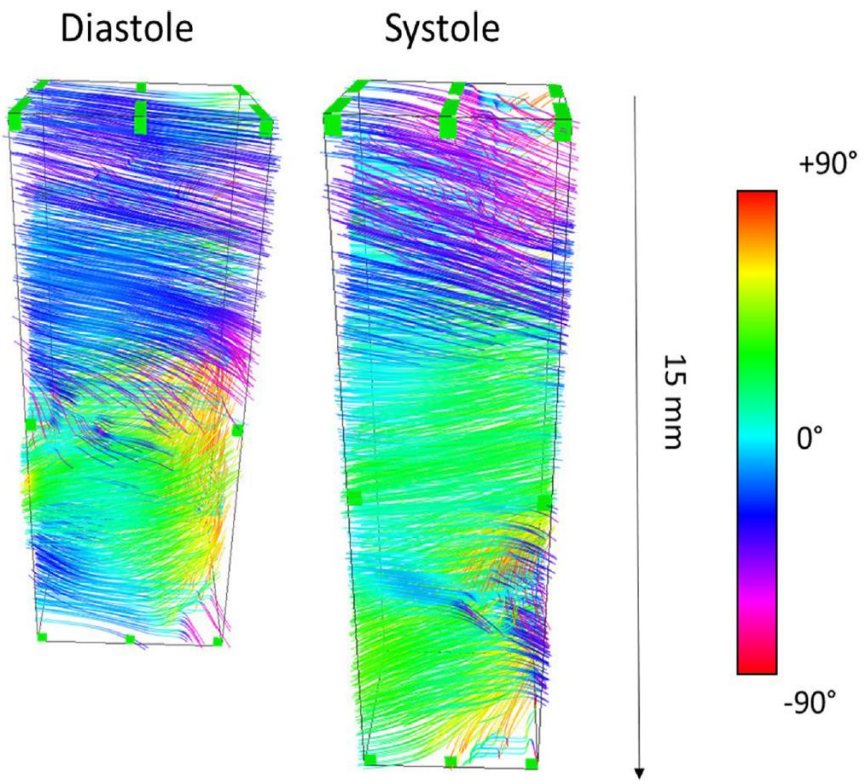

Figure 6. Transthoracic imaging of myocardial fiber orientation in the human heart. The fiber orientations of the antero-septal LV wall is shown in end-diastole and end-systole.

One of the current limitations of 3D-BTI is its incapability to map the z component of the fiber direction. Despite this limitation, mapping of fiber directions remains possible in anisotropic soft tissues in which the fibers are parallel to the 2D array plane, which is the case for the skeletal muscle or the anterior wall of the myocardium in standard parasternal short and long axis views. However, to apply 3D-BTI to other tissues in which structures can be oriented along the z-axis in sagittal and coronal views, tilted synthetic foci would be required. This could be achieved using subapertures in reception[30], which is the object of on-going work in our group. Moreover, while the ultrasound acquisitions required to perform 3D-BTI are very short (~10 ms), postprocessing operations required up to twenty minutes to achieve the vectorial representation of a full volume. Further optimization of the algorithms along with the rapid growth of computational power of video cards and processors could potentially lead to a real-time implementation of 3D-BTI in the future. Segmentation of the epicardium and endocardium remained challenging using the ultrafast Bmode images and required to be performed manually by a trained

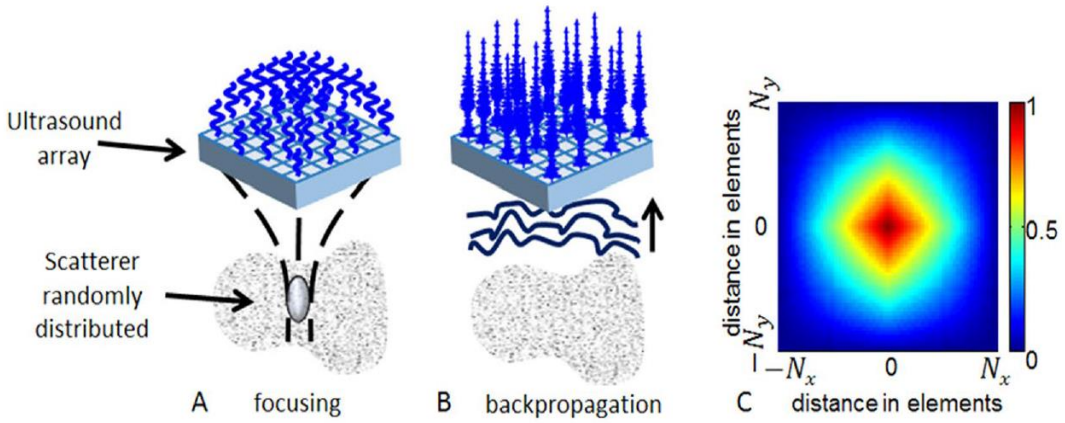

Figure 7. Principle of spatial coherence estimation on a 2D matrix array probe. (**A**) An ultrasound wave is focused in a random media by applying delays in emission. (**B**) The backscattered echoes are recorded for each element of the 2D array. The autocorrelation of the rephased signals is calculated for each pair of elements as a function of distance between elements that composed the pair. (**C**) Represents the theoretical coherence function for a focused emission in a random media that we would obtain with a matrix probe of $N_x \times N_y$ elements.

cardiologist. A dedicated anatomical high quality imaging sequence based on harmonic imaging for example could improve considerably the detection of the wall boundaries.

BTI may be affected by low ultrasound signal to noise ratio at large depths. The performance of BTI need to be investigated in more details for low SNR configurations. Nevertheless, we can anticipate BTI to be robust to incoherent noise such as clutter and thermal noise due to the suppression of a large part of incoherent noises by the coherence function. However, we can also anticipate that the performance of BTI will drop considerably in very low SNR situations where incoherent noise becomes larger that the coherent signals.

Finally, while presenting similar advantages in terms of portability, safety, and real-time imaging capabilities, the 3D ultrafast ultrasound system that we used is a unique laboratory prototype that is not currently available in clinical practice. In summary, 3D-BTI may constitute a unique tool for non-invasively evaluating the myocardial fiber structure of a patient suffering from myocardial fibrosis or hypertrophic cardiomyopathy for diagnosis, treatment monitoring and follow-up.

Materials and Methods

Spatial coherence on a matrix array transducer. Ultrasonic spatial coherence was assessed experimentally by focusing an ultrasound wave in a medium and by receiving the backscattered echoes on a 2D matrix array transducer (Fig. 7A and B). The 2D spatial coherence function $R(\Delta x, \Delta y)$ was obtained by computing the auto-correlation of the signals received by pairs of elements i and j distant by Δx and Δy, along the main two coordinate axis of the matrix array:

$$R(\Delta x, \Delta y) = \frac{1}{N_x - |\Delta x|}\frac{1}{N_y - |\Delta y|}\sum_i\sum_j \frac{\sum_{t=T_1}^{T_2} S_i(x_i, y_i, t) S_j(x_j, y_j, t)}{\sqrt{\sum_{t=T_1}^{T_2} S_i(x_i, y_i, t)^2 S_j(x_j, y_j, t)^2}} \quad (1)$$

where $S_k(x_k, y_k, t)$ is the signal received on the element k of the matrix transducer with coordinates x_k, y_k after applying a time-delay to compensate the propagation path. Δx and Δy are the distances between and element i and element j:

$$\Delta x = x_i - x_j; \quad \Delta y = y_i - y_j \quad (2)$$

T_1 and T_2 represents the averaging temporal window (equivalent to depth).

In random media, i.e. in absence of fibers, ultrasound scatterers are randomly distributed, (Fig. 7A), so that the coherence function is predicted by the so-called Van Cittert-Zernike theorem[31]: the coherence function is given by the spatial Fourier transform of the intensity distribution at the focal spot. For a square matrix array, the pressure distribution at the focal spot is a 2D sinc function so that the coherence function appears as the Fourier Transform of a squared 2D sinc function. The pyramidal shape coherence function of a $N_x \times N_y$ 2D matrix array transducer is displayed on Fig. 7C.

Data acquisition and signal processing. In order to focus the ultrasonic wave at specific locations in the medium, conventional ultrasound imaging relies on applying time delays to the transmitted wave (Fig. 7). A large number of transmitted waves focused at different locations of the medium is then required to obtain one single image of the medium. In volumetric imaging, the number of transmitted waves can reach several thousands of waves which results in very low volume rates. To overcome this issue, our approach consisted in using ultrafast plane wave imaging with a coherent compounding approach[26]. Coherent compounding can generate, at

any location of the region of interest, synthetic focal zones using only a few tens of emissions. Therefore, with this approach, large volumes can be imaged at very high volume rate between 50 and 5000 volumes/s.

The emissions consisted in the transmission of several tilted 2D plane waves (i.e. Fig. 1A). Each plane wave was defined by two angles. All pairs of angles ranging from −6° to 6° with a step angle of 2° were emitted, for a total of 49 tilted plane waves. Plane waves were emitted from a 2D matrix array probe with 32 (x-axis) by 35 (y-axis) elements (3 MHz, 0.3 mm pitch, 50% bandwidth at −3 dB, Vermon) connected to a customized, programmable, 1024 channel ultrasound system described in Provost *et al.*[26]. This system was designed and built in-house for 3D ultrafast imaging applications. This system allowed us to perform the first *in vivo* 3D ultrafast imaging acquisitions in various applications such as 3D imaging of the cardiac blood flows[26], 3D elastography of soft tissues[32] and 3D mapping of blood vessels[33]. The 1024 independent channels could be used simultaneously in transmission, whereas receive channels were multiplexed to 1 of 2 transducer elements. Therefore, each emission was repeated twice, with the first half of the elements receiving during the first emission, and the second half of the elements receiving during the second emission.

The received signals were sampled at 12 MHz, for all the 1024 elements and the radio-frequency data were recorded. The 3D images were computed off-line using a dynamic receive focusing beamforming algorithm followed by coherent compounding (see Fig. 1B). The 3D volume had a lateral size of 9.6 × 9.6 mm and a 3 cm to 6 cm depth depending on the region of interest. The lateral sampling of the image was 0.3 mm laterally (32 × 32 lines) and the axial sampling was 0.05 mm.

2D coherence functions were computed at each point of the 3D volume (Fig. 1C) using equation (1). The temporal window $[\boldsymbol{T_1}\ \boldsymbol{T_2}]$, was set to 1.6 µs (i.e. five periods at 3 MHz). The coherence functions were averaged at each depth of the 3D volume using a lateral sliding window with a kernel of (0.15 × 0.15 mm). The algorithm was implemented on parallelized Nvidia GPU using CUDA language.

An algorithm based on the Radon transform was applied on the 2D coherence functions, to determine the fiber orientation. The first step of the algorithm consisted in computing the integral of the 2D coherence function along a line y = 0. The line was then rotated step by steps in the 2D coherence function plane, to compute the integrals at each angle in the range 0–179 degrees. The fiber orientation was determined by the angle that corresponded to the maximum value of the integral (i.e. Fig. 1D). In this study, steps 1 degree were chosen. Finally, a vector representation was used to visualize the fibers directions in 3D using the Amira software (Visualization Sciences Group, Burlington, MA) (i.e. Fig. 1E).

Experimental Setup. *1) In vitro experiments and histology.* *In vitro* experiments were performed on five porcine fresh left ventricle myocardial samples embedded in a 2% gelatin gel. A cross-marker whose orientation matched the local cardiac circumferential-longitudinal coordinates was labeled on the myocardial sample. The probe was positioned at 15 mm of the epicardium. Each myocardial region examined by BTI was dissected from the intact porcine heart into a rectangular block (10 × 10 × 25 mm). This block was fixed in formalin for 48 h. To keep the orientation of the tissue block in the wright direction, the basal aspect of the tissue block was labeled with tattoo ink. Then the tissue block was cut in 4 to 5 tissue slices which were embedded in paraffin. Each paraffin block was completely cut at 5 µm of thickness in serial sections. One histological section out of 50 was stained with H&E: the resulting gap between two stained adjacent sections was 250 µm. All the sections were scanned with a Hamamatsu Nano Zoomer (Hamamatsu City, Japan). Fiber angles in all the histological digitalized images studied were computed using the Hough transform[34].

2) In vivo experiments. Animal experiments were performed in an open chest sheep on the mid-anterior region. The experimental procedure was approved prior to use by the Institutional Animal Care and Use committee of Hôpital Européen Georges Pompidou (Paris Descartes) according to the European Commission guiding principles (2010/63/EU). 3D-BTI was thus performed within an entire cardiac cycle. The 3D-BTI acquisition was performed at a volume rate of 90 volumes/s during 1.2 seconds in order to cover more than one cardiac cycle. It enabled the reconstruction of 100 fiber volumes. During the experiment, the electrocardiogram was recorded.

Human experiments were performed by a trained cardiologist. The volunteer was positioned on the left lateral decubitus position. The probe was placed in the parasternal view and 2D real-time imaging was performed to position the probe and image the antero-septal wall. The 3D BTI acquisition was then launch to acquire 1 s of data at a rate 90 volumes/s. The study was carried out in accordance with the Declaration of Helsinki and was approved by the French ethical committee (CPP Paris Ile de France VI, N° 15–15). Informed consent was signed by the volunteer.

References

1. Streeter, D. D. & Bassett, D. L. An engineering analysis of myocardial fiber orientation in pig's left ventricle in systole. *Anat. Rec.* **155**, 503–511 (1966).
2. Arts, T., Costa, K. D., Covell, J. W. & McCulloch, A. D. Relating myocardial laminar architecture to shear strain and muscle fiber orientation. *Am. J. Physiol. Heart Circ. Physiol* **280**, H2222–2229 (2001).
3. Costa, K. D., Takayama, Y., McCulloch, A. D. & Covell, J. W. Laminar fiber architecture and three-dimensional systolic mechanics in canine ventricular myocardium. *Am. J. Physiol.* **276**, H595–607 (1999).
4. Waldman, L. K., Nosan, D., Villarreal, F. & Covell, J. W. Relation between transmural deformation and local myofiber direction in canine left ventricle. *Circ. Res.* **63**, 550–562 (1988).
5. Taber, L. A., Yang, M. & Podszus, W. W. Mechanics of ventricular torsion. *J. Biomech.* **29**, 745–752 (1996).
6. Hansen, D. E. *et al.* Effect of volume loading, pressure loading, and inotropic stimulation on left ventricular torsion in humans. *Circulation* **83**, 1315–1326 (1991).
7. Hooks, D. A. *et al.* Laminar arrangement of ventricular myocytes influences electrical behavior of the heart. *Circ. Res.* **101**, e103–112 (2007).
8. Kadish, A. *et al.* Interaction of fiber orientation and direction of impulse propagation with anatomic barriers in anisotropic canine myocardium. *Circulation* **78**, 1478–1494 (1988).

9. Roberts, D. E., Hersh, L. T. & Scher, A. M. Influence of cardiac fiber orientation on wavefront voltage, conduction velocity, and tissue resistivity in the dog. *Circ. Res.* **44**, 701–712 (1979).
10. Taccardi, B. *et al.* Effect of myocardial fiber direction on epicardial potentials. *Circulation* **90**, 3076–3090 (1994).
11. Tseng, W.-Y. I., Dou, J., Reese, T. G. & Wedeen, V. J. Imaging myocardial fiber disarray and intramural strain hypokinesis in hypertrophic cardiomyopathy with MRI. *J. Magn. Reson. Imaging* **23**, 1–8 (2006).
12. Savadjiev, P. *et al.* Heart wall myofibers are arranged in minimal surfaces to optimize organ function. *Proc. Natl. Acad. Sci. USA* **109**, 9248–9253 (2012).
13. Hsu, E. W., Muzikant, A. L., Matulevicius, S. A., Penland, R. C. & Henriquez, C. S. Magnetic resonance myocardial fiber-orientation mapping with direct histological correlation. *Am. J. Physiol.* **274**, H1627–1634 (1998).
14. Scollan, D. F., Holmes, A., Winslow, R. & Forder, J. Histological validation of myocardial microstructure obtained from diffusion tensor magnetic resonance imaging. *Am. J. Physiol.* **275**, H2308–2318 (1998).
15. Reese, T. G. *et al.* Imaging myocardial fiber architecture *in vivo* with magnetic resonance. *Magn. Reson. Med. Off. J. Soc. Magn. Reson. Med. Soc. Magn. Reson. Med.* **34**, 786–791 (1995).
16. Wu, M.-T. *et al.* Diffusion Tensor Magnetic Resonance Imaging Mapping the Fiber Architecture Remodeling in Human Myocardium After Infarction: Correlation With Viability and Wall Motion. *Circulation* **114**, 1036–1045 (2006).
17. Fleming, C. P., Ripplinger, C. M., Webb, B., Efimov, I. R. & Rollins, A. M. Quantification of cardiac fiber orientation using optical coherence tomography. *J. Biomed. Opt.* **13**, 30505 (2008).
18. Huang, H. *et al.* Three-dimensional cardiac architecture determined by two-photon microtomy. *J. Biomed. Opt.* **14**, 44029 (2009).
19. Mottley, J. G. & J. G. M. Anisotropy of the ultrasonic attenuation in soft tissues: measurements *in vitro*. *J. Acoust. Soc. Am.* **88**, 1203–10 (1990).
20. Baldwin, S. L. *et al.* Measurements of the anisotropy of ultrasonic attenuation in freshly excised myocardium. *J. Acoust. Soc. Am.* **119**, 3130 (2006).
21. Wickline, S. A., Verdonk, E. D. & Miller, J. G. Three-dimensional characterization of human ventricular myofiber architecture by ultrasonic backscatter. *J. Clin. Invest.* **88**, 438–446 (1991).
22. Madaras, E. I., Perez, J., Sobel, B. E., Mottley, J. G. & Miller, J. G. Anisotropy of the ultrasonic backscatter of myocardial tissue: II. Measurements *in vivo*. *J. Acoust. Soc. Am.* **83**, 762–769 (1988).
23. Lee, W.-N. *et al.* Mapping myocardial fiber orientation using echocardiography-based shear wave imaging. *IEEE Trans. Med. Imaging* **31**, 554–562 (2012).
24. Derode, A. & Fink, M. Spatial coherence of ultrasonic speckle in composites. *IEEE Trans. Ultrason. Ferroelectr. Freq. Control* **40**, 666–675 (1993).
25. Papadacci, C., Tanter, M., Pernot, M. & Fink, M. Ultrasound backscatter tensor imaging (BTI): analysis of the spatial coherence of ultrasonic speckle in anisotropic soft tissues. *IEEE Trans. Ultrason. Ferroelectr. Freq. Control* **61**, 986–996 (2014).
26. Provost, J. *et al.* 3D ultrafast ultrasound imaging *in vivo*. *Phys. Med. Biol.* **59**, L1 (2014).
27. Streeter, D. D., Spotnitz, H. M., Patel, D. P., Ross, J. & Sonnenblick, E. H. Fiber orientation in the canine left ventricle during diastole and systole. *Circ. Res.* **24**, 339–347 (1969).
28. Papadacci, C., Pernot, M., Couade, M., Fink, M. & Tanter, M. High-contrast ultrafast imaging of the heart. *IEEE Trans. Ultrason. Ferroelectr. Freq. Control* **61**, 288–301 (2014).
29. Provost, J., Gambhir, A., Vest, J., Garan, H. & Konofagou, E. E. A clinical feasibility study of atrial and ventricular electromechanical wave imaging. *Heart Rhythm Off. J. Heart Rhythm Soc* **10**, 856–862 (2013).
30. Tanter, M., Bercoff, J., Sandrin, L. & Fink, M. Ultrafast compound imaging for 2-D motion vector estimation: application to transient elastography. *IEEE Trans. Ultrason. Ferroelectr. Freq. Control* **49**, 1363–1374 (2002).
31. Mallart, R. & Fink, M. The van Cittert–Zernike theorem in pulse echo measurements. *J. Acoust. Soc. Am.* **90**, 2718–2727 (1991).
32. Gennisson, J.-L. *et al.* 4-D ultrafast shear-wave imaging. *IEEE Trans. Ultrason. Ferroelectr. Freq. Control* **62**, 1059–1065 (2015).
33. Provost, J. *et al.* 3-D ultrafast Doppler imaging applied to the noninvasive mapping of blood vessels *in vivo*. *IEEE Trans. Ultrason. Ferroelectr. Freq. Control* **62**, 1467–1472 (2015).
34. Duda, R. O. & Hart, P. E. Use of the Hough Transformation to Detect Lines and Curves in Pictures. *Commun ACM* **15**, 11–15 (1972).

Acknowledgements

This work was supported by the European Research Council under the European Union's Seventh Framework Program (FP/2007–2013)/ERC Grant Agreement no. 311025 and by LABEX WIFI (Laboratory of Excellence ANR-10-LABX-24) within the French Program "Investments for the Future" under reference ANR-10-IDEX-0001-02 PSL. J.P. was funded in part by a Marie Curie International Incoming Fellowship under the Seventh Framework Program for research (FP7) of the European Union.

Author Contributions

C.P., J.P., O.V. and M.P. wrote the main manuscript. C.P., V.F., J.P., J.L.G., O.V. and M.P. performed experiments. P.B. performed histology. M.T., M.F. and M.P. designed study. All authors reviewed the manuscript.

Additional Information

Supplementary information accompanies this paper at doi:10.1038/s41598-017-00946-7

Competing Interests: The authors declare that they have no competing interests.

Publisher's note: Springer Nature remains neutral with regard to jurisdictional claims in published maps and institutional affiliations.

Open Access This article is licensed under a Creative Commons Attribution 4.0 International License, which permits use, sharing, adaptation, distribution and reproduction in any medium or format, as long as you give appropriate credit to the original author(s) and the source, provide a link to the Creative Commons license, and indicate if changes were made. The images or other third party material in this article are included in the article's Creative Commons license, unless indicated otherwise in a credit line to the material. If material is not included in the article's Creative Commons license and your intended use is not permitted by statutory regulation or exceeds the permitted use, you will need to obtain permission directly from the copyright holder. To view a copy of this license, visit http://creativecommons.org/licenses/by/4.0/.

© The Author(s) 2017

4.3. Perspectives

L'orientation des fibres du myocarde obtenues par 3D-BTI sur les myocardes de porcs correspondent aux mesures effectuées par histologie. La moyenne des orientations des fibres effectuées sur 5 échantillons varie continuellement à travers la paroi du myocarde avec une différence 98.6° +/- 8.9° entre l'endocardium et l'epicardium. L'orientation des fibres cardiaques in-vivo a été obtenue pendant un cycle cardiaque complet. La différence d'angle entre epicardium et endocardium est entre 60 et 80° pendant le cycle cardiaque. Ces résultats suggèrent donc que le 3D-BTI peut être utilisé pour l'étude de l'orientation des fibres myocardiques et ses dynamiques.

D'un point de vue plus général, l'enjeu ici est de comprendre que la cohérence spatiale ultrasonore permet d'avoir des informations sur la structure même des tissus, avec une précision bien supérieure à la résolution spatiale de l'imagerie ultrasonore conventionnelle, classiquement dépendante de la longueur d'onde λ (du moins pour la résolution spatiale axiale), donc de l'ordre du millimètre. Cela ouvre donc des perspectives d'exploration et d'analyse à une échelle tissulaire, de l'ordre du micromètre.

En physiologie, très peu de travaux scientifiques ont apporté des réponses sur l'évolution durant un cycle cardiaque des fibres de cardiomyocytes (cf références du manuscrit). Nous n'avons pas d'information sur leur évolution et leur organisation durant l'embryogénèse cardiaque, ce qui pourrait aider à la compréhension de certaines cardiomyopathies congénitales. A l'autre extrême de la vie, il pourrait être intéressant de mieux comprendre l'évolution naturelle avec l'âge des fibres de cardiomyocytes. En effet, à travers la littérature, nous avons de plus en plus d'information sur l'évolution des structures valvulaires (Goldbarg et al. 2007) (Aikawa et al. 2006) ou des structures coronariennes (Minamino and Komuro 2007) (Kurz et al. 2006), mais nous manquons encore d'outil d'imagerie pour avoir accès in vivo au tissu (et la fibre) du myocarde (Lombaert et al. 2012).

En physiopathologie, de nombreuses cardiopathies congénitales ou acquises entrainent une attente des fibres musculaires. Du moins nous avons beaucoup d'arguments pour le penser, mais un outil d'imagerie comme le 3D-BTI permettrait d'aller plus loin dans la compréhension de ces phénomènes. Dans nos travaux sur l'élastographie myocardique, nous avions apporté des argument supplémentaires sur la déstructuration tissulaire dans ces cardiopathies, via la fraction d'anisotropie estimée par ETI (Lee et al. 2010) (Lee et al. 2012).Mais l'analyse dynamique durant tout un cycle est limitée par les risques thermique

(I_{SPTA}) et surtout mécanique (MI), cf paragraphes 2.3.2 et 2.4.2. Le 3D-BTI pourrait permettre de mieux comprendre l'évolution de l'organisation des fibres myocardiques durant un cycle cardiaque, et la différence entre le sain et le pathologique. D'autres études cliniques spécifiques permettaient de savoir si la 3D-BTI pourrait être un outil de dépistage de cardiomyopathie ou un outil permettant de mieux estimer le pronostic de certaines cardiomyopathies identifiées en corrélant l'organisation des fibres et l'état d'avancement de la maladie.

Evidemment, en parallèle des perspectives d'application, l'amélioration de la technologie doit se faire. Des sondes à plus hautes fréquences de ce type (matricielle 1024 voies à pilotage par système d'acquisition ultrarapide personnalisé et programmable) permettraient d'avoir une résolution spatiale encore plus favorable. Elles sont actuellement en cours de fabrication. De plus, le temps réel (« 4-D ») est encore impossible du fait du temps du post-processing (analyse et obtention de l'image de la représentation vectorielle du volume) et cela ne pourra être amélioré que par une optimisation de la capacité de calcul et des cartes vidéo des systèmes. Mais comme toujours, ce n'est qu'en proposant de nouvelles applications qu'on poussera la technologie à s'améliorer.

5. Imagerie des flux coronaires par ultrasons

5.1. Introduction et Objectifs

Le cœur est l'organe responsable de la perfusion sanguine de tout le corps humain. Il est également constitué d'un système d'auto-perfusion, le système coronarien. Tout dysfonctionnement ou maladie de ce système peut conduire à des complications cliniques. Différentes maladies peuvent affecter le flux sanguin coronarien, comme par exemple le diabète, l'athérosclérose (pouvant entraîner une coronaropathie), l'hypertension, l'ischémie et l'insuffisance cardiaque. Différentes techniques permettent d'évaluer ce système de perfusion, mais en raison de leurs limitations (résolution d'image, cadence d'imagerie, caractère invasif ou injection de contraste-agents), ces techniques n'arrivent pas à imager complètement et de manière quantitative la circulation coronaire. L'échographie est l'examen le plus utilisé en cardiologie, toutefois, l'imagerie conventionnelle est inadéquate pour accéder correctement à la circulation coronarienne. Par conséquent, le développement de l'imagerie ultrasonore ultrarapide non-invasive pour accéder au flux coronarien et l'évaluer serait d'un grand intérêt en cardiologie. Le développement de cette technique d'imagerie ultrasonore est l'objet des travaux présentés dans ce chapitre.

Nous avons commencé à développer l'imagerie ultrasonore ultrarapide en deux dimensions pour accéder à la circulation coronarienne avec une meilleure résolution (permettant l'accès à des diamètres allant jusqu'à 100 µm). Ce développement a été apporté grâce un traitement du signal dédié à cette application. Ce traitement particulier repose sur un filtrage des mouvements du tissu par un filtre spatiotemporel (SVD, pour singular value decomposition) pondéré par l'énergie et adapté temporellement au mouvement de la paroi cardiaque. Nous appliquons la SVD dans de petites fenêtres temporelles glissantes (d'une durée d'environ 25 ms) tout au long du cycle cardiaque, le mouvement global du tissu dans chaque fenêtre est considéré comme faible. Puis, afin de prendre en compte l'énergie et donc l'inertie de l'arrangement de valeurs propres, on calcule, pour chaque fenêtre temporelle et SVD, la somme cumulée des valeurs propres (gain en puissance). Finalement, on trouve le seuil de coupure en calculant le maximum de la dérivée seconde de la somme cumulée des valeurs propres.

Nous avons également développé un nouveau concept pour accéder aux changements de débit volumétrique en utilisant les ultrasons : « l'intégral gain-vitesse ». Cette métrique permet d'obtenir des débits relatifs, soit des images de Doppler puissance corrigées par la vitesse axiale. Le Dr Mafalda Correia, au cours de son travail de thèse à l'Institut Langevin, a testé l'intégral gain-vitesse in vitro sur un fantôme artériel pour trois débits différents (120

ml/min, 241 ml/min et 376 ml/min). Pour ces expériences, l'intégral gain-vitesse n'a pas permis de déterminer directement une mesure absolue du débit volumétrique, cependant, les résultats présentés montrent que cette méthode est sensible et proportionnelle aux changements de débit au vue de l'analyse du signal d'intensité Doppler. L'intensité du signal Doppler pour un débit 120 ml/min était environ deux fois inférieure à l'intensité du signal Doppler pour un débit de 241 ml/min et trois fois inférieure à celle pour un débit de 376 ml/min.

De façon à améliorer et valider notre traitement d'imagerie dédié et le principe de l'intégral gain-vitesse in vivo, nous avons réalisé des séries d'expériences chez le cochon. Les objectifs de ces expériences étaient les suivants: (1) démontrer si l'imagerie Doppler ultrarapide avec notre traitement de données pourrait donner accès in vivo à la circulation coronarienne intramurale ; (2) évaluer les variations de débit coronarien pendant l'hyperémie réactive, induite par une brève occlusion de l'artère coronaire; (3) mesurer la réserve coronaire (rapport du flux coronaire pendant une vasodilatation coronarienne maximale et le flux coronaire de référence) (CFR) intramurale par injection d'adénosine; et finalement (4) imager les effets potentiels de l'infarctus du myocarde sur le système vasculaire coronaire.

Dans le but de se rapprocher de la pratique clinique, nous avons également évalué la capacité de notre méthode à détecter la circulation coronarienne en transthoracique chez des humains. Nous avons effectué l'imagerie Doppler ultrarapide sur deux volontaires sains au sein d'une étude de recherche clinique en cardiologie pédiatrique, à l'hôpital Necker-Enfants malades. La faisabilité chez l'humain a été évaluée sur un sujet féminin et un autre masculin, âgés de 5 et 7 ans, respectivement.

5.2. Manuscrit "*Non-invasive imaging of the coronary vasculature using ultrafast ultrasound*" + Editorial Comment

Ce travail est publié dans JACC : Cardiovascular Imaging (Maresca et al. 2017)

JACC: CARDIOVASCULAR IMAGING
VOL. ■, NO. ■, 2017
ISSN 1936-878X
http://dx.doi.org/10.1016/j.jcmg.2017.05.021
© 2017 THE AUTHORS. PUBLISHED BY ELSEVIER ON BEHALF OF THE AMERICAN COLLEGE OF CARDIOLOGY FOUNDATION. THIS IS AN OPEN ACCESS ARTICLE UNDER THE CC BY-NC-ND LICENSE (http://creativecommons.org/licenses/by-nc-nd/4.0/).

Noninvasive Imaging of the Coronary Vasculature Using Ultrafast Ultrasound

David Maresca, PhD,[a] Mafalda Correia, PhD,[a] Olivier Villemain, MD,[a] Alain Bizé, MSc,[b] Lucien Sambin, BSc,[b] Mickael Tanter, PhD,[a] Bijan Ghaleh, PhD,[b] Mathieu Pernot, PhD[a]

ABSTRACT

OBJECTIVES The aim of this study was to investigate the potential of coronary ultrafast Doppler angiography (CUDA), a novel vascular imaging technique based on ultrafast ultrasound, to image noninvasively with high sensitivity the intramyocardial coronary vasculature and quantify the coronary blood flow dynamics.

BACKGROUND Noninvasive coronary imaging techniques are currently limited to the observation of the epicardial coronary arteries. However, many studies have highlighted the importance of the coronary microcirculation and microvascular disease.

METHODS CUDA was performed in vivo in open-chest procedures in 9 swine. Ultrafast plane-wave imaging at 2,000 frames/s was combined to an adaptive spatiotemporal filtering to achieve ultrahigh-sensitive imaging of the coronary blood flows. Quantification of the flow change was performed during hyperemia after a 30-s left anterior descending (LAD) artery occlusion followed by reperfusion and was compared to gold standard measurements provided by a flowmeter probe placed at a proximal location on the LAD ($n = 5$). Coronary flow reserve was assessed during intravenous perfusion of adenosine. Vascular damages were evaluated during a second set of experiments in which the LAD was occluded for 90 min, followed by 150 min of reperfusion to induce myocardial infarction ($n = 3$). Finally, the transthoracic feasibility of CUDA was assessed on 2 adult and 2 pediatric volunteers.

RESULTS Ultrahigh-sensitive cine loops of venous and arterial intramyocardial blood flows were obtained within 1 cardiac cycle. Quantification of the coronary flow changes during hyperemia was in good agreement with gold standard measurements ($r^2 = 0.89$), as well as the assessment of coronary flow reserve (2.35 ± 0.65 vs. 2.28 ± 0.84; $p = NS$). On the infarcted animals, CUDA images revealed the presence of strong hyperemia and the appearance of abnormal coronary vessel structures in the reperfused LAD territory. Finally, the feasibility of transthoracic coronary vasculature imaging was shown on 4 human volunteers.

CONCLUSIONS Ultrafast Doppler imaging can map the coronary vasculature with high sensitivity and quantify intramural coronary blood flow changes. (J Am Coll Cardiol Img 2017;■:■-■) © 2017 The Authors. Published by Elsevier on behalf of the American College of Cardiology Foundation. This is an open access article under the CC BY-NC-ND license (http://creativecommons.org/licenses/by-nc-nd/4.0/).

Coronary arteries secure the heart supply in blood and oxygen. Any dysfunction or disease of these vessels can lead in turn to adverse clinical outcomes. The coronary vasculature is organized in 3 compartments. The first is made of the epicardial coronary arteries, which run along the heart's surface and exhibit diameters ranging from a few millimeters to 500 μm. The second includes the

From the [a]Institut Langevin, ESPCI ParisTech, CNRS UMR 7587, INSERM U979, Paris, France; and [b]INSERM U955, Equipe 03, F94000, Créteil et Université Paris Est, et Ecole Nationale Vétérinaire d'Alfort, F-94000, Maisons-Alfort, France. This work was supported by the European Research Council (ERC) under the European Union's Seventh Framework Programme (FP/2007-2013)/ERC grant agreement 311025 and the ANR-10-IDEX-0001-02 PSL Research University. Dr. Tanter is a cofounder of SuperSonic Imagine. All other authors have reported that they have no relationships relevant to the contents of this paper to disclose. Drs. Maresca and Correia contributed equally to this work and are joint first authors. Drs. Ghaleh and Pernot contributed equally to this work and are joint senior authors.

Manuscript received February 2, 2017; revised manuscript received May 3, 2017, accepted May 13, 2017.

ABBREVIATIONS AND ACRONYMS

CFR = coronary flow reserve

CUDA = coronary ultrafast Doppler angiography

LAD = left anterior descending coronary artery

PVI = power-velocity integral

pre-arterioles, which penetrate the myocardium from the epicardium to the endocardium and exhibit diameters ranging from 500 μm to 100 μm. The third corresponds to the coronary microvasculature, which exhibits vessel diameters below 100 μm (1). To date, the epicardial coronary vasculature is the only compartment that can be imaged in vivo in humans (1) with current angiography techniques such as x-ray, computed tomography (CT) scan, or magnetic resonance imaging (2). As a consequence, cardiology practice has been centered on focal macroscopic coronary artery disease, that is, the functional assessment of epicardial stenoses based on fractional flow reserve and subsequent pharmacological or invasive treatment via percutaneous coronary interventions or surgery (3).

It is now recognized that coronary microvascular dysfunction, that is, including pre-arterioles, is another prognostic marker of myocardial ischemia (1,4). Yet clinical guidelines in the management of stable ischemic heart disease only consider coronary microvascular dysfunction after excluding signs of epicardial disease (5). Therefore, there is a clear role for novel imaging tools capable of imaging and characterizing the pre-arteriolar coronary vasculature.

On the technology front, echocardiography capabilities are being redefined in the advent of ultrafast cardiac ultrasound imaging (6). Relying on plane-wave transmissions, ultrafast ultrasound enables the imaging of the heart at thousands of images per second, that is, 100 times faster than conventional clinical echocardiography (7). The major benefit of this technology lies in the acquisition of spatially synchronous, temporally highly resolved ultrasound datasets. Earlier studies have shown that post-processing of ultrafast ultrasound datasets can lead to a 30-fold increase in power Doppler sensitivity and generate rodent cerebrovascular atlases of 100 μm resolution (8,9).

In the myocardium, 2-mm-thick cryomicrotome projections of swine coronary vasculature (10) reveal that dense vascular networks are being insonified during 2-dimensional echocardiography examinations (3- to 10-mm image slice thickness). In 2012, Osmanski et al. (11) presented a first sparse detection of intramyocardial blood flow in open-chest sheep experiments using directional ultrafast-power Doppler. More recently, we used ultrafast cardiac Doppler imaging to resolve left ventricle hemodynamics with millisecond accuracy (12). These advances exhibited the potential of ultrafast Doppler in mapping cardiac hemodynamics.

In this paper, we report noninvasive ultrasound imaging of the coronary vasculature and assessment of the coronary flow reserve (CFR) using a new technique we call coronary ultrafast Doppler angiography (CUDA). This technique involves acquiring ultrasound images of the beating heart at 2,000 frames per second and processing them adaptively to account for myocardial wall motion and retrieve Doppler signals from tissue clutter throughout the heart cycle. We present ultrasound images of the epicardial and pre-arteriolar (Ø 500 to 100 μm) coronary compartments in a series of in vivo open-chest swine experiments and assess pre-arteriolar CFR using a metric that is proportional to blood flow, referred to as power-velocity integrals (13). Finally, we demonstrate contrast agent-free, transthoracic ultrasound images of the human coronary vasculature.

METHODS

ANIMAL EXPERIMENT PROTOCOL. Eight 2.5-month-old female domestic swine (*Sus scrofa domesticus*) weighing 20 to 25 kg were anesthetized with isoflurane 2%, intubated, and ventilated. After sternotomy, a coronary flow probe (Transonic, Ithaca, New York) was placed around the left anterior descending coronary artery (LAD). During a first set of experiments, the LAD was transiently occluded for 30 s to induce reactive hyperemia (n = 5). Then the swine received intravenous adenosine infusion (0.5 mg/kg/min) to induce major pharmacological coronary artery vasodilation. During a second set of experiments, the LAD was transiently occluded for 90 min, followed by 150 min of reperfusion to induce myocardial infarction (n = 3). After the animals were euthanized, the heart was excised and cut in slices that were incubated with triphenyltetrazolium chloride to reveal infarcted areas in white and viable tissues in red. The animal procedure was approved by the Institutional Animal Care and Use Committee of Ecole Veterinaire de Maison-Alfort (ComEth ANSES-ENVA-UPEC) according to the European Commission guiding principles (2010/63/EU).

HUMAN APPLICATION. In this set of transthoracic experiments in humans, we used the same ultrafast ultrasound scanner and ultrasound probe as in open-chest experiments. A trained sonographer positioned the probe in real time using B-mode imaging. Subsequently, the ultrafast sequence was launched, and ultrafast ultrasound datasets were acquired. The processing was identical to the animal experiments. This study had been approved by the proper ethics committee (Comité de Protection des Personnes-Ile-de-France VI, study identifications:

FIGURE 1 Coronary Ultrafast Doppler Angiography Acquisition Sequence and Processing

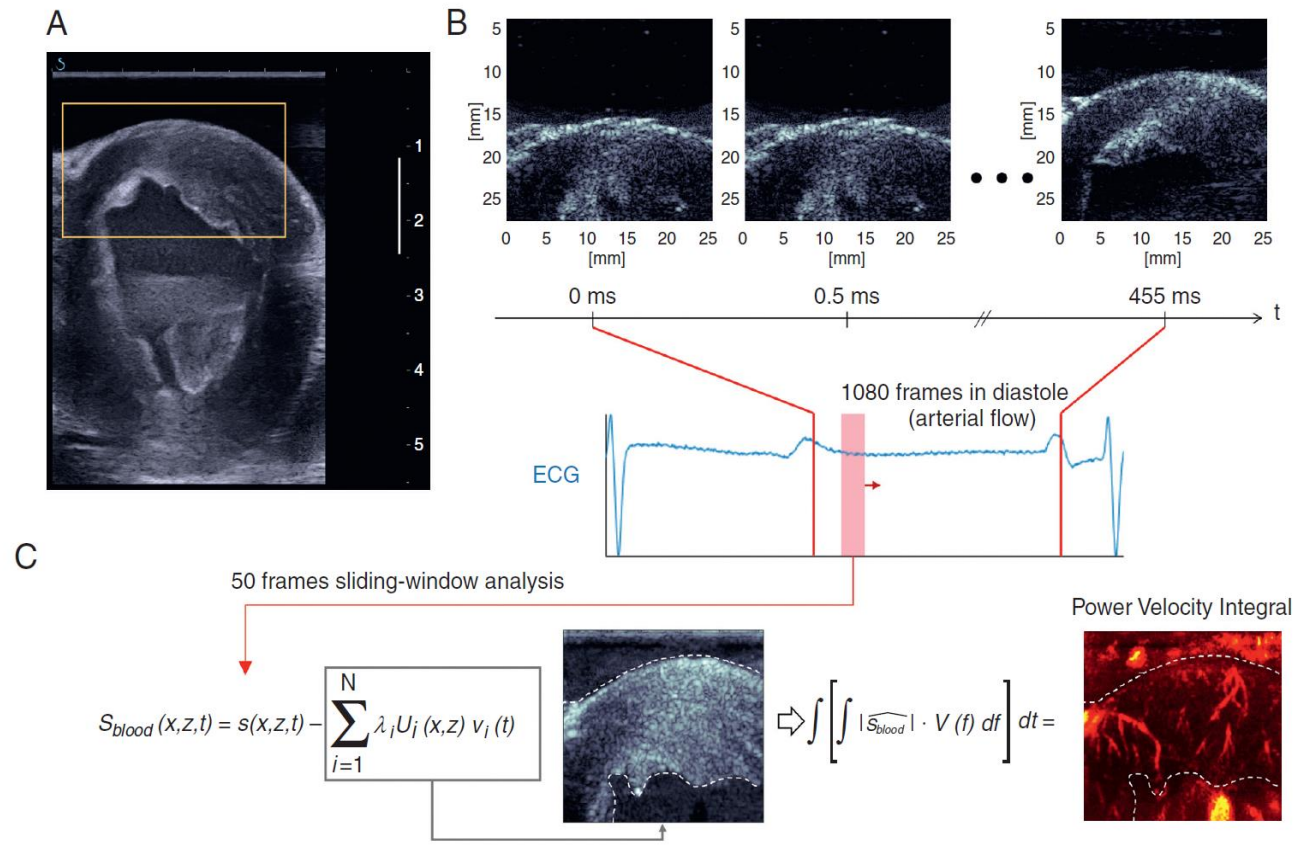

(A) Conventional ultrasound imaging in real time was used to select the heart section of interest (mid parasternal short-axis view here). The region of interest of the anterior wall is outlined in yellow. **(B)** Ultrafast acquisition of the anterior wall region of interest and corresponding electrocardiogram. A total of 1,000 frames were typically acquired in diastole over 0.5 s. **(C)** An adaptive spatiotemporal filter was used to separate coronary flow from tissue clutter through diastole using a sliding window analysis. Using a singular value decomposition on sliding short ensembles of frames (<50), we separated tissue signal (gray-scale image) contained in the highest eigenvectors from blood signal contained in the lowest eigenvectors (red-scale image). Our filtering method relies on the fact that tissue is highly echogenic and exhibits cohesive motion throughout the image plane, whereas coronary blood signal is weakly echogenic and has a random motion nature, because erythrocytes are freely floating within vessels.

2015-A00438-41 and 2015-A00187-42), and informed consent was signed by the adults or by the parents of the children.

ULTRAFAST ULTRASOUND IMAGING SEQUENCE. All experiments were conducted with a linear 6-MHz ultrasound probe (Vermon, Tours, France) and a programmable ultrafast ultrasound scanner (Aixplorer, SuperSonic Imagine, Aix-en-Provence, France). High-sensitivity Doppler imaging was achieved by use of a dedicated ultrafast plane-wave imaging sequence. We designed a plane-wave ultrasound sequence consisting of 8 tilted plane waves to perform 1 image (14), which enabled imaging of the myocardial wall at a frame rate of 2,000 images/s (**Figure 1B**) at a depth of up to 45 mm. Considering the 6-MHz central frequency, this allowed us to sample coronary blood flows below 24 cm/s (15). Each ultrafast Doppler image consisted of a 0.5-s ultrafast acquisition (or 1,080 images), which fully covered the diastolic phase of the heart cycle in swine and in humans under normal physiological conditions.

CUDA VASCULATURE DETECTION. Post-processing was performed after the acquisition of the ultrasound dataset. We performed a sliding spatiotemporal analysis of short ensembles of frames (typically 50 frames covering 25 ms) throughout the ultrafast ultrasound datasets. For each ensemble of frames, an adaptive spatiotemporal temporal clutter filter retrieved Doppler signals from the coronary vasculature (**Figure 1C**, Online Appendix). Signed power Doppler maps were generated and superimposed to the ultrafast B-mode images. To establish the ability of CUDA to provide a quantitative readout of myocardial perfusion, we analyzed CUDA signals using power-velocity integrals (PVI), a metric proportional to flow rate (13).

STATISTICAL ANALYSIS. Continuous variables are presented as mean ± SD. Comparisons of flow changes were made with the Student 2-tailed paired *t* test. A Bartlett test was used to check the homogeneity of variances. The level of significance was set at an alpha level of ≤0.05. Linear regression and Bland-Altman plots were used for correlation of LAD flow variations between a flowmeter probe and ultrasound Doppler imaging. Analyses were conducted using MedCalc software (MedCalc Software, Mariakerke, Belgium).

RESULTS

CORONARY ULTRAFAST ULTRASOUND DOPPLER ANGIOGRAPHY UNVEILS THE INTRAMURAL CORONARY VASCULATURE IN VIVO. To show the capability of the CUDA imaging method to visualize surface and subsurface coronary vasculature, we conducted a series of open-chest swine experiments (n = 9). We present here long-axis and short-axis images of the coronary vasculature overlaid on B-mode anatomic images of the myocardium (**Figure 2**, Online Video 1). Vessels were color-coded using the echocardiography color Doppler conventions: upward flows in red and downward flows in blue. In **Figures 2A and 2B**, acquired in end systole before the transition to arterial flow, blood flows upward in intramural coronary veins from the endocardium to the epicardium and downward in the epicardial vein. In **Figures 2C and 2D**, acquired in protodiastole after the transition to arterial flow, the opposite takes place: blood flows up in the epicedial artery and down in the pre-arteriolar compartment in the direction of the endocardium. Note that in **Figure 2D**, the epicardial artery appears in cross section, which is more likely to happen in a short-axis view. These results demonstrate the feasibility of anterior wall color Doppler coronary angiography using ultrafast ultrasound.

CUDA QUANTITATIVELY ASSESSES CORONARY FLOW VARIATIONS DURING REACTIVE HYPEREMIA INDUCED BY BRIEF CORONARY ARTERY OCCLUSION. We evaluated the capacity of our imaging method to assess physiological coronary flow variations in a set of experiments with brief episodes of coronary artery occlusion followed by reperfusion, that is, inducing reactive hyperemia (n = 5). We positioned a flow probe on the LAD proximal to the ultrasound mid-ventricle parasternal short-axis view to compare flow variations assessed by ultrafast Doppler against flow variations measured by the flow probe used as a gold standard. **Figure 3A** presents the coronary blood flow recording acquired with a flowmeter probe on the LAD, which underwent a 30-s total occlusion. We acquired ultrafast Doppler images of the coronary microvasculature at specific time points, for instance, baseline, occlusion, peak of hyperemia, and during follow-up. In the reported example (**Figure 3B**), 2 branches of the LAD vasculature can be observed. The branches disappear during occlusion as blood flow is restricted in the epicardial artery. At the peak of hyperemia, the vasculature reappears with a higher-power Doppler intensity because the flow has increased and vessels are dilated. Power Doppler intensity subsequently decays during follow-up of the hyperemia event toward baseline levels. This result demonstrates that ultrafast-power Doppler intensities correlated with the coronary flow.

To establish the ability of CUDA to provide a quantitative readout of myocardial perfusion, we present in **Figure 3C** the correlation of ultrafast Doppler-derived PVI flow variations against coronary blood flow variations measured with the flow probe in 5 swine. We found a strong correlation between this metric and invasive flow probe measurements (mean r^2 = 0.89 for 5 swine), corroborated by a Bland-Altman plot (**Figure 3D**). These results demonstrate that quantitative hyperemia-to-baseline ratios can be derived using ultrafast Doppler imaging.

NONINVASIVE MEASUREMENT OF INTRAMURAL CORONARY FLOW RESERVE WITH ADENOSINE. CFR, the ratio of coronary flow during maximal coronary vasodilatation to coronary flow at baseline, is a prognostic physiological parameter widely used to diagnose stable ischemic heart disease (5). To assess whether we could determine this ratio using CUDA, we induced maximal coronary vasodilatation using adenosine while imaging or measuring blood flow using an LAD flowmeter. **Figure 4A** presents ultrafast Doppler images of the coronary vasculature at baseline and during adenosine-induced vasodilatation, revealing a clear Doppler signal increase under adenosine administration. **Figure 4B** shows statistically significant mean blood flow variations assessed with a LAD flowmeter proximal to the imaging plane of interest, which evolved from 14.2 ml/min at baseline to 33.6 ml/min under adenosine administration (p = 0.04). **Figure 4C** shows a comparison of CFR values derived from PVI measurements at the pre-ateriolar level to CFR values derived from flowmeter measurements. We performed 16 measurements in 4 swine: 4 at baseline and 4 under adenosine using ultrasound coregistered with 4 measurements at baseline and 4 under adenosine using flowmeter. The mean ultrasound-derived CFR was 2.28 ± 0.84, whereas the flowmeter CFR was 2.35 ± 0.65 (p = NS). Values were in excellent agreement and demonstrated the capacity of

FIGURE 2 Ultrafast Color Doppler Imaging of Intramural Coronary Vasculature in Open-Chest Swine Experiments

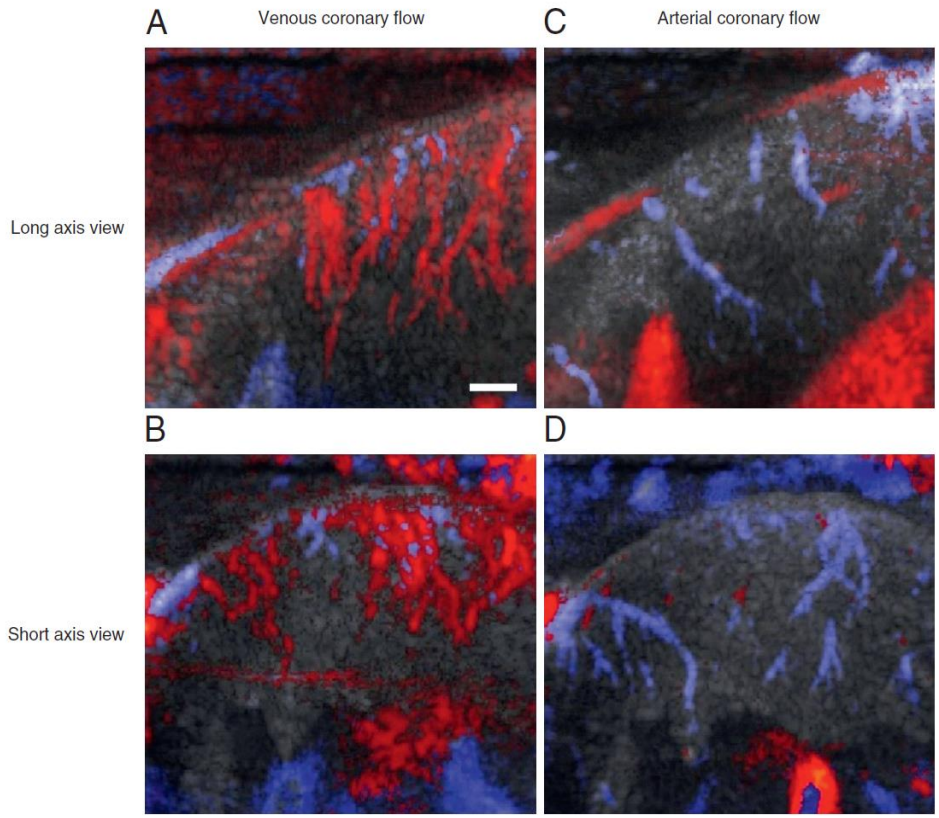

Red indicates blood flows moving upward, and **blue** indicates blood flows moving downward. **(Top)** An example of long-axis results in 1 animal: **(A)** venous coronary flow in mid-systole and **(C)** arterial coronary flow in mid-diastole. **(Bottom)** Results in a mid-level short-axis view showing **(B)** venous and **(D)** arterial flow in the same animal. Inversion of venous and arterial flow patterns is clearly visible: in systole, venous blood flow moves upward from the endocardium to the epicardium before moving downward in the epicardial veins. In diastole, arterial blood flow goes up in the epicardial vessels before flowing down in the myocardium. The epicardial and arteriolar compartments are successfully detected. Vessels below 100 μm remain below resolution. See Online Video 1. Scale bar = 3 mm.

ultrafast Doppler ultrasound imaging to assess CFR noninvasively.

EXPLORING THE CORONARY VASCULATURE DURING MYOCARDIAL INFARCTION USING CUDA. After validating the quantitative assessment of blood flow variations using CUDA, we explored whether our imaging method could monitor coronary hemodynamics during myocardial infarction. To induce myocardial infarction, the LAD was fully occluded for 90 min and then reperfused (experiment performed in 3 swine). We monitored the anterior wall coronary vasculature with ultrafast Doppler at baseline, during occlusion, and for 250 min after reperfusion. In all 3 experiments, coronary blood flow peaked 20 min after reperfusion (Figure 5A). Subsequent heart sections stained with triphenyltetrazolium chloride revealed the presence of large infarcted LAD regions, as well as viable reperfused regions (Figure 5C). Although anatomic B-mode images of infarcted regions did not provide specific insights on tissue damage, ultrafast Doppler images revealed the presence of dilated vessels and strong hyperemia in the reperfused region, which peaked at 20 min after reperfusion and decreased slowly during the following 2 h. In addition to hyperemia, we observed the appearance of abnormal coronary vessel structures in the reperfused LAD territory. An example of abnormal arterial flows is shown in Figure 5B: the arterial network in the LAD territory ends with a larger arterial flow region within the myocardial wall, which could be related to vascular damage and hemorrhagic spots. Additionally, abnormal venous flows were observed with large dilated and disorganized vessels. Similar patterns were observed in all 3 animals.

FIGURE 3 Quantitative CUDA Assessment of Coronary Flow Variations

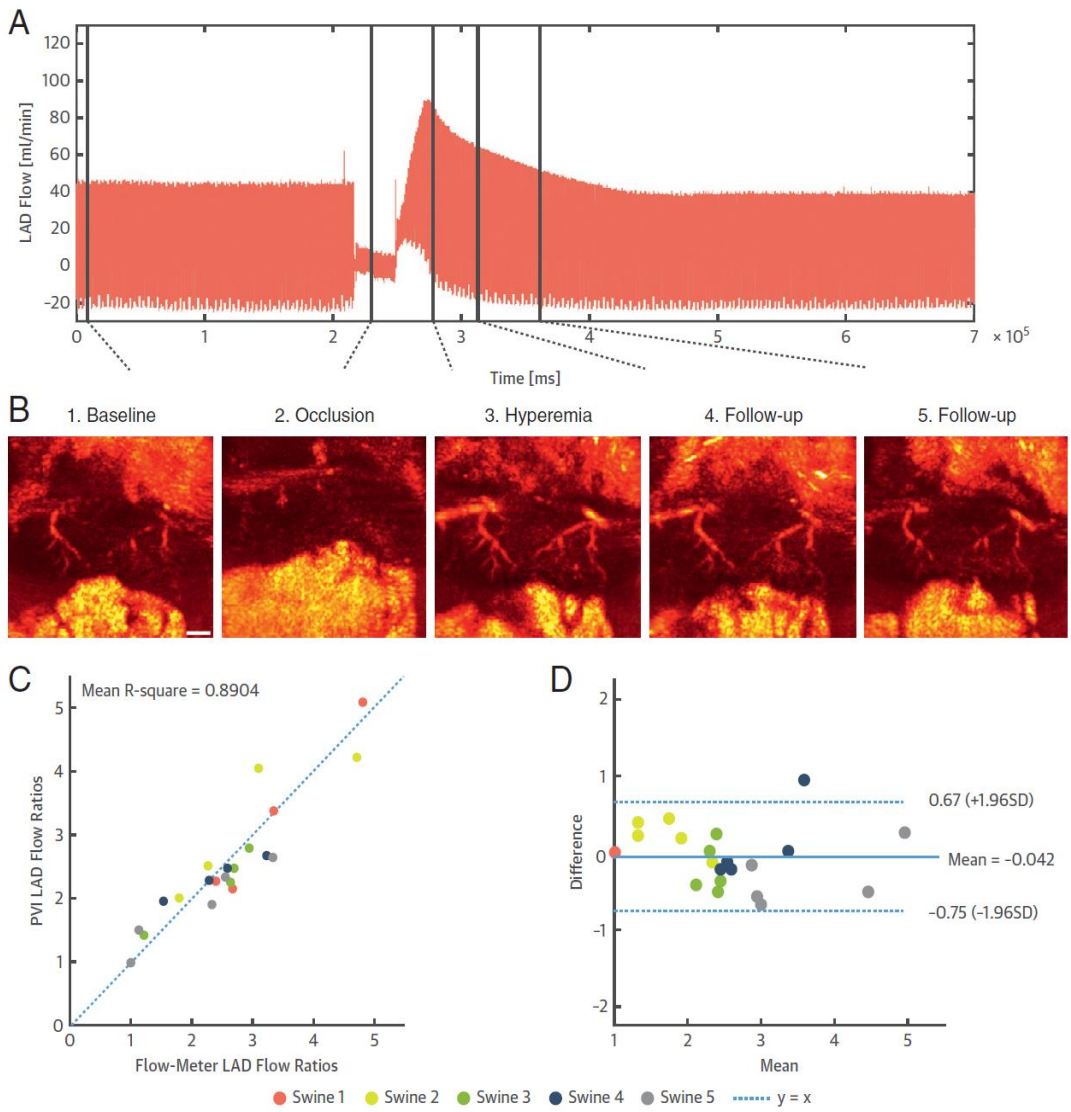

(A) Flow rate in the epicardial LAD assessed with an invasive flow probe positioned proximal to the image plane. A baseline phase is followed by a 30-s occlusion and subsequent reperfusion, inducing hyperemia. **(B)** Corresponding ultrafast Doppler images in 1 animal at baseline and during occlusion, peak hyperemia, and decay of the hyperemia event. The intramural coronary vasculature disappears during occlusion before reappearing brighter during hyperemia, which demonstrates that ultrafast Doppler imaging is sensitive to blood flow variations. Scale bar = 3 mm. **(C)** LAD blood flow variations derived from PVIs and correlation with flowmeter-derived flow variations in 5 animals. **(D)** Corresponding Bland-Altman plot of the data. CUDA = coronary ultrafast Doppler angiography; LAD = left anterior descending coronary artery; PVI = power-velocity integral.

NONINVASIVE TRANSTHORACIC IMAGING OF THE CORONARY VASCULATURE IN HUMANS. In a step toward translation to clinical practice, we evaluated the capability of our method to detect the coronary vasculature transthoracically in humans. We imaged the coronary vasculature in 2 children and 2 adults. In Figure 6, we present the first transthoracic images of coronary vasculature in humans that were obtained with CUDA during the examination of 2 adults (29 and 39 years of age) and 2 children (4.5 and 9.7 years of age). These results demonstrate that it is possible to detect intramural coronary veins and arteries in a transthoracic clinical in vivo setting.

DISCUSSION

These results establish that ultrafast ultrasound combined with adaptive coronary Doppler processing is capable of visualizing the epicardial and intramural coronary vasculature, a vascular

FIGURE 4 CFR Assessment With CUDA

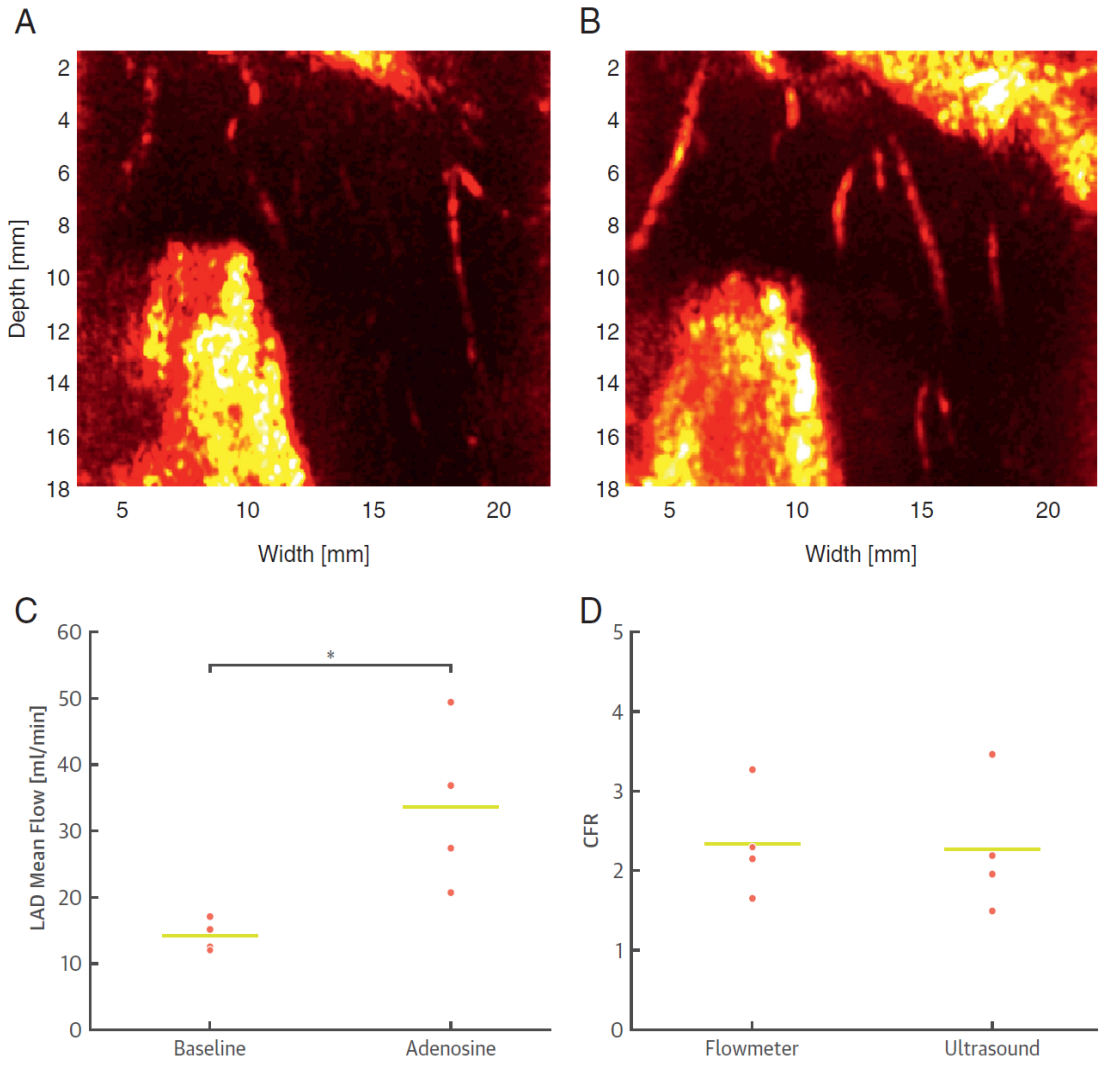

(A) Comparison of ultrafast Doppler images of the anterior wall coronary artery vasculature at baseline and with intravenous adenosine administration (0.5 mg/kg/min) in 1 animal. The increase in intramural vessel intensity denotes an increase in blood volume, which reveals the vasodilatative action of adenosine. **(B)** Statistical significance of vasodilatation induced by adenosine compared with baseline assessed with a flow probe connected to a flowmeter in 4 animals. LAD mean flow was more than doubled under the action of adenosine ($p < 0.05$). **(C)** CFR assessed with power-velocity integrals in intramural coronary arteries versus CFR assessed by flowmeter (gold standard) in 4 animals. Both metrics showed excellent agreement, demonstrating the capability of ultrafast Doppler imaging to assess CFR noninvasively. CFR = coronary flow reserve; LAD = left anterior descending coronary artery.

compartment currently uncharted in vivo in humans by existing clinical angiography techniques. Furthermore, this imaging technique allows the determination of PVI, a metric proportional to coronary flow, providing a quantitative measurement of coronary flow variations and CFR. This opens new possibilities for the noninvasive characterization of intramural CFR in patients with microvascular angina. Ultrafast Doppler imaging of the coronary vasculature could also play a role in cardiovascular research, because it can monitor physiological changes and anatomic changes of epicardial and intramural vessels in animal models of infarction, including abnormal coronary vessel structures. Moreover, the capability of CUDA to image both venous and arterial flows could also be useful for better understanding of the venous myocardial drainage, which remains somewhat unknown. In a final effort toward clinical translation, we demonstrated that our method could be readily used to image intramural coronary flow in pediatric cardiology.

FIGURE 5 Imaging and Pathology Before, During, and After Reperfusion

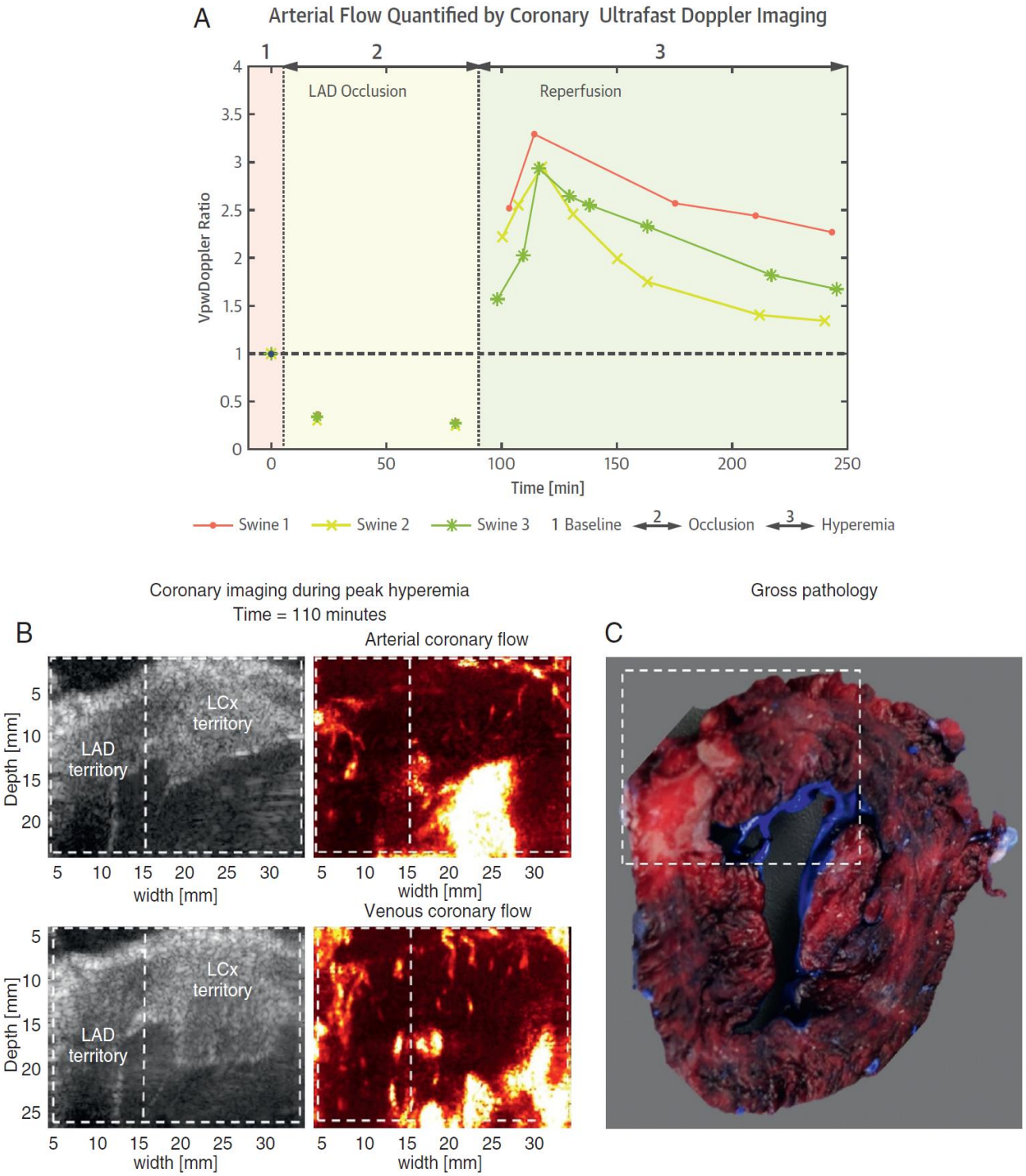

(A) PVI ratios are shown for 3 swine at baseline, during 90-min LAD occlusion, and during reperfusion. The hyperemia peak is observed after 20 min of reperfusion. **(B)** Strong local hyperemia and dilated arteries and veins presenting abnormal structures are observed with ultrafast Doppler imaging during reperfusion in the LAD territory (time = 110 min). **(C)** Corresponding heart section stained with triphenyltetrazolium chloride. Infarcted tissue appears white. White dotted lines outline regions that contain infarcted areas of interests in the heart section, and corresponding B-mode and Doppler images. LAD = left anterior descending coronary artery; LCx = left circumflex artery; VpwDoppler ratio = power velocity integral ratio.

FIGURE 6 Transthoracic CUDA Feasibility in Human Volunteers

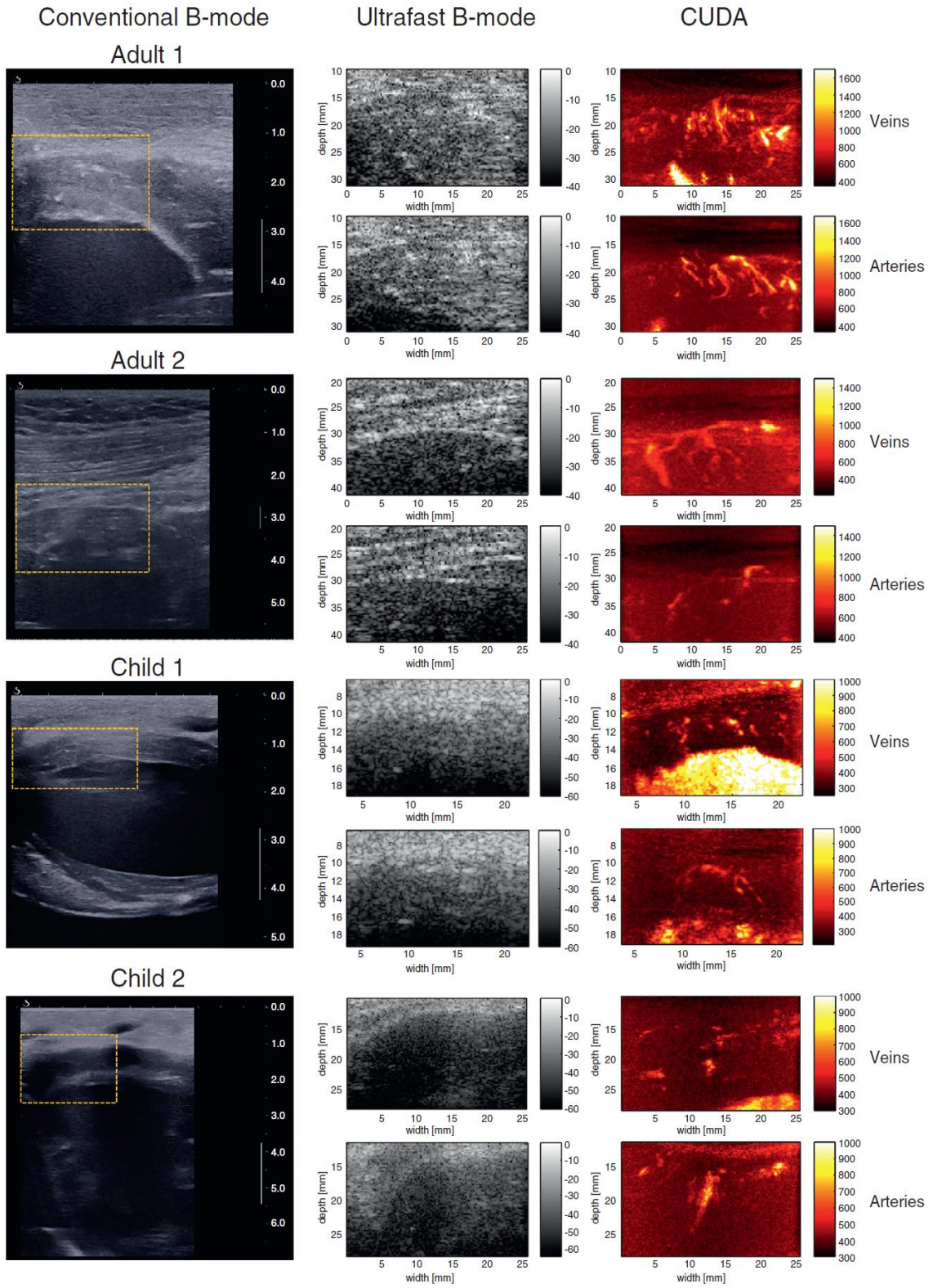

(Left) Conventional ultrasound image showing the region of interest selected for coronary ultrafast Doppler angiography (CUDA) processing. This real-time imaging mode of the ultrasound scanner was used for positioning (the scale bar is in centimeters). **(Middle)** Ultrafast B-mode images of the region of interest depicted in yellow. The resolution is lower, but the edges of the myocardial wall can be detected. Note that contrary to the open-chest experiments, parenchyma echogenicity is present above the myocardium, because it is a transthoracic measurement. **(Right)** CUDA images of coronary veins in systole and coronary arteries in diastole.

CLINICAL APPLICATION. Estimating CFR is critical to diagnose patients with stable coronary artery disease (16,17). It remains difficult, however, to assess CFR noninvasively. Fractional flow reserve is the current gold standard (18) according to European Society of Cardiology and American College of Cardiology guidelines but is an invasive, catheter-based method. Current clinical guidelines recommend coronary CT and stress-rest imaging (encompassing echocardiography, magnetic resonance imaging, positron emission tomography, and single-photon emission CT) (5). New tools are appearing, in particular CT-derived fractional flow reserve (19,20), but require further clinical validation. In this context, CUDA may become a novel major tool for measuring the CFR noninvasively with a nonionizing and portable imaging modality that can be used at the patient's bedside. Another cumbersome situation in clinical practice is the evaluation of angina due to microvascular disease, or microvascular angina. European Society of Cardiology guidelines (5) refer to this condition as angina with normal coronary arteries. This patient population currently represents a challenge, because their condition cannot be diagnosed with existing imaging tools, which cannot visualize intramural coronary vasculature. Finally, the technology could immediately play a role in interventional cardiology, for example, to assess reperfusion after a bypass surgery or a percutaneous coronary intervention.

STUDY LIMITATIONS. In this study, CUDA did not provide an absolute quantification of flow rate because of the angle dependency of Doppler imaging and could only quantify the flow rate changes during hyperemia or adenosine infusion thanks to the PVI. The feasibility of transthoracic imaging was shown only on 4 normal human hearts (2 adults and 2 children), and the clinical interest of this technology remains to be demonstrated on patients with coronary diseases. Another limitation of the study is the use of a linear transducer array, which is not suitable for transthoracic imaging in adult patients. A maximal imaging depth of 45 mm was achieved in this study due to the limited penetration of our linear transducer array. Imaging at a larger depth will require the use of a lower frequency, which implies a decrease of the spatial resolution. Therefore, the performance of CUDA at large depths remains to be investigated in further study. Future development of ultrafast Doppler imaging is ongoing, and the application of this technology to the human adult heart is emerging. The feasibility of transthoracic ultrafast imaging has already been demonstrated in adults (21) and was used to map intracardiac blood flows (12), electromechanical coupling (22), and myocardial stiffness (23,24). Therefore, CUDA could be translated to the human adult heart in the near future in both a transthoracic setup and in transesophageal echocardiography. Moreover, we have recently introduced ultrafast imaging in 3 dimensions (3D) and have shown the feasibility of imaging in 3D the human adult heart at a volume rate of 2,500 volumes/s using a prototype of a 3D ultrafast imaging scanner (25). CUDA imaging will highly benefit from this volumetric imaging, enabling the mapping of the entire complex vascular anatomy.

CONCLUSIONS

In this study, intramyocardial coronary vasculature of open-chest swine were imaged at ultrahigh sensitivity using CUDA. The change in coronary flow rate was quantified by CUDA during hyperemia and infusion of adenosine and validated by invasive flowmeter measurements. The transthoracic feasibility of this approach was shown in 4 human cases. These results could open new possibilities for the noninvasive characterization of intramural CFR in patients with microvascular angina.

ADDRESS FOR CORRESPONDENCE: Dr. Mathieu Pernot OR David Maresca, Institut Langevin, ESPCI ParisTech, CNRS UMR 7587, INSERM U979, 17 rue Moreau, 75012 Paris, France. E-mail: mathieu.pernot@inserm.fr OR dmaresca@caltech.edu.

PERSPECTIVES

COMPETENCY IN MEDICAL KNOWLEDGE: Estimating CFR is critical to diagnose patients with stable coronary artery disease and is valuable for the evaluation of any ischemic heart disease. However, it remains difficult to assess CFR noninvasively. The results of this study show that noninvasive assessment of CFR could be performed using ultrafast echocardiography. This may provide a nonionizing, contrast-free, and portable technique for noninvasive CFR assessment.

TRANSLATIONAL OUTLOOK: The major impact of this study is the finding that ultrafast ultrasound can visualize intramural coronary vasculature in a beating heart and quantify the change in coronary blood flow.

REFERENCES

1. Camici PG, d'Amati G, Rimoldi O. Coronary microvascular dysfunction: mechanisms and functional assessment. Nat Rev Cardiol 2015;12:48-62.

2. Fihn SD, Blankenship JC, Alexander KP, et al. 2014 ACC/AHA/AATS/PCNA/SCAI/STS focused update of the guideline for the diagnosis and management of patients with stable ischemic heart disease: a report of the American College of Cardiology/American Heart Association Task Force on Practice Guidelines, and the American Association for Thoracic Surgery, Preventive Cardiovascular Nurses Association, Society for Cardiovascular Angiography and Interventions, and Society of Thoracic Surgeons. J Am Coll Cardiol 2014;64:1929-49.

3. Velazquez EJ, Lee KL, Jones RH, et al., for the STICHES Investigators. Coronary-artery bypass surgery in patients with ischemic cardiomyopathy. N Engl J Med 2016;374:1511-20.

4. van de Hoef TP, Siebes M, Spaan JAE, Piek JJ. Fundamentals in clinical coronary physiology: why coronary flow is more important than coronary pressure. Eur Heart J 2015;36:3312-19a.

5. Task Force Members, Montalescot G, Sechtem U, Achenbach S, et al. 2013 ESC guidelines on the management of stable coronary artery disease: the Task Force on the management of stable coronary artery disease of the European Society of Cardiology [published correction appears in Eur Heart J 2014;35:2260-2261]. Eur Heart J 2013;34:2949-3003.

6. Cikes M, Tong L, Sutherland GR, D'hooge J. Ultrafast cardiac ultrasound imaging: technical principles, applications, and clinical benefits. J Am Coll Cardiol Img 2014;7:812-23.

7. Tanter M, Fink M. Ultrafast imaging in biomedical ultrasound. IEEE Trans Ultrason Ferroelectr Freq Control 2014;61:102-19.

8. Demené C, Tiran E, Sieu L-A, et al. 4D microvascular imaging based on ultrafast Doppler tomography. Neuroimage 2016;127:472-83.

9. Macé E, Montaldo G, Cohen I, Baulac M, Fink M, Tanter M. Functional ultrasound imaging of the brain. Nat Methods 2011;8:662-4.

10. Spaan J, Kolyva C, van den Wijngaard J, et al. Coronary structure and perfusion in health and disease. Philos Trans A Math Phys Eng Sci 2008;366:3137-53.

11. Osmanski B-F, Pernot M, Montaldo G, Bel A, Messas E, Tanter M. Ultrafast Doppler imaging of blood flow dynamics in the myocardium. IEEE Trans Med Imaging 2012;31:1661-8.

12. Osmanski B-F, Maresca D, Messas E, Tanter M, Pernot M. Transthoracic ultrafast Doppler imaging of human left ventricular hemodynamic function. IEEE Trans Ultrason Ferroelectr Freq Control 2014;61:1268-75.

13. Buck T, Mucci RA, Guerrero JL, Holmvang G, Handschumacher MD, Levine RA. The power-velocity integral at the vena contracta: a new method for direct quantification of regurgitant volume flow. Circulation 2000;102:1053-61.

14. Montaldo G, Tanter M, Bercoff J, Benech N, Fink M. Coherent plane-wave compounding for very high frame rate ultrasonography and transient elastography. IEEE Trans Ultrason Ferroelectr Freq Control 2009;56:489-506.

15. Bercoff J, Montaldo G, Loupas T, et al. Ultrafast compound Doppler imaging: providing full blood flow characterization. IEEE Trans Ultrason Ferroelectr Freq Control 2011;58:134-47.

16. Ahmadi A, Stone GW, Leipsic J, et al. Prognostic determinants of coronary atherosclerosis in stable ischemic heart disease: anatomy, physiology, or morphology? Circ Res 2016;119:317-29.

17. De Bruyne B, Fearon WF, Pijls NHJ, et al., for the FAME 2 Trial Investigators. Fractional flow reserve-guided PCI for stable coronary artery disease [published correction appears in N Engl J Med 2014;371:1465]. N Engl J Med 2014;371:1208-17.

18. Takx RAP, Blomberg BA, El Aidi H, et al. Diagnostic accuracy of stress myocardial perfusion imaging compared to invasive coronary angiography with fractional flow reserve meta-analysis. Circ Cardiovasc Imaging 2015;8:e002666.

19. Nørgaard BL, Leipsic J, Gaur S, et al., for the NXT Trial Study Group. Diagnostic performance of noninvasive fractional flow reserve derived from coronary computed tomography angiography in suspected coronary artery disease: the NXT trial (Analysis of Coronary Blood Flow Using CT Angiography: Next Steps). J Am Coll Cardiol 2014;63:1145-55.

20. Taylor CA, Fonte TA, Min JK. Computational fluid dynamics applied to cardiac computed tomography for noninvasive quantification of fractional flow reserve: scientific basis. J Am Coll Cardiol 2013;61:2233-41.

21. Papadacci C, Pernot M, Couade M, Fink M, Tanter M. High-contrast ultrafast imaging of the heart. IEEE Trans Ultrason Ferroelectr Freq Control 2014;61:288-301.

22. Provost J, Gambhir A, Vest J, Garan H, Konofagou EE. A clinical feasibility study of atrial and ventricular electromechanical wave imaging. Heart Rhythm 2013;10:856-62.

23. Correia M, Provost J, Chatelin S, Villemain O, Tanter M, Pernot M. Ultrafast harmonic coherent compound (UHCC) imaging for high frame rate echocardiography and shear-wave elastography. IEEE Trans Ultrason Ferroelectr Freq Control 2016;63:420-31.

24. Song P, Bi X, Mellema DC, et al. Quantitative assessment of left ventricular diastolic stiffness using cardiac shear wave elastography. J Ultrasound Med 2016;35:1419-27.

25. Provost J, Papadacci C, Arango JE, et al. 3D ultrafast ultrasound imaging in vivo. Phys Med Biol 2014;59:L1-13.

KEY WORDS angiography, blood flow, coronary, Doppler, imaging, ultrasound

APPENDIX For an expanded Methods section and Online Video, please see the online version of this paper.

JACC: CARDIOVASCULAR IMAGING
VOL. ■, NO. ■, 2017
© 2017 BY THE AMERICAN COLLEGE OF CARDIOLOGY FOUNDATION
ISSN 1936-878X/$36.00
PUBLISHED BY ELSEVIER
http://dx.doi.org/10.1016/j.jcmg.2017.06.007

EDITORIAL COMMENT

The Fast and the Curious

Physiological Insights From Fast Frame Rate Imaging*

Jonathan R. Lindner, MD

Clinical experts in the field of noninvasive cardiovascular imaging are perpetually on the prowl for engineering solutions to medical problems. In echocardiography, technical innovations have positively impacted patient care through improvements in spatial resolution, reduction of noise, and new approaches for measuring cardiac structure and function. Innovations sometimes occur in direct response to unmet clinical needs, such as the development of 3-dimensional echocardiography to better guide procedures for structural heart disease and the advent of contrast echocardiography to better assess left ventricular dimension and function. Alternatively, new technology is sometimes introduced with somewhat vague expectations of how it should be used in routine practice, as was the case for strain echocardiography and vorticity imaging.

The major innovation described in the study by Maresca et al. (1) in this issue of *iJACC* is the detection of intramyocardial arterial blood flow, which was made possible by increasing temporal resolution by an order of magnitude compared to conventional imaging. This ultrafast form of echocardiography was achieved through plane-wave imaging, which deserves some explanation. Conventional echocardiography relies on forming a 2-dimensional image through sequential transmission of many lines that are narrowly focused by large aperture size and with phase delay of the piezoelectric elements (**Figure 1A**). With either plane-wave or divergent-beam imaging, a single beam or a few much broader unfocused beams are transmitted (**Figure 1B**), which results in much higher frame rates (2). Defocusing of the beams reduces spatial resolution which can be addressed by using advanced computer processing to localize signals based on temporal delay in returning signals (referred to by some as retrospective beamforming) and by imaging the same tissue at slightly different angles, called *coherent spatial compounding*. As a result, in the study by Maresca et al. (1), 2-dimensional datasets were acquired at around 2,000 frames/s, albeit at a rather shallow depth, which also influences frame rate.

It is self-evident that increasing temporal resolution can provide unique information such as cardiac electromechanical timing by echocardiography. In the study by Maresca et al. (1), fast frame rates enabled imaging of intramyocardial arterial and venous flow. The underlying principle is that at extremely fast frame rates, wall filters become much more efficient in removing high-amplitude, slow-moving features (3). Accordingly, the investigators were able to detect rapidly moving blood in large intramyocardial vessels, but not necessarily flow in the microcirculation, where blood velocity is much slower.

Understanding how flow in large arteries was not only visualized with ultrafast imaging but quantified is key to understanding the robustness of the approach as a potential clinical tool. The algorithm used to detect flow in this study was power Doppler imaging, which is infrequently used in cardiac ultrasound. Power Doppler relies on the measurement of pulse-to-pulse decorrelation of returning echocardiographic signals from the same location to detect moving objects. Signal is displayed according to amplitude without velocity encoding. Ordinarily, bulk blood flow, such as through vessels, is quantified by ultrasound as the product of velocity and cross-sectional area or by integrating velocity vectors over a defined area. In the study by Maresca et al. (1), the power and velocity within a region of interest was integrated over time, thereby providing an index of

*Editorials published in *JACC: Cardiovascular Imaging* reflect the views of the authors and do not necessarily represent the views of *JACC: Cardiovascular Imaging* or the American College of Cardiology.

From the Knight Cardiovascular Institute and Oregon National Primate Research Center, Oregon Health & Science University, Portland, Oregon. Dr. Lindner is supported by grants R01-HL078610 and R01-HL130046 from the National Institutes of Health and grant 14NSBRI1-0025 from the National Space Biomedical Research Institute (NASA). Dr. Lindner has reported that he has no relationships relevant to the contents of this paper to disclose.

FIGURE 1 **Basis for Ultrafast Echocardiography**

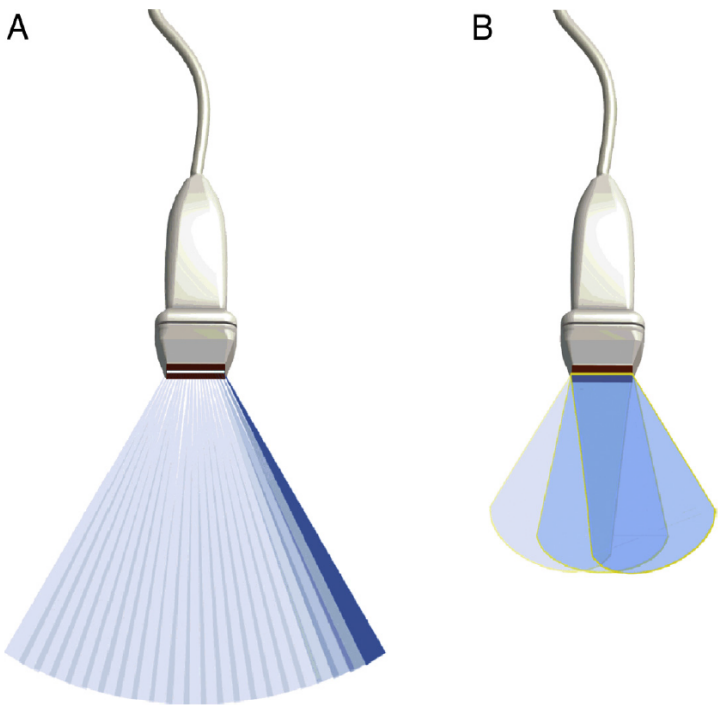

Illustration of **(A)** conventional echocardiography based on sequential transmission of highly focused lines by phased delay of piezoelectric activation and **(B)** ultrafast echocardiography with plane-wave or divergent-beam imaging, which relies on simultaneous or near-simultaneous element activation and slight angle change for coherent spatial compounding.

large vessel flow, although description of the velocity component and directionality is not provided in detail.

With the achievement of ultrafast intramyocardial vessel imaging, one now has to ask, "For what purpose?" The information provided does not address a specific unmet clinical need, which is not necessarily a negative criticism, because many important innovations in noninvasive cardiovascular imaging have had similar origins. Contextually, one could disagree with the authors' statement that large epicardial arteries are the only coronary vascular compartment that can be imaged in vivo in humans. When evaluating nutritive blood flow, it is not necessary to "resolve" microvessels. One only needs to be able to gather kinetic information that reliably reflects microvascular perfusion. Myocardial contrast echocardiography does not have a resolution of 2 to 4 μm, but it can reliably measure the concentration of 2- to 4-μm microbubbles to quantify microvascular blood volume, blood flux rate, and blood flow within the microvascular compartment (4). Similarly, magnetic resonance contrast kinetics and the perfusion-dependent uptake of radionuclide tracers are used to image flow in microvessels that are well under the detector spatial resolution limit.

Despite the widespread application of quantitative myocardial perfusion imaging, there are potential applications for imaging intramyocardial arterial flow. Again, Maresca et al. (1) are not entirely accurate when they state that the coronary intramural compartment is "uncharted." There is much known about the dynamic nature of these vessels. Since initial studies by Gregg and colleagues in 1935, it has been known that epicardial arteries are compliant, which allows their volume to expand by 20% to 40% during typical systolic pulse pressures (5,6). This knowledge, together with the observations by Chilian and Marcus (7,8) that intramyocardial arterial flow velocity becomes retrograde in early ventricular systole (**Figure 2**), indicates that backward motion of blood from intramyocardial arteries is stored in small epicardial arteries that distend and act as "capacitors" that discharge in early diastole. Key to the potential application of plane-wave imaging, relative phasic changes in flow velocity during the cardiac cycle in intramyocardial vessels were shown to be influenced by extravascular pressure (i.e., regional myocardial contractile function), intra-arterial pressure (i.e., systemic blood pressure), and various hyperemic stimuli.

In previous studies, assessment of phasic changes in intramyocardial arteries has been imaged noninvasively by specialized myocardial contrast echocardiography protocols in which transmit power is increased sufficiently to selectively destroy microbubble contrast agents in the distal microcirculation but not intramyocardial arteries (9,10). This approach provides information on left-sided phasic coronary arterial blood volume, which under normal circumstances is higher in diastole than systole. A major finding from these canine and human studies was that coronary stenosis produced an increase in coronary blood volume, especially during systole (9,10). These findings were explained by backward "milking" of an increased arteriolar blood volume that occurs from autoregulatory vasodilation (11). As a result, the systolic-to-diastolic intramyocardial blood volume ratio could be used to estimate severity of coronary stenosis without recourse to hyperemic stimulus.

In the study by Maresca et al. (1), phasic changes in intramyocardial arteries were not measured. Instead, the power-velocity integral (PVI) in diastole only was used as a "readout of myocardial perfusion." Without velocity encoding, the power signal in a single defined region is reflective of cross-sectional area (i.e., the number of scatters) (12). Accordingly, in conditions such as valve insufficiency, in which regurgitation is dictated primarily by orifice area, the power integral

FIGURE 2 **Differences in Phasic Blood Flow Velocity Based on Arterial Location**

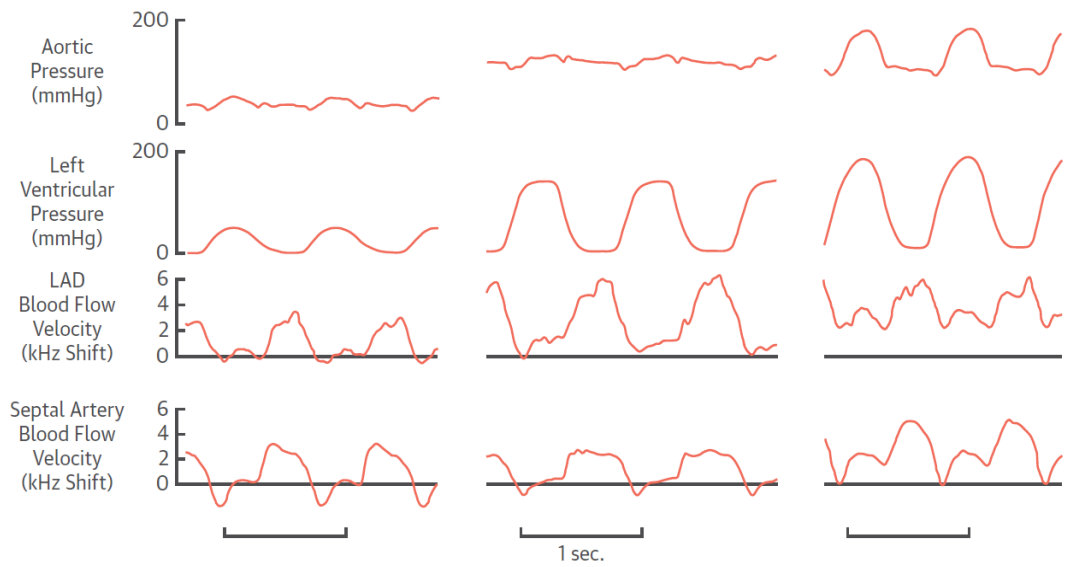

Blood flow velocity tracings from the left anterior descending coronary artery (LAD) and a small intramyocardial septal artery at aortic systolic blood pressures of 50, 125, and 200 mm Hg **(left to right)**. These tracings show phasic differences between the vessels with retrograde flow only in the intramyocardial artery (except at 200 mm Hg systolic blood pressure), which can be explained by capacitance function of small epicardial arteries. Reproduced with permission from Chilian et al. (8).

alone and the PVI (integrated velocity and "area" product) both perform well to quantify flow (12). Intramyocardial PVI is not so simple. The power Doppler signal and velocity are summed over a range of vessels along the fractal arterial tree. Hence, the PVI likely reflects an integration of the product of velocity and volume, which is not equivalent to flow. Many of the images from Maresca et al. (1) (e.g., Figures 3 and 6) indicate that increased PVI during adenosine is, in part, from detection of additional vessels farther down the arterial tree. These vessels were present and patent at rest but not visualized until the hyperemic increase in blood velocity allowed them to be registered above clutter. It is possible that the "appearance" of more vessels was able to compensate for inefficiencies using power Doppler to reflect "arterial diameter." On the basis of this finding, it would have been interesting to examine whether velocity integral alone provided the same information, because the clinical practice of measuring coronary flow velocity reserve is based on the notion that flow augmentation in the arterial compartment is largely from changes in velocity and that diameter changes are small.

Despite some of the nuances above, the demonstration that intramyocardial arterial blood vessels can be imaged by plane-wave imaging is exciting. The technique could be used to evaluate flow reserve abnormalities from coronary disease without the use of contrast. When this is attempted, investigators will need to take into account the issues raised above regarding autoregulatory changes in intramyocardial blood volume at rest, as well as the alterations in small-vessel capacitance function (filling and discharge) that occur according to aortic blood pressure and myocardial function. Technical hurdles are also substantial. Power Doppler signal and velocity are highly influenced by angle, and power Doppler is influenced by attenuation, frequency, and focus. These limitations explain why only vessels coaxial with the direction of ultrasound in the nearfield were measured in the feasibility study by Maresca et al. (1). Nonetheless, many important advances in noninvasive imaging have begun with the simple observation that some unique physiological phenomenon could be newly visualized by an engineering advance. As in the past, partnership between engineers and experts in physiology and clinical medicine will be essential for moving this technology forward.

ACKNOWLEDGMENTS The author would like to thank Patrick Rafter for his helpful review of the editorial for accuracy and Eran Brown for his aid in creating illustrations.

ADDRESS FOR CORRESPONDENCE: Dr. Jonathan R. Lindner, Knight Cardiovascular Institute, Oregon Health & Science University, 3181 SW Sam Jackson Park Road, Portland, Oregon 97239. E-mail: lindnerj@ohsu.edu.

REFERENCES

1. Maresca D, Correia M, Villemain O, et al. Noninvasive imaging of the coronary vasculature using ultrafast ultrasound. J Am Coll Cardiol Img 2017;10:xxx-xx.

2. Cikes M, Tong L, Sutherland GR, D'Hooge J. Ultrafast cardiac ultrasound imaging: technical principles, applications, and clinical benefits. J Am Coll Cardiol Img 2014;7:812-23.

3. Tanter M, Fink M. Ultrafast imaging in biomedical ultrasound. IEEE Trans Ultrason Ferroelectr Freq Control 2014;61:102-19.

4. Wei K, Jayaweera AR, Firoozan S, Linka A, Skyba DM, Kaul S. Quantification of myocardial blood flow with ultrasound-induced destruction of microbubbles administered as a constant venous infusion. Circulation 1998;97:473-83.

5. Gregg DE, Green JE, Wiggers CJ. Phasic variations in peripheral coronary resistance and their determinants. J Clin Endocrinol Metab 1935;112:362-73.

6. Douglas JE, Greenfield JC Jr. Epicardial coronary artery compliance in the dog. Circ Res 1970; 27:921-9.

7. Chilian WM, Marcus ML. Phasic coronary blood flow velocity in intramural and epicardial coronary arteries. Circ Res 1982;50:775-81.

8. Chilian WM, Marcus ML. Effects of coronary and extravascular pressure on intramyocardial and epicardial blood velocity. Am J Physiol 1985;248:H170-8.

9. Wei K, Le E, Jayaweera AR, Bin JP, Goodman NC, Kaul S. Detection of noncritical coronary stenosis at rest without recourse to exercise or pharmacological stress. Circulation 2002;105:218-23.

10. Wei K, Tong KL, Belcik T, et al. Detection of coronary stenoses at rest with myocardial contrast echocardiography. Circulation 2005;112: 1154-60.

11. Lindner JR, Skyba DM, Goodman NC, Jayaweera AR, Kaul S. Changes in myocardial blood volume with graded coronary stenosis. Am J Physiol 1997;272:H567-75.

12. Buck T, Mucci RA, Guerrero JL, Holmvang G, Handschumacher MD, Levine RA. The power-velocity integral at the vena contracta: a new method for direct quantification of regurgitant volume flow. Circulation 2000;102:1053-61.

KEY WORDS angiography, blood flow, coronary, imaging, ultrasound

5.3. Perspectives

Au cours de ce travail, nous avons démontré in vivo sur modèle porcin que : (1) l'imagerie Doppler ultrarapide avec notre traitement de données permet d'accéder in vivo à la circulation coronarienne intramurale ; (2) l'intégral gain-vitesse était fortement corrélé avec le débit coronarien estimé par bague de débit (r^2 de 0,89 pour 5 animaux) ; (3) l'imagerie ultrasonore ultrarapide avait la capacité d'évaluer la CFR de façon non-invasive (via le test à l'injection d'adénosine) ; et (4) les images de Doppler ultrarapides permettaient de mieux caractériser des tissus nécrosé post infarctus que le B-mode classique. Concernant l'application humaine (n=2), nos résultats ont démontré qu'il est possible de détecter des veines et des artères coronariennes intramurales en transthoracique dans un contexte clinique in vivo.

Maintenant que la preuve de concept a été réalisée, il va falloir montrer que cette technique d'imagerie peut apporter une valeur ajoutée à une pratique clinique. Evidemment, les cardiopathies ischémiques chez l'adulte semblent être une application naturelle et évidente, notamment pour l'évaluation d'une ischémie stable et d'éviter de faire une CFR invasive. De plus, certaines cardiomyopathies, comme la CMH, souffrent d'une atteinte de la microcirculation coronaire qui pourrait impacter sur le pronostic (et donc le suivi) de ces pathologies. Mais à l'heure actuelle, aucune technique d'imagerie ne nous permet de l'évaluer. Le Doppler ultrarapide pourrait apporter des solutions. Enfin, en cardiologie congénitale et malformative, de multiples situations exposent le myocarde à une ischémie, soit par défaut de débit de perfusion intracoronarienne (par exemple dans le cas d'hypoplasie du ventricule gauche après intervention de Norwood avec défaut de montage (Baffa et al. 1992) (Charpie et al. 2001)) ou par hypoxie intracoronarienne (par exemple dans le cas des transpositions des gros vaisseaux (Weindling et al. 1994) (Bonhoeffer et al. 1997)).

Une étude prospective a été débutée à l'hôpital Necker-Enfants malades dans le service de cardiologie pédiatrique, s'intitulant *Evaluation De L'anatomie Et Du Flux Coronarien Par Doppler Ultrafast – Application En Cardiologie Pediatrique, Etude Pilote « Coronaire-Pediatrie »*. Elle bénéficie du financement RMA de la Fondation de l'Avenir, AP-RMA-16-032. L'objectif principal est de comparer la perfusion myocardique dans la transposition des gros vaisseaux avant et après correction chirurgicale, puis à distance de voir si cela est corrélé avec le devenir de ces patients. L'objectif est d'inclure 40 sujets, en deux groupes : groupe « sujets sains » (n=20) et groupe cardiopathie « TGV » (transposition des gros vaisseaux,

n=20). Chaque sujet bénéficiera d'une exploration par échocardiographie et par doppler ultrafast en transthoracique afin d'évaluer l'anatomie et le flux des coronaires intra-myocardiques. Les sujets du groupe « TGV » auront deux évaluations distinctes (avant et après la chirurgie correctrice qui intervient dans les premiers jours de vie). L'analyse statistique sera essentiellement descriptive et évaluera les différences entre chaque groupe. Les inclusions sont actuellement en cours.

Concernant les limites actuelles de la technologie, il est clair que la reconstruction volumique (en non plus en 2-D) sera l'étape suivante. Due à l'architecture complexe du réseau vasculaire coronarien, l'imagerie 3-D sera particulièrement importante pour cette application. Un des avantages majeurs par rapport aux images 2-D est l'évaluation volumétrique du débit sanguin, en remplacement de l'intégral gain-vitesse qui reste une mesure relative et non absolue. Récemment, l'institut Langevin a montré que l'imagerie ultrarapide 4-D pourrait être effectuée en utilisant un système ultrasonore possédant un grand nombre de canaux électroniques programmables et une sonde matricielle (Provost et al. 2014). De façon à accéder au réseau vasculaire coronarien en quatre-dimensions, les équipes de l'institut Langevin ont développé l'imagerie Doppler ultrarapide 4-D avec un traitement d'imagerie dédié, de même que pour l'imagerie 2-D (Correia et al. 2016) (Demené et al. 2016).

L'imagerie Doppler ultrarapide en deux- et quatre-dimensions pourrait devenir un outil d'imagerie important pour le diagnostic ou évaluation des maladies coronariennes, anatomiques ou de perfusion. Les principaux avantages par rapport à d'autres modalités d'imagerie sont l'aspect non-invasif, le faible coût, le temps réel, et le traitement des données pourrait être effectué rapidement lors d'une consultation.

6. Couplage électromécanique

6.1. Introduction et Objectifs

Si on synthétise les choses, le cœur peut être considéré comme un moteur musculaire commandé par des impulsions électriques, dont la mission est de pomper une fraction du volume sanguin dans le circuit vasculaire à chaque excitation électrique reçue.

L'origine de ces impulsions électriques est le nœud sinusal, « pacemaker naturel », qui est un ensemble de cellules auto-excitables et synchronisées d'où part un courant de dépolarisation à destination de toutes les cellules musculaires cardiaques (figure 6). Ces cellules ainsi excitées se contractent dans la direction de leurs fibres, provoquant à chaque battement cardiaque l'éjection de sang des ventricules dans la circulation. Le cœur comporte deux types de cellules musculaires : 1) des cellules qui produisent et conduisent des impulsions ; 2) des cellules qui répondent à ces impulsions par un raccourcissement (contraction). Du point de vue fonctionnel, le myocarde ventriculaire est un syncitium, c'est-à-dire que les cellules ne sont pas isolées les unes des autres : une excitation qui naît quelque part dans les ventricules conduit, quelle que soit sa localisation, à une contraction complète des deux ventricules (Silbernagl, Despopoulos, and Laurent 1992), et les membranes des cellules communiquent par des gap-junctions. Le couplage excitation-contraction repose sur l'intervention d'une « commande calcique » (la concentration Ca2+ à l'intérieur des cellules musculaires cardiaques, elle-même sous la dépendance directe de la différence de potentiel transmembranaire) dans le mécanisme des ponts d'union actine-myosine à la base de la contraction musculaire (Cranefield and Hoffman 1958)(Bers 2002), figure 7. A l'échelle macroscopique, l'activité électrique du cœur se mesure de façon non invasive grâce à l'électrocardiogramme (ECG), qui est un tracé de la différence de potentiel électrique entre 2 électrodes placées à la surface du corps. Il y a plusieurs dérivations standards, chaque dérivation correspondant à une position de ces 2 électrodes de mesure. A l'échelle tissulaire, aucune technique d'imagerie n'est actuellement capable de visualiser la propagation de l'activité mécanique, dépendante donc de l'excitation mécanique. Ce couplage électromécanique permet donc de comprendre qu'en visualisant l'activité mécanique, on peut remonter à l'excitation l'électrique, et par conséquent réaliser une cartographie de cette excitation.

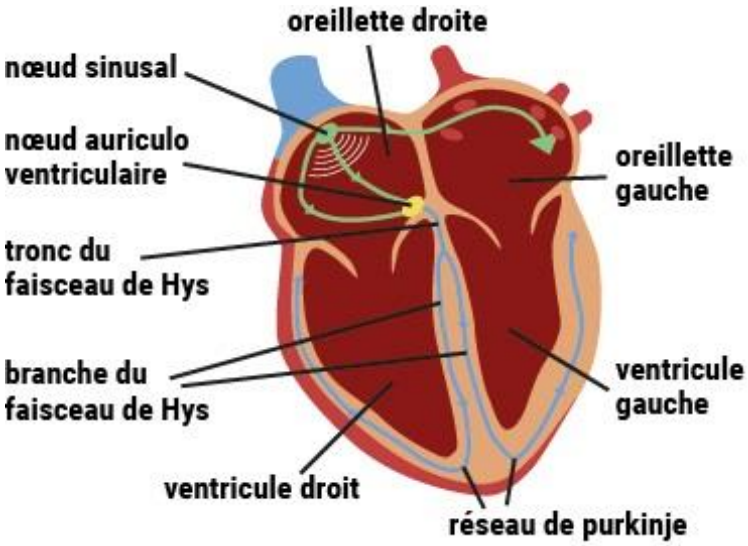

Figure 6 : Le courant électrique physiologique du cœur humain

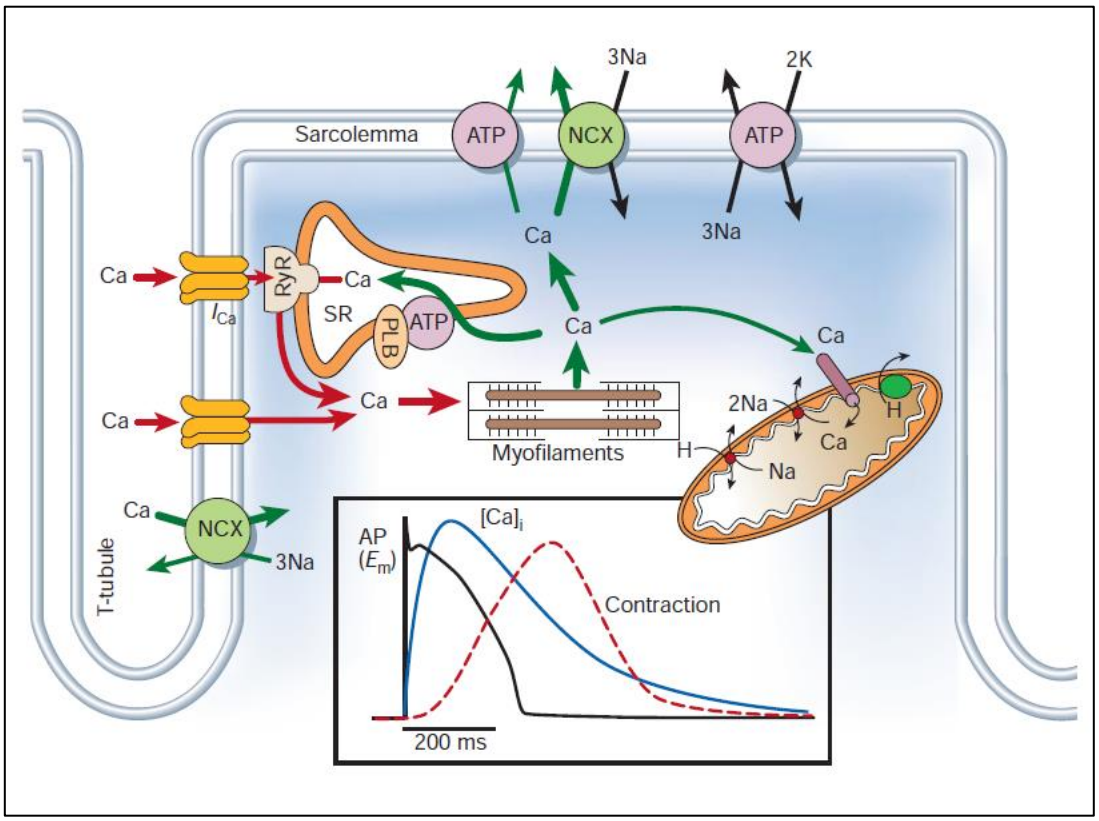

Figure 7 : (D'après Bers et al., *Nature*, 2002) Le transport des ions Ca2+ dans les myocytes ventriculaires, et le phénomène de contraction engendré.

Il y a encore quelques années, le seul moyen d'avoir accès à cette cartographie électrique et les délais d'activation entre deux zones do cœur était de réaliser un cathétérisme cardiaque, ce qui par définition est invasif, donc potentiellement dangereux. Plus récemment, différentes techniques non invasives ont vu le jour, notamment la technique d'imagerie combiné TDM-ECG appelé CardioInsight (Medtronic®) permettant de réaliser une cartographie de l'activité électrique du cœur en trois dimensions et de manière non-invasive (Ramanathan et al. 2004). Les principaux écueils de cette technique sont : 1) l'accès uniquement à l'activité électrique épicardique, et notamment aucune information possible sur les septums intracardiaques ; 2) la lourdeur de la procédure (TDM nécessaire et veste de 252 électrodes) ; 3) le cout de la procédure, qui reste très élevé, notamment à cause de l'ensemble du matériel nécessaire.

En parallèle, l'imagerie des ondes électromécaniques par ultrasons (aussi appelé EWI, pour electromechanical acoustic wave imaging (M. Pernot and Konofagou 2005)(Pernot et al. 2007)) a également été développée pour visualiser et cartographier les déplacements (Konofagou et al. 2010) et les déformations (Provost et al. 2011) du myocarde liés au couplage électromécanique. Les vitesses de propagation du flux électrique dans le myocarde étant de l'ordre du mètre par seconde, seule l'imagerie à haute cadence d'image pouvait permettre la visualisation des ces phénomènes (cf paragraphe 1.2). Il reste cependant à valider certains concepts fondamentaux, à améliorer les techniques d'acquisition et d'analyse du signal acoustique, et enfin à trouver des application cliniques compatibles avec la technique.

6.2. Manuscrit "*Electromechanical wave imaging in human foetus*" (In preparation) et Perspectives

Ce travail est encore en cours et les résultats présentés restent préliminaires et sujets à évolution.

Les troubles du rythme et de la conduction cardiaque chez le fœtus peuvent exposer à un risque de défaut de croissance fœtale, de prématurité, et de mort fœtale ou post-natale immédiate (van Engelen et al. 1994)(Eliasson et al. 2011). Le paradoxe est qu'il est

actuellement très difficile d'avoir accès à l'activité électrique du fœtus, car l'ECG de surface est par définition impossible. Il fallait donc trouver de nouvelles solutions pour tenter d'y avoir accès. Budin et al furent parmi ceux présentant des travaux ayant pour objectif une amélioration du traitement du signal ECG, avec des électrodes placées sur la mère (Budin and Abboud 1994). Puis des techniques d'imagerie, comme le magnétogramme, ont été utilisées en clinique (Kähler et al. 2001) après avoir été testées en preuve de concept (Kariniemi et al. 1974). Malgré tout, c'est à nouveau l'échocardiographie qui s'imposa progressivement comme l'outil le plus applicable et le plus productif pour analyser l'activité électrique fœtale. Hormis le B-mode et les mode TM permettant d'avoir des délais d'activation entre oreillettes et ventricules ou des estimations de durées (systole/diastole), le Doppler tissulaire (TVI) a permis le développement du kinetocardiogramme (Rein et al. 2002) qui apporta quelques résultats notamment dans sa capacité à mieux préciser les délais d'activation entre les cavités cardiaques, principalement grâce à une cadence d'image légèrement supérieure (entre 48 et 136 Hz) aux outils échographiques précédents.

A la lumière de ce qui a été présenté dans le chapitre 6.1, l'ultrafast écho ouvre de nouvelles perspectives pour la visualisation et l'analyse des mouvements cardiaques fœtaux, et par conséquent de l'activité électrique sous-jacente.

Méthodes

5 fœtus (18, 22, 22, 25 et 32 SA) ont été inclus. L'ensemble des paramètres échographiques utilisables ont été collectés chez chaque fœtus (B-mode, Doppler TM, Doppler pulsé et Doppler tissulaire), permettant d'obtenir les données cliniques suivantes : fréquence cardiaque (FC), intervalle RR, durée onde E, durée onde A, durée systole, durée diastole, intervalle PR, durée relaxation isovolumique, durée contraction isovolumique. Dans la continuité des acquisitions cliniques, des acquisitions d'ultrafast écho ont été réalisées en coupe cardiaque fœtale 4 cavités. Les acquisitions ont été faites en utilisant une sonde linéaire (fréquence centrale 6.42MHz, 128 éléments, distance inter-éléments 0.2mm). Les images ultrarapides sont obtenues à une cadence de 2532 images/secondes. Concernant le post-traitement, les signaux RF (radio-fréquence) enregistrés lors de l'acquisition sont encodés (beamformés) en modulation IQ. Les déplacements et déformations inter-frames sont ensuite estimés par un algorithme de Kasai et un estimateur des moindres carrés, respectivement. Une fois les données de déplacement/déformations obtenues, un tracé est effectué sur le BMode (figure 8) afin de sélectionner une région d'intérêt (septum, paroi VG, etc.). Un M-Mode (ou Mode-TM) des déplacements/déformations des points composant le tracé effectué est ensuite affiché (figure 9). En définitive, nous avions accès aux

déplacements, aux vitesses de déplacement, à l'accélération et à la déformation des tissus. L'activité électrique a été obtenue grâce à l'analyse du déplacement et de la déformation du myocarde.

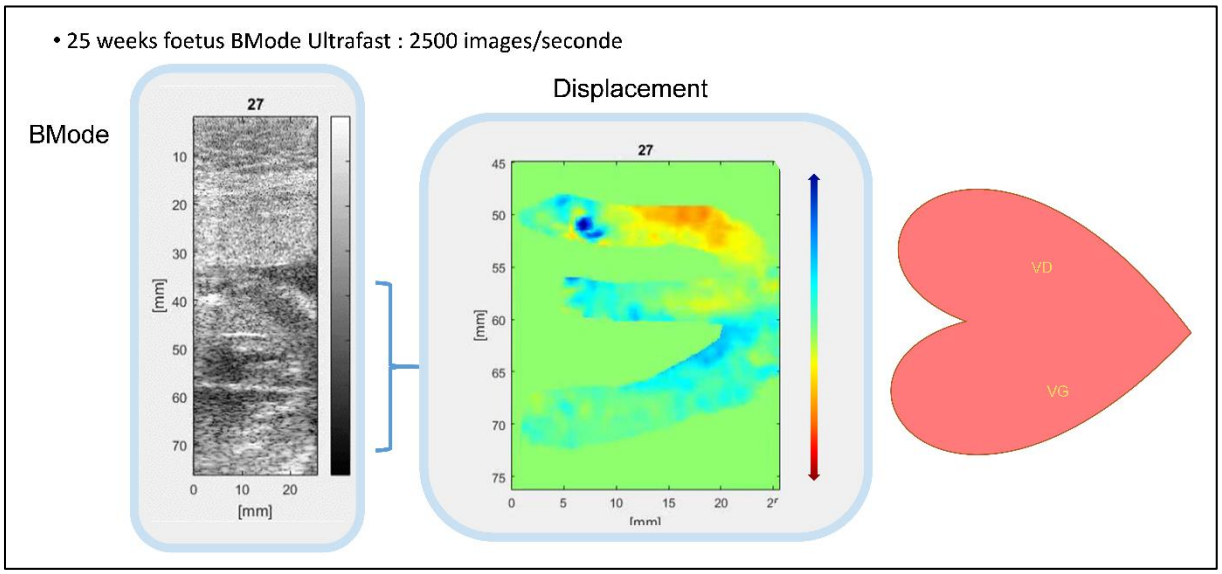

Figure 8 : Visualiation du B-Mode (à gauche) puis du déplacement du myocarde (centre)

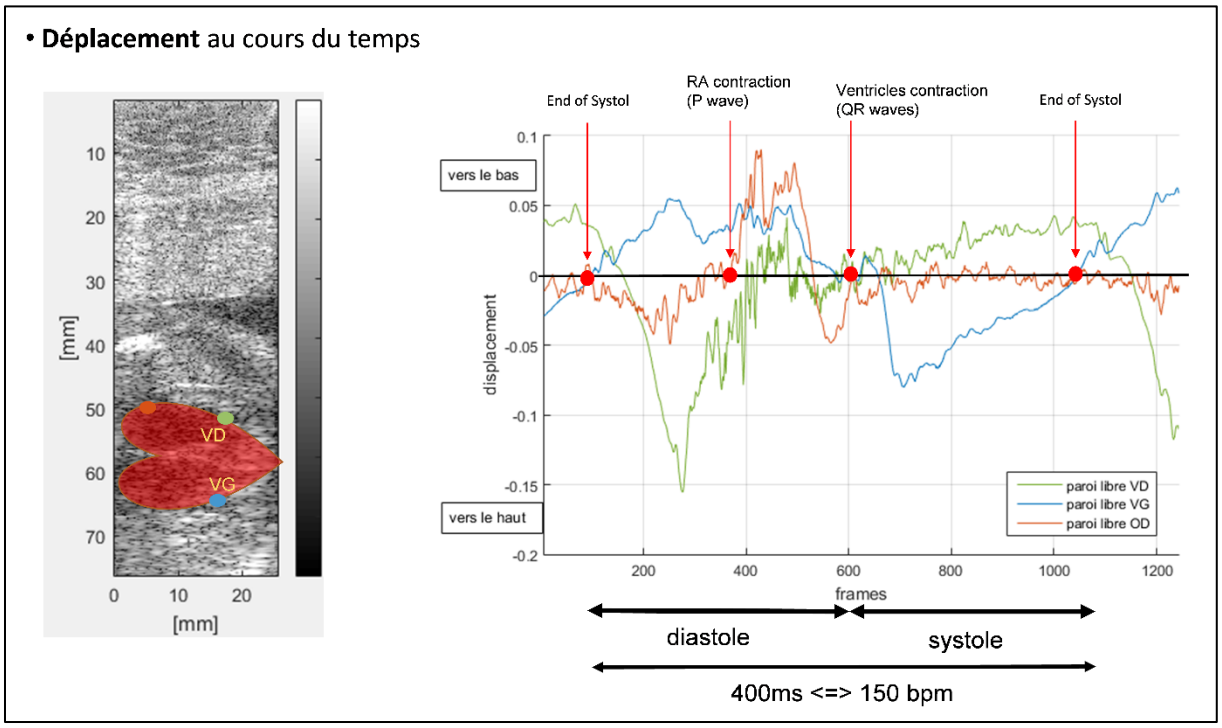

Figure 9 : Représentation spatio-temporelle du déplacement selon trois pixels, localisés dans la paroi libre de l'OD (courbe rouge), la paroi libre du VD (courbe verte) et la paroi libre du VG (courbe bleu).

Résultats

Les 5 fœtus ont été explorés et l'ensemble des datas cliniques a été colligé. Pour chaque fœtus, une cartographie électromécanique a été obtenue par ultrafast écho (figure 10).

Il n'y avait pas de différence statistique entre les datas cliniques et les datas obtenues pour ultrafast écho : FC (p=0.58), RR (p=0.61), PR (p=0.32), Systole aortique (p=0.71).

L'ultrafast écho a permis d'obtenir de nouvelles données anténatales comprenant notamment :

- Temps d'activation auriculaire (moyenne=9ms)
- Vitesse de propagation intra-auriculaire (moyenne=0.65m/s)
- Temps d'activation VG (moyenne=30ms)
- Temp d'activation VD (moyenne=33ms)
- Vitesse de propagation septum interventriculaire (moyenne=3.4m/s)
- Vitesse de propagation paroi libre VG (moyenne=0,52m/s)
- Vitesse de propagation paroi libre VD (moyenne=0,46m/s)

De plus, nous avons observé chez ces cinq fœtus (figure 11 et 12) que la propagation de l'activité électromécanique dans le septum interventriculaire se faisait de la base vers la pointe, et non pas du tiers apical qui remonte vers la base comme décrit chez l'adulte (Wyman et al. 1999).

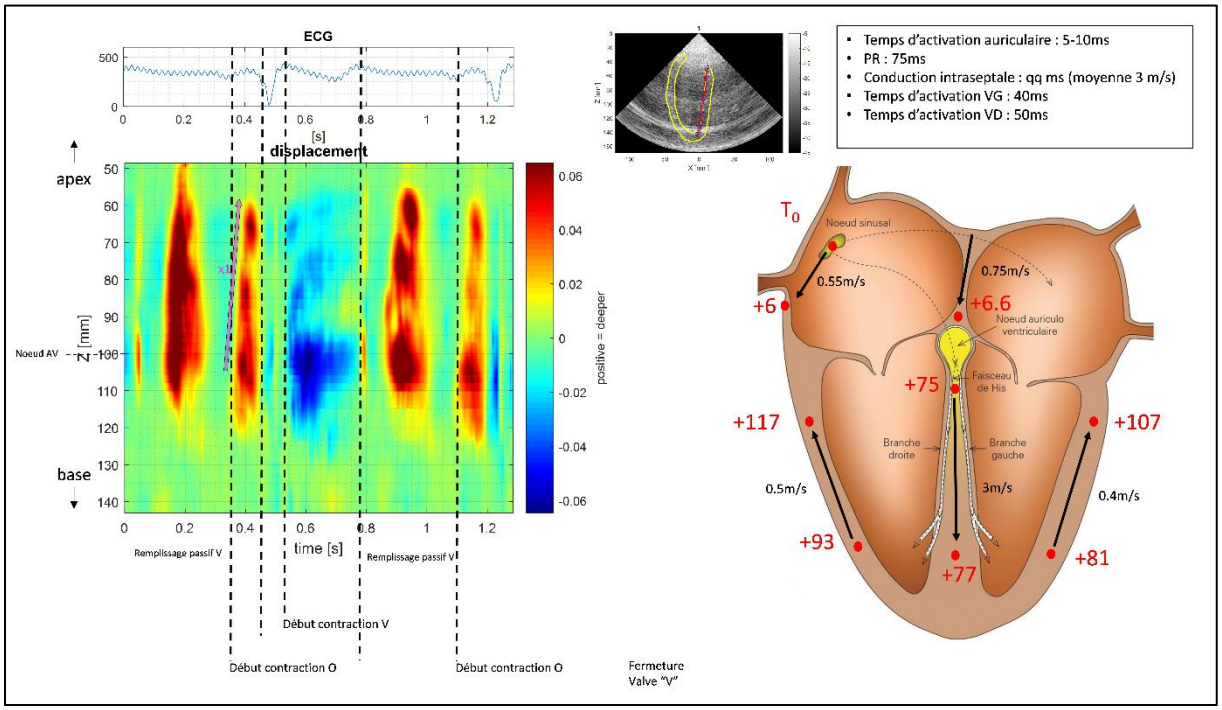

Figure 10 : Représentation spatiotemporelle (à gauche) du déplacement des pixels le long du septum interventriculaire, avec au final obtention de vitesses de propagation et cartographie de l'activité électromécanique (à droite)

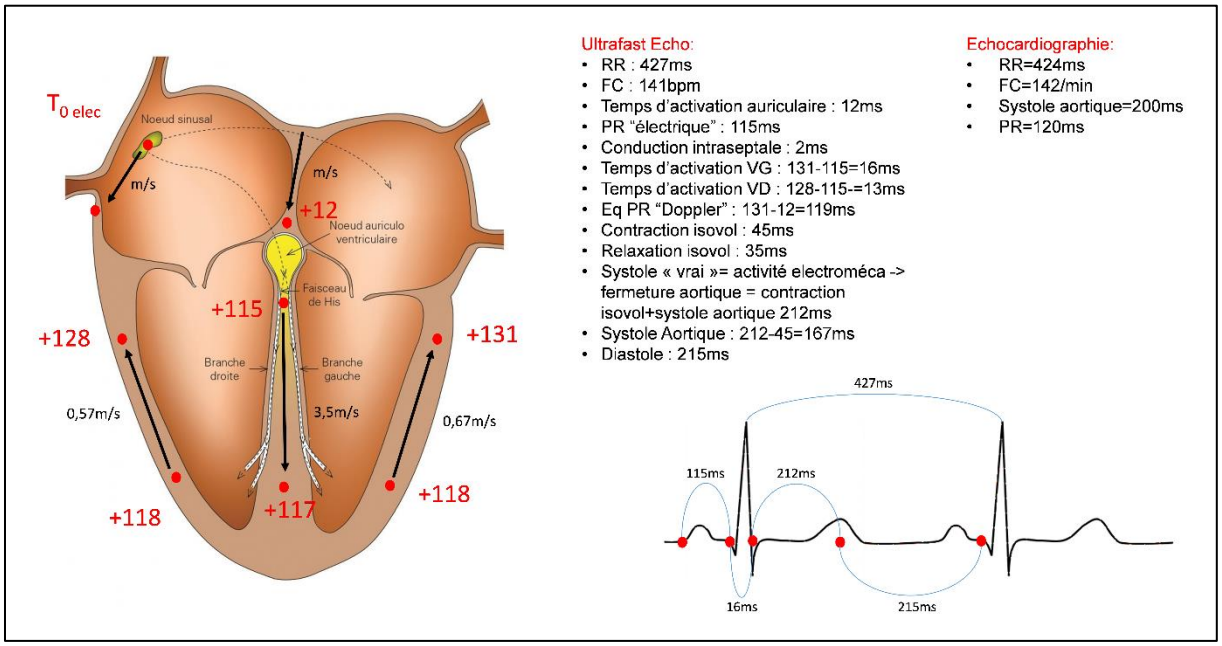

Figure 11 : Exemple de cartographie de l'activité électromécanique (à gauche). Résumé des délais d'activation, des vitesses et des intervalles de temps obtenus par Ultrafast echo (au centre), avec données cliniques en comparaison (à droite)

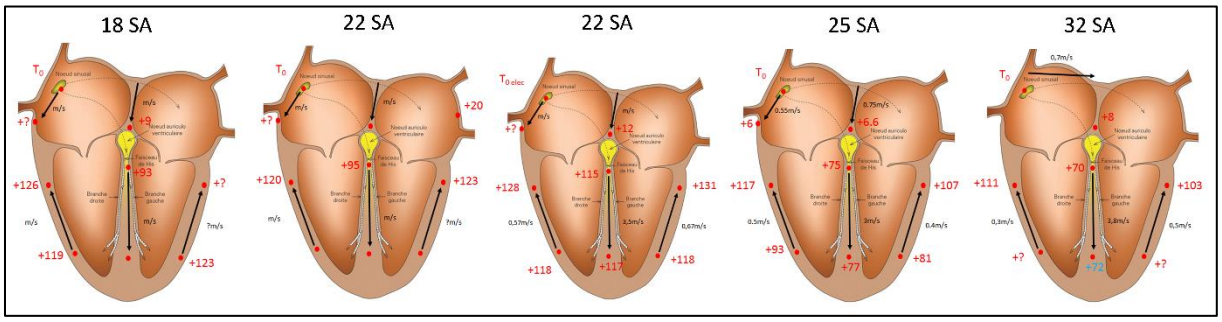

Figure 12 : Résumé des 5 fœtus explorés avec cartographie électromécanique.

Discussion du travail en cours, de ses limites et de ses perspectives

Les résultats de notre travail ainsi que leur interprétation restent sujet à caution, car ils sont encore inaboutis. Malgré tout, ils nous ont permis de savoir que l'application de l'ultrafast echo sur le fœtus était possible et surtout aboutissait à des observations nouvelles. En effet, la visualisation des déplacements et/ou des déformations du myocarde à cette échelle temporelle (2000 à 3000 images/seconde) donne accès à des informations encore inconnue chez le fœtus humain. Les temps d'activation, les vitesses de propagation, les voies de conduction intra-septale, ou la variation en fonction du terme (semaines d'aménorrhée) sont des données électromécaniques qu'aucun autre type d'exploration n'avait été capable de fournir à ce jour.

Il reste cependant plusieurs limites à ce travail :

- Le post-traitement et l'interprétation du signal : les cinq fœtus ont été analysés à travers des reconstructions spatiotemporelles qui étaient ensuite interprétées manuellement par deux opérateurs. Cela implique une certaine subjectivité et il est évident qu'un post-traitement automatisé serait préférable, afin d'essayer de garantir une reproductibilité des résultats.
- L'acquisition en 2-D : nos acquisitions ont été réalisées avec une sonde linéaire, permettant uniquement une imagerie en 2-D. Cela nous a permis de reconstruire une carte d'activité sur ce plan d'imagerie, mais sans pouvoir prendre en compte les autres segments et volumes du cœur fœtal.
- La comparaison à un gold standard : ce travail a été initialement motivé par le fait qu'il était impossible d'avoir accès à une cartographie d'activation électrique chez le fœtus, ou tout simplement un ECG fœtal. Nos résultats souffriront donc, par définition, d'un manque de comparaison avec un outil permettant d'estimer ces données.

Concernant les perspectives, il reste un travail d'analyse de données à réaliser. En effet, certaines cartographies obtenues souffrent de quelques données manquantes qu'il faut compléter avant de pouvoir conclure. De plus, ce travail nous a poussés à reconsidérer les méthodes d'acquisition et d'analyse, selon les limites évoquées ci-dessus. En premier lieu, l'utilisation d'une sonde 3-D avec reconstruction volumique semble l'avenir indispensable de la cartographie électromécanique par ultrasons. Victor Finel, étudiant en thèse à l'institut Langevin, entreprend actuellement ces recherches et fournit des premiers résultats positifs. En parallèle, le même groupe de recherche réalise actuellement des validations sur cœurs battants isolés (type Langendroff) afin d'optimiser les modes d'acquisitions et de confirmer les premiers résultats obtenus, en ayant la possibilité de les comparer à un gold standard

(électrodes épicardiques). Enfin, un autre travail a été entrepris, en parallèle des acquisitions chez le fœtus humain. Des acquisitions du même type, mais avec des sondes phased-array (cf paragraphe 1.1), ont été réalisées chez l'adulte, en collaboration avec l'équipe de cardiologie congénitale du CHU Haut-Lévêque de Bordeaux (France). L'objectif de ce travail est de montrer que l'ultrafast écho peut réaliser des cartographies d'activation électrique, en les comparant aux acquisitions CardioInsight et à des cartographies invasives. Nous espérons que ce travail additionnel pourra apporter d'autres arguments sur la faisabilité et l'intérêt de cette technique en pratique clinique.

7. Thérapie par ultrasons focalisés

7.1. Introduction et Objectifs

L'action « mécanique » du phénomène de cavitation (cf paragraphe 1.3) interpelle depuis une quinzaine d'années la communauté cardiologique par ses possibles applications. Les cardiopathies ischémiques avec l'IM post ischémique sur cordage restrictif, les cardiopathies congénitales avec la nécessité d'engendrer des shunts additionnels (ex : atrioseptostomie) ou encore les cardiopathies valvulaires obstructives (et particulièrement le Rétrécissement Aortique Calcifié, RAC) seraient des applications thérapeutiques potentielles du phénomène de cavitation. Encore faut-il développer et maitriser la technologie.

A l'heure actuelle, les différentes options pour perforer ou modifier le tissu cardiaque (ou l'anatomie des cavités cardiaques) sont la chirurgie et le cathétérisme interventionnel. Bien que ces deux outils thérapeutiques aient été couronnés de succès, les complications qui peuvent en résulter sont une des principales limites à leur indication. En effet, toute décision thérapeutique impliquant la chirurgie ou le cathétérisme interventionnel concernant la prise en charge d'une cardiopathie doit prendre en considération la balance « bénéfice-risque » de cette stratégie. Dans cette réflexion portant sur la diminution du risque thérapeutique, les stratégies endovasculaires (par cathétérisme interventionnel) ont été une réelle révolution. La chirurgie n'était plus l'unique possibilité de stratégie interventionnelle. Cependant, comme l'outil échographique, le cathétérisme, qui est apparu dans les années 60, fut d'abord exclusivement un outil diagnostique. C'est dans un second temps qu'une perspective thérapeutique apparut chez les cathétériseurs. En conséquence, le cathétérisme interventionnel est actuellement un outil thérapeutique prédominant chez l'adulte (coronarographie, valvulation cardiaque percutanée, implantation de prothèse, vasculaire périphérique, AVC) ainsi que chez l'enfant, qui retrouve les mêmes champs d'application que chez l'adulte.

Cependant, le cathétérisme interventionnel connait des limites et des risques inhérents à sa définition, car le cathétérisme est et restera une procédure invasive. Et comme lui il y a 50 ans, l'échographie propose depuis quelques années une évolution technologique qui ouvre une porte sur l'option de « l'échographie interventionnelle ». Celle-ci existe depuis une vingtaine d'années environ avec l'HIFU (High Intensity Focused Ultrasound) qui permet une destruction par la chaleur de tissus en vivo (tumeur de prostate (Madersbacher et al. 1995) ou adénome hyperparathyroidien) ou avec la lithotripsie ultrasonique utilisée pour le traitement des calculs rénaux (Sackmann et al. 1988).

Une autre technique utilisant des ultrasons ayant un impact tissulaire est apparue depuis quelques années : l'histotripsie (cf paragraphe 1.3). Son application semble très prometteuse en cardiologie. Cependant, les mouvements du cœur rendaient difficile d'un point de vue technique l'indication aux ultrasons focalisés.

C'est la prise en charge de l'hypoplasie du VG (hypoVG) avec septum inter-auriculaire (SIA) intact ou restrictif qui a poussé les équipes médicales et scientifiques à reconsidérer l'intérêt des procédés non-invasifs en cardiologie. Evidemment, la première révolution pour le pronostic de l'hypoVG fut chirurgicale avec la procédure de Norwood (1981). Mais avec le recul, nous nous sommes rendus compte que le pronostic de l'hypoVG à SIA intact et restrictif restait sombre (Atz et al. 1999), et cela malgré le développement du cathétérisme post et pré natal (Vlahos et al. 2004)(Marshall et al. 2004). Une équipe en particulier (à Ann Arbor, Michigan, USA) a décidé d'explorer d'autres voies thérapeutiques et s'est particulièrement concentrée sur l'histotripsie, qui avait la vertu évidente d'offrir une solution non-invasive, mais qui était à l'époque un simple concept biophysique.

La première publication de l'application de l'histotripsie en cardiologie parut en 2004 (Xu et al. 2004). Les auteurs démontrèrent que la réalisation d'une perforation d'un septum inter-auriculaire in vitro par phénomène de cavitation était possible [figure 13].

Figure 13 (Xu et al., 2004)

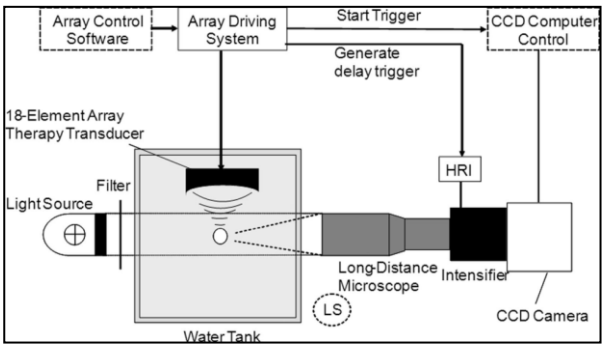

Schéma simplifié du montage matériel permettant le phénomène de cavitation avec transducteur multi-éléments

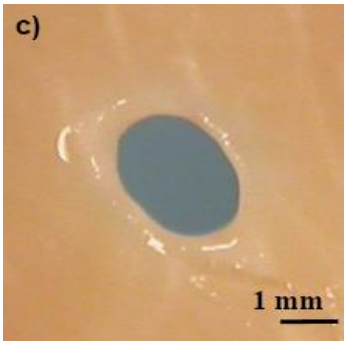

Perforation d'un septum inter-auriculaire (in vitro) par histotripsie

Trois ans plus tard, en 2008, cette équipe d'Ann Arbor détaillait un peu plus la technique en précisant le phénomène biophysique de cavitation et l'importance des ondes

de chocs à hautes fréquences nécessaires à la majoration de la pression intra-cavitaire (dans une microbulle d'air) permettant la lyse tissulaire (Xu et al. 2008). L'année suivante, toujours par la même équipe, un article fut publié permettant d'évoquer les possibles effets secondaires de la procédure, notamment le phénomène embolique (Xu et al. 2009) [figure 14].

Figure 14 (Xu et al., 2009, Ultrasound in medecine)

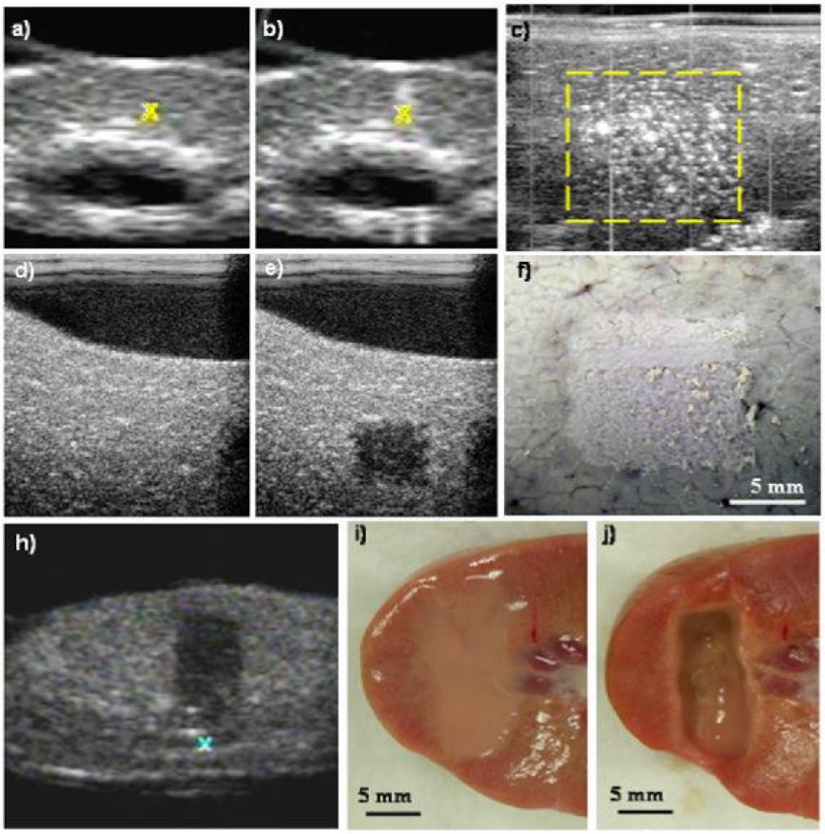

Images échographiques et macroscopiques à différents temps de procédure de l'histotripsie. Les images i et j représentent un rein en fin de procédure (i) puis après nettoyage des tissus lysés pour analyse des micro-fragments

Mais la publication majeure parut en 2010 dans la revue Circulation (Xu et al. 2010). Ce fut la première fois que l'histotripsie fut appliquée in vivo (modèle canin) à visée cardiologique. Leurs résultats permirent de démontrer que la réalisation d'une perforation d'un septum inter-auriculaire à cœur battant par voie non invasive était possible et reproductible [figure 15]. Ils expliquent d'ailleurs que l'application de la procédure a été étudiée en anatomopathologie et histologie, ce qui permit de démontrer l'efficacité et la précision de la technologie.

Figure 15 (Xu et al., 2010, Circulation)

Table 1. Summary of Results

Canine	Treatment Time, min	Atrial Septal Axial Motion, mm	Ultrasound (Center),* mm	ASD, mm Pathology†		Hemorrhage, mm Pathology‡	
				RA Side	LA Side	RA Side	LA Side
1	6	5.2	1.7	3.4	2.9	1.2	1.9
2	10	17.1		No ASD was created			
3	8	8.4	3.3	5.1	2.2	2.3	2.1
4	6	10.3	5.0	5.7	2.4	4.2	2.2
5	10	10.0	4.2	4.7	2.6	1.6	2.3
6	6	8.7	3.0	6.6	3.0	1.6	2.0
7	6	9.7	3.0	4.5	2.2	2.3	1.7
8	6	6.5	3.2	6.2	2.5	3.2	2.4
9	16	6.1	4.0	No pathology result§			
10	12	8.1	3.6	4.1	3.3	4.0	2.6
Mean	8.4	8.1	3.4	5.0	2.6	2.6	2.2
SD	3.4	3.3	0.9	1.1	0.4	1.1	0.3

Résultats de l'étude parue en 2010 dans Circulation concernant l'application in vivo (modèle canin) de l'histotripsie.

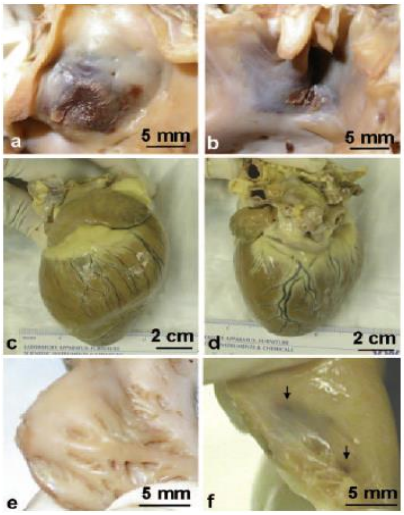

Exploration anatomopathologique des cœurs canins après procédure d'histotripsie

Par la suite, cette équipe de biophysiciens et de médecins a publié différents articles permettant de démontrer que la procédure pouvait se réaliser en transthoracique (Miller et al. 2012) ([figure 16] sans sternotomie, ce qui était une limite majeure de l'étude de 2010, et que cette technologie pouvait avoir des applications évidemment en anténatal (Kim et al. 2011) [figure 17] ainsi que dans la thrombolyse (Maxwell et al. 2011). Enfin, un dernier article plus récent, publié en 2014, a permis d'avoir des résultats de l'efficacité de l'histotripsie, in vitro, sur différents type de tissus biologiques (Vlaisavljevich et al. 2014).

Figure 16 (Miller et al., 2012, Catheterization and cardiovascular interventions)

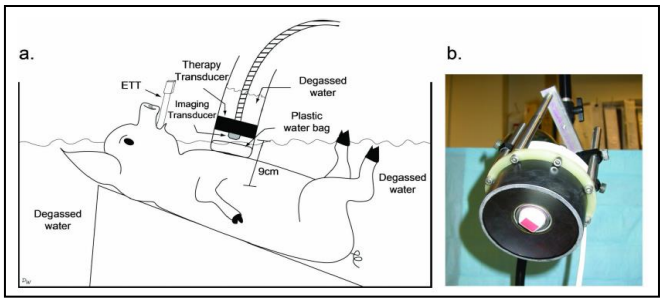

Réalisation de l'histotripsie en trans-thoracique (modèle porcin). Procédure réaliser en milieu liquide pour conserver en échogénicité permettant aux ondes de chocs d'arriver à cible. L'image b montre une photo du transducteur avec la sonde écho de tracking au centre.

Figure 17 (Kim et al., 2011, Ultrasound in obstetrics & gynecology)

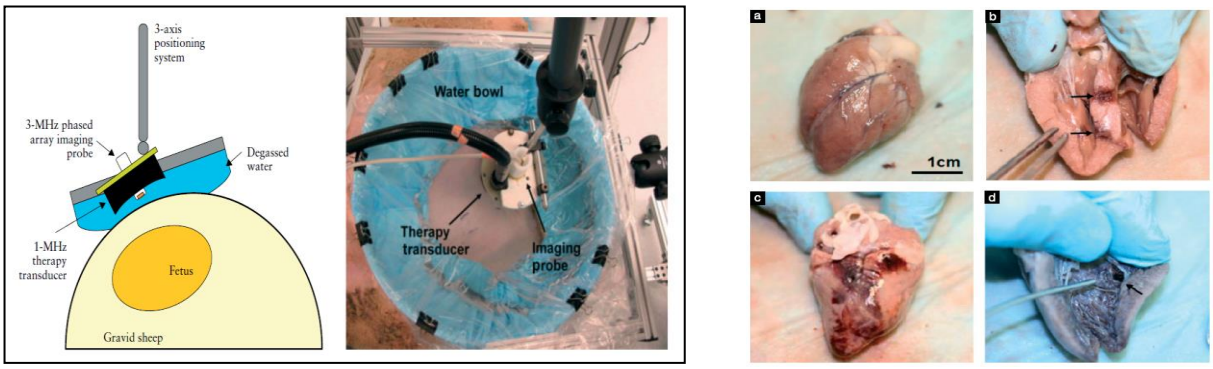

Réalisation de l'histotripsie en anté-natal (modèle canin). Analyse anatomopathologique de cœurs canins après procédure d'histotripsie in utéro (in vivo). Les flèches montrent les zones cibles avec perforations des parois (septum inter-ventriculaire sur images b et d)

Cependant, force est de constater que cette équipe du Michigan, pionnière dans le développement et l'application du phénomène de cavitation par ultrasons, n'a plus publié de travaux sur l'applicatif cardiaque depuis 2014. Ils s'étaient probablement beaucoup focalisés sur l'atrioseptostomie et ses vertus pour l'hypoVG, et n'ont pas réussi à aller jusqu'au *first-in-man*, pour les limites et les contraintes que nous évoquerons dans les chapitres suivants de ce manuscrit.

Durant mon travail de thèse à l'Institut Langevin, nous avons repris la technologie "en l'état", c'est à dire un monoélément émettant des ultrasons focalisés en un point focal fixe, et avons cherché à élargir le champs applicatif du phénomène de cavitation. Le but évidemment, comme dans les travaux présentés dans les chapitres précédents, était de réfléchir aux applications afin d'améliorer la technologie, notamment avec la cavité à retournement temporel et le travail de thèse de Justine Robin (Robin et al. 2017b)(J Robin et al. 2017)(Robin et al. 2017a).

Pour cela, deux applications ont été développées et sont présentées dans les chapitres qui suivent: la section de cordage valvulaire et l'assouplissement de feuillet valvulaire calcifié.

7.2. Section de cordage valvulaire

7.2.1. Présentation du travail

L'enjeu de ce travail était d'aller aux limites de la technologie disponible tout en proposant une nouvelle application clinique.

Les premières limites de la technologie étaient principalement la capacité à être précis dans le traitement et la capacité à agir sur des structures résistantes. Pour cela, le cordage valvulaire semblait être une cible « parfaite », car c'est une structure fine et très mobile, et surtout particulièrement résistante (Kunzelman and Cochran 1991). De plus, la section de cordage valvulaire mitraux est réalisée en pratique chirurgicale dans certaines situations d'insuffisance mitrale sur phénomène restrictif suite à une cardiopathie ischémique. Ce sont Emmanuel Messas et Robert Levine qui présentèrent en premier l'approche théorique sur modèle animal (Messas et al. 2001)(Messas et al. 2001) puis l'application clinique en découla (Wakiyama et al. 2004)(Borger et al. 2007), voire s'élargissait (Ferrazzi et al. 2015). Cependant, ce geste thérapeutique n'est réalisé actuellement que de manière chirurgicale en pratique clinique, donc nécessitant une sternotomie et une circulation extra-corporelle.

Développer une stratégie non-invasive pour la section de cordage valvulaire devenait donc un enjeu à la fois technologique et médical. Le phénomène de cavitation présentait beaucoup d'avantages pour être testé.

7.2.2. Manuscrit "*Pulsed cavitational ultrasound for non-invasive chordal cutting guided by real-time 3D echocardiography"* + Editorial Comment

Ce travail est publié dans European Heart Journal – Cardiovascular Imaging (Villemain et al. 2016)

European Heart Journal – Cardiovascular Imaging (2016) **17**, 1101–1107
doi:10.1093/ehjci/jew145

Pulsed cavitational ultrasound for non-invasive chordal cutting guided by real-time 3D echocardiography

Olivier Villemain[1,2]*, Wojciech Kwiecinski[2], Alain Bel[3,4], Justine Robin[2], Patrick Bruneval[5,6], Bastien Arnal[2], Mickael Tanter[2], Mathieu Pernot[2†], and Emmanuel Messas[1†]

[1]Cardio-Vascular Departement, Hôpital Européen Georges Pompidou, Université Paris Descartes, UMR 970 Paris, France; [2]Institut Langevin, ESPCI, CNRS, Inserm U979, PSL Research University, France; [3]Cardiovascular Surgery, Hôpital Européen Georges Pompidou, Université Paris Descartes, Paris, France; [4]Laboratoire de recherches Biochirurgicales de la Fondation Alain Carpentier; [5]INSERM PARCC U970; and [6]Department of Pathology, Hôpital Européen Georges Pompidou, Université Paris Descartes, Paris, France

Received 20 June 2016; accepted after revision 10 April 2016; online publish-ahead-of-print 12 August 2016

Aims Basal chordae surgical section has been shown to be effective in reducing ischaemic mitral regurgitation (IMR). Achieving this section by non-invasive mean can considerably decrease the morbidity of this intervention on already infarcted myocardium. We investigated *in vitro* and *in vivo* the feasibility and safety of pulsed cavitational focused ultrasound (histotripsy) for non-invasive chordal cutting guided by real-time 3D echocardiography.

Methods and results Experiments were performed on 12 sheep hearts, 5 *in vitro* on explanted sheep hearts and 7 *in vivo* on beating sheep hearts. *In vitro*, the mitral valve (MV) apparatus including basal and marginal chordae was removed and fixed on a holder in a water tank. High-intensity ultrasound pulses were emitted from the therapeutic device (1-MHz focused transducer, pulses of 8 μs duration, peak negative pressure of 17 MPa, repetition frequency of 100 Hz), placed at a distance of 64 mm under 3D echocardiography guidance. *In vivo*, after sternotomy, the same therapeutic device was applied on the beating heart. We analysed MV coaptation and chordae by real-time 3D echocardiography before and after basal chordal cutting. After sacrifice, the MV apparatus were harvested for anatomical and histological post-mortem explorations to confirm the section of the chordae. *In vitro*, all chordae were completely cut after a mean procedure duration of 5.5 ± 2.5 min. The procedure duration was found to increase linearly with the chordae diameter. *In vivo*, the central basal chordae of the anterior leaflet were completely cut. The mean procedure duration was 20 ± 9 min (min = 14, max = 26). The sectioned chordae was visible on echocardiography, and MV coaptation remained normal with no significant mitral regurgitation. Anatomical and histological post-mortem explorations of the hearts confirmed the section of the chordae.

Conclusions Histotripsy guided by 3D echo achieved successfully to cut MV chordae *in vitro* and *in vivo* in beating heart. We hope that this technique will open the door in the near future to the non-invasive treatment of functional IMR.

Keywords ultrasonics • mitral regurgitation • surgery

Introduction

Minimally invasive therapeutic approaches are becoming more and more available in valvular surgery thanks to the progress of 3D multimodality imaging[1] and therapeutic devices. Real-time 3D echocardiography has emerged in the cardiovascular (CV) imaging world 15 years ago, and since that time, this technique has helped to better understand and describe valve disease.[2] Ischaemic mitral regurgitation (IMR), which is caused by 3D left ventricle (LV) remodelling displacing papillary muscle away from the annulus,[3] appears in more than 20% of myocardial infarction[4] (MI) and increases the mortality by two-fold.[5] Messas and Levine[6,7] described thanks to this new understanding of IMR a new surgical technique called 'chordal cutting', which target basal chordae attached to the body of the anterior leaflet and which are mostly responsible of the apical tenting and leaflet tethering of the mitral valve (MV). This surgical technique was then applied by multiple teams[8,9] all over the world, along with other cardiac indications such as dilated heart with mitral

* Corresponding author. Tel: +33 1 80 96 30 40, Fax: +33 1 80 96 33 55. E-mail: olivier.villemain@inserm.fr

† M.P. and E.M. contributed equally to this work.

Published on behalf of the European Society of Cardiology. All rights reserved. © The Author 2016. For permissions please email: journals.permissions@oup.com.

Downloaded from by guest on September 25, 2016

regurgitation (MR).[10] This variability of clinical applications of chordal cutting is part of the widespread recognition of the need for subvalvular repair in front of MR.[11,12]

Achieving to cut this chordae non-invasively will improve considerably the benefice/risk ratio of MV repair in this patient in whom the real benefit of this technique is still debated.[4,13] High-intensity focused ultrasound (HIFU) has been proposed for non-invasive section of MV basal chordae[14]; however, this approach remains limited *in vivo* due to the thermal mechanism of HIFU which is not well adapted to the treatment of rapid moving cardiac tissues.

Cavitational ultrasound therapy has emerged in the past decade[15] as another non-invasive surgical tool that uses very short, high-pressure ultrasound pulses to generate a dense, energetic, lesion-producing bubble cloud. The so-called histotripsy treatment can create controlled tissue erosion on a fluid–tissue interface (for example, cardiac applications[16–18]), well-demarcated tissue fractionation within tissue,[19,20] and controlled fragmentation of model kidney stones at a fluid–stone interface.[21,22] This technology has been explored for ~10 years for therapeutic cardiac applications. The perforation of the cardiac septum by histotripsy (including inter atrial septum) provided a potential new therapeutic method for some congenital heart diseases, such as hypoplastic or restrictive LV intact inter atrial septum.[17]

The goal of our study was to evaluate the feasibility of a non-invasive chordal cutting technique using histotripsy under the guidance of real-time 3D echocardiography. We tested this new technique on normal valve *in vitro* and *in vivo* on sheep beating hearts.

Methodology

Ultrasound generation and histotripsy acoustic parameters

A 916-kHz focused single-element transducer (f-number = 1, Imasonic®, Besançon, France) was used to generate histotripsy. Its focal length is of 64 mm. The transducer was driven by a high-voltage amplifier (RITEC, Warwick, USA). Tissue erosion was produced using 10-cycle pulses, pulses of 8 μs duration, delivered at a pulse repetition frequency (PRF) of 100 Hz. The pressure peak amplitude at the focal spot was estimated to be 80 MPa positive peak and −17 MPa negative peak. The transducer was immersed in a heated, degassed external water bag (Supplementary data online, *Figure S1*). The same material was used for *in vitro* and *in vivo* procedures.

3D Echocardiography guidance and monitoring

3D Echocardiography was used to guide and monitor the treatment. An IE33 (Philips) scanner and X5-1 probe (xMATRIX array, 3 MHz, 3040 elements with microbeam-forming) were used. The imaging probe was attached onto the lateral side of the histotripsy transducer, with an angle of 45° (Supplementary data online, *Figure S1*) using a dedicated holder. The focal spot of the histotripsy transducer was positioned on the central axis of the imaging probe at a depth of 60 mm. A biplane imaging mode with two imaging planes set at 90° was used during the whole procedure. The histotripsy focal spot was visible within the two imaging planes as a small cloud of bubbles. The combination of histotripsy transducer and imaging probe was called the 'therapy device'. The same material was used for *in vitro* and *in vivo* procedures.

In vitro procedure (explanted sheep heart)

Five sheep hearts were explanted and then preserved in physiological serum (NaCl 4%), at +4°C temperature. Sheep hearts were used for the *in vitro* procedure 48 h after having been harvested. The anterior papillary muscle and the anterior MV leaflet were then individualized, keeping all concerned chordae intact (marginal and basal chordae) between the two structures. They were then fixed with a holder in a water tank filled with degassed saline. The set of anatomical structures was fixed during the procedure. We applied histotripsy on five basal and five marginal chordae. The initial diameter (or thickness) of the chordae was measured thanks to a calliper measurement system (with an accuracy of 1 μm). The therapeutic device was placed at a distance of 64 mm towards from the MV apparatus. The procedure duration to complete the chordae section was measured.

In vivo procedure

Seven sheep [race: Ile de France, weight: 39 kg (min = 32 kg, max = 48 kg)] were anaesthetized with thiopentothal (0.5 mL/kg), intubated and ventilated at 15 mL/kg with 2% isoflurane and oxygen. A median sternotomy was performed, and the thorax was filled with degassed saline water. The therapy device was immersed in the water in the thoracic cage, facing the LV's free wall. Echocardiography was initially performed to ensure the absence of heart disease or abnormal chordae implantation. The basal chordae of the anterior leaflet was identified anatomically by echocardiography, and the therapy device was manually positioned for the focal spot to be placed on the basal chordae. With the focal spot in the target area, we performed repeated histotripsy treatments, each 10 min long. Between each treatment, we made a complete echocardiographic assessment. The procedure was stopped when the target chordae was cut. Thirty minutes after the chordal cutting, we analysed the evolution of the MV and LV by echocardiography. The animal was then sacrificed (Dolethal intravenous injection, 1 mL/kg).

The animal procedures were in accordance with institutional guidelines (national reference number of the study: 02255.01).

Anatomic exploration after *in vivo* procedure

The heart was explanted in order to achieve a macroscopic anatomical analysis. The heart incision was achieved through the ascending aorta to the heart's apex (with complete section of the aortic annulus). The MV was then released. The posterior and anterior leaflets were analysed with inspection of all concerned chordae. Finally, the other anatomical structures were thoroughly analysed to detect secondary lesions especially the LV free wall from where the histotripsy went.

Histological exploration

Immediately after the sacrifice and the anatomic exploration of the heart, all the anatomic structures adjacent to the sectioned basal chordae (the anterior papillary muscle, the sectioned chordae, and the anterior mitral leaflet) were dissected and fixed in formalin. Both edges of the cut chordae (the part close to the leaflet insertion and the distal part) were embedded in individual paraffin blocks. Serial sections were stained with H&E (haematoxylin and eosin) for histopathological analysis.

Results

In vitro procedure

All the chordae were cut after a maximal treatment duration of 9 min (see *Table 1*). The chordae's average diameter was 0.45 mm

Downloaded from by guest on September 25, 2016

(0.22–0.74). The average time to complete the section was 5.5 ± 2.5 min (min = 3, max = 9).

For basal chordae, the average diameter was 0.60 mm (0.43–0.74) with an average time of 7 min (min = 5, max = 9) to complete the section. For marginal chordae, the average diameter was 0.30 mm (0.22–0.42) with an average time to complete section of 4 min (3–5).

A video of one of our *in vitro* procedures is available in the Supplementary data online, *In vitro procedure*.

As shown in *Figure 1*, the procedure duration correlated to some extent with the thickness of the chordae (R^2= 0.65).

In vivo procedure

Chordal cutting was achieved in all animals, which was the original goal. For all the sheep, the haemodynamic tolerance during the entire procedure was excellent. The average process time was 20 ± 9 min (min = 14, max = 26). The section of basal chordae of the anterior MV was visible by echocardiography in all experiments and confirmed by post-mortem anatomic exploration (*Figure 2*). A video of an example of our *in vivo* procedure is available in the Supplementary data online, *Example of application*.

In five sheep, only the targeted basal chordae appeared to be cut (*Table 2*). No haemodynamic consequences of the chordal cutting (no MR, prolapse, or heart failure) were observed on these animals, and the section was visible by ultrasound acquisitions (monitoring probe). A floating chordae was visible on the echo images after histotripsy (*Figure 3*). In the two first sheep, marginal chordae were also cut, and a small haematoma on LV wall was detected. This effect corresponds to the learning curve of the adjustment of the device's power and precision. After improving the focus point localization and the power of the device, severed marginal chordae or LV haematoma was not anymore observed.

After sacrifice, during anatomical exploration, we confirmed the section of the anterior basal chordae (middle segment section) for all the sheep. The rest of the post-mortem cardiac exploration revealed no other lesion (apart from the LV haematoma of the first sheep).

The histological analysis of the sectioned basal chordae showed partial (i.e. ulceration) and complete cut of the chordae (*Figure 4*). The section was smooth, with no indication of the tissue fragment presence. The collagen bundles making the chordae tendineae remained compact and were not disrupted in the cutting area. There was no histological evidence for acute inflammation or acute thrombosis in the sites of the cut or ulceration.

Table 1 Characteristics of *in vitro* chordal cutting

	1	2	3	4	5
Basal chordae (five chordae)					
Diameter (mm)	0.61	0.64	0.43	0.57	0.74
Time to cut (min)	5	9	7	6	8
Marginal chordae (five chordae)					
Diameter (mm)	0.24	0.22	0.36	0.42	0.27
Time to cut (min)	4	4	4	5	3

Discussion

In this study, we have demonstrated that the section of cardiac chordae by real-time 3D echo-guided histotripsy was possible, through *in vitro* and *in vivo* procedures. To our knowledge, it is the first time that chordal cutting was achieved remotely in a beating heart.

Histotripsy has been envisioned for a wide variety of applications in non-invasive surgery, but so far, the technique has been used mainly in soft tissues including the myocardium,[17] the kidney,[23] and the prostate.[24] Cardiac chordae are much stiffer and solid than these tissues and were not seen as potential targets for histotripsy. Recently, Vlaisavljevich *et al.*[25] reported the threshold for tissue fractionation in a wide variety of tissues, including chordae tendineae. According to their publication, they were not able to

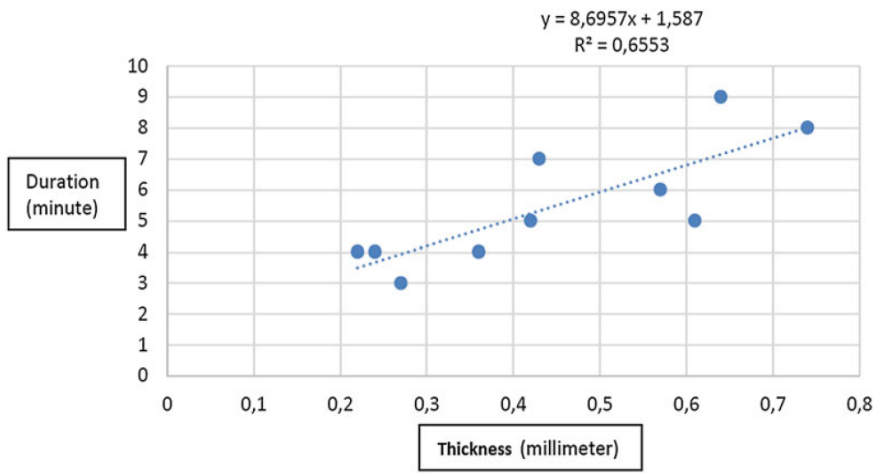

Figure 1 In vitro chordal cutting. Relation between the thickness of the chordae (abscissa, in minutes) and the duration of the procedure (ordinate, in millimetre). Ten chordae have been evaluated.

Downloaded from by guest on September 25, 2016

cut chordae (heart valve tendon) *in vitro* within 10 min of histotripsy exposure. In contrast, we have shown here that the thinnest chordae can be cut after only 3 min of exposure. We have also showed that the duration required for chordal cutting depended on the chordae's thickness and that the section of the thickest chordae in the study required 9 min. Therefore, we hypothesize that the chordae investigated in the work of Vlaisavljevich were probably too thick to allow a section in 10 min (fixed term of procedure and *ex vivo* porcine tissues). Kunzelman *et al.*[26] demonstrated that the basal chordae's diameter was larger than the marginal one (0.98 vs. 0.52 mm, from porcine heart)[27] emphasizing the importance of this parameter for ultrasound-based chordal cutting.

Several years ago, Abe *et al.*[14] also performed mitral chordal cutting *in vitro*, but using HIFU. This technology, also based on focused ultrasound, relies on heating the chordae tendineae using the thermal effect on the focal spot of the high-intensity ultrasonic beam. Histotripsy has the advantage of using a mechanical mechanism for tissue fragmentation, which does not heat the surrounding tissues, in particular the ribs on the path of the ultrasound beam. Moreover, tissue heating with HIFU is very challenging to perform on moving tissues because it requires accumulating heat at the exact same location to reach the threshold for tissue denaturation. In contrast, the effect of histotripsy is cumulative all over the exposures. Of course, the treatment efficiency is reduced by motion because part of the exposure does not reach the chordae. This explains the differences of procedure duration observed between *in vitro* experiments (7 min of exposure for the basal chordae) and *in vivo* experiments (20 min of exposure).

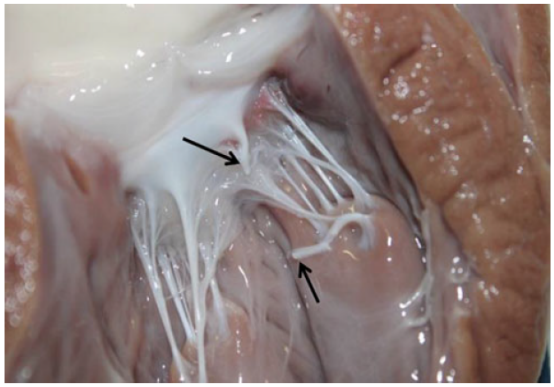

Figure 2 Results of *in vivo* chordal cutting by histotripsy. It shows one of the sheep hearts just after the application of histotripsy, where a basal chordae cut is visible.

The histological analysis confirms the absence of risk for secondary embolism. There was no argument for isolated tissue fragment, inflammation, or thrombosis. Xu *et al.* found that, after *in vitro* histotripsy on inter atrial septum,[28] more than 99% of tissue particles had a diameter of <6 μm (the size of red blood cell). These elements lead us to think that there is no embolic risk after chordal cutting by histotripsy.

To our knowledge, this study is the first proof of concept of non-invasive chordal cutting on beating heart. We deliberately chose to target the basal rope anterior mitral leaflet of the valve because (i) it is the MV's thickest chordae and (ii) its section is a treatment option facing IMR. Our goal was to demonstrate the feasibility of cutting very thick chordae by histotripsy on beating heart. The stakes are high, when identifying the risks of cardiopulmonary bypass[29,30] and more broadly of sternotomy.[31,32]

Limitations and future perspective

The main limitation of our *in vivo* study is the accuracy and safety of this non-invasive treatment. The objective of cutting the basal chordae by histotripsy was achieved in all of the experiments. However, in the first two animals, we also cut accessories (marginal) chordae arising from the targeted basal chordae. This unwanted effect comes from two technical limitations: the size of the focal spot which, in some case, may be too large to treat only the basal chordae, and the inaccuracy of the target position due to motion. Concerning the two first animals, the chordae was overtreated using an intensity level at the focus higher than necessary. As a consequence, cavitation occurred along the beam axis within the myocardial wall before reaching the focus. For all the following experiments, we decided to increase slowly the intensity level until a sufficient intensity was

Table 2 Characteristics of the seven sheep (*in vivo* procedures)

	Sheep 1	Sheep 2	Sheep 3	Sheep 4	Sheep 5	Sheep 6	Sheep 7
Weight	45	48	36	40	36	32	35
Haemodynamic per procedure	Stable	Stable	Stable	Stable	Stable	Stable	Stable
ECG	VES	VES	Normal	Normal	Normal	Normal	Normal
Heart rate (mean/min)	102	117	121	85	97	86	91
Systolic blood pressure (mean)	112	117	123	101	106	108	129
Time of procedure (min)	18	23	26	21	16	14	22
Section of basal chordae	Yes	Yes	Yes	Yes	Yes	Yes	Yes
Section of marginal chordae	Yes	Yes	No	No	No	No	No
MR/prolapsus	Yes (mild)	Yes (moderate)	No	No	No	No	No
Anatomic confirmation of chordal cutting	Yes	Yes	Yes	Yes	Yes	Yes	Yes
Haematoma (additional anatomic lesions)	Yes (LV lateral wall)	No	No	No	No	No	No

ECG, electrocardiogram; VES, ventricular extra systole; MR, mitral regurgitation; LV, left ventricle; IVS, interventricular septum.

Downloaded from by guest on September 25, 2016

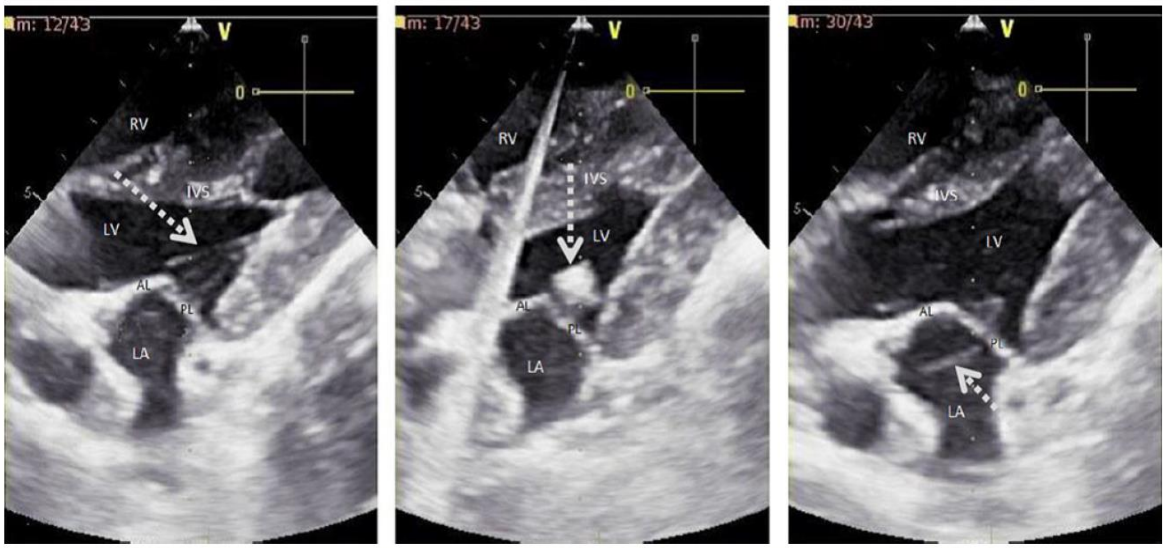

Figure 3 Images of echocardiography during procedure. Before histotripsy (left image), the basal chordae of the anterior mitral leaflet are clearly identifiable (arrow). During histotripsy (central image), the 'cloud of cavitation' (microbubbles) is visible (arrows). After histotripsy (right image), the section of the basal chordae is confirmed thanks to the echocardiography (arrows). IVS, interventricular septum; LA, left atrium; LV, left ventricle; RV, right ventricle; AL, anterior leaflet; PL, posterior leaflet.

reached at the focus to generate the cavitation cloud and did not observe any myocardial damages. We succeeded to improve our set-up for the remaining five sheep, allowing an adapted focal size without any other side effect (no marginal chordae cut and no LV wall haematoma).

The second limitation is the fact that our experimentation was not done on ischaemic MR model. However, the setting was already quite complex with need to put the thorax cavity with the device immerged in water to make the cavitation possible. Therefore, we prefer to get the maximum chance of success by cutting the basal chordae on normal beating heart keeping in mind that the ultimate clinical application should be transthoracic without the need of thoracotomy and water immersion.

3D Echo guiding and histotripsy

In future perspective, several strategies can provide a solution to improve the accuracy and safety of this procedure. First, the size of the focal spot could be reduced by increasing the ultrasonic frequency. Second, motion could be corrected in order to track accurately the basal chordae all over the cardiac cycle. The focal point can be moved in real time by using electronic steering with a multi-element transducer array instead of using a single-element transducer.[33] 3D Motion correction is feasible in real time,[34] based on an accurate ultrasonic speckle-tracking method and has been demonstrated for HIFU applications in 2004 and more recently for histotripsy. Such a motion correction technique would allow to 'lock the ultrasonic beam on the target'. A more basic solution would be to trigger histotripsy exposures by electrocardiogram.[14] This would allow selecting only a specific time in the cardiac cycle for the treatment, for example at the end of systole for mitral chordae. Another possibility is to preselect patients before the procedure by 3D transoesophageal echocardiography and computerized tomography scanner to have a map of the anatomy of the MV chordae[35]; we would then be able to exclude patients with marginal chordae arising from the basal one or for whom the whole length of the basal chordae is not clearly visible. One can also emphasize that the challenge of avoiding marginal chord cutting (marginal attached to same basal chord in an arcade) may actually be reduced in the clinical population to be treated with inferior MI and IMR. Indeed, the basal and marginal chords in such patients are stretched apart by >1.5 cm, thus minimizing chances of marginal chordal section.[36]

Moreover, although the therapeutic and imaging frequencies were not the same, the imaging ultrasound beam could potentially improve the therapy effect. Lin *et al.*[37] have reported that a dual-beam system can be used to achieve precise lesion formation. However, in order to generate this effect, the two beams have to be synchronized accurately which was not the case in our experimental set-up. Therefore, the probability that the pulses coincide in time and space is very small, and this effect may be considered as negligible in our experiments.

Future direction: transthoracic approach

Another limitation was the fact that we performed a sternotomy for the *in vivo* procedure. Transthoracic treatment should be feasible but requires further development of the therapy device. The main challenge of the transthoracic approach is to overcome the effect of the deep heterogeneous tissue layers on the path of the ultrasound beam. The ribs are a particularly strong barrier for ultrasound so that the ultrasonic beam will propagate only through the intercostal space. This limited aperture reduces the energy at the focal point as well as the quality of the focus. However, previous works in the field of histotripsy[38,39] and HIFU[40] have shown the feasibility of transcostal focusing.

Embolic debris and myocardial damage

The last limitation of our *in vivo* study is the lack of safety evaluation, including embolism risks. Xu *et al.*[28] described a low risk of

Downloaded from by guest on September 25, 2016

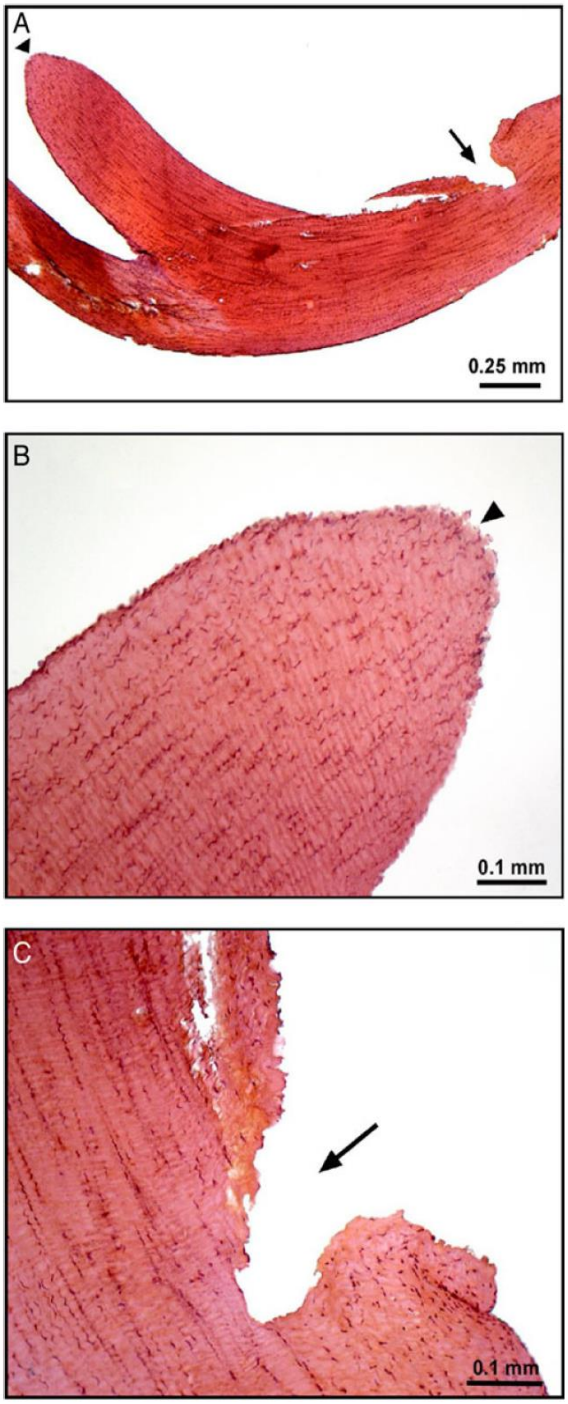

Figure 4 Histological explorations of chordae post chordal cutting by histotripsy. (*A*) Low magnification showing the cut (arrow head) and the ulceration (arrow) of the MV chordae tendineae; H&E stain. (*B*) MV chordae tendineae: the cut edge is smooth (arrowhead). The collagen bundles making the chordae tendineae are dense and not disrupted in the area of the cutting. H&E stain. (*C*) MV chordae tendineae: the ulceration is smooth (arrow). The collagen bundles making the chordae tendineae are dense and not disrupted in the area of the cutting. H&E stain.

pathological fragments (>6 μm) after histotripsy on myocardium (*in vitro* essay). However, an additional study is required to evaluate the fragment's size after histotripsy on chordae. Concerning rhythmic complications, we observed during our *in vivo* procedures that some ventricular extra systoles (VES) were generated but never ventricular tachycardia or life-threatening arrhythmia. It is known that focused ultrasound at high intensity could have an impact on cardiac rhythm[41,42] so that the ultrasound focal spot should not be positioned over the myocardium to avoid VES, which was always the case in our study. The superficial haematoma observed on the second sheep was due to too high an exposure level which generated unwanted cavitation activity in the myocardium. The anatomical impact of this haematoma was analysed only by histopathological explorations because biological measurements as CK/troponin curves or MRI were incompatible with our procedure with no survival or follow-up. The amplitude was set to a lower level for all the other animals, and we did not observe any other haematoma.

Preclinical perspective

The animal models of mitral valve prolapse (MVP) or primary MR are all obtained thanks to genetic knockdown experiments, endovascular procedures, or surgical strategies.[43] Histotripsy of marginal chordae could offer a new solution for creating this type of experimental model, which has the advantage to be immediately effective, reproducible, and relatively inexpensive.

Clinical perspective

Finally, we hope that if we succeed to decrease the functional mitral regurgitation (FMR) by transthoracic mean in a very sick patient, this would be applicable to a completely new indication of FMR treatment which, up to now, lacks survival benefit. The drawback of lack of annuloplasty associated with non-invasive chordal cutting can be addressed by the fact that in the majority of patient, the main mechanism is leaflet tethering, especially in the one with LVEDD >65–70 mm, coaptation depth >10 mm, anterior leaflet angle >27–39.5°, posterior leaflet angle >45°, and interpapillary muscle distance >20 mm.[44] It may also be explained by the fact that this technique can be applied on patients with mild MR at rest which increases after exercise like in the Fayad experience.[5] Moreover, Mitraclip device (alone without ring) has been developed based on Alfieri edge-to-edge surgical technique which always used MV annuloplasty.[41]

In addition, we can hypothesize that the non-invasive chordal cutting by histotripsy could be a useful adjunct to other procedures that do not reduce tethering, such as Mitraclip or after a surgical annuloplasty turning out to be not effective enough. However, it is clear that specific clinical or preclinical studies will be needed to validate these perspectives.

Conclusion

We have demonstrated that the section of MV chordae was achievable by real-time 3D echo-guided histotripsy *in vitro* and *in vivo* on sheep beating hearts. We hope that in the near future, this technique will gain on manoeuvrability and could be applied transthoracic on patient with IMR.

Supplementary data

Supplementary data are available at *European Heart Journal – Cardiovascular Imaging* online.

Downloaded from by guest on September 25, 2016

Conflict of interest: None declared.

Funding

This work is supported by LABEX WIFI (Laboratory of Excellence within the French Program 'Investments for the Future') under references Agence Nationale pour la Recherche (ANR)-10-LABX-24 and ANR-10-IDEX-0001-02 (P.S.L.).

References

1. Lancellotti P, Moura L, Pierard L, Agricola E, Popescu BA, Tribouilloy C *et al.* European Association of Echocardiography recommendations for the assessment of valvular regurgitation. Part 2: mitral and tricuspid regurgitation (native valve disease). *Eur J Echocardiogr* 2010;**11**:307–32.
2. Dal-Bianco JP, Levine RA. The mitral valve is an actively adapting tissue: new imaging evidence. *Eur Heart J Cardiovasc Imaging* 2015;**16**:286–7.
3. Agricola E, Oppizzi M, Pisani M, Meris A, Maisano F, Margonato A. Ischemic mitral regurgitation: mechanisms and echocardiographic classification. *Eur J Echocardiogr* 2007;**9**:207–21.
4. Iung B, Vahanian A, eds. *Prevalence and Definition of Secondary Mitral Valve Regurgitation*. London: Springer; 2015. pp. 1–6.
5. Acker MA, Parides MK, Perrault LP, Moskowitz AJ, Gelijns AC, Voisine P *et al.* Mitral-valve repair versus replacement for severe ischemic mitral regurgitation. *N Engl J Med* 2014;**370**:23–32.
6. Messas E, Guerrero JL, Handschumacher MD, Conrad C, Chow C-M, Sullivan S *et al.* Chordal cutting: a new therapeutic approach for ischemic mitral regurgitation. *Circulation* 2001;**104**:1958–63.
7. Messas E, Pouzet B, Touchot B, Guerrero JL, Vlahakes GJ, Desnos M *et al.* Efficacy of chordal cutting to relieve chronic persistent ischemic mitral regurgitation. *Circulation* 2003;**108**(Suppl):II111–5.
8. Borger MA, Murphy PM, Alam A, Fazel S, Maganti M, Armstrong S *et al.* Initial results of the chordal-cutting operation for ischemic mitral regurgitation. *J Thorac Cardiovasc Surg* 2007;**133**:1483–92.
9. Calafiore AM, Refaie R, Iacò AL, Asif M, Al Shurafa HS, Al-Amri H *et al.* Chordal cutting in ischemic mitral regurgitation: a propensity-matched study. *J Thorac Cardiovasc Surg* 2014;**148**:41–6.
10. Murashita T, Okada Y, Kanemitsu H, Fukunaga N, Konishi Y, Nakamura K *et al.* Midterm outcomes of chordal cutting in combination with downsized ring annuloplasty for ischemic mitral regurgitation. *Ann Thorac Cardiovasc Surg* 2014;**20**:1008–15.
11. Timek TA, Lai DT, Bothe W, Liang D, Daughters GT, Ingels NB *et al.* Geometric perturbations in multiheaded papillary tip positions associated with acute ovine ischemic mitral regurgitation. *J Thorac Cardiovasc Surg* 2015;**150**:232–7.
12. Smith PK, Hung JW, Michler RE. Surgical treatment of moderate ischemic mitral regurgitation. *N Engl J Med* 2015;**372**:1773–4.
13. Pierard L, Carabello BA. Ischaemic mitral regurgitation: pathophysiology, outcomes and the conundrum of treatment. *Eur Heart J* 2010;**31**:2996–3005.
14. Abe Y, Otsuka R, Muratore R, Fujikura K, Okajima K, Suzuki K *et al.* In vitro mitral chordal cutting by high intensity focused ultrasound. *Ultrasound Med Biol* 2008;**34**:400–5.
15. Dijkmans PA, Juffermans LJM, Musters RJP, van Wamel A, ten Cate FJ, van Gilst W *et al.* Microbubbles and ultrasound: from diagnosis to therapy. *Eur J Echocardiogr* 2004;**5**:245–56.
16. Xu Z, Ludomirsky A, Eun LY, Hall TL, Tran BC, Fowlkes JB *et al.* Controlled ultrasound tissue erosion. *IEEE Trans Ultrason Ferroelectr Freq Control* 2004;**51**:726–36.
17. Xu Z, Owens G, Gordon D, Cain CA, Ludomirsky A. Noninvasive creation of an atrial septal defect by histotripsy in a canine model. *Circulation* 2010;**121**:742–9.
18. Kim Y, Gelehrter SK, Fifer CG, Lu JC, Owens GE, Berman DR *et al.* Non-invasive pulsed cavitational ultrasound for fetal tissue ablation: feasibility study in a fetal sheep model. *Ultrasound Obstet Gynecol* 2011;**37**:450–7.
19. Roberts W. Focused ultrasound ablation of renal and prostate cancer: current technology and future directions. *Urol Oncol* 2005;**23**:367–71.
20. Lake AM, Hall TL, Kieran K, Fowlkes JB, Cain CA, Roberts WW. Histotripsy: minimally invasive technology for prostatic tissue ablation in an in vivo canine model. *Urology* 2008;**72**:682–6.
21. Duryea AP, Hall TL, Maxwell AD, Xu Z, Cain CA, Roberts WW. Histotripsy erosion of model urinary calculi. *J Endourol* 2011;**25**:341–4.
22. Duryea AP, Maxwell AD, Roberts WW, Xu Z, Hall TL, Cain CA. In vitro comminution of model renal calculi using histotripsy. *IEEE Trans Ultrason Ferroelectr Freq Control* 2011;**58**:971–80.
23. Styn NR, Hall TL, Fowlkes JB, Cain CA, Roberts WW. Histotripsy of renal implanted VX-2 tumor in a rabbit model: investigation of metastases. *Urology* 2012;**80**:724–9.
24. Schade GR, Styn NR, Ives KA, Hall TL, Roberts WW. Prostate histotripsy: evaluation of prostatic urethral treatment parameters in a canine model. *BJU Int* 2014;**113**:498–503.
25. Vlaisavljevich E, Kim Y, Owens G, Roberts W, Cain CA, Xu Z. Effects of tissue mechanical properties on susceptibility to histotripsy-induced tissue damage. *Phys Med Biol* 2014;**59**:253–70.
26. Kunzelman KS, Cochran RP. Mechanical properties of basal and marginal mitral valve chordae tendineae. *ASAIO Trans* 1991;**36**:M405–8.
27. Kunzelman KS, Cochran RP. Stress/strain characteristics of porcine mitral valve tissue: parallel versus perpendicular collagen orientation. *J Card Surg* 1992;**7**:71–8.
28. Xu Z, Fan Z, Hall TL, Winterroth F. Size measurement of tissue debris particles generated from pulsed ultrasound cavitational therapy–histotripsy. *Ultrasound Med Biol* 2009;**35**:245–55.
29. Kirklin JK, Westaby S, Blackstone EH, Chenoweth DE, Pacifico AD. Complement and the damaging effects of cardiopulmonary bypass. *J Thorac Cardiovasc Surg* 1983;**86**:845–57.
30. Taylor KM. Brain damage during cardiopulmonary bypass. *Ann Thorac Surg* 1998;**65**:S20–6.
31. Ulicny KS, Hiratzka LF. The risk factors of median sternotomy infection: a current review. *J Card Surg* 1991;**6**:338–51.
32. Park CB, Suri RM, Burkhart HM, Greason KL, Dearani JA, Schaff HV *et al.* Identifying patients at particular risk of injury during repeat sternotomy: analysis of 2555 cardiac reoperations. *J Thorac Cardiovasc Surg* 2010;**140**:1028–35.
33. Miller RM, Kim Y, Lin K-W, Cain CA, Owens GE, Xu Z. Histotripsy cardiac therapy system integrated with real-time motion correction. *Ultrasound Med Biol* 2013;**39**:2362–73.
34. Pernot M, Tanter M, Fink M. 3-D real-time motion correction in high-intensity focused ultrasound therapy. *Ultrasound Med Biol* 2004;**30**:1239–49.
35. McCarthy K, Ring L, Rana BS. Anatomy of the mitral valve: understanding the mitral valve complex in mitral regurgitation. *Eur J Echocardiogr* 2010;**11**:i3–9.
36. He S, Weston MW, Lemmon J, Jensen M, Levine RA, Yoganathan AP. Geometric distribution of chordae tendineae: an important anatomic feature in mitral valve function. *J Heart Valve Dis* 2000;**9**:495–501; discussion 502-3.
37. Lin K-W, Hall TL, McGough RJ, Xu Z, Cain CA. Synthesis of monopolar ultrasound pulses for therapy: the frequency-compounding transducer. *IEEE Trans Ultrason Ferroelectr Freq Control* 2014;**61**:1123–36.
38. Kim Y, Wang T-Y, Xu Z, Cain CA. Lesion generation through ribs using histotripsy therapy without aberration correction. *IEEE Trans Ultrason Ferroelectr Freq Control* 2011;**58**:2334–43.
39. Kim Y, Vlaisavljevich E, Owens GE, Allen SP, Cain CA, Xu Z. In vivo transcostal histotripsy therapy without aberration correction. *Phys Med Biol* 2014;**59**:2553–68.
40. Aubry JF, Pernot M, Marquet F, Tanter M, Fink M. Transcostal high-intensity-focused ultrasound: ex vivo adaptive focusing feasibility study. *Phys Med Biol* 2008;**53**:2937–51.
41. Lee KL, Lau C-P, Tse H-F, Echt DS, Heaven D, Smith W *et al.* First human demonstration of cardiac stimulation with transcutaneous ultrasound energy delivery: implications for wireless pacing with implantable devices. *J Am Coll Cardiol* 2007;**50**:877–83.
42. Auricchio A, Delnoy P-P, Regoli F, Seifert M, Markou T, Butter C. First-in-man implantation of leadless ultrasound-based cardiac stimulation pacing system: novel endocardial left ventricular resynchronization therapy in heart failure patients. *Europace* 2013;**15**:1191–7.
43. Delling FN, Vasan RS. Epidemiology and pathophysiology of mitral valve prolapse: new insights into disease progression, genetics, and molecular basis. *Circulation* 2014;**129**:2158–70.
44. Kron IL, Perrault LP, Acker MA. We need a better way to repair ischemic mitral regurgitation. *J Thorac Cardiovasc Surg* 2015;**150**:428.

Downloaded from by guest on September 25, 2016

European Heart Journal – Cardiovascular Imaging (2016) **17**, 1108–1109
doi:10.1093/ehjci/jew154

EDITORIAL

The power of ultrasound: treating secondary MR with sound waves

Jacob P. Dal-Bianco, Philipp E. Bartko, and Robert A. Levine*

Harvard Medical School, Cardiac Ultrasound Laboratory, Massachusetts General Hospital, 55 Fruit Street, Yawkey 5B, Boston, MA 02114, USA

Online publish-ahead-of-print 22 August 2016

Innovations in physics and its applications often enable medical advances. Collaboration between physicists who developed a high-frame-rate ultrasound system and cardiovascular investigators has allowed non-invasive measurement of vascular and myocardial stiffness.[1,2] In this current issue of the *European Heart Journal—Cardiovascular Imaging*, members of these groups, using a related technology, have employed ultrasound to treat as well as to image the heart[3] in mitral regurgitation (MR) secondary to myocardial infarction (MI) that causes mitral valve (MV) leaflet tethering mediated by chordae to the displaced papillary muscles (PMs).[4] This is a condition for which a strong need is perceived for improved approaches.[5]

Although there is evidence for adaptive MV growth in secondary MR,[6,7] this extra leaflet tissue is often insufficient to compensate adequately for mitral annular (MA) enlargement and chordal tethering.[8] The MV leaflets thus become increasingly taut, being pulled by the annulus towards the base, and by chordae towards the left ventricular (LV) apex. The normally convex MV closing configuration towards left atrium becomes concave, and the anterior MV leaflet appears like a 'hockey stick' on Echo.[9] Once the necessary leaflet tissue redundancy for MV coaptation is exhausted, MR will develop, which will over time further advance annular remodelling and tethering by the collagen-based chordae[6,7,10] and therefore MR (*Figure 1A*).

Current medical and surgical and transcatheter repair therapies for secondary MR thus aim to reduce overall leaflet tethering to restore leaflet coaptation by addressing the impaired LV (optimal medical heart failure therapy, revascularization, resynchronization, potential myocardial regeneration) and the mitral annulus (restoration of normal sinus rhythm, annuloplasty). Not as clinically established, but shown to be safe and effective is to directly target the chordal apparatus by cutting secondary chordae attaching to the leaflet bodies to relieve their tethering and to restore a greater surface for leaflet coaptation[11,12] (*Figure 1B*). Such chordal cutting reduces both MR and its associated LV remodelling[13] and has been successfully applied by several surgical groups.[14–16] The pathological changes observed in chordae post-infarction[7] and the recent reported relation between secondary MR and chordal shortening, imposing additional restriction on the tethered leaflets, lend further support to the potential benefits of chordal cutting to relieve such MR.[17]

The current paper reports a proof of concept for using pulsed cavitational focused ultrasound (histotripsy) to cut chordae non-invasively guided by real-time 3D echocardiography.[3] The authors show that secondary anterior chordae can be selectively cut *in vitro* and *in vivo* in the beating sheep heart with a high-energy

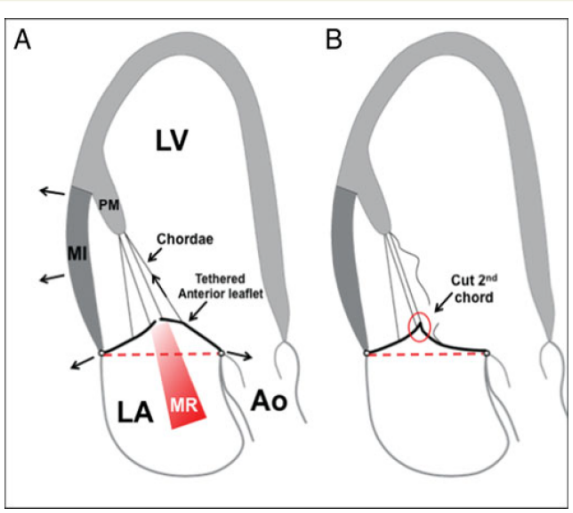

Figure 1 (*A*) Functional/ischaemic MR: the PM is displaced posteriorly, laterally, and apically because of local LV dilatation and remodelling (arrows) caused by MI (shaded area). This LV wall-PM displacement tethers the anterior mitral leaflet apically and changes its shape relative to the annulus (dashed redline). Chordal and annulus tethering limits coaptation, resulting in MR. Targeted cutting of secondary chords (*B*) restores the normal geometry of the anterior leaflet (convex towards the left atrium). The reduction of systolic leaflet tenting area/volume (compare intra-leaflet area above dashed redlines *A* vs. *B*) provides enough leaflet tissue for adequate leaflet coaptation (*B*, red circle).

The opinions expressed in this article are not necessarily those of the Editors of *EHJCI*, the European Heart Rhythm Association, or the European Society of Cardiology.

* Corresponding author. Tel: +1 617 724 1995; Fax: +1 617 643 1616. E-mail: rlevine@partners.org

Published on behalf of the European Society of Cardiology. All rights reserved. © The Author 2016. For permissions please email: journals.permissions@oup.com.

Downloaded from by guest on September 21, 2016

'bubble cloud' formed by very short, high-pressure ultrasound pulses. The amount of time required to cut a chord correlated with its thickness (average 20 min). After a learning curve, no significant anatomic damage to surrounding structures was noted. Arrhythmic events were rare and non-significant. It is important to point out that with the currently available technology, chordal cutting was guided non-invasively by 3D Echo, but a thoracotomy to expose the heart was needed to allow for adequate ultrasound energy penetration; the authors indicate transcutaneous delivery is being developed. All sheep had healthy hearts without MV disease, so chordal cutting effects on MR reduction could not been tested.

Histotripsy has also been applied experimentally with the aim of palliating or treating congenital heart defects through non-invasive shunt creation.[18] High-intensity focused ultrasound, previously applied *in vitro*, can likewise cut chordae[19] but depends upon heating that may be difficult to maintain within the rapidly moving cardiac blood pool.

The authors should be congratulated on pushing the boundaries of ultrasound, as one can conceive a future where ultrasound is not only used for the diagnosis and guidance but also for the treatment of secondary MR! Based on the progress to date, we can anticipate some additional refinements: (i) demonstrating the absence of important embolization, a foremost need pointed out by the authors, and suggested by Xu *et al.*,[20] who found that >99% of total particles after myocardial histotripsy were <6 μm in diameter, smaller than a red blood cell. (ii) Refining sample volume and precise chordal targeting. Interestingly, this may be easier after infarction, when chordal tension increases the separation between secondary and marginal chordae.[21] The direct visualization of the microcavitation cloud can facilitate this process. (iii) Potential motion tracking to maximize target interaction with ultrasound energy, particularly for the thickened chordae following infarction.[7] Immobility of the strut chordae relative to the LV in the normal heart, augmented by the increased chordal tension in secondary MR, makes these chordae particularly suitable targets for non-invasive section. Three-dimensional transoesophageal echocardiography may offer improved guidance.[17] (iv) Application of cavitational focused ultrasound will need to be achieved without thoracotomy. Optimally, a transoesophageal or gastric window may prove to be sufficient. (v) Acute and long-term durability of MR reduction will need to be demonstrated as this non-invasive approach of chordal cutting does not address the dilated mitral annulus, although *in vivo* data so far indicate that it relieves progressive LV remodelling.[13]

Cutting chords by this technique may also be a beneficial partner procedure with transcatheter MV repair strategies such as the MitraClip or the Cardioband. Such a combined and complementary less-invasive MV repair approach will target leaflet tethering as well as annular dilatation and thus should effectively restore MV leaflet coaptation; the less-invasive approach can allow more patients to benefit from relief of tethering than is currently possible. Overall, the proof of concept for this ingenious therapeutic use of ultrasound is encouraging and with further animal investigations along the lines noted can lead to potential human application.

Funding

This work is supported in part by grant 07CVD04 of the Leducq Foundation, Paris, France, for the Leducq Transatlantic MITRAL Network, and by National Institutes of Health grants R01 HL109506 and HL128099. Additional support was from an American Society of Echocardiography Career Development Award and an Erwin-Schrödinger Stipend (FWF Austrian Science Fund).

Conflict of interest: none declared.

References

1. Mirault T, Pernot M, Frank M, Couade M, Niarra R, Azizi M *et al.* Carotid stiffness change over the cardiac cycle by ultrafast ultrasound imaging in healthy volunteers and vascular Ehlers-Danlos syndrome. *J Hypertens* 2015;**33**:1890–6; Discussion 6.
2. Pernot M, Lee WN, Bel A, Mateo P, Couade M, Tanter M *et al.* Shear wave imaging of passive diastolic myocardial stiffness: stunned versus infarcted myocardium. *JACC* 2016; doi: 10.1016/j.jcmg.2016.01.022.
3. Villemain O, Kwiecinski W, Bel A, Robin J, Bruneval P, Arnal B *et al.* Pulse cavitational ultrasound for non-invasive chordal cutting guided by real-time 3D echocardiography. *Eur Heart J Cardiovasc Imaging* 2016;**17**:1101–1107.
4. Otsuji Y, Handschumacher MD, Schwammenthal E, Jiang L, Song JK, Guerrero JL *et al.* Insights from three-dimensional echocardiography into the mechanism of functional mitral regurgitation: direct in vivo demonstration of altered leaflet tethering geometry. *Circulation* 1997;**96**:1999–2008.
5. Kron IL, Perrault LP, Acker MA. We need a better way to repair ischemic mitral regurgitation. *J Thorac Cardiovasc Surg* 2015;**150**:428.
6. Dal-Bianco JP, Aikawa E, Bischoff J, Guerrero JL, Handschumacher MD, Sullivan S *et al.* Active adaptation of the tethered mitral valve: insights into a compensatory mechanism for functional mitral regurgitation. *Circulation* 2009;**120**:334–42.
7. Dal-Bianco JP, Aikawa E, Bischoff J, Guerrero JL, Hjortnaes J, Beaudoin J *et al.* Myocardial infarction alters adaptation of the tethered mitral valve. *J Am Coll Cardiol* 2016;**67**:275–87.
8. Chaput M, Handschumacher MD, Tournoux F, Hua L, Guerrero JL, Vlahakes GJ *et al.* Mitral leaflet adaptation to ventricular remodeling: occurrence and adequacy in patients with functional mitral regurgitation. *Circulation* 2008;**118**:845–52.
9. Levine RA, Schwammenthal E. Ischemic mitral regurgitation on the threshold of a solution: from paradoxes to unifying concepts. *Circulation* 2005;**112**:745–58.
10. Ritchie J, Warnock JN, Yoganathan AP. Structural characterization of the chordae tendineae in native porcine mitral valves. *Ann Thorac Surg* 2005;**80**:189–97.
11. Messas E, Guerrero JL, Handschumacher MD, Conrad C, Chow CM, Sullivan S *et al.* Chordal cutting: a new therapeutic approach for ischemic mitral regurgitation. *Circulation* 2001;**104**:1958–63.
12. Messas E, Yosefy C, Chaput M, Guerrero JL, Sullivan S, Menasche P *et al.* Chordal cutting does not adversely affect left ventricle contractile function. *Circulation* 2006;**114**(1 Suppl):I524–8.
13. Szymanski C, Bel A, Cohen I, Touchot B, Handschumacher MD, Desnos M *et al.* Comprehensive annular and subvalvular repair of chronic ischemic mitral regurgitation improves long-term results with the least ventricular remodeling. *Circulation* 2012;**126**:2720–7.
14. Borger MA, Murphy PM, Alam A, Fazel S, Maganti M, Armstrong S *et al.* Initial results of the chordal-cutting operation for ischemic mitral regurgitation. *J Thorac Cardiovasc Surg* 2007;**133**:1483–92.
15. Fayad G, Modine T, Azzaoui R, Larrue B, Cracco A, Pansard E *et al.* Chordal cutting technique through aortotomy to treat chronic ischemic mitral regurgitation: surgical technique. *Int J Surg* 2008;**6**:36–9.
16. Calafiore AM, Refaie R, Iaco AL, Asif M, Al Shurafa HS, Al-Amri H *et al.* Chordal cutting in ischemic mitral regurgitation: a propensity-matched study. *J Thorac Cardiovasc Surg* 2014;**148**:41–6.
17. Obase K, Weinert L, Hollatz A, Farooqui F, Roberts JD, Minhaj MM *et al.* Elongation of chordae tendineae as an adaptive process to reduce mitral regurgitation in functional mitral regurgitation. *Eur Heart J Cardiovasc Imaging* 2016;**17**:500–9.
18. Xu Z, Owens G, Gordon D, Cain C, Ludomirsky A. Noninvasive creation of an atrial septal defect by histotripsy in a canine model. *Circulation* 2010;**121**:742–9.
19. Abe Y, Otsuka R, Muratore R, Fujikura K, Okajima K, Suzuki K *et al.* In vitro mitral chordal cutting by high intensity focused ultrasound. *Ultrasound Med Biol* 2008;**34**:400–5.
20. Xu Z, Fan Z, Hall TL, Winterroth F, Fowlkes JB, Cain CA. Size measurement of tissue debris particles generated from pulsed ultrasound cavitational therapy-histotripsy. *Ultrasound Med Biol* 2009;**35**:245–55.
21. He S, Weston MW, Lemmon J, Jensen M, Levine RA, Yoganathan AP. Geometric distribution of chordae tendineae: an important anatomic feature in mitral valve function. *J Heart Valve Dis* 2000;**9**:495–501; Discussion 2–3.

Downloaded from by guest on September 21, 2016

7.3. Valve calcifiée

7.3.1. Présentation du travail

Après avoir montré que le phénomène de cavitation pouvait sectionner un cordage valvulaire (cf paragraphe 7.2), l'enjeu était d'élargir encore le champ d'application. De multiples pathologies cardiaques n'ont pas encore de thérapeutique non invasive accessible, mais une des plus symboliques, et la plus fréquente (Freeman and Otto 2005), reste la maladie de valve aortique calcifiée (RAC, pour rétrécissement aortique calcifié). En effet, cette cardiopathie valvulaire est un réel enjeu de santé publique, de par son incidence, son coût de prise en charge et ses risques. De surcroit, cette maladie étant lié à l'âge, et face au vieillissement des populations dans les pays industrialisés, il est évident que la prise en charge du RAC nécessite une attention scientifique particulière (Messika-Zeitoun et al. 2007). En un mot, nous devons trouver des solutions pour améliorer nos pratiques, encore et encore.

Le constat actuel est qu'il n'existe aucune solution thérapeutique non invasive pour soigner le RAC. Comme décrit dans le manuscrit qui suit, de multiples solutions ont été testées mais aucune n'a pour l'instant abouti. La chirurgie a été pendant longtemps la « seule » solution. Puis au début des années 2000, l'avènement du remplacement valvulaire aortique percutané (TAVI, pour transaortic valve implantation) a révolutionné la prise en charge de ces malades, du moins pour les plus sévères (Leon et al. 2016). L'amélioration des technologies, des méthodes de largage et du matériel utilisé (Meredith et al. 2016) permet de maintenir une progression dans l'optimisation de la prise en charge de ces malades.

Cependant, le TAVI reste invasif, coûteux et comporte des risques maintenant bien identifiés (Nishimura et al. 2017). Explorer d'autres solutions, d'autres stratégies permettant d'améliorer le fonctionnement d'une valve calcifiée doit rester une priorité, notamment si cela peut être non invasif, plus rapide et moins coûteux.

Nous avons donc, dans le manuscrit qui suit, présenté nos premiers résultats concernant l'effet du phénomène de cavitation sur la valve calcifiée.

L'objectif était simple : montrer que les ultrasons à haute intensité pouvaient agir sur la rigidité des feuillets calcifiés.

Les limites étaient importantes : nous avons évalué principalement l'efficacité de l'approche, sans apporter des arguments forts sur la sûreté de la procédure notamment sur

le risque embolique ; nous n'avons pas fait de suivi in vivo afin de vérifier nos résultats positifs initiaux ; enfin, l'approche non invasive reste discutable en l'état car nous avons réalisé la preuve de concept sur modèle animal à thorax ouvert.

Au-delà de ça, les difficultés ont été nombreuses : étant donné qu'il est très compliqué, voire impossible, d'avoir un modèle gros animal de valve calcifiée native, nous avons travaillé sur des bioprothèses calcifiées humaines explantées ; la tolérance du modèle animal lors de l'implantation de la bioprothèse malade a été très variable ; enfin, nos résultats ayant été montrés sur bioprothèse bovine, nous restons très prudents sur leur transposition à des valves humaines natives.

Malgré tout, ce travail permet d'ouvrir une piste nouvelle, non-invasive, pour le traitement de la valve calcifiée. Il permet de prendre conscience que les ultrasons à haute intensité peuvent agir sur les tissus, quelque ce soit leur constitution, pour modifier les propriétés viscoélastiques et notamment leur rigidité.

7.3.2. Manuscrit "*Pulsed Cavitational Ultrasound Softening: a new non-invasive therapeutic approach of calcified bioprosthetic valve stenosis"* + Editorial Comment

Ce travail est publié dans JACC : Basic to Translational Science (Villemain et al. 2017)

Author's Personal Copy

JACC: BASIC TO TRANSLATIONAL SCIENCE
VOL. 2, NO. 4, 2017
ISSN 2452-302X
http://dx.doi.org/10.1016/j.jacbts.2017.03.012

© 2017 THE AUTHORS. PUBLISHED BY ELSEVIER ON BEHALF OF THE AMERICAN COLLEGE OF CARDIOLOGY FOUNDATION. THIS IS AN OPEN ACCESS ARTICLE UNDER THE CC BY-NC-ND LICENSE (http://creativecommons.org/licenses/by-nc-nd/4.0/).

MINI-FOCUS: AORTIC VALVE DISEASE

Pulsed Cavitational Ultrasound Softening

A New Noninvasive Therapeutic Approach for Calcified Bioprosthetic Valve Stenosis

Olivier Villemain, MD,[a,b] Justine Robin, MS,[a] Alain Bel, MD,[c] Wojciech Kwiecinski, PhD,[a] Patrick Bruneval, MD,[d] Bastien Arnal, PhD,[a] Mathieu Rémond, PhD,[e] Mickael Tanter, PhD,[a] Emmanuel Messas, MD, PhD,[b] Mathieu Pernot, PhD[a]

VISUAL ABSTRACT

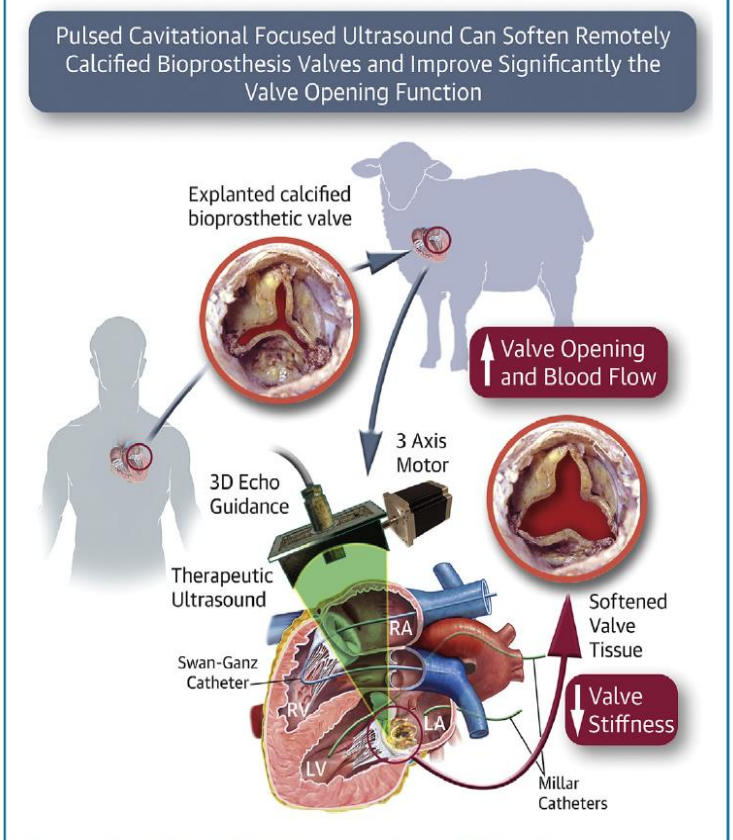

Villemain, O. et al. J Am Coll Cardiol Basic Trans Science. 2017;2(4):372-83.

HIGHLIGHTS

- **Bioprosthetic heart valves have limited durability, with a progressive deterioration of the bioprosthesis after 12 to 15 years, mainly due to intravalvular calcifications.**
- **In this proof-of-concept study, we demonstrated in vivo using an ovine model and in vitro that pulsed cavitational focused ultrasound can be used to remotely soften human degenerative calcified bioprosthetic valves and significantly improve the valve opening function.**
- **This new noninvasive approach has the potential to improve the outcome of patients with severe bioprosthesis stenosis.**

From the [a]Institut Langevin, Ecole Supérieure de Physique Chimie Industrielles de Paris, Centre National de la Recherche Scientifique, Inserm U979, PSL Research University, Paris, France; [b]Hôpital Européen Georges Pompidou, Université Paris Descartes, Cardio-Vascular Departement, UMR 970, Paris, France; [c]Hôpital Européen Georges Pompidou, Cardiovascular Surgery, Université Paris Descartes, Laboratoire de Recherche Biochirurgical, Paris, France; [d]Hôpital Européen Georges Pompidou, Université Paris Descartes, Department of Pathology, Paris, France; and [e]Cardiawave SAS, Paris, France. This work was supported by the LABEX WIFI (Laboratory of Excellence ANR-10-LABX-24) and the French Program "Investments for the Future" under reference ANR-10-IDEX-0001-02 PSL* Research University. Drs. Tanter, Messas, and Pernot are cofounders and shareholders of Cardiawave SAS. Dr. Rémond is an employee of Cardiawave SAS. All other authors have reported that they have no relationships relevant to the contents of this paper to disclose. Drs. Messas and Pernot contributed equally to this work.

Manuscript received January 3, 2017; revised manuscript received March 3, 2017, accepted March 5, 2017.

Author's Personal Copy

SUMMARY

The authors propose a novel noninvasive therapeutic approach for degenerative calcified bioprosthetic heart valves based on pulsed cavitational ultrasound (PCU) to improve the valvular function by remotely softening calcified stiff cusps. This study aims to demonstrate both in vivo, using an ovine model with implanted human calcified bioprosthesis, and in vitro that PCU can significantly improve the bioprosthesis function. A 50% decrease of the transvalvular gradient was found, demonstrating a strong improvement of the valve opening function. This new noninvasive approach has the potential to improve the outcomes of patients with severe bioprosthesis stenosis. (J Am Coll Cardiol Basic Trans Science 2017;2:372–83) © 2017 The Authors. Published by Elsevier on behalf of the American College of Cardiology Foundation. This is an open access article under the CC BY-NC-ND license (http://creativecommons.org/licenses/by-nc-nd/4.0/).

ABBREVIATIONS AND ACRONYMS

CPB = cardiopulmonary bypass

PCU = pulsed cavitational ultrasound

PHT = pressure half time

Bioprosthetic valves are becoming increasingly common in patients with valvular heart diseases. They are often favored over mechanical valves because of a lower risk of thrombotic or bleeding events, as well as the desire to avoid lifetime anticoagulation medications (1). However, bioprosthetic valves have limited durability, with a progressive deterioration of the bioprosthesis after 12 to 15 years, mainly due to intravalvular calcifications (2). The need for a redo surgery due to the incidence of structural valve deterioration is expected to increase (3). Nevertheless, redo valve surgery is associated with significant morbidity and mortality (4). Transcatheter valve-in-valve implantation has emerged as a promising, less invasive alternative to redo surgery; however, it still comes with its own various set of complications (5).

SEE PAGE 384

In parallel, for about 30 years, other therapeutic strategies (6,7) have been investigated to treat calcified valves (native or bioprosthetic). One promising approach was ultrasound-based (8), but it remained limited at the time by the need for open surgery with cardiopulmonary bypass (CPB). Nevertheless, this limitation must be challenged again with the recent improvement of technologies and concepts of pulsed cavitational focused ultrasound (PCU) or histotripsy. Histotripsy is a noninvasive, cavitation-based therapy (mechanical effect) based on very short, high-pressure ultrasound pulses focused in tissues to generate a dense, energetic, lesion-producing bubble cloud. Although histotripsy can be used to produce sharp lesions in soft tissues (9,10), recent studies have suggested that cavitation activity can also soften biological tissues (11).

The objective of our study was to evaluate the efficacy of PCU to significantly improve valve opening of severe degenerative calcified bioprosthetic valves. First, we demonstrated in vitro the efficacy of PCU on a human explanted calcified bioprosthesis mounted on an artificial heart pump and quantified the improvement of the valvular function. Then, we demonstrated its feasibility and efficacy in vivo in the beating heart of an ovine model with implanted calcified bioprosthesis.

METHODS

MODEL OF HEART CALCIFIED VALVE. We used Carpentier-Edwards Perimount Magna (stented bovine pericardial bioprosthesis, Edwards Lifesciences, Irvine, California), explanted on a human, as a model of heart calcified valve stenosis. For all patients, the indication of explant was a severe stenosis with calcification. Each valve was fixed in glutaraldehyde 0.6% immediately after explant. Before each experiment, the valve was immersed for 5 min in saline serum (0.9% NaCl) 3 consecutive times. This protocol was in agreement with institutional guidelines (national reference number of the 143 study: 02255.02).

ULTRASOUND GENERATION AND PCU ACOUSTIC PARAMETERS. A 1.25-MHz focused single-element transducer (Imasonic, Besançon, France), called a therapy transducer, was used to generate PCU. This transductor had a 100-mm focal length (f-number = 1) and was driven by a high-voltage amplifier (GA-2500A, RITEC, Warwick, Rhode Island). We produced PCU using 10-cycle pulses, each 8 μs long, delivered at a pulse repetition frequency of 100 Hz. We estimated the pressure peak amplitudes at the focal spot to be 70 and −19 MPa, respectively, for the positive and negative peak pressure.

ULTRASOUND CAVITATIONAL TREATMENT GUIDANCE AND MONITORING. Three-dimensional echocardiography was used to guide and monitor the treatment. An IE33 scanner and X5-1 probe (xMATRIX array, 3 MHz, 3,040 elements with microbeam-forming) (Philips Healthcare, Bothell, Washington) were

Author's Personal Copy

FIGURE 1 Image-Guided Therapy Setup

The imaging probe was fixed through a hole in the center of the pulsed cavitational ultrasound therapy transducer.

used. The imaging probe was fixed through a hole in the center of the therapy transducer (Figure 1). The focal spot of the therapy transducer was positioned on the central axis of the imaging probe at a depth of 100 mm. A biplane imaging mode with 2 imaging planes set at 90° was used during the entire procedure. The cavitation bubble cloud generated at the PCU focal spot was visible within the 2 imaging planes. The combination of therapy transducer and imaging probe was called the "therapy device." The same material was used for in vitro and in vivo procedures.

For all the procedures, 10 min sequences of PCU were applied and repeated until the transvalvular gradient was stabilized for 3 consecutive sequences (considered as the ineffective threshold for PCU procedures). The therapy device was controlled by a 3-axis motor to scan the PCU continuously and uniformly over the entire valve.

SHEAR WAVE ELASTOGRAPHY EVALUATION. The assessment of valve leaflet biomechanical properties remains challenging and requires destructive strain-stress mechanical tests. To noninvasively assess the modification of the biomechanical properties induced by PCU, we used shear wave elastography, an ultrasound-based tool for noninvasive evaluation of soft tissue's stiffness. We used the Aixplorer ultrasound imaging system (Aixplorer, Supersonic Imagine, Aix-en-Provence, France) with a linear probe (SL10-2) to evaluate the stiffness of each valvular leaflet. Three acquisitions were made for each leaflet, using the shear wave elastography imaging mode (SWE) of the Aixplorer scanner in the "penetration" setting. A ''QBox'' region of interest (mean diameter 1 mm) was positioned inside the elasticity image after each acquisition to obtain a mean stiffness value.

IN VITRO PROCEDURE. The objective of the in vitro procedure was to analyze the effect of the PCU on the anterograde transvalvular flow, with a pulsatile flow equivalent to the cardiac flow (Figures 2A and 2B). The flow was generated by an artificial heart pump (Pulsatile Blood Pump, Harvard Apparatus, Holliston, Massachusetts) with flow controlled variation. The flow rates were applied at 3, 4, and 5 l/min, and were monitored by a flow sensor (Small Flow Meter Kit, Atlas Scientific, Jacksonville, Florida) (accuracy ± 1 ml/min). The valve and the therapy device were immersed in degassed water. A total of 8 bioprostheses were explanted and used for this procedure. The transvalvular pressure gradient was estimated by:

- A pulsed Doppler ultrasound assessment by applying the Bernoulli equation: $\Delta P = 4\ (Vmax)^2$
- Hemodynamic assessment by pressure sensor before and after the valve (sensor IXIAN 0 to 7.5 PSI Industrial Control Pressure Sensor, Atlas Scientific; accuracy ± 1 mm Hg).

The pump operated during 2 h at a 4 l/min flow rate (70 cycles/min, ejection volume: 57 ml) to control the variation of the gradient before PCU, after which sequences of PCU were applied. All post-PCU transvalvular gradients were reassessed 1 month after the procedure (each valve was fixed in glutaraldehyde between these evaluations). Elastography was performed before and after the procedure on each valve.

Finally, the bioprostheses were sent to the department of pathology for histopathological analysis.

IN VIVO PROCEDURE: SHEEP MODEL. The in vivo procedure is shown in Figure 2C. The animal procedure was approved by the Institutional Animal Care and Use Committee of the Hôpital Européen Georges Pompidou (PARCC) according to the European Commission guiding principles (2010/63/EU).

The sheep were anesthetized with thiopentothal (0.5 ml/kg), intubated, ventilated at 15 ml/kg with 2% isoflurane, and given glycopyrrolate (0.4 mg intravenous) and vancomycin (0.5 g intravenous). A sterile sternotomy was performed. The calcified bioprosthesis was implanted in the mitral position after CPB. Vital signs (including heart rate, oxygen saturation, and arterial blood pressure), left atrial and

Author's Personal Copy

ventricle pressure (by 2 Mikro-Tip Millar Catheter Transducers, to have the transvalvular pressure gradient in real time), and cardiac flow (by a Swan-Ganz CCOmbo Pulmonary Artery Catheter, Edwards Lifesciences) were monitored. The CPB was stopped and removed to restore independent cardiac activity. Sternotomy was maintained and the thorax was filled with degassed saline water. A complete echocardiography was performed, especially to evaluate the calcified bioprosthesis (12–14). A total of 14 explanted bioprostheses were used for this procedure.

We then applied the sequences of PCU. An echocardiographic evaluation was performed between each 10-min sequence, concurrent with the catheter's evaluation (pressure and cardiac flow).

At the end of the procedure, the animal was sacrificed (Dolethal intravenous injection, 1 ml/kg) and an anatomic macroscopic evaluation of the cardiac structure was performed. Elastography examination of the bioprosthesis was performed before and after each procedure. The bioprosthesis was then explanted and sent after elastography to the department of pathology for histopathological analysis.

MICROSCOPIC ANALYSIS. Histological exploration. Immediately after the procedure (in vitro and in vivo), the bioprosthesis was dissected, fixed in formalin, and embedded in individual paraffin blocks. Regions of interest, such as macroscopic calcification on leaflet, were labelled with tattoo ink. Serial sections were stained with hematoxylin and eosin for histopathological analysis.

In addition, we also analyzed 5 calcified bioprostheses directly after their explantation from humans, without any PCU procedure. The objective was to perform a histopathological comparison between bioprostheses with or without PCU.

Micro-computed tomography imaging. The micro-computed tomography (CT) device used in this study was the Quantum FX Caliper (Life Sciences, Perkin Elmer, Waltham, Massachusetts). Samples up to a 10-mm diameter field of view and 3-dimensional acquisitions were performed using an isotropic voxel size of 20 × 20 × 20 μm^3. Full 3-dimensional, high-resolution raw data were obtained by rotating both the x-ray source and the flat panel detector 360° around the sample, with a rotation step of 0.1°. The corresponding 3,600 image projections were then automatically reconstructed (RigakuSW software, Caliper, Newton, Massachusetts) into a DICOM (Digital Imaging and Communications in Medicine) stack of 512 files, using standard back-projection techniques.

STATISTICAL ANALYSIS. Continuous variables were presented as mean ± SD. A Wilcoxon matched-pairs signed-ranks test was performed to evaluate the SD between individual mean values before and after therapy. The level of significance was set at an alpha level of ≤0.05. The analysis was conducted using MedCalc software (version 14.10.2, MedCalc, Mariakerke, Belgium).

FIGURE 2 Experimental and In Vivo Procedures

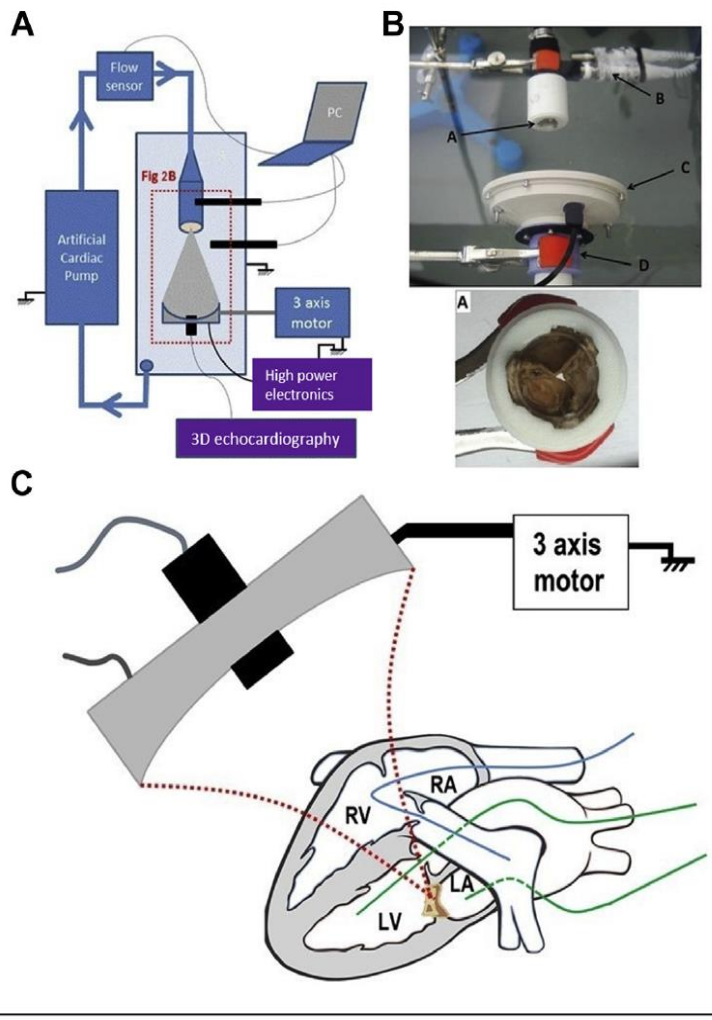

(A) In vitro procedure setup. **(B)** Photography of a part of the in vitro setup. The bioprosthesis (A) was placed in front of the therapy device composed of a therapy transducer (C) and an imaging transducer (D). The 2 pressure sensors (B) were positioned before and after the valve. **(C)** In vivo procedure, in the beating heart. The bioprosthesis was implanted in the mitral position, between the LA and the LV. The Swan-Ganz catheter (**blue**, to estimate the cardiac flow in real time), was positioned into the right heart (RV and RA) and the pulmonary artery. The Millar catheters (**green**), were positioned into the LA and LV to estimate the transvalvular gradient in real time. PCU was then applied all over the bioprosthesis by moving the therapy device using the 3-axis motorized stage. LA = left atrium; LV = left ventricle; RA = right atrium; RV = right ventricle.

RESULTS

All of our results consistently showed a softening of the valve leaflets, allowing a decrease of the

Author's Personal Copy

FIGURE 3 In Vitro Results

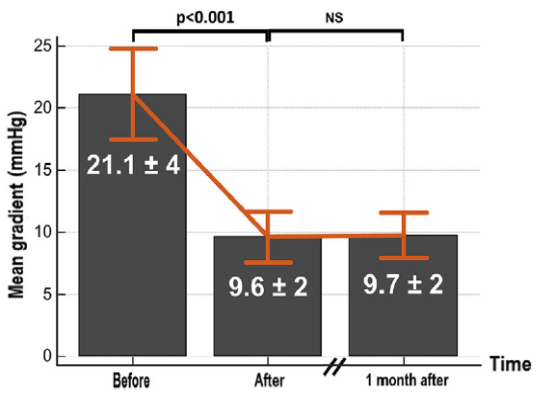

Mean transvalvular gradient measured before and after pulsed cavitational ultrasound.

anterograde gradient after PCU. This decrease persisted 1 month after the procedure. The decrease of transvalvular gradient measured by Doppler echocardiography was confirmed by invasive pressure sensors in both the in vitro and in vivo setup.

IN VITRO PROCEDURE. Eight bioprosthesis were explanted and used for the in vitro procedure (Figure 3). At a flow rate of 4 l/min, the mean transvalvular gradient over the set of valves was 21.1 ± 3.9 mm Hg (maximum 38 mm Hg, minimum 10 mm Hg) (Figure 3), and the maximum gradient was 39 ± 6.9 mm Hg (maximum 73 mm Hg, minimum 22 mm Hg). After 2 h of controlled pulsatile flow without PCU, we observed no statistically significant change of the transvalvular gradients. The mean duration of PCU was 70 ± 12 min with a maximum duration of 90 min and a minimum of 50 min. After the procedure, the mean transvalvular gradient was 9.6 ± 1.7 mm Hg (maximum 19 mm Hg; minimum 4 mm Hg), corresponding to a decrease of 55 ± 10% ($p < 0.001$). The maximum gradient was 19.6 ± 3.5 mm Hg (maximum 37 mm Hg; minimum 10 mm Hg), corresponding to a decrease of 51 ± 9% ($p < 0.001$). The results of each individual bioprosthesis are shown in Supplemental Figure 1.

Hemodynamic parameters were also measured at 3 and 5 l/min before and after procedure. The gradients also showed a significant decrease at the different flow rates ($p < 0.001$) (Supplemental Figure 2). At 3 l/min, the mean gradient varied from 14.2 ± 2.5 mm Hg to 7.1 ± 1.2 mm Hg ($p < 0.001$) and the maximum gradient from 29.1 ± 5.1 mm Hg to 14.9 ± 2.6 mm Hg ($p < 0.001$). At 5 l/min, the mean gradient varied from 23.8 ± 4.2 mm Hg to 13.0 ± 2.3 mm Hg ($p < 0.001$) and the maximum gradient from 42.3 ± 7.5 mm Hg to 24.1 ± 4.3 mm Hg ($p < 0.001$).

The gradient dependence with flow rate allowed us to assess the pliability of the valve cusps before and after the procedure. Pliability is indeed inversely linked to the slope of the gradient-flow rate relationship. The slope of the maximum gradient-flow rate relationship was found to decrease from 9 ± 4.3 mm Hg/l/min to 4.9 ± 2.9 mm Hg/l/min ($p < 0.001$), which confirmed an improved pliability of the valve cusps after the procedure.

All post-PCU transvalvular gradients were reassessed 1 month after the procedure, and no statistically significant difference was observed (Figure 3).

TABLE 1 In Vivo Results

	Before Therapy	After Therapy	Variation (%)*	p Value
Shear wave imaging				
Elastography (kPa)	76.1 ± 23.7	35.6 ± 7.2	−52 ± 7	<0.001
Echocardiography				
Doppler mitral valve (Figure 5)				
Maximal velocity, m/s	2.41 ± 0.50	1.73 ± 0.21	−28 ± 6	0.007
Maximal pressure gradient, mm Hg	24.0 ± 4.4	12.1 ± 1.4	−49 ± 11	0.003
Mean velocity, m/s	1.95 ± 0.36	1.38 ± 0.24	−29 ± 6	0.001
Mean pressure gradient, mm Hg	16.2 ± 3.2	8.2 ± 1.3	−48 ± 7	<0.001
Mitral valve area, cm^2				
By pressure half time (Figure 5)	1.09 ± 0.09	1.57 ± 0.08	+143 ± 18	<0.001
By continuity equation	1.10 ± 0.15	1.58 ± 0.15	+142 ± 15	<0.001
By planimetry (Figure 5)	1.13 ± 0.13	1.54 ± 0.14	+137 ± 14	<0.001
Pulmonary artery pressure, mm Hg				
Maximal (tricuspid valve)	64.7 ± 12.8	34.1 ± 10.2	−47 ± 12	<0.001
Cardiac output,† l/min	2.98 ± 0.10	2.96 ± 0.14	−1.0 ± 0.2	0.83
Pressure sensors (Millar), mm Hg				
Mean diastolic LAP	36.8 ± 6.2	20.2 ± 5.1	−44 ± 11	0.004
Mean diastolic LVP	17.4 ± 2.7	11.4 ± 1.9	−35 ± 10	0.014
Mean diastolic gradient LVP-LAP	17.4 ± 2.4	8.8 ± 1.2	−50 ± 13	0.002
Cardiac flow captor (l/min)				
Swan-Ganz catheter	2.87 ± 0.11	2.96 ± 0.14	+3.0 ± 0.4	0.74

Values are mean ± SD. *Variation = ([result after − result before]/result before) × 100. †Cardiac output = HR × LVOT area × LVOT VTI.

HR = heart rate; LAP = left atrial pressure; LVOT = left ventricular outflow tract; LVP = left ventricular pressure; VTI = velocity time integral.

IN VIVO PROCEDURE. Fourteen explanted bioprosthesis were used for this procedure (Table 1, Figures 4 and 5, Supplemental Video 1). A total of 7 animals experienced a massive acute pulmonary edema with severe heart failure just after the implantation of the valve and the cessation of the CPB. These animals died before the PCU procedure. The other animals tolerated the implantation. Thus, 7 valves were treated and analyzed. The mean weight of the animals was 37.8 ± 4.6 kg (minimum 29 kg; maximum 43 kg).

Author's Personal Copy

FIGURE 4 Images of Echocardiography During Procedure

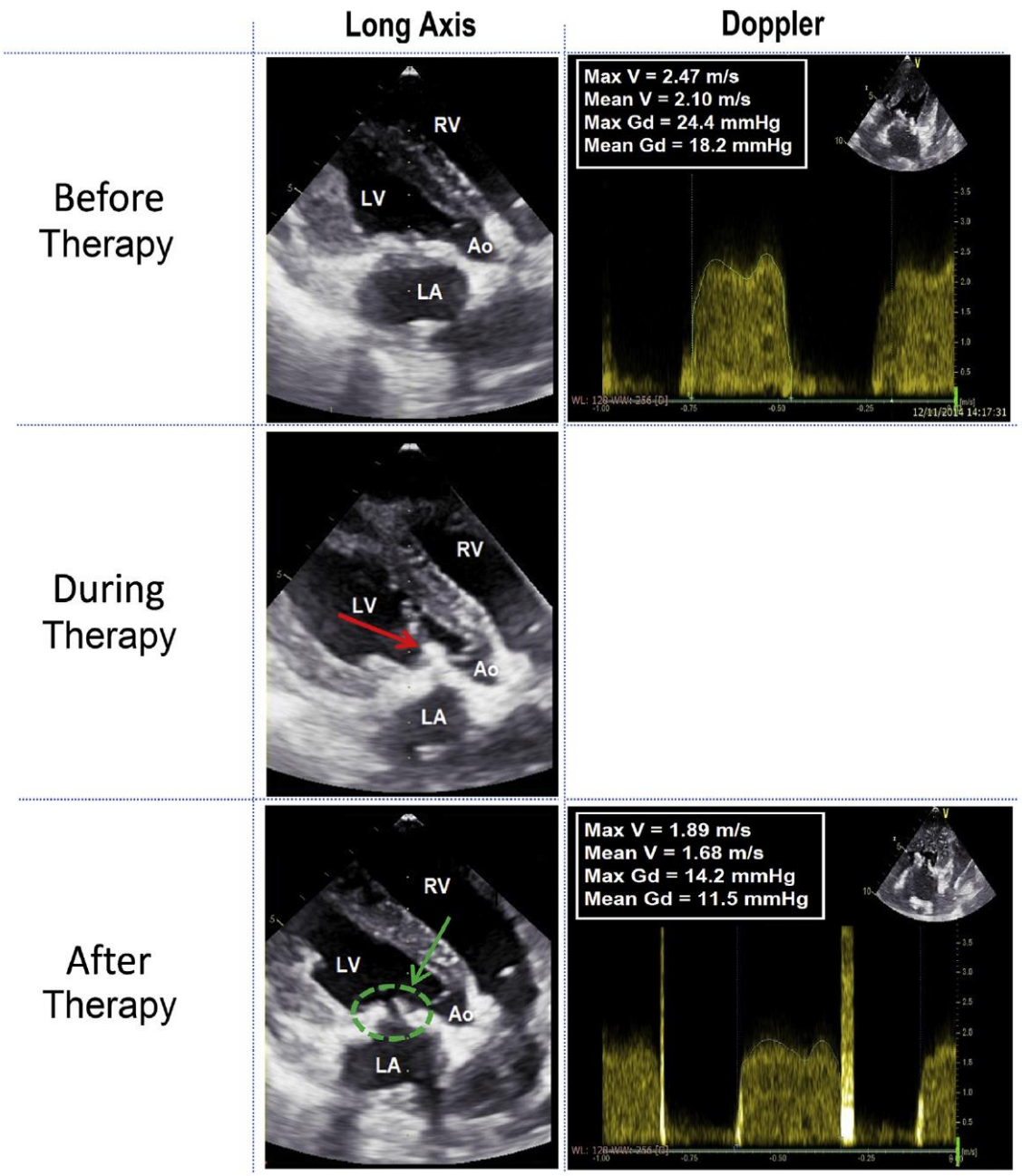

During PCU a "cavitation bubble cloud" is visible as a hyperechogenic zone **(red arrow)**. After PCU, the improvement of the bioprosthesis opening is confirmed thanks to the echocardiography **(green arrow)**. The images are realized during diastasis (closed aortic valve). See Supplemental Video 1. Ao = aorta; other abbreviations as in Figure 2.

Just after the valve implantation, we monitored all parameters for 1 h before any PCU procedure. From the beginning (just after the valve implantation) to 1 h after implantation (before any PCU procedure), there was no statistical significant difference of the transvalvular gradients ($p = 0.45$) and mitral valve areas (planimetry, $p = 0.38$; continuity equation, $p = 0.74$; pressure half time, $p = 0.51$).

The mean procedure duration was 60 ± 13 min (maximum 100 min; minimum 40 min) (see Supplemental Video 1 of an in vivo procedure). We observed an important decrease of the transvalvular gradient after PCU (**Table 1**), which was on average reduced by 50%. The results of elastography, echocardiography, and of pressure/flow cardiac catheters after the PCU procedures are synthesized in

Author's Personal Copy

FIGURE 5 Results In Vivo, Before and After Pulsed Cavitational Focused Ultrasound

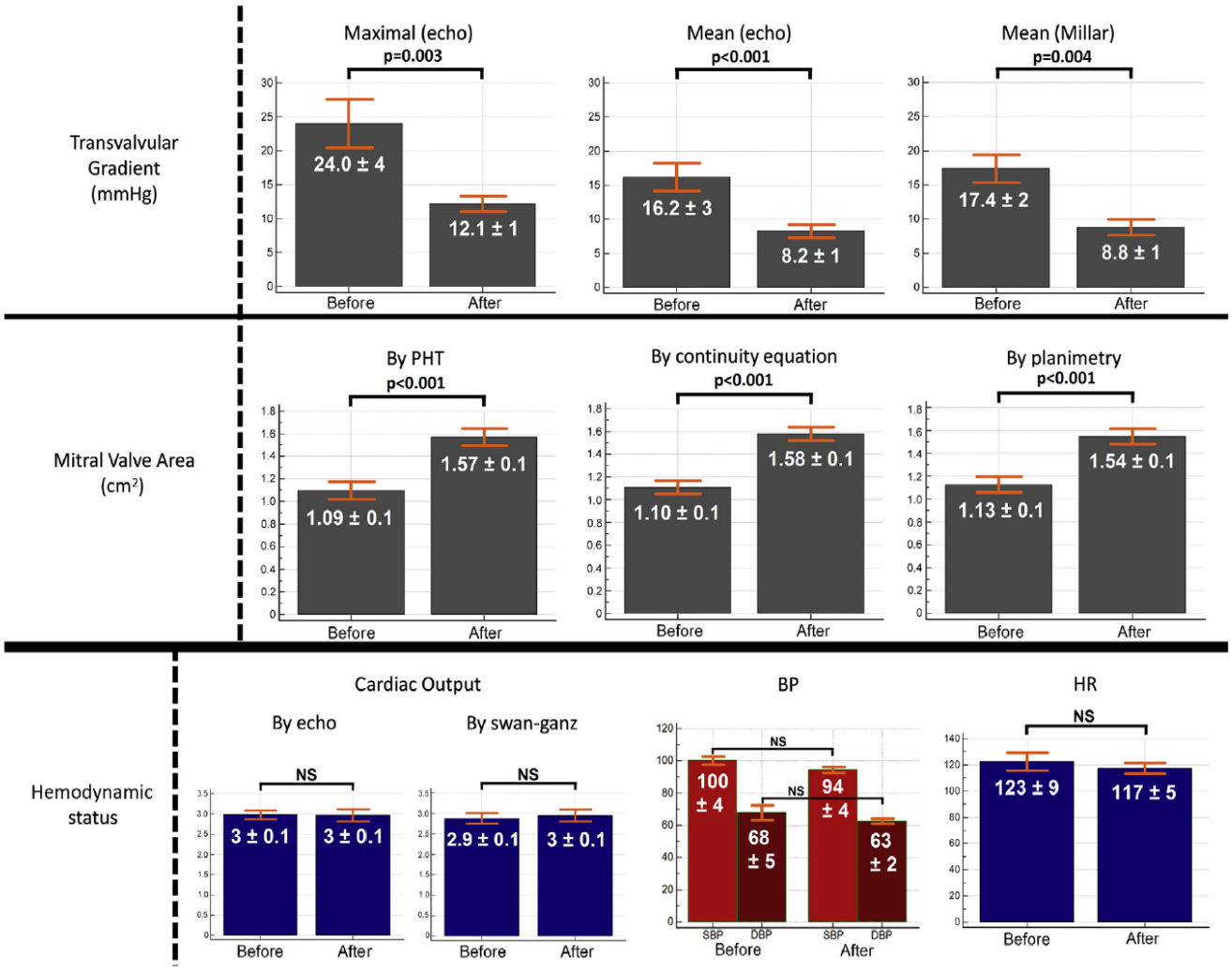

BP = blood pressure; HR = heart rate; PHT = pressure half-time method.

Table 1. The mean cardiac frequency was 123 ± 9 (minimum 94; maximum 154), and all hemodynamic parameters were stable during the procedures: heart rate ($p = 0.24$), blood pressure ($p = 0.27$), and O_2 saturation ($p = 0.42$).

No mitral valve regurgitation was observed at the end of the procedures.

We observed isolated ventricular extrasystoles in 2 animals, without any repercussion in hemodynamic parameters. As long as the focal spot of the therapy device remained on the bioprosthesis, no arrhythmia was visible.

After the threshold was reached and all parameters were re-evaluated, the animal was sacrificed and the heart was explanted. Macroscopic analysis showed that all cardiac structures were intact (**Figure 6**), except in 1 animal in which a 7-mm diameter superficial hematoma (epicardium) was visible at the lateral left ventricle wall (on the path of the ultrasound beam). This animal was also 1 of 2 animals that presented isolated ventricular extrasystoles. At the end of the procedure, the bioprosthesis was sent to the department of pathology for histopathological analysis.

ELASTOGRAPHY. Elastography results are displayed in **Figures 7A and 7B**. In vitro, before PCU, the mean stiffness of the valve leaflets measured by elastography was 105.8 ± 9 kPa. After the procedure, the mean stiffness of the valve leaflets measured by elastography was 46.6 ± 4 kPa, corresponding to a decrease of 55 ± 8% ($p < 0.001$).

Author's Personal Copy

FIGURE 6 Macroscopic Postmortem Analysis

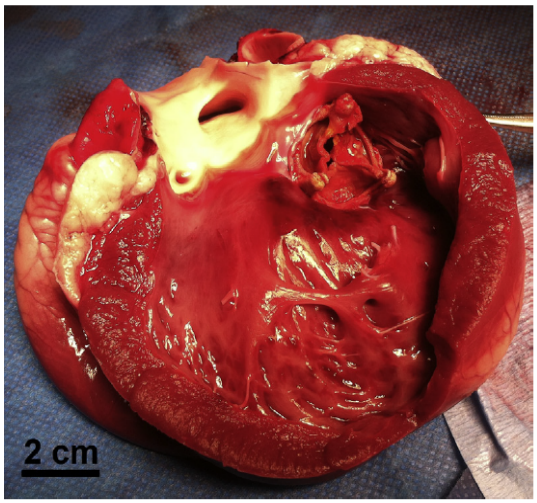

Macroscopic analysis showed that all cardiac structures were intact. The whole hearts appeared intact from the outside, with no visible damage on the epicardial surfaces (except in 2 animals in which a 7-mm diameter superficial hematoma [epicardium] was visible). After dissection, no damage was observed inside of the heart.

We observed a similar stiffness decrease for the bioprosthesis used in vivo (82.6 ± 10 kPa before the procedure and 41.7 ± 7 kPa after PCU, 49 ± 7% decrease; $p < 0.001$). The results of each individual bioprosthesis are shown in Supplemental Figure 3.

MICROSCOPIC ANALYSIS. Histological exploration. The histological exploration is described in **Figure 8**. All superficial structures of the leaflets were intact (fibrosa and ventricularis). In comparison with the 5 bioprosthesis explanted without PCU procedure, we observed:

- A fragmentation of the calcification.
- Presence of vacuoles inside the calcification.

There was no histological evidence for acute inflammation or acute thrombosis on the bioprosthesis.

Micro-CT imaging. Micro-CT imaging did not show modifications of the calcification shapes (Supplemental Figure 4). However, we did observe qualitatively multiple fragmentations inside of the calcification after PCU. These micro-fragmentations are visible as subvoxel modifications of the CT image (size <20 μm) so that quantitative analysis remains limited.

The estimation of calcification volume shows no statistical difference before PCU (mean volume = 294.9 mm^3 [minimum 45.7 mm^3; maximum 662.3 mm^3]) and after PCU (mean volume = 288.9 mm^3 [minimum 42.9 mm^3; maximum 659.9 mm^3]), with a mean diminution of 2.02% ($p = 0.44$).

DISCUSSION

In this study, we demonstrated in vitro and in vivo that PCU can remotely decrease the transvalvular gradients of calcified bioprosthetic valves. The mean and maximal transvalvular gradients decreased by 2-fold on average in both the in vitro and in vivo setups. Moreover, these hemodynamic modifications persisted after 1 month (evaluated only in vitro). The evolution of other echocardiographic parameters measured in vivo (valve area, pulmonary artery pressure) confirmed a consistent decrease of the valvular stenosis. Finally, we showed that PCU induced a decrease of the valves leaflet stiffness.

We believe that PCU can have a real clinical effect on the treatment of calcified bioprosthesis stenosis. Its 2 main advantages are: 1) it could be potentially applied in a transthoracic configuration completely noninvasively; and 2) it would allow the preservation of the bioprosthesis valve ad integrum.

EFFECT OF PCU ON CALCIFIED BIOPROSTHESIS VALVE. Using quantitative shear wave elastography, we demonstrated that the biomechanical properties of calcified leaflets were modified by PCU. The stiffness was decreased on average by 2-fold. The softening mechanism induced by PCU may be complex and needs to be further investigated; however, we can hypothesize that calcifications are mostly affected by the treatment. The histological analyses showed a fragmentation of calcifications with the preservation of the leaflet superficial structures. Micro-CT imaging, which can be considered a gold standard for valvular calcification evaluation (15,16), confirmed that microfragmentations appeared inside the calcification after PCU. This microfragmentation of large calcifications could explain the overall change of biomechanical properties, which leads to the improvement of the leaflet motion. Further investigation is required to better understand other potential mechanisms of PCU and, in particular, its effect on soft valvular tissues.

SAFETY. Accuracy of therapy. For 2 animals, we observed a few nonpersistent ventricular extrasystoles, and post-mortem anatomic exploration showed bruising of the cardiac wall due to off-target cavitation. These 2 undesirable effects are mostly induced by the actual complexity of the target positioning and motion, and could be greatly reduced with some

Author's Personal Copy

FIGURE 7 Elastography

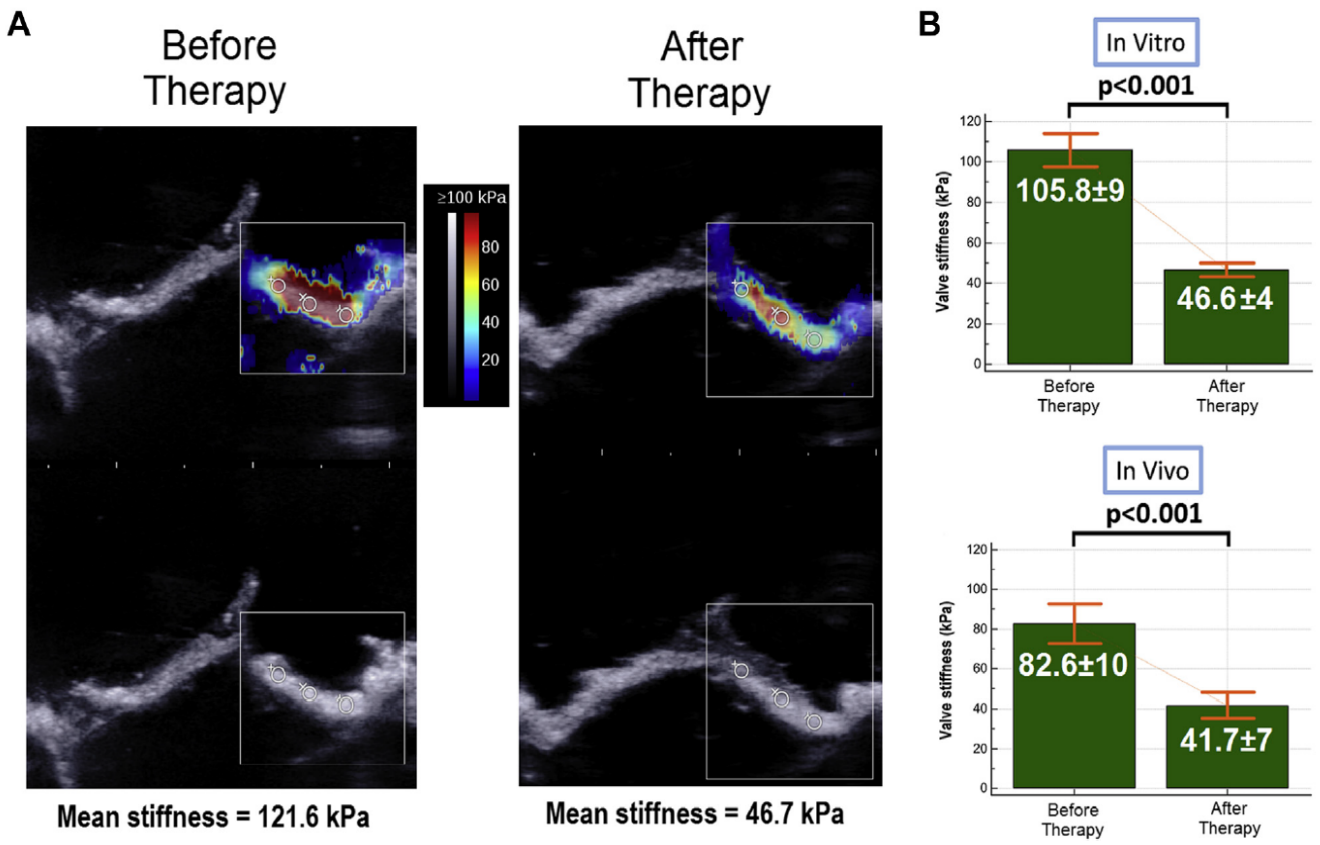

(A) Example of bioprosthesis elastography in vitro by shear wave elastography. **(B)** Elastrography results (in vitro and in vivo).

technical improvements. As our therapeutic transducer is readily focused at a single location, the target position can only be changed by mechanically and slowly moving the therapy device with millimetric motors. To solve this problem, a multielement transducer could be used to steer the focal spot electronically in real time. Three-dimensional motion correction would then be feasible in real-time, based on an accurate ultrasonic speckle-tracking method that has been demonstrated for high-intensity focused ultrasound applications in 2004 by our team (17) and, more recently, for histotripsy (18). With such a motion correction technique, we would be able to track the valve motion all along the cardiac cycle and avoid off-target cavitation. An easier strategy would be to trigger PCU exposures by electrocardiogram (19). We could, for instance, select specific moments in the cardiac cycle when the valve is closed. Thus, its whole surface would be equally exposed and far away from the cardiac wall.

Emboli. Our study aimed to demonstrate proof of concept of efficacy. We have thus not precisely evaluated the clinical risk of emboli during and after PCU by endovascular filter or brain magnetic resonance imaging/CT, and these explorations should be performed during specific risk evaluation studies. Nevertheless, our histological exploration after in vitro and in vivo procedures have shown the preservation of the leaflet superficial structures (fibrosa and ventricularis). These are fundamental structures around the calcification (20), meaning that our action seems to be confined within the leaflet. This result was confirmed by the micro-CT explorations, which found no statistical difference in calcification volumes before and after PCU. This local intravalvular effect is a reassuring argument against the major risk of emboli. Moreover, the specific histological lesions due to PCU noted inside the calcification (vacuole) seem to preserve the overall architecture of the valve leaflet.

Concerning cardiac application of PCU, in 2009, Xu et al. (21) showed that the size of myocardium debris obtained after histotripsy was inferior to the size of a red blood cell for >99% of the debris. As of now, no studies have been conducted specifically on valvular calcifications and PCU.

Author's Personal Copy

FIGURE 8 Histological Analysis

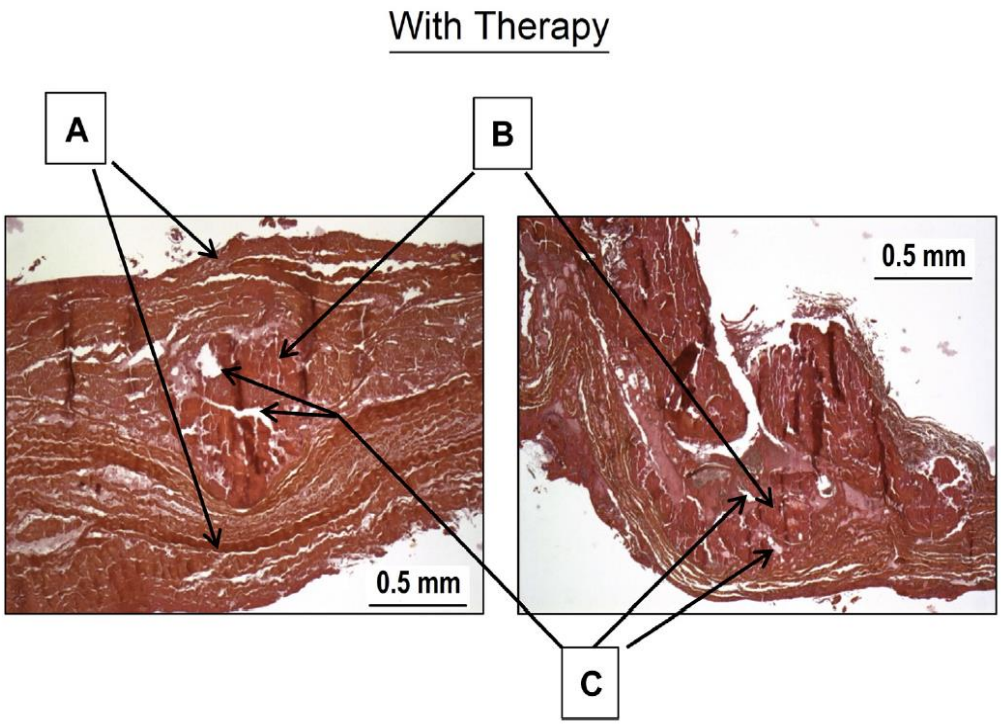

After pulsed cavitational focused ultrasound, the superficial structures remain intact **(A)**. An aspect of calcification fragmentation is visible **(B)**. Some vacuoles are also found inside of the calcifications **(C)**.

STUDY LIMITATIONS. In vivo follow-up. We observed stability of the transvalvular gradient in vitro 1 month after the procedure. However, this was not confirmed for the in vivo procedure, because we sacrificed the animals directly after the procedure. It is, therefore, difficult to evaluate the persistence of the therapeutic effect.

Shear wave elastography evaluation. Shear wave elastography has never been used for the stiffness evaluation of valve leaflets; therefore, this application needs to be validated in further studies. In particular, previous studies have shown the limitation of shear wave elastography in thin layers such as in the arterial wall. In such a medium, the shear waves are guided inside the 2-dimensional leaflet, and correspond to leaky lamb wave propagation (22). This affects the elastography measures, which prohibits direct derivation of the absolute values of leaflet stiffness. Nevertheless, semiquantitative evaluation of leaflet stiffness remains possible by performing elastography before and after PCU on the same leaflet (22,23).

Transthoracic approach. Transthoracic treatment should be feasible but requires further development of the therapy device. The main challenge of the transthoracic approach is to overcome the effect of the deep heterogeneous tissue layers on the path of the ultrasound beam. The ribs are a particularly strong barrier for ultrasound, allowing the ultrasonic beam to propagate only through the intercostal space. This limited aperture reduces the energy at the focal point as well as the quality of the focus. However, previous work in the field of histotripsy (24,25) and high-intensity focused ultrasound (26) have shown the feasibility of transcostal focusing.

CLINICAL APPLICATIONS. The treatment of calcified bioprosthesis stenosis in the mitral or aortic position is currently still a challenge. Redo surgery or transapical transcatheter valve-in-valve implantation expose the patient to significant risks, especially for patients with comorbidities (5,27). The results presented in this study may provide a new treatment option for these patients. From a general point of view, the PCU could be applied to a calcified bioprosthesis whatever its localization (aortic, mitral, tricuspid, or pulmonary), and this should be confirmed in further animal and human studies. If these results are confirmed and stable in the long-

Author's Personal Copy

term, the indication of bioprosthesis could be expanded to a wider and younger population with the acceptable perspective of noninvasive redux therapy in the long-term. This application, however, still needs to be confirmed by further prospective studies and significant follow-up.

CONCLUSIONS

We have demonstrated in vitro and in vivo that PCU can significantly decrease the transvalvular gradient of a calcified bioprosthesis stenosis by softening the leaflets remotely and improving valve opening. We believe that this novel ultrasound therapy could become a noninvasive therapeutic strategy in cardiology. This new noninvasive approach has the potential to improve the outcome of patients with severe calcified bioprosthesis stenosis by avoiding risky surgical or transcatheter reintervention.

ACKNOWLEDGMENTS The authors thank Hicham Serroune (Institut Langevin), Julie Piquet, and the staff of the Fondation Alain Carpentier and the Laboratoire biochirurgical.

ADDRESS FOR CORRESPONDENCE: Dr. Emmanuel Messas, Hôpital Européen Georges Pompidou, Cardio-vascular Department Faculté de médecine Paris Descartes, Université Paris Descartes Inserm UMR 970 Paris Research Cardiovascular Center. Paris, Ile-de-France 75908, France. E-mail: emmanuel.messas@aphp.fr.

PERSPECTIVES

COMPETENCY IN MEDICAL KNOWLEDGE: Heart valves are being increasingly replaced by bioprostheses. These bioprostheses have a limited lifespan, and degenerative calcified bioprosthesis carries a dire prognosis despite recent advances in surgery and transcatheter valve-in-valve implantation. Less-invasive strategies to treat calcified valves are needed. The results of this study show that PCU can soften calcified leaflets noninvasively and improve their opening function.

TRANSLATIONAL OUTLOOK: The present study is a proof of concept of the efficacy of PCU to soften bioprosthesis valves. This is an important initial step in translating PCU softening toward clinical applications. Future experimental and translational studies are required to investigate the feasibility and the safety of this new therapeutic approach in human patients.

REFERENCES

1. Vahanian A, Alfieri O, Andreotti F, et al. Guidelines on the management of valvular heart disease (version 2012). The Joint Task Force on the Management of Valvular Heart Disease of the European Society of Cardiology (ESC) and the European Association for Cardio-Thoracic Surgery (EACTS). G Ital Cardiol (Rome) 2013;14:167–214.

2. Jamieson WRE, Rosado LJ, Munro AI, et al. Carpentier-Edwards standard porcine bioprosthesis: primary tissue failure (structural valve deterioration) by age groups. Ann Thorac Surg 1988;46:155–62.

3. Thourani VH, Weintraub WS, Guyton RA, et al. Outcomes and long-term survival for patients undergoing mitral valve repair versus replacement. Circulation 2003;108:298–304.

4. Potter DD, Sundt TM, Zehr KJ, et al. Risk of repeat mitral valve replacement for failed mitral valve prostheses. Ann Thorac Surg 2004;78:67–72.

5. Ye J, Cheung A, Yamashita M, et al. Transcatheter aortic and mitral valve-in-valve implantation for failed surgical bioprosthetic valves. J Am Coll Cardiol Intv 2015;8:1735–44.

6. Williamson WA, Aretz HT, Weng G, et al. In vitro decalcification of aortic valve leaflets with the Er:YSGG laser, Ho:YAG laser, and the cavitron ultrasound surgical aspirator. Lasers Surg Med 1993;13:421–8.

7. Hutcheson JD, Aikawa E, Merryman WD. Potential drug targets for calcific aortic valve disease. Nat Rev Cardiol 2014;11:218–31.

8. Freeman WK, Schaff HV, Orszulak TA, Tajik AJ. Ultrasonic aortic valve decalcification: serial Doppler echocardiographic follow-up. J Am Coll Cardiol 1990;16:623–30.

9. Xu Z, Owens G, Gordon D, Cain CA, Ludomirsky A. Noninvasive creation of an atrial septal defect by histotripsy in a canine model. Circulation 2010;121:742–9.

10. Villemain O, Kwiecinski W, Bel A, et al. Pulsed cavitational ultrasound for non-invasive chordal cutting guided by real-time 3D echocardiography. Eur Heart J Cardiovasc Imaging 2016;17:1101–7.

11. Ebbini ES, ter Haar G. Ultrasound-guided therapeutic focused ultrasound: current status and future directions. Int J Hyperthermia 2015;31:77–89.

12. Zoghbi WA, Chambers JB, Dumesnil JG, et al. Recommendations for evaluation of prosthetic valves with echocardiography and Doppler ultrasound. J Am Soc Echocardiogr 2009;22:975–1014, quiz 1082–4.

13. Vahanian A, Alfieri O, Andreotti F, et al. Guidelines on the management of valvular heart disease (version 2012). Eur Heart J 2012;33:2451–96.

14. Baumgartner H, Hung J, Bermejo J, et al. Echocardiographic assessment of valve stenosis: EAE/ASE recommendations for clinical practice. Eur J Echocardiogr 2009;10:1–25.

15. Baker M. Whole-animal imaging: the whole picture. Nature 2010;463:977–80.

16. Gillis K, Bala G, Roosens B, et al. Quantification of calcium amount in a new experimental model: a comparison between ultrasound and computed tomography. PLoS One 2016;11:e0148904.

17. Pernot M, Tanter M, Fink M. 3-D real-time motion correction in high-intensity focused ultrasound therapy. Ultrasound Med Biol 2004;30:1239–49.

18. Miller RM, Kim Y, Lin K-W, Cain CA, Owens GE, Xu Z. Histotripsy cardiac therapy system integrated with real-time motion correction. Ultrasound Med Biol 2013;39:2362–73.

19. Abe Y, Otsuka R, Muratore R, et al. In vitro mitral chordal cutting by high intensity focused ultrasound. Ultrasound Med Biol 2008;34:400–5.

20. Dweck MR, Boon NA, Newby DE. Calcific aortic stenosis: a disease of the valve and the myocardium. J Am Coll Cardiol 2012;60:1854–63.

21. Xu Z, Fan Z, Hall TL, Winterroth F. Size measurement of tissue debris particles generated from

Author's Personal Copy

pulsed ultrasound cavitational therapy-histotripsy. Ultrasound Med 2009;35:245-55.

22. Nguyen T-M, Couade M, Bercoff J, Tanter M. Assessment of viscous and elastic properties of sub-wavelength layered soft tissues using shear wave spectroscopy: theoretical framework and in vitro experimental validation. IEEE Trans Ultrason Ferroelectr Freq Control 2011;58:2305-15.

23. Couade M, Pernot M, Prada C, et al. Quantitative assessment of arterial wall biomechanical properties using shear wave imaging. Ultrasound Med Biol 2010;36:1662-76.

24. Kim Y, Wang T-Y, Xu Z, Cain CA. Lesion generation through ribs using histotripsy therapy without aberration correction. IEEE Trans Ultrason Ferroelectr Freq Control 2011;58:2334-43.

25. Kim Y, Vlaisavljevich E, Owens GE, Allen SP, Cain CA, Xu Z. In vivo transcostal histotripsy therapy without aberration correction. Phys Med Biol 2014;59:2553-68.

26. Marquet F, Aubry JF, Pernot M, Fink M, Tanter M. Optimal transcostal high-intensity focused ultrasound with combined real-time 3D movement tracking and correction. Phys Med Biol 2011;56:7061-80.

27. Maciejewski M, Piestrzeniewicz K, Bielecka-Dąbrowa A, Piechowiak M, Jaszewski R. Redo surgery risk in patients with cardiac prosthetic valve dysfunction. Arch Med Sci 2011;7:271-7.

KEY WORDS bioprosthesis, therapy, ultrasonic

APPENDIX For supplemental figures and a video, please see the online version of this article.

SUPPLEMENTARY FIGURES (ONLINE)

Supp Figure 1. In vitro results

Mean transvalvular gradient results of each valve

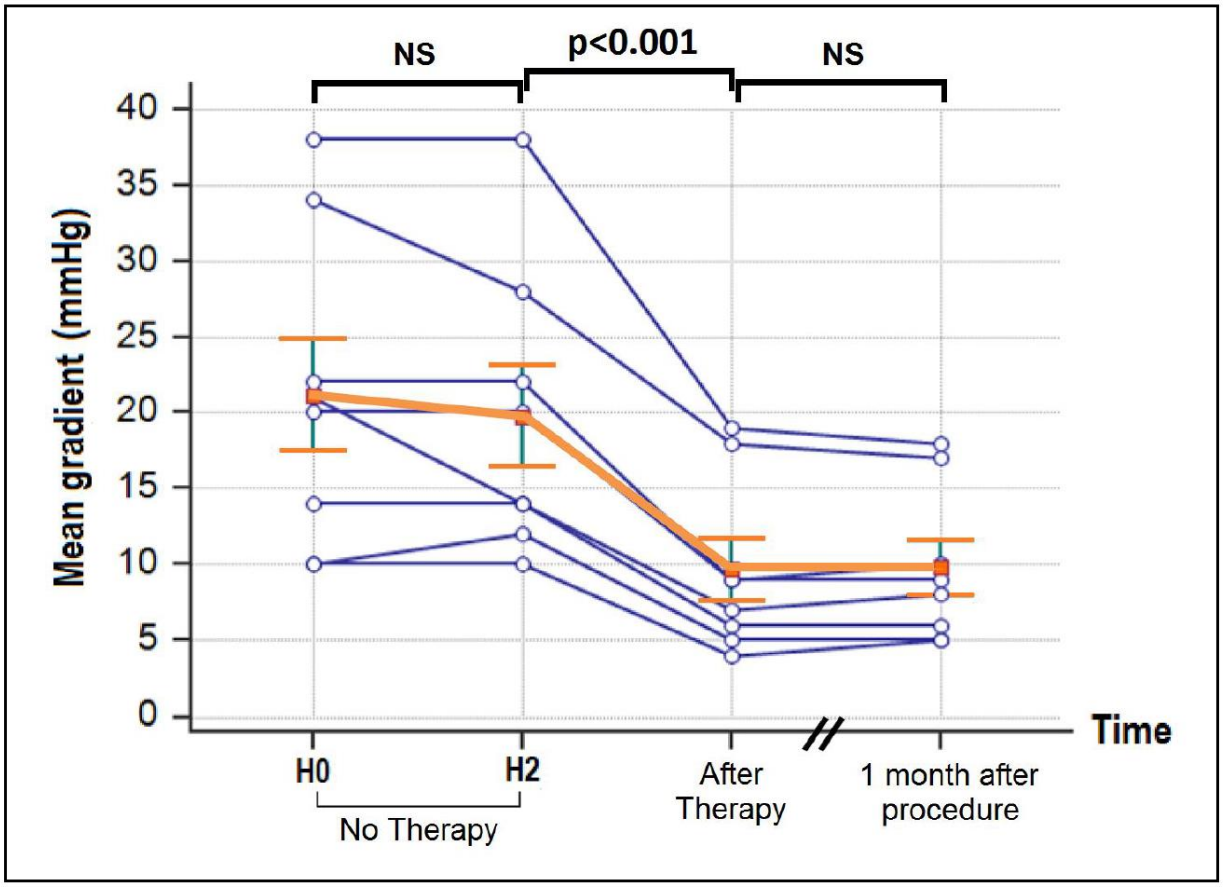

Supp Figure 2. In vitro results at increasing flow rates

Multi flow rates results (3L, 4L and 5L/min) of each valve

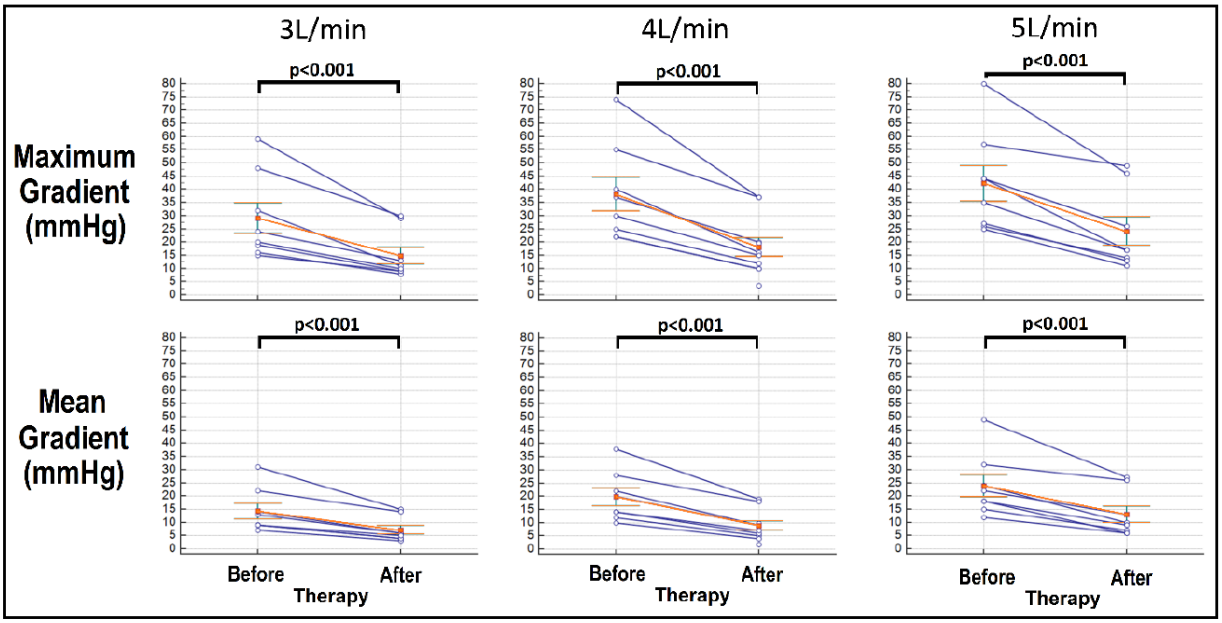

Supp Figure 3. Elastography results (in vitro and in vivo) of each valve

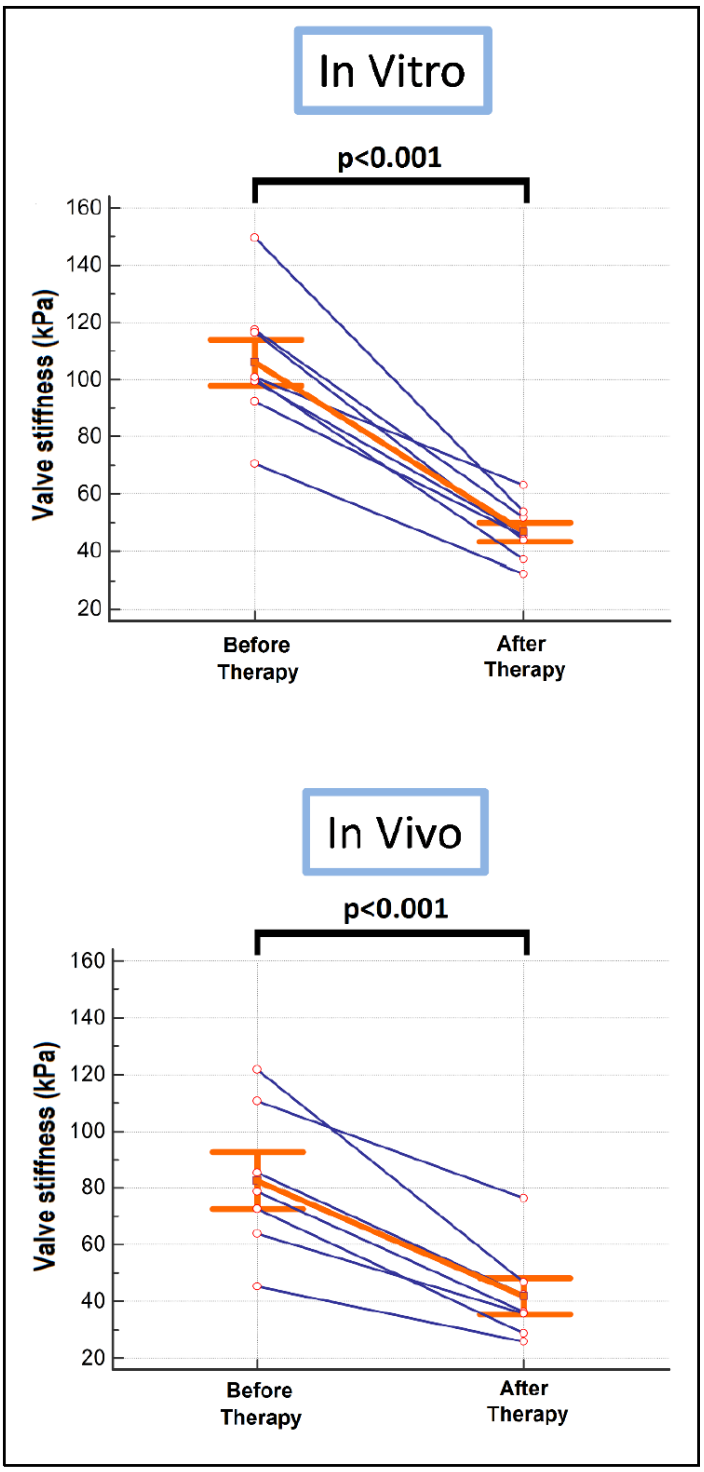

Supp Figure 4. Micro-CT Imaging (spatial resolution = 20 µm).

Thanks to a 3D reconstruction and a multi 2D plans evaluation, the valvular calcification were analyzed before and after pulsed cavitational focused ultrasound. The red arrows show the fragmentations inside the calcification.

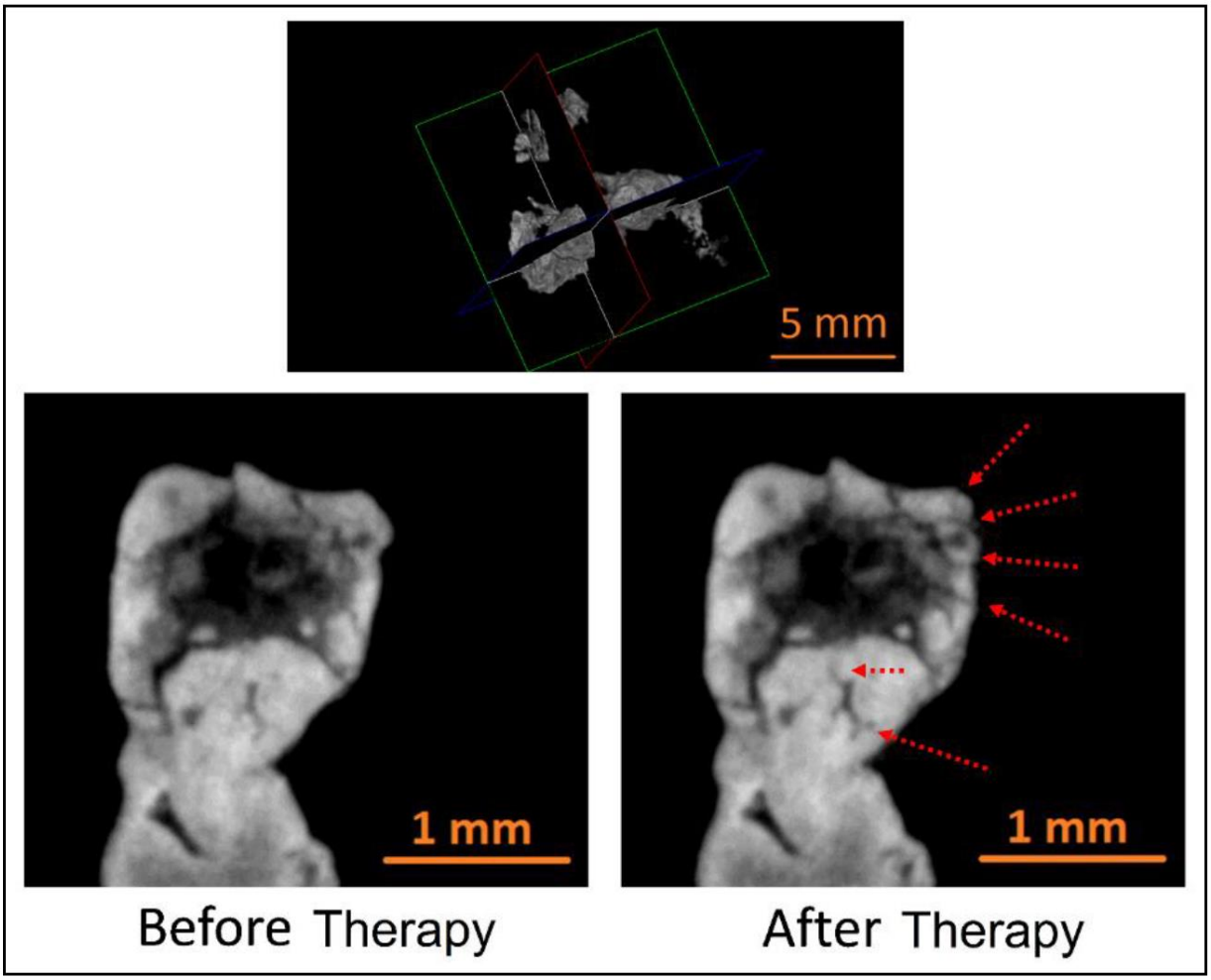

JACC: BASIC TO TRANSLATIONAL SCIENCE
VOL. 2, NO. 4, 2017
ISSN 2452-302X
http://dx.doi.org/10.1016/j.jacbts.2017.06.002
© 2017 THE AUTHORS. PUBLISHED BY ELSEVIER ON BEHALF OF THE AMERICAN COLLEGE OF CARDIOLOGY FOUNDATION. THIS IS AN OPEN ACCESS ARTICLE UNDER THE CC BY-NC-ND LICENSE (http://creativecommons.org/licenses/by-nc-nd/4.0/).

EDITORIAL COMMENT

Unbreak My Heart (Valve)

Can Ultrasound Be Used for the Treatment of a Degenerated Surgical Bioprosthesis?*

Jan-Malte Sinning, MD, Eberhard Grube, MD

Surgical aortic valve replacement increasingly uses bioprosthetic implants rather than mechanical valves. Because of this and the expanding indications for transcatheter heart valve therapies, the majority of patients undergoing an aortic valve replacement procedure will receive a pericardial tissue valve (1). Owing to this considerable shift toward bioprosthesis implantation, it is expected that patients will increasingly present with degenerated bioprostheses over time. Structural valve deterioration can result in leaflet degeneration and failure, as evidenced by valve stenosis, regurgitation, or a combination of both (2). Treatment of such patients remains a clinical challenge. Although reoperation is considered the standard of care, these patients are frequently elderly and repeat cardiac surgery is associated with a significant risk of morbidity and mortality. Transcatheter valve-in-valve implantation has emerged as a promising alternative treatment option for patients at high surgical risk; however, it comes with its own complications and limitations (3). Therefore, repair of a structurally degenerated bioprosthetic valve would be an intriguing causative therapy approach.

For more than 3 decades, other therapeutic strategies have been investigated to "unbreak" calcified native or bioprosthetic valves. One promising approach was ultrasound-based but remained limited at that time, because it still needed open heart surgery with cardiopulmonary bypass (4,5). Nevertheless, this limitation must be revisited again with the recent improvement of technologies and concepts of pulsed cavitational focused ultrasound (PCU). PCU or histotripsy is a noninvasive, cavitation-based technique that focuses very short, high-pressure ultrasound pulses in tissues to generate a dense, energetic, and lesion-producing bubble cloud. Although histotripsy can be used to produce sharp lesions, recent studies have suggested that cavitation activity can also soften biological tissues.

SEE PAGE 372

In this issue of *JACC: Basic to Translational Science*, Villemain et al. (6) demonstrated the in vitro efficacy of PCU on human explanted calcified bioprosthetic aortic valves mounted on an artificial heart pump, and they quantified the improvement of the valvular function by elastography. With PCU for approximately 1 h, the investigators showed a reduction in both the mean and maximum gradient of more than 50%.

In a second step, the investigators demonstrated the in vivo feasibility and efficacy by implanting explanted human calcified aortic bioprostheses in the mitral position of an ovine beating heart model. Valvular function was assessed by echocardiography, catheter-based hemodynamic measurement, and elastography, and again, gradients across the aortic bioprosthetic valves implanted in the mitral position were reduced by 50% on average after a mean PCU duration of 1 h.

Although the sheep study had some limitations, for example one-half of the animals did not survive the hemodynamic deterioration caused by the degenerated, severely stenosed, human bioprostheses, the investigators can be congratulated for presenting a

*Editorials published in *JACC: Basic to Translational Science* reflect the views of the authors and do not necessarily represent the views of *JACC: Basic to Translational Science* or the American College of Cardiology.

From the Department of Medicine II, Heart Center Bonn, University Hospital Bonn, Bonn, Germany. Dr. Sinning has received speaker honoraria and research grants from Medtronic, Edwards Lifesciences, and Boston Scientific. Dr. Grube is proctor for Medtronic and Boston Scientific; and has received speaker honoraria and research grants from Medtronic, Edwards Lifesciences, and Boston Scientific.

promising approach for percutaneous transthoracic treatment of degenerated bioprosthetic heart valves without the need for resternotomy or transcatheter valve-in-valve implantation. Interestingly, the investigators found no modification of the calcium pattern in the degenerated leaflets or reduction of the calcium volume but observed multiple microfragmentations within the calcification after PCU. Therefore, the investigators hypothesized that this "leaflet softening" might have led to an overall change in biomechanical properties with improvement of leaflet motion and simultaneous reduction of transvalvular gradients.

With further technical improvement such as the addition of a multielement transducer to steer the focal spot electronically in real time, the investigators hope to increase the accuracy of this therapy and avoid off-target cavitation. However, the clinical risks such as the possibility of cerebral debris embolization need to be further evaluated in future studies. Although the nonchanged calcium volume per leaflet in computed tomography imaging is an argument against a major risk of cerebral embolization, this should be evaluated in magnetic resonance imaging studies.

The major limitation of this report by Villemain et al. (6), and therefore the whole therapeutic approach, is that the persistence of the tissue-softening effect on degenerated prostheses was not evaluated, because all animals were sacrificed directly after the procedure. Surgical decalcification often leaves a fibrillar structure that tends rapidly to accumulate calcium. Even normal-appearing tissue from diseased valves has a higher potential for calcification than normal valvular tissue does. From other therapeutic approaches we have unfortunately learned that the therapeutic effect after the procedure may not be sustainable. For example, because of the high restenosis rates, balloon aortic valvuloplasty nowadays only plays a minor role as a palliative treatment choice or bridging therapy to transcatheter aortic valve replacement. Another issue is that we do not know how PCU would affect degenerated bioprostheses properly implanted in the aortic position and whether the results would be the same.

Taken together, we are looking forward to learn more about this promising approach in future studies and hope this could be the beginning of a new way to "unbreak" a heart valve (prosthesis)!

ADDRESS FOR CORRESPONDENCE: Dr. Eberhard Grube, Heart Center Bonn, Department of Medicine II, University Hospital Bonn, Sigmund-Freud-Strasse 25, 53105 Bonn, Germany. E-mail: grubee@aol.com.

REFERENCES

1. Holmes DR Jr., Mack MJ, Kaul S, et al. 2012 ACCF/AATS/SCAI/STS expert consensus document on transcatheter aortic valve replacement. J Am Coll Cardiol 2012;59:1200–54.

2. Foroutan F, Guyatt GH, O'Brien K, et al. Prognosis after surgical replacement with a bioprosthetic aortic valve in patients with severe symptomatic aortic stenosis: systematic review of observational studies. BMJ 2016;354:i5065–9.

3. Dvir D, Webb JG, Bleiziffer S, et al., for the Valve-in-Valve International Data Registry Investigators. Transcatheter aortic valve implantation in failed bioprosthetic surgical valves. JAMA 2014;312:162–70.

4. Worley SJ, King RM, Edwards WD, Holmes DR Jr. Electrohydraulic shock wave decalcification of stenotic aortic valves: postmortem and intraoperative studies. J Am Coll Cardiol 1988;12:458–62.

5. Freeman WK, Schaff HV, Orszulak TA, Tajik AJ. Ultrasonic aortic valve decalcification: serial Doppler echocardiographic follow-up. J Am Coll Cardiol 1990;16:623–30.

6. Villemain O, Robin J, Bel A, et al. Pulsed cavitational ultrasound softening: a new noninvasive therapeutic approach for calcified bioprosthetic valve stenosis. J Am Coll Cardiol Basic Trans Science 2017;2:372–83.

KEY WORDS heart valve, histotripsy, pulsed cavitational ultrasound, surgical bioprosthesis

7.4. Perspectives

A l'heure actuelle, l'histotripsie n'a pas encore été appliquée à visée cardiologique chez l'homme. Mais à la vue des dernières publications référencées précédemment, les limites technologiques sont de moins en moins nombreuses. En définitive, les deux principaux facteurs encore limitants semblent être le mouvement cardiaque et l'analyse du risque embolique.

Différentes solutions sont possibles pour passer outre les difficultés inhérentes à une cible en mouvement. Il existe finalement deux grands axes de travail : soit vous déclenchez les émissions acoustiques de hautes intensités à chaque fois que la cible passe dans le point focal, en triguant les émissions ; soit vous suivez la cible, en modifiant la localisation du point focal dans un volume. L'équipe de Michigan, qui a beaucoup publié entre 2004 et 2012 sur le phénomène de cavitation et les applications cardiaques potentielles (notamment la perforation de septum inter-atrial), a principalement travaillé sur la première solution. A l'institut Langevin, initiée par le travail de thèse de Bastien Arnal (Arnal et al. 2012) puis continué par le travail de thèse de Justine Robin (Robin et al. 2017)(Robin et al. 2017), c'est la seconde solution qui a été privilégiée. En effet, la thérapie cardiaque extracorporelle est un vrai défi technologique. Non seulement, le cœur est un organe peu accessible depuis l'extérieur du corps humain, situé en profondeur et protégé par les côtes, mais également en mouvement permanent. La cavité à retournement temporel permet de focaliser avec précision des impulsions ultrasonores très intenses sous guidage échographique. Cette innovation rendrait possible le ciblage de tous les tissus cardiaques comme les valves et les cordages en permettant de :

- Focaliser un faisceau ultrasonore très intense et déplacer le point focal dans un large volume grâce à la focalisation par retournement temporel.
- Focaliser avec une précision millimétrique grâce au guidage échographique en temps-réel
- Corriger en temps-réel les mouvements cardiaques grâce à la focalisation électronique et au couplage échographique
- Préserver totalement les tissus en amont du point focal, en particulier les côtes, grâce à la focalisation d'une impulsion extrêmement brève (~ 1µs).

La focalisation d'ondes par retournement temporel a été présentée par Mathias Fink dans les années 90 (Fink 1992). A partir de cela est né le concept de cavité à retournement

temporel permettant une focalisation modifiable dans un volume grâce à un nombre restreint de transducteurs ultrasonores.

Le second facteur limitant concerne les risques emboliques, encore explorés de manière incomplète. L'analyse des fragments de myocarde post fragmentation par phénomène de cavitation avait fait l'objet d'une publication par Xu et al en 2009 (Xu et al. 2009). La principale information était que plus de 99% des fragments avaient une taille inférieure à 6 µm, soit la taille moyenne d'un globule rouge, donc avec un risque nul d'occlusion intravasculaire. Concernant les fragments tissulaires des cordages mitraux et surtout des valves calcifiées, les seules résultats disponibles à ce jour sont ceux présents dans les manuscrits présentés ci-dessus. Il reste évidemment un travail spécifique à fournir pour comprendre et analyser ce risque. Pour cela, des analyses additionnelles in vitro sont possibles et des modèles animaux du risque embolique également (par filtre endovasculaire ou par imagerie cérébrale post PCUS). A ce titre, nous avions essayé de développer durant mon travail de thèse un modèle de lapin avec valve calcifiée acquise (par régime alimentaire spécifique +/- insuffisance rénale chronique post néphrectomie sub-totale). L'obtention de ce modèle fut extrêmement laborieuse, voir irréalisable, du fait de la mauvaise tolérance de l'animal au régime et/ou à la maladie se constituant. Malgré tout, ce projet présentait l'avantage de proposer un modèle animal acquis et non-invasif, avec possibilité théorique de follow-up longs terme post PCUS et imagerie par IRM pour surveillance de risque embolique cérébral. En définitive, sur 36 lapins ayant débuté le protocole, 1 seul a constitué la maladie et a survécu. Il a pu bénéficier de plusieurs procédures de PCUS montrant une diminution de gradient transvalvulaire.

Nous n'avons pas abouti ce projet de modèle animal complet faute de modèle viable. Cependant, cela reste une perspective importante de cette thématique de projet. Dans la continuité, l'application humaine devient de plus en plus palpable. Une spin-off (Cardiawave) a été créée en 2014, naissant du partenariat de l'Institut Langevin, de l'hopital Européen Georges Pompidou et du milieu industriel, pour permettre à cette technologie d'aller jusqu'au l'humain et de devenir applicable. Cardiawave travaille actuellement pour réaliser le first-in-human à horizon 2018.

Pour conclure concernant les perspectives de la thérapie par ultrasons en cardiologie, et pour parler d'un point de vue plus personnel, je pense que les applications en cardiologie congénitale seraient accessibles, passionnantes et variées. En l'état actuel de la technologie et de ses limites, il semble déjà possible de réaliser une perforation de myocarde de manière strictement non-invasive. Un objectif concret à moyen terme serait de réaliser

une atrioseptostomie par ultrason. L'Histoire serait belle car, après la chirurgie (première circulation extra-corporelle pédiatrique en 1955, Minneapolis, US), après le cathétérisme initialement diagnostique puis devenant thérapeutique notamment à travers la manœuvre de Rashkind (1963, atrioseptostomie par voie percutanée), les ultrasons pourraient modifier les stratégies thérapeutiques en cardiologie congénitale. Après avoir été uniquement un outil diagnostique depuis les années 1960, il semble que les ultrasons puissent trouver une place dans la réflexion de soins actifs. Finalement, il serait illégitime de penser que cela reste très théorique, trop à distance de réelle possibilité d'application. A la lumière de la littérature et des avancées récentes, je suis convaincu que cela sera réalisé dans les prochaines années.

8. Perspectives générales

Chaque chapitre de cette thèse a ses résultats et ses limites. Malgré tout, pour un travail réalisé à l'interface entre la physique acoustique et l'application médicale, il semble important de conceptualiser une « mise en application » de futurs projets pouvant être initiés dans la continuité de travaux réalisés. D'un point de vue personnel, ces perspectives seront principalement axées sur les applications de cardiologie pédiatrique, de par ma formation et mon environnement futur.

Concernant l'élastographie myocardique, nous avons présenté la preuve de concept applicative chez l'enfant et chez l'adulte, en distinguant une cardiopathie caractéristique (cardiomyopathie hypertrophique) et des volontaires sains. Je pense que des travaux futurs pourraient être structurés autour de deux axes :

- Montrer que l'élastographie myocardique pourrait être un outil diagnostique additionnel à l'échocardiographie conventionnelle pour caractériser et définir ? quantitativement la fonction diastolique
- Montrer que l'élastographie myocardique serait capable d'être un outil de suivi de modification thérapeutique, comme dans l'insuffisance cardiaque (aigue ou chronique).

C'est en répétant les protocoles cliniques que nous déterminerons au mieux les champs d'application (et les limites) de l'élastographie myocardique.

Concernant l'élastographie hépatique, il semble maintenant évident que cet outil d'imagerie pourrait être intégré dans de multiples projets de recherche. Il est simple, facile d'utilisation, ne nécessite aucune démarche éthique particulière et donne un résultat quantitatif interprétable aisément. Dans la cardiologie pédiatrique, les cœurs univentriculaires avec montage de type Fontan (dérivation des retours veineux systémiques directement dans les artères pulmonaires, qui se fait classiquement en trois temps chirurgicaux espacés de plusieurs mois voire années) sont une population particulièrement intéressante car nombreuse, souffrant de troubles hépatiques, et vivant avec un foie « directement » connecté aux poumons (du moins d'un point de vue hémodynamique). Nous réalisons actuellement un recueil de données prospectif sur toutes les cardiopathies avec stratégie de Fontan, dans le service de cardiologie de l'hôpital Necker, avec l'élastographie avant et après différents temps chirurgicaux, afin d'observer les modifications de rigidités hépatiques en fonction du temps et des délais chirurgicaux. L'objectif est de voir si l'élastographie hépatique serait un outil non invasif fiable pour évaluer le risque de morbi/mortalité de ces cardiopathies.

Concernant le BTI (imagerie d'orientation de fibres musculaires) et le Power doppler, les applications cliniques restent encore limitées à mon avis par la nécessité d'une analyse volumique. A travers le développement des sondes matricielles (donc 3-D) à très hautes cadence d'images, ces nouveaux outils d'imagerie trouveront assez spontanément des champs d'application en pratique clinique. En l'état actuel des choses, avec des sondes linéaires (donc 2-D), nous réalisons actuellement un protocole de recherche clinique prospectif, dans le service de cardiologie à l'hôpital Necker, sur l'imagerie coronarienne des transpositions des gros vaisseaux (TGV) avant et après leur réparation chirurgicale à quelques jours de vie, consistant à inverser les gros vaisseaux de position (pour qu'ils retrouvent une position anatomique normale) et réimplanter les coronaires dans l'aorte. L'objectif de cette étude est de montrer qu'il est possible d'imager les flux intra-coronarien chez des nouveaux patients atteints de TGV. Les résultats seront principalement descriptifs, et permettront d'observer (ou non) des variations de perfusion avant-après chirurgie correctrice.

Concernant le couplage électromécanique, le protocole de recherche sur les fœtus (décrit dans le paragraphe 6.2) est actuellement en cours, toujours dans le service de cardiologie à Necker. A travers les résultats obtenus sur le fœtus et les résultats obtenus en 3-D grâce aux travaux de Victor Finel à l'Institut Langevin, les futures perspectives en cardiologie congénitale seraient de cartographier l'ensemble de l'activité électromécanique sur un cœur de nouveau-né de manière non-invasive (par ultrason). La taille du cœur d'un nouveau-né pourrait être un avantage (en comparaison à celui d'un cœur d'adulte), si l'acquisition se faisait en ondes planes (et non pas en ondes divergentes) car la taille du volume serait déterminée par la taille de la matrice d'élément piézoélectriques et par la profondeur d'acquisition. En définitive, nous restons encore dépendants de certains développements technologiques pour pouvoir nous projeter pleinement sur des applications cliniques variées.

Enfin, la thérapie par ultrason focalisés. Comme déjà développé dans le paragraphe 7.4, la future étape me semble être l'atrioseptostomie par ultrason. Cela pourrait être réalisé de manière séquentielle : d'abord au bloc chirurgical en sternotomie avec thorax immergé d'eau dégazée (comme sur nos protocoles pré-cliniques) et à cœur battant, puis en transthoracique chez un nouveau-né en milieu de sauvetage si nécessaire (bloc opératoire). Le seul enjeu actuel reste à savoir quelle équipe dans le monde le réalisera en premier, car les verrous techniques et technologiques ont tous sauté ces dernières années.

9. Conclusions

Durant ce travail de thèse, nous avons montré que les ultrasons pouvaient agir sur les tissus cardiaques, soit en les stimulant à distance afin de modifier leurs propriétés viscoélastiques (élastographie), soit en les fragmentant à visée thérapeutique (phénomène de cavitation); Nous avons également montré que l'imagerie ultrasonore à haute cadence d'image ouvrait des perspectives de compréhension (orientation des fibres myocardiques par BTI), d'analyse (couplage électromécanique) ou de diagnostic (Power doppler et élastographie).

C'est à l'interface entre le fondamental et l'applicatif que ce travail de thèse s'est construit, permettant d'apporter plusieurs preuves de concept, soit à distance de l'humain soit directement au contact de celui-ci.

Comme tout travail de recherche, cette thèse n'est qu'une pierre ajoutée à un projet d'une autre envergure, porté par l'institut Langevin et notamment par mon directeur de recherche Mathieu Pernot, ayant pour objectif d'élargir le champ d'application des ultrasons en cardiologie. A l'instar des autres techniques d'imagerie comme les rayons-X, l'imagerie par résonnance magnétique, ou l'imagerie nucléaire, ce n'est que par l'innovation et l'optimisation de l'aide au clinicien que les ultrasons resteront l'outil de première ligne du cardiologue. Ce travail de thèse, qui avait pour but de montrer que les ultrasons ont de nouvelles choses à apporter en cardiologie clinique, permet de résumer une partie de ces innovations.

Je conclurai ce manuscrit de thèse en plagiant avec plaisir Jonathan Lindner qui, dans son Edito sur notre travail concernant l''imagerie des coronaires par ultrasons ((Lindner 2017),cf paragraphe 5.2), a parfaitement résumé mon sentiment général sur l'importance d'une collaboration « à plusieurs visages » dans ces projets de recherche avec technologie de rupture : "As in the past, partnership between engineers and experts in physiology and clinical medicine will be essential for moving this technology forward". Ce n'est que par le développement de ces interfaces entre plusieurs spécialistes que des technologies de ruptures peuvent s'imposer, particulièrement dans le domaine médical.

10. Références bibliographiques (autres que celles incluses dans les manuscrits)

Aikawa, Elena et al. 2006. “Human Semilunar Cardiac Valve Remodeling by Activated Cells From Fetus to Adult.” *Circulation* 113(10).

Arnal, B, Mathieu Pernot, M Fink, and Mickael Tanter. 2012. “Tunable Time-Reversal Cavity for High-Pressure Ultrasonic Pulses Generation: A Tradeoff between Transmission and Time Compression.” *Applied Physics Letters* 101(6): 64104.

Atz, A M et al. 1999. “Preoperative Management of Pulmonary Venous Hypertension in Hypoplastic Left Heart Syndrome with Restrictive Atrial Septal Defect.” *The American journal of cardiology* 83(8): 1224–28.

Baffa, Jeanne Marie et al. 1992. “Coronary Artery Abnormalities and Right Ventricular Histology in Hypoplastic Left Heart Syndrome.” *Journal of the American College of Cardiology* 20(2): 350–58.

Bailey, M. R. et al. 2003. “Physical Mechanisms of the Therapeutic Effect of Ultrasound (a Review).” *Acoustical Physics* 49(4): 369–88.

Bers, Donald M. 2002. “Cardiac Excitation–contraction Coupling.” *Nature* 415(6868): 198–205.

Bonhoeffer, Philipp et al. 1997. “Coronary Artery Obstruction After the Arterial Switch Operation for Transposition of the Great Arteries in Newborns.” *Journal of the American College of Cardiology* 29(1): 202–6.

Borger, Michael A. et al. 2007. “Initial Results of the Chordal-Cutting Operation for Ischemic Mitral Regurgitation.” *The Journal of Thoracic and Cardiovascular Surgery* 133(6): 1483–1492.e1.

Budin, Nahum, and Shimon Abboud. 1994. “Real-Time Multichannel Abdominal Fetal ECG Monitor Using Digital Signal CoProcessor.” *Computers in Biology and Medicine* 24(6): 451–62.

Charpie, John R et al. 2001. “Postoperative Hemodynamics after Norwood Palliation for Hypoplastic Left Heart Syndrome.” *The American Journal of Cardiology* 87(2): 198–202.

Correia, M. et al. 2016. “Ultrafast Harmonic Coherent Compound (UHCC) Imaging for High Frame Rate Echocardiography and Shear Wave Elastography.” *IEEE transactions on ultrasonics, ferroelectrics, and frequency control* 63(3): 420–31.

Correia, Mafalda, Jean Provost, Mickael Tanter, and M Pernot. 2016. “4D Ultrafast Ultrasound Flow Imaging: *In Vivo* Quantification of Arterial Volumetric Flow Rate in a Single Heartbeat.” *Physics in Medicine and Biology* 61(23): L48–61.

Cranefield, Paul F., and Brian F. Hoffman. 1958. “Electrophysiology of Single Cardiac Cells.” *Physiological Reviews* 38(1).

Demené, Charlie et al. 2016. “4D Microvascular Imaging Based on Ultrafast Doppler Tomography.” *NeuroImage* 127: 472–83.

Eliasson, H. et al. 2011. “Isolated Atrioventricular Block in the Fetus: A Retrospective, Multinational, Multicenter Study of 175 Patients.” *Circulation* 124(18): 1919–26.

van Engelen, Andries D. et al. 1994. “Management Outcome and Follow-up of Fetal Tachycardia.” *Journal of the American College of Cardiology* 24(5): 1371–75.

Ferrazzi, Paolo et al. 2015. “Transaortic Chordal Cutting.” *Journal of the American College of Cardiology* 66(15): 1687–96.

Fink, M. 1992. “Time Reversal of Ultrasonic Fields. I. Basic Principles.” *IEEE Transactions on Ultrasonics, Ferroelectrics and Frequency Control* 39(5): 555–66.

Freeman, Rosario V, and Catherine M Otto. 2005. “Spectrum of Calcific Aortic Valve Disease: Pathogenesis, Disease Progression, and Treatment Strategies.” *Circulation* 111(24): 3316–26.

Fujimoto, Naoki et al. 2012. “Effect of Ageing on Left Ventricular Compliance and Distensibility in Healthy Sedentary Humans.” *The Journal of physiology* 590(8): 1871–80.

Goldbarg, Seth H., Sammy Elmariah, Marc A. Miller, and Valentin Fuster. 2007. “Insights Into Degenerative Aortic Valve Disease.” *Journal of the American College of Cardiology* 50(13): 1205–13.

Jenne, Jürgen W., and et al. 2012. “High-Intensity Focused Ultrasound: Principles, Therapy Guidance, Simulations and Applications.” *Zeitschrift für Medizinische Physik* 22(4): 311–22.

Kähler, C. et al. 2001. “The Application of Fetal Magnetocardiography (FMCG) to Investigate Fetal Arrhythmias and Congenital Heart Defects (CHD).” *Prenatal Diagnosis* 21(3): 176–82.

Kariniemi, V, J Ahopelto, P J Karp, and T E Katila. 1974. “The Fetal Magnetocardiogram.” *Journal of perinatal medicine* 2(3): 214–16.

Kim, Y et al. 2011. “Non-Invasive Pulsed Cavitational Ultrasound for Fetal Tissue Ablation: Feasibility Study in a Fetal Sheep Model.” *Ultrasound in obstetrics & gynecology : the official journal of the International Society of Ultrasound in Obstetrics and Gynecology* 37(4): 450–57.

Konofagou, Elisa E. et al. 2010. “Noninvasive Electromechanical Wave Imaging and Conduction-Relevant Velocity Estimation in Vivo.” *Ultrasonics* 50(2): 208–15.

Kunzelman, K S, and R P Cochran. 1991. “Mechanical Properties of Basal and Marginal Mitral Valve Chordae Tendineae.” *ASAIO transactions / American Society for Artificial Internal Organs* 36(3): M405-8.

Kurz, David J. et al. 2006. “Degenerative Aortic Valve Stenosis, but Not Coronary Disease, Is Associated With Shorter Telomere Length in the Elderly.” *Arteriosclerosis, Thrombosis, and Vascular Biology* 26(6).

Lee, Wei-Ning et al. 2010. “Noninvasive Assessment of Myocardial Anisotropy in Vitro and in Vivo Using Supersonic Shear Wave Imaging.” In *2010 IEEE Ultrasonics Symposium (IUS)*, , 690–93.

Lee, Wei-Ning et al. 2012. “Mapping Myocardial Fiber Orientation Using Echocardiography-Based Shear Wave Imaging.” *IEEE transactions on medical imaging* 31(3): 554–62.

Leon, Martin B. et al. 2016. “Transcatheter or Surgical Aortic-Valve Replacement in Intermediate-Risk Patients.” *New England Journal of Medicine* 374(17): 1609–20.

Lindner, Jonathan R. 2017. “The Fast and the Curious.” *JACC: Cardiovascular Imaging*.

Lombaert, H. et al. 2012. “Human Atlas of the Cardiac Fiber Architecture: Study on a Healthy Population.” *IEEE Transactions on Medical Imaging* 31(7): 1436–47.

Madersbacher, S et al. 1995. “Effect of High-Intensity Focused Ultrasound on Human Prostate Cancer in Vivo.” *Cancer research* 55(15): 3346–51.

Maron, B.J., and Martin S Maron. 2013. “Hypertrophic Cardiomyopathy.” *The Lancet*

381(9862): 242–55.

Marshall, Audrey C et al. 2004. “Creation of an Atrial Septal Defect in Utero for Fetuses with Hypoplastic Left Heart Syndrome and Intact or Highly Restrictive Atrial Septum.” *Circulation* 110(3): 253–58.

Maxwell, Adam D et al. 2011. “Noninvasive Treatment of Deep Venous Thrombosis Using Pulsed Ultrasound Cavitation Therapy (Histotripsy) in a Porcine Model.” *Journal of vascular and interventional radiology : JVIR* 22(3): 369–77.

Mcmurray, John J V et al. 2012. “ESC Guidelines for the Diagnosis and Treatment of Acute and Chronic Heart Failure 2012.” *European Journal of Heart Failure* 14(8): 803–69.

Meredith, Ian T. et al. 2016. “1-Year Outcomes With the Fully Repositionable and Retrievable Lotus Transcatheter Aortic Replacement Valve in 120 High-Risk Surgical Patients With Severe Aortic Stenosis.” *JACC: Cardiovascular Interventions* 9(4): 376–84.

Messas, E., J. L. Guerrero, M. D. Handschumacher, C. Conrad, et al. 2001. “Chordal Cutting: A New Therapeutic Approach for Ischemic Mitral Regurgitation.” *Circulation* 104(16): 1958–63.

Messas, E., J. L. Guerrero, M. D. Handschumacher, C.-M. Chow, et al. 2001. “Paradoxic Decrease in Ischemic Mitral Regurgitation With Papillary Muscle Dysfunction: Insights From Three-Dimensional and Contrast Echocardiography With Strain Rate Measurement.” *Circulation* 104(16): 1952–57.

Messika-Zeitoun, David et al. 2007. “Aortic Valve Calcification.” *Arteriosclerosis, Thrombosis, and Vascular Biology* 27(3).

Miller, Ryan M, G Owens, Achiau Ludomirsky, and Zhen Xu. 2012. “Therapeutic Ultrasound to Non-Invasively Create Intra-Cardiac Communications in an Intact Animal Model.” *Catheterization and cardiovascular interventions* 77(4): 580–88.

Minamino, Tohru, and Issei Komuro. 2007. “Vascular Cell Senescence.” *Circulation Research* 100(1).

Nishimura, Rick A., Patrick T. O’Gara, Robert O. Bonow, and Bleiziffer S. 2017. “Guidelines Update on Indications for Transcatheter Aortic Valve Replacement.” *JAMA Cardiology* 312(2): 162–70.

Papadacci, Clement et al. 2017. “Imaging the Dynamics of Cardiac Fiber Orientation in Vivo

Using 3D Ultrasound Backscatter Tensor Imaging." *Scientific Reports* 7(1): 830.

Pernot, M., and E.E. Konofagou. 2005. "Electromechanical Imaging of the Myocardium at Normal and Pathological States." In *IEEE Ultrasonics Symposium*, IEEE, 1091–94.

Pernot, Mathieu, Kana Fujikura, Simon D. Fung-Kee-Fung, and Elisa E. Konofagou. 2007. "ECG-Gated, Mechanical and Electromechanical Wave Imaging of Cardiovascular Tissues In Vivo." *Ultrasound in Medicine & Biology* 33(7): 1075–85.

Plesset, MS. 1949. "The Dynamics of Cavitation Bubbles." *Journal of applied mechanics*.

Provost, Jean et al. 2014. "3D Ultrafast Ultrasound Imaging in Vivo." *Physics in Medicine and Biology* 59(19): L1.

Provost, Jean, Wei-Ning Lee, Kana Fujikura, and Elisa E Konofagou. 2011. "Imaging the Electromechanical Activity of the Heart in Vivo." *Proceedings of the National Academy of Sciences of the United States of America* 108(21): 8565–70.

Ramanathan, Charulatha et al. 2004. "Noninvasive Electrocardiographic Imaging for Cardiac Electrophysiology and Arrhythmia." *Nature medicine* 10(4): 422–28.

Rein, A.J.J.T. et al. 2002. "Use of Tissue Velocity Imaging in the Diagnosis of Fetal Cardiac Arrhythmias." *Circulation* 106(14).

Robin, J, B Arnal, M. Tanter, and M. Pernot. 2017a. "3D Imaging with a Time Reversal Cavity: Towards Transcostal Focusing for Shock Wave Therapy." *IRBM* 38(4): 234–37.

Robin, J, B Arnal, M Tanter, and M Pernot. 2017b. "A 3D Time Reversal Cavity for the Focusing of High-Intensity Ultrasound Pulses over a Large Volume." *Physics in Medicine and Biology* 62(3): 810–24.

Robin, J, Mickael Tanter, and Mathieu Pernot. 2017. "A Semi-Analytical Model of Time Reversal Cavity for High Amplitude Focused Ultrasound Applications." *Physics in Medicine and Biology*.

Sackmann, M et al. 1988. "Shock-Wave Lithotripsy of Gallbladder Stones. The First 175 Patients." *The New England journal of medicine* 318(7): 393–97.

Silbernagl, Stefan., Agamemnon. Despopoulos, and Daniel Laurent. 1992. Médecine-sciences *Atlas de Poche de Physiologie*. Flammarion médecine sciences.

Tempany, Clare M. C., Nathan J. McDannold, Kullervo Hynynen, and Ferenc A. Jolesz.

2011. “Focused Ultrasound Surgery in Oncology: Overview and Principles.” *Radiology* 259(1): 39–56.

Tzu-Yin Wang et al. 2011. “Active Focal Zone Sharpening for High-Precision Treatment Using Histotripsy.” *IEEE Transactions on Ultrasonics, Ferroelectrics and Frequency Control* 58(2): 305–15.

Villemain, O. et al. 2016. “Pulsed Cavitational Ultrasound for Non-Invasive Chordal Cutting Guided by Real-Time 3D Echocardiography.” *European Heart Journal – Cardiovascular Imaging* 17(10): 1101–7.

Villemain, O., J Robin, et al. 2017. “Pulsed Cavitational Ultrasound Softening.” *JACC: Basic to Translational Science*.

Villemain, O., Fidelio Sitefane, et al. 2017. “Toward Noninvasive Assessment of CVP Variations Using Real-Time and Quantitative Liver Stiffness Estimation.” *JACC: Cardiovascular Imaging*.

Vlahos, Antonios P, James E Lock, Doff B McElhinney, and Mary E van der Velde. 2004. “Hypoplastic Left Heart Syndrome with Intact or Highly Restrictive Atrial Septum: Outcome after Neonatal Transcatheter Atrial Septostomy.” *Circulation* 109(19): 2326–30.

Vlaisavljevich, E et al. 2014. “Effects of Tissue Mechanical Properties on Susceptibility to Histotripsy-Induced Tissue Damage.” *Physics in medicine and biology* 59(2): 253–70.

Wakiyama, Hidetaka et al. 2004. “Chordal Cutting for the Treatment of Ischemic Mitral Regurgitation: Two Case Reports.” *Journal of cardiology* 44(3): 113–17.

Weindling, Steven N. et al. 1994. “Myocardial Perfusion, Function and Exercise Tolerance after the Arterial Switch Operation.” *Journal of the American College of Cardiology* 23(2): 424–33.

Wyman, Bradley T., William C. Hunter, Frits W. Prinzen, and Elliot R. McVeigh. 1999. “Mapping Propagation of Mechanical Activation in the Paced Heart with MRI Tagging.” *American Journal of Physiology - Heart and Circulatory Physiology* 276(3).

Xu, Zhen et al. 2004. “Controlled Ultrasound Tissue Erosion.” *IEEE transactions on ultrasonics, ferroelectrics, and frequency control* 51(6): 726–36.

Xu, Zhen et al. 2008. “Evolution of Bubble Clouds Induced by Pulsed Cavitational Ultrasound

Therapy - Histotripsy." *IEEE transactions on ultrasonics, ferroelectrics, and frequency control* 55(5): 1122–32.

Xu, Zhen et al. 2010. "Noninvasive Creation of an Atrial Septal Defect by Histotripsy in a Canine Model." *Circulation* 121(6): 742–49.

Xu, Zhen, Zhenzhen Fan, Timothy L Hall, and Frank Winterroth. 2009. "Size Measurement of Tissue Debris Particles Generated from Pulsed Ultrasound Cavitational Therapy–histotripsy." *Ultrasound in medicine …* 35(2): 245–55.

Résumé du travail scientifique

Brevet :

1. Methods and Apparatus for Treating Valvular Disease.(PCT/FR2016/050751). Inventors : Messas E, Pernot M, Tanter M, Villemain O

Publications dans des journaux avec comité de relecture :

1. Villemain O, Kwiecinski W, Bel A, Robin J, Bruneval P, Arnal B, Tanter M, Pernot M, Messas E. *Pulsed cavitational ultrasound for non-invasive chordal cutting guided by real-time 3D echocardiography*. Eur Heart J Cardiovasc Imaging. 2016
2. Villemain O, Sitefance F, Pernot M, Malekzadeh-Milani S, Tanter M, Bonnet D, Boudjemline Y. *Towards non-invasive assessment of central venous pressure using real time and quantitative liver stiffness estimation.* JACC Cardiovasc Imaging. 2017
3. Villlemain O, Robin J, Bel A, Kwiecinski W, Bruneval P, Arnal B, Rémond M, Tanter M, Messas E, Pernot M. *Pulsed Cavitational Ultrasound Softening: a new non-invasive therapeutic approach of calcified bioprosthetic valve stenosis.* JACC Basic to Trans Science. 2017
4. Villemain O, Correia M, Mousseaux E, Baranger J, Zarka S, Podetti I, Soulat G, Damy T, Hagège A, Tanter M, Pernot M, Messas E. *Myocardial stiffness and aging: non-invasive shear wave imaging evaluation in healthy and hypertrophic cardiomyopathy adults.* In review
5. Villemain O, Correia M, Khraiche D, Podetti I, Meot M, Legendre A, Tanter M, Bonnet D, Pernot M. *Myocardial stiffness assessment using shear wave imaging in heathy children and hypertrophic cardiomyopathy.* JACC Cardiovasc Imaging. 2017 (In Press)
6. Villemain O et al. *Myocardial stiffness in cardiac amyloidosis and heart failure*. In preparation
7. Papadacci C, Finel V, Provost J, Villemain O, Bruneval P, Gennisson JL, Tanter M, Fink M, Pernot M*. Imaging the dynamics of cardiac fiber orientation in vivo using 3D Ultrasound Backscatter Tensor Imaging.* Sci Rep. 2017
8. Maresca D, Correia M, Villemain O, Bizé A, Sambin L, Tanter M, Ghaleh B, Pernot M. *Non-invasive imaging of the coronary vasculature using ultrafast ultrasound*. JACC Cardiovasc Imaging. 2017

9. Correia M, Provost J, Chatelin S, Villemain O, Tanter M, Pernot M. *Ultrafast harmonic coherent compound (UHCC) imaging for high frame rate echocardiography and shear wave elastography*. IEEE Trans Ultrason Ferroelectr Freq Control. 2016
10. Correia M, Podetti I, Villemain O, Baranger J, Tanter M, Pernot M. *Validation of a non-invasive Myocardial Shear Wave Elastography device for clinical applications in cardiology*. IRBM, 2017
11. Pontailler M, Ahmad B, Blanchy M, Voisin A, Villemain O, Menasché P, Williams G, Kalfa D. *TPU/PCL Polymer As A Candidate For Tissue Engineered Heart Valve Replacement Scaffold*. (In preparation)
12. Baranger J et al. *Korotkoff noises*. (In preparation)
13. Finel V et al. *Electromechanical wave imaging in human fetus.* (In preparation)
14. Soulat G et al. *Thoracic aorta PWV assessment by using 4D flow in MRI.* (In preparation)

Résumés acceptés dans des conférences internationales :

1. Mafalda Correia, Simon Chatelin, Clement Padacci, Jean Provost, Olivier Villemain, Mickael tanter, and Mathieu Pernot, "*Ultrafast Harmonic Compounding for cardiac shear wave imaging*", IEEE International Ultrasonics Symposium, Chicago, United States, 2014.
2. Olivier Villemain. *L'histotripsie (thérapie par ultrasons focalisés) a-t-elle des indications possibles en cardiologie ?* RFMCC, Bordeaux, 2014 (speaking invitation)
3. Olivier Villemain, Mathieu Pernot, Wojciech Kwiecinski, Justine Robin, Alain Bel, Mickael Tanter, Albert Hagege, Emmanuel Messas. *Non invasive ultrasonic chordal cutting*. ESC, London, UK, 2015
4. Mafalda Correia, Jean Provost, Simon Chatelin, Olivier Villemain, Mickael Tanter, and Mathieu Pernot, "*In vivo transthoracic cardiac shear wave elastography using ultrafast harmonic coherent compound imaging*", Fourteenth International Tissue Elasticity Conference (ITEC), Verona, Italy, 2015. (Student Award Finalist)
5. Olivier Villemain, Wojciech Kwiecinski, Alain Bel, Justine Robin, Mickael Tanter, Albert Hagege, Emmanuel Messas, Mathieu Pernot. *Non invasive ultrasonic chordal cutting*. ParisEcho, Paris, 2015
6. Olivier Villemain, Wojciech Kwiecinski, Alain Bel, Justine Robin, Mickael Tanter, Albert Hagege, Emmanuel Messas, Mathieu Pernot. *Non invasive ultrasonic chordal cutting*. ISTU, Ultrecht, Netherland, 2015
7. Olivier Villemain, Wojciech Kwiecinski, Alain Bel, Justine Robin, Mickael Tanter,

Albert Hagege, Emmanuel Messas, Mathieu Pernot. *Non invasive ultrasonic chordal cutting*. AEPC, Prague, Czech republic, 2015

8. David Maresca, Mafalda Correia, Olivier Villemain, Biajn Ghaleh, Mickael Tanter, and Mathieu Pernot, "*Ultrafast Doppler imaging of intramyocardial coronary arteries* ", IEEE International Ultrasonics Symposium, Taipei, Taiwan, 2015.
9. Olivier Villemain, Wojciech Kwiecinski, Alain Bel, Justine Robin, Mickael Tanter, Albert Hagege, Emmanuel Messas, Mathieu Pernot. *Non invasive ultrasonic chordal cutting*. IEEE, Taipei, Taiwan, 2015
10. Olivier Villemain. *Histotripsy Cardiac Therapy*. RFMCC, Martinique, 2015 (speaking invitation)
11. David Maresca, Mafalda Correia, Olivier Villemain, Biajn Ghaleh, Mickael Tanter, and Mathieu Pernot, "*Ultrafast Doppler imaging of intramyocardial coronary arteries* ", European Hear Journal – Cardiovascular Imaging, Seville, Spain, 2015. (Young investigator Award)
12. Olivier Villemain, Wojciech Kwiecinski, Alain Bel, Justine Robin, Mickael Tanter, Albert Hagege, Emmanuel Messas, Mathieu Pernot. *Non invasive ultrasonic chordal cutting*. EuroEcho, Seville, Spain, 2015. (Young investigator Award)
13. Olivier Villemain. *Néo-cordages : des moutons et des hommes*. JESFC, Paris, France, 2016 (speaking invitation)
14. Olivier Villemain, Mafalda Correia, Diala Khraiche, Mathieu Pernot, Damien Bonnet, "M*yocardial stiffness assessment using shear wave imaging in healthy children and hypertrophic cardiomyopathy*", ESC congress, Rome, Italy, 2016.
15. Olivier Villemain, Fidelio Sitefane, Mathieu Pernot, Sophie Malekzadeh-Milani, Jérome Baranger, Damie Bonnet, Younes Boudjemline. *Liver stiffness by shear wave elastography, new noninvasive and quantitative tool for acute variation estimation of central venous pressure in real-time?* ESC congress, Rome, Italy, 2016.
16. Olivier Villemain, Mafalda Correia, Emmanuel Mousseaux, Diala Khraiche, Jerôme Baranger, Gilles Soulat, Albert Gagège, Samuel Zarka, Youssef Alattar, Mathieu Pernot, Damien Bonnet and Emmanuel Messas, "*Myocardial stiffness assessment using shear wave imaging in healthy children and adults and hypertrophic cardiomyopathy*", IEEE International Ultrasonics Symposium, Tours, France, 2016.
17. Olivier Villemain. *Myocardial Elastography and Hypertrophic Cardiomyopathy*. RFMCC, Bordeaux, 2016 (speaking invitation)
18. Olivier Villemain, Mafalda Correia, Emmanuel Mousseaux, Jerôme Baranger, Gilles Soulat, Albert Gagège, Samuel Zarka, Youssef Alattar, Mathieu Pernot and Emmanuel Messas, "*Evaluation of myocardial stiffness changes over age in healthy*

and hypertrophic cardiomyopathy populations using new noninvasive ultrasound shear wave imaging", AHA congress, New Orleans, United States, 2016.

19. David Maresca, Mafalda Correia, Olivier Villemain, Biajn Ghaleh, Mickael Tanter, and Mathieu Pernot, "*Ultrafast Doppler imaging of intramyocardial coronary arteries* ", ASE congress, United States, 2016.
20. Olivier Villemain, Fidelio Sitefane, Mathieu Pernot, Sophie Malekzadeh-Milani, Jérome Baranger, Damie Bonnet, Younes Boudjemline. *Liver stiffness by shear wave elastography, new noninvasive and quantitative tool for acute variation estimation of central venous pressure in real-time?* EuroEcho, Leipzig, Germany, 2016
21. Olivier Villemain, Mafalda Correia, Diala Khraiche, Mathieu Pernot, Damien Bonnet, "M*yocardial stiffness assessment using shear wave imaging in healthy children and hypertrophic cardiomyopathy*", EuroEcho, Leipzig, Germany, 2016
22. Olivier Villemain, Mafalda Correia, Emmanuel Mousseaux, Jerôme Baranger, Gilles Soulat, Albert Gagège, Samuel Zarka, Youssef Alattar, Mathieu Pernot and Emmanuel Messas. *Myocardial stiffness assessment using shear wave imaging in healthy adult population.* EuroEcho, Leipzig, Germany, 2016
23. Olivier Villemain, Mafalda Correia, Diala Khraiche, Mathieu Pernot, Damien Bonnet, "M*yocardial stiffness assessment using shear wave imaging in healthy children and hypertrophic cardiomyopathy*", 27th JESFC, Paris, France, 2017.
24. Olivier Villemain, Mafalda Correia, Emmanuel Mousseaux, Jerôme Baranger, Gilles Soulat, Albert Gagège, Samuel Zarka, Youssef Alattar, Mathieu Pernot and Emmanuel Messas. *Myocardial stiffness assessment using shear wave imaging in healthy adult population.* 27th JESFC, Paris, France, 2017.
25. Olivier Villemain, Fidelio Sitefane, Mathieu Pernot, Sophie Malekzadeh-Milani, Jérome Baranger, Damie Bonnet, Younes Boudjemline. *Liver stiffness by shear wave elastography, new noninvasive and quantitative tool for acute variation estimation of central venous pressure in real-time?* 27th JESFC, Paris, France, 2017.
26. Olivier Villemain. *Myocardial stiffness assessment using shear wave imaging.* DMI, Leuven, Belgium, 2017 (speaking invitation)
27. Olivier Villemain. *Ultrafast doppler imaging of intramyocardial coronary arteries.* DMI, Leuven, Belgium, 2017 (speaking invitation)
28. Olivier Villemain, Mafalda Correia, Diala Khraiche, Mathieu Pernot, Damien Bonnet, "M*yocardial stiffness assessment using shear wave imaging in healthy children and hypertrophic cardiomyopathy*", AEPC, Lyon, France, 2017.
29. Olivier Villemain, Mafalda Correia, Emmanuel Mousseaux, Jerôme Baranger, Gilles Soulat, Albert Gagège, Samuel Zarka, Youssef Alattar, Mathieu Pernot and

Emmanuel Messas. *Myocardial stiffness assessment using shear wave imaging in healthy adult population.* AEPC, Lyon, France, 2017.

30. Olivier Villemain, Fidelio Sitefane, Mathieu Pernot, Sophie Malekzadeh-Milani, Jérome Baranger, Damie Bonnet, Younes Boudjemline. *Liver stiffness by shear wave elastography, new noninvasive and quantitative tool for acute variation estimation of central venous pressure in real-time?* AEPC, Lyon, France, 2017.
31. Olivier Villemain, Justine Robin, Alain Bel, Wojciech Kwiencinski, Patrick Bruneval, Bastien Arnal, Mathieu Rémond, Mickael Tanter, Emmanuel Messas, Mathieu Pernot. *Pulsed Cavitational Ultrasound Softening: a new noninvasive therapeutic approach for calcified bioprosthetic valve stenosis*. IEEE, Washington, USA, 2017.

Prix:

1. **Young Investigator Award (YIA) EuroEcho Imaging 2015.** *Pulsed cavitational ultrasound for non-invasive chordal cutting guided by real-time 3D echocardiography*
2. **Best Rapid Presentation ParisEcho 2015.** *Pulsed cavitational ultrasound for non-invasive chordal cutting guided by real-time 3D echocardiography*
3. **Highscorer Abstract EuroEcho Imaging 2016.** *Towards non-invasive assessment of central venous pressure using real time and quantitative liver stiffness estimation*
4. **Highlights Abstract EuroEcho Imaging 2016.** *Myocardial stiffness assessment using shear wave imaging in healthy children and hypertrophic cardiomyopathy*

Financement obtenu :

Appel à Projet de la Fondation de l'Avenir, AP-RMA-A6-032 (32.000€): *"Evaluation de l'anatomie et du flux coronarien par doppler ultrafast – application en cardiologie pédiatrique*

Résumé de Thèse

Cette thèse avait pour but d'élargir le champ d'application des ultrasons en cardiologie, dans le domaine de l'imagerie et dans le domaine de la thérapie.

Concernant l'imagerie, ce sont les capacités, les atouts et les limites des ultrasons à hautes cadences d'image (ultrafast echo) qui ont été explorés. Dans un premier temps, nous avons montré la possibilité et l'intérêt d'estimer la rigidité du myocarde par ultrason en pratique clinique, chez l'enfant et chez l'adulte. La technique de l'élastographie par onde de cisaillement, utilisant une nouvelle approche de l'imagerie par sommation cohérente harmonique ultrarapide (imagerie non-linéaire), a été appliquée pour la première fois chez l'humain en cardiologie. De plus, nous avons montré que la rigidité du foie, également estimée grâce à l'élastographie par onde de cisaillement, était directement corrélée aux pressions de remplissage du cœur droit, qui sont difficiles à évaluer de manière quantitative en pratique clinique. Dans un second temps, nous nous sommes intéressés à caractériser l'orientation des fibres myocardiques durant le cycle cardiaque en développant l'imagerie du tenseur de rétrodiffusion ultrasonore en trois dimensions. Le but était de réaliser la preuve de concept sur un cœur battant afin d'ouvrir sur les possibilités d'applications. Dans un troisième temps, le doppler de puissance en ultrafast echo nous a permis d'estimer les capacités des ultrasons à visualiser et analyser les flux (et donc les débits) intra coronariens. C'est à l'heure actuelle la seule technique d'imagerie clinique ayant une résolution spatiale (et temporelle) suffisante pour voir les flux dans des vaisseaux ayant un diamètre inférieur à 500 micromètres. Enfin, l'ultrafast echo nous a permis de visualiser les micro déplacements du myocarde, qui sont eux-mêmes initiés par l'activité électrique intra-myocardique, dans un intervalle de temps très réduit. Ceci est le couplage électromécanique, et y avoir accès par ultrason ouvrirait de multiples perspectives. Nous avons commencé à l'appliquer chez le fœtus humain et chez l'adulte en transthoracique.

Concernant la thérapie, nous avons exclusivement utilisé les effets mécaniques des ultrasons focalisés à hautes intensités (phénomène de cavitation). Plusieurs équipes avaient déjà montré que cela était applicable en médecine cardiovasculaire, notamment pour perforer le septum inter-atrial (zone musculaire séparant les deux oreillettes cardiaques) ou pour détruire un thrombus intravasculaire. Nous avons décidé de montrer que le phénomène de cavitation pour avoir deux autres applications distinctes : 1) la section de cordage valvulaire mitral, qui est une technique utilisée actuellement en chirurgie (donc à cœur ouvert et en circulation extra-corporelle) visant à diminuer une fuite valvulaire à cause de cordage restrictif ; 2) l'assouplissement des feuillets valvulaires calcifiés, qui est une maladie représentant un enjeu de santé publique touchant des millions de personnes, et n'ayant à ce jour aucune stratégie non invasive disponible et applicable en pratique clinique. Pour ces deux applications, nous avons réalisé des preuves de concept in vitro puis in vivo à cœur battant, sur modèle animal (ovin). L'application humaine sera la prochaine étape.

C'est donc la translation de nouvelles technologies ultrasonores vers des applications cliniques en cardiologie qui a motivé et guidé ce travail de thèse.